Polar föhn winds and warming over the Larsen C Ice Shelf, Antarctica

A thesis submitted to the
School of Environmental Sciences
of the
University of East Anglia
in candidature for the degree of
Doctor of Philosophy

By
Andrew David Elvidge
September 2013

Abstract

Recent hypotheses that the foehn effect is partly responsible for warming to the east of the Antarctic Peninsula (AP) and enhanced melt rates on the Larsen C Ice Shelf are supported in a study combining the analysis of observational and high resolution model data. Leeside warming and drying during foehn events is observed in new aircraft, radiosonde and automatic weather station data and simulated by the UK Met Office Unified Model at ~1.5 km grid spacing (MetUM 1.5 km). Three contrasting cases are investigated. In *Case A* relatively weak southwesterly flow induces a non-linear foehn event. Strongly accelerated flow above and a hydraulic jump immediately downwind of the lee slopes lead to high amplitude warming in the immediate lee of the AP, downwind of which the warming effect diminishes rapidly due to the upward 'rebound' of the foehn flow. *Case C* defines a relatively linear case associated with strong northwesterly winds. The lack of a hydraulic jump enables foehn flow to flood across the entire ice shelf at low levels. Melt rates are high due to a combination of large radiative heat flux, due to dry, clear leeside conditions, and sensible heat flux downward from the warm, well-mixed foehn flow. Climatological work suggests that such strong northwesterly cases are often responsible for high Larsen C melt rates. *Case B* describes a weak, relatively non-linear foehn event associated with insignificant daytime melt rates.

Previously unknown jets – named polar foehn jets – emanating from the mouths of leeside inlets are identified as a type of gap flow. They are cool and moist relative to adjacent calmer regions, due to lower-altitude upwind source regions, and are characterised by larger turbulent heat fluxes both within the air column and at the surface.

The relative importance of the three mechanisms deemed to induce leeside foehn warming (isentropic drawdown, latent heating and sensible heating) are quantified using a novel method analysing back trajectories and MetUM 1.5 km model output. It is shown that, depending on the linearity of the flow regime and the humidity of the air mass, each mechanism can dominate. This implies that there is no dominant foehn warming mechanism, contrary to the conclusions of previous work.

Acknowledgements

Polar Föhn

Have you the time,

for an Antarctic fable?

It regards a boundary layer,
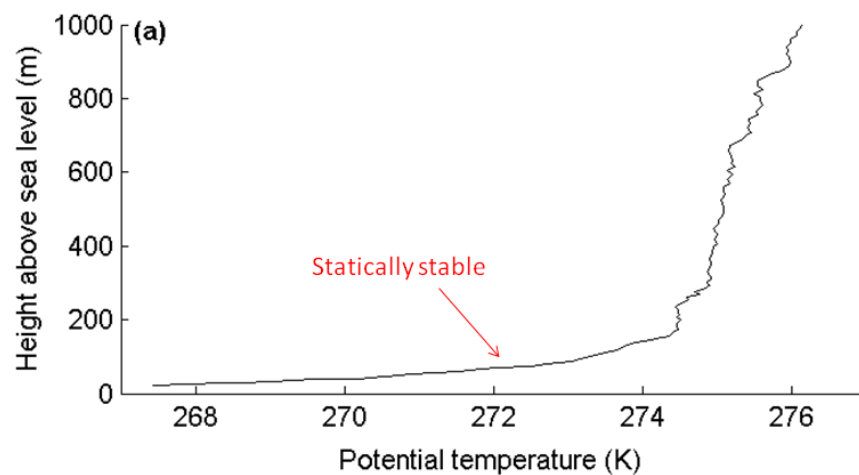
that was statically stable;

For weeks it persists,

unyielding, omnipresent;

The penguins are chilly,

their lives most unpleasant;

On their minds ~ the sun...

...or rather the lack thereof;
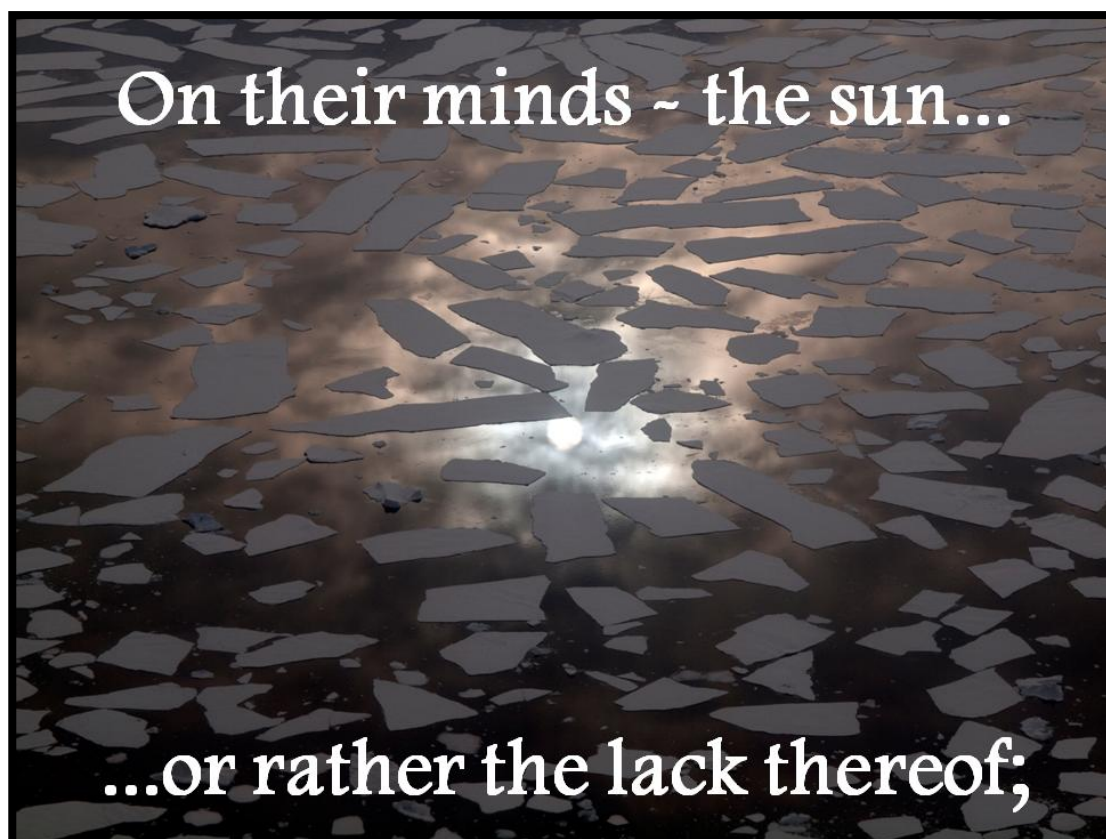
Katabatics, cold-air pooling,
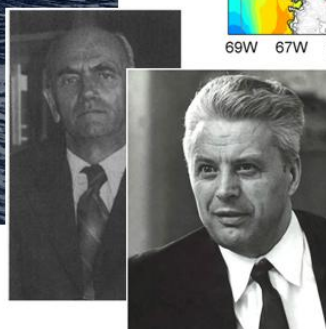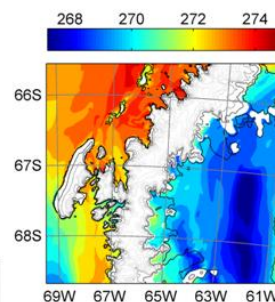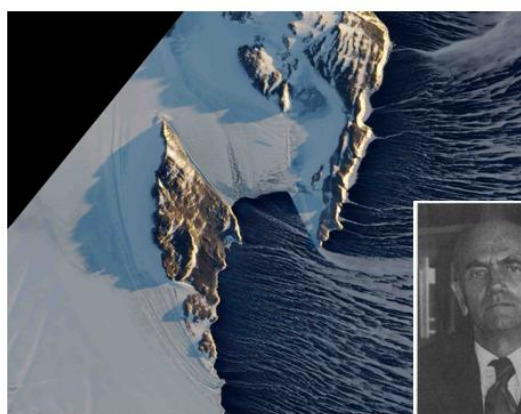
Monin-Obukhov...?

Then one day, a strong wind approaches;
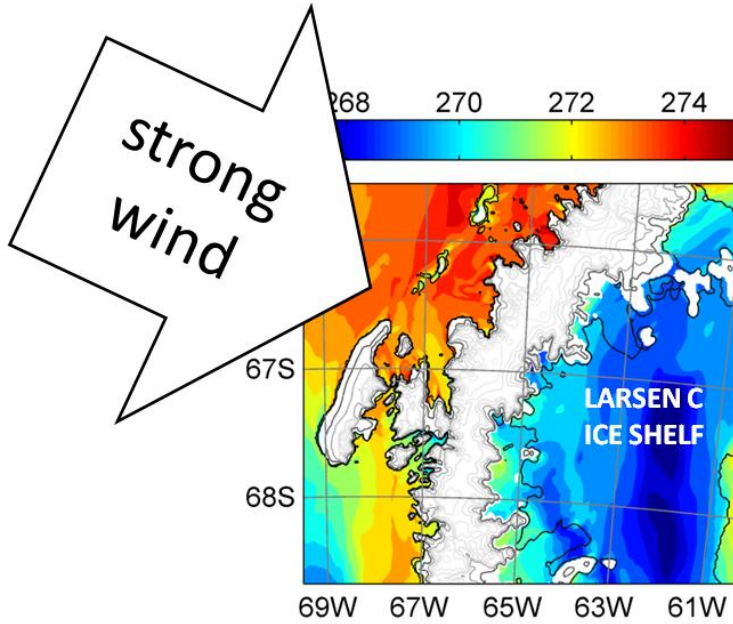
Across the mountains, it encroaches;

Cascading down, it grows quite warm;

Lovely sunshine, downslope windstorm;
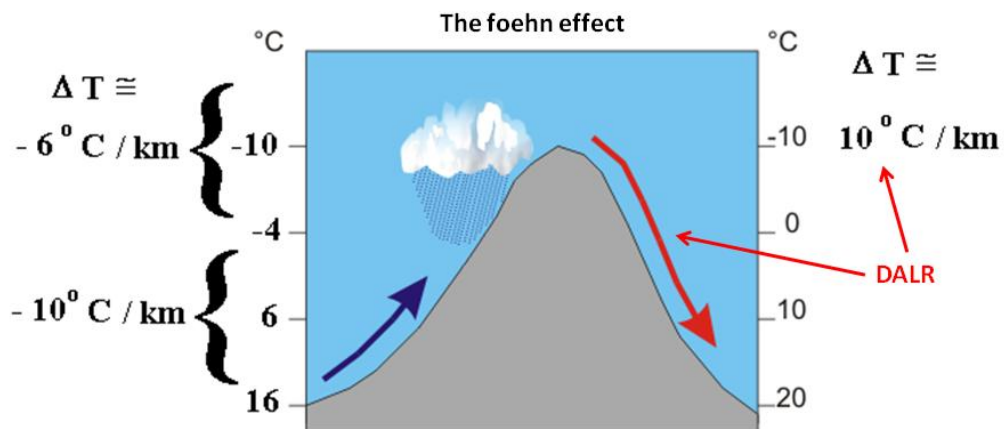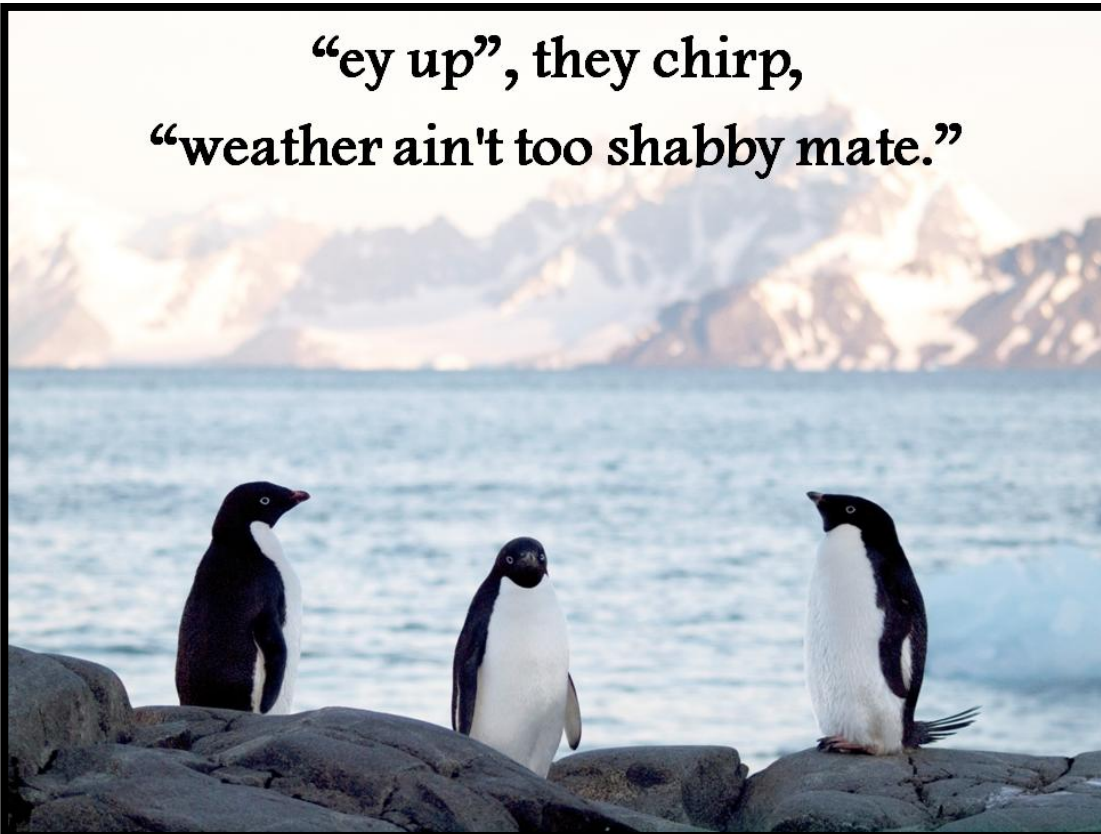
And so the deep SBL is conquered...

SBL = Stable Boundary Layer

BEFORE AFTER
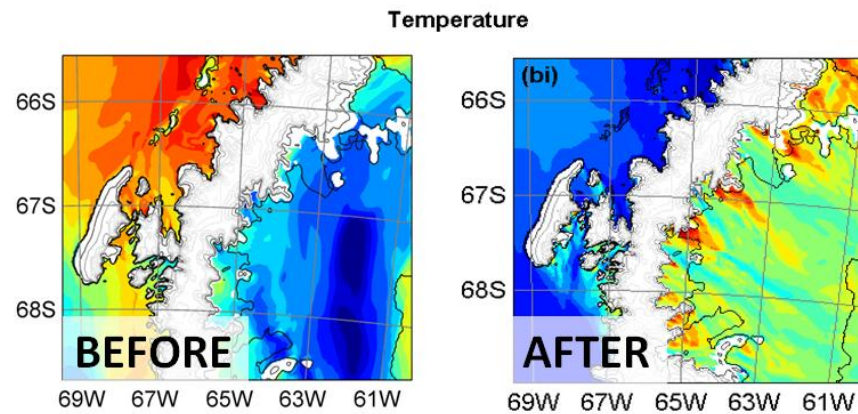
forced to adjourn;

For this is life in the lee of the hills,

SW radiation + Sensible heat
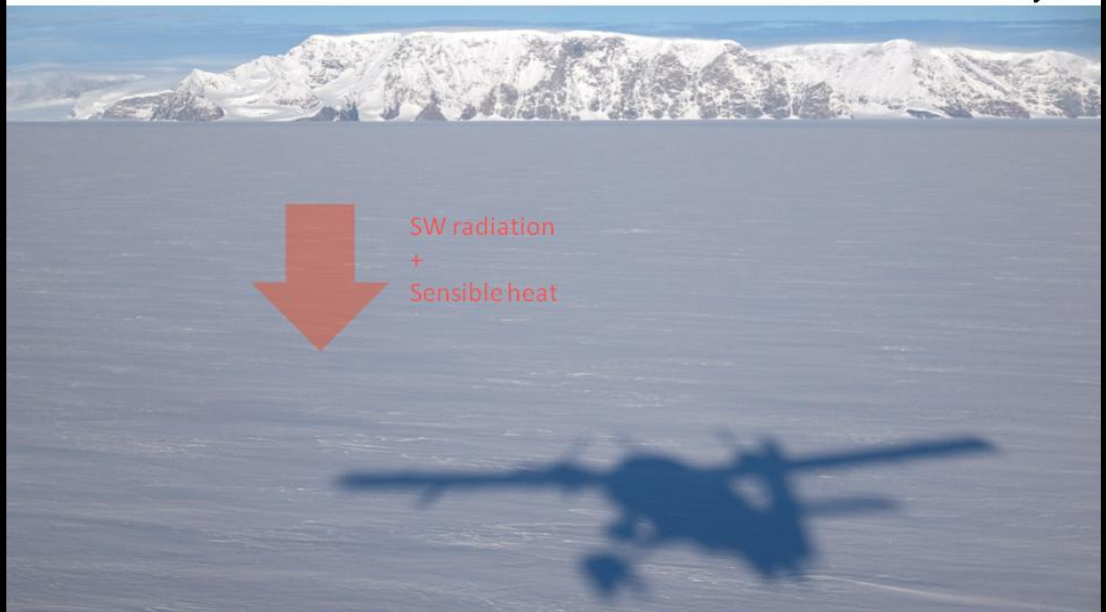
during a polar föhn.

Contents

Chapter 1

Background: The effect of mountains on the atmosphere in relation to westerly flow across the Antarctic Peninsula

Contents

List of figures

List of tables

1.1 Introduction

1.1.1 Climate change and föhn winds over the Antarctic Peninsula

Over the past 50 years the Antarctic Peninsula (AP) has warmed more rapidly than any other region in the southern hemisphere. This warming has been particularly great during the summer months on the eastern coast of the AP, where large ice shelves extend eastwards over the Weddell Sea. In response to the warming these ice shelves have experienced steady southward retreat since records began. In 1995 the northernmost section of the massive Larsen ice shelf – the Larsen A – collapsed, followed in 2002 by the next northernmost section – the Larsen B. The latter disintegrated in spectacular fashion, over a two day period losing 3300 km^2 of ice – an area over twice that of London. It has been established that atmospheric warming (as opposed to basal warming by the sea) was likely the driving mechanism for this collapse.

The warming on the AP has been attributed to changes in large scale circulation. Recent strengthening of the mean westerly winds that circumnavigate the pole are thought to have increased the prevalence of relatively warm, maritime westerlies impinging on the AP, at the expense of cool continentally derived air from the south. However, to explain the asymmetry of the warming (east coast warming surpassing that to the west), Antarctic scientists have turned to a smaller-scale phenomenon. They suggested that warming to the east of the AP during westerly flow may not only be due to the increased advection of warm westerly winds replacing cooler continental air masses, but to the effect of leeside föhn warming associated with cross-Peninsula flow.

The föhn is a much-studied phenomenon describing the warm, dry downslope winds which occur to the lee of mountains in response to the passage of stably stratified flow over the top of the mountains. Since the dawn of foehn theory in the 19th century the mechanisms involved have been a matter of dispute in the scientific community. Why are föhn winds stronger than the mean flow? Where are föhn winds sourced from? How far downwind do föhn winds penetrate? What makes the föhn warm and dry? Such questions have been addressed in the literature to variable degrees of success. Many studies have used idealised models of flow over 2-dimensional terrain to simplify the problem, though the relevance of such studies to

the real world of complex, multi-scale 3-dimensional orography is questionable. The AP, as an isolated north-south orientated high level ridge emerging from the ocean in a region renowned for its strong westerly wind, provides an excellent natural laboratory for the investigation of the föhn. As such, the study of föhn across the AP provides an opportunity to not only investigate the as yet relatively untested hypothesis that it may be to a large extent responsible for the particularly high amplitude warming to the east of the AP, but also to improve our understanding of its nature and the mechanisms involved.

This study forms part of the Orographic Flows and Climate of the Antarctic Peninsula (OFCAP) project, and uses a combination of observational data gathered during a field campaign and high resolution Numerical Weather Prediction model output to investigate the problem of föhn flow over the AP more thoroughly and at a higher resolution than any previous study. More specifically, the study focuses on the causes and consequences of föhn flow using results from three different case studies.

Before the presentation and examination of the results, explanation of the relevant background theory and the methods used to tackle the problem is presented. In chapter 2 the climatic aspects introduced here which motivate this study are expanded upon, and the methodology is described. In this chapter the background theory of flow over mountains is reviewed, focussing on phenomena relevant to the case of the Antarctic Peninsula (AP).

1.1.2 The effect of mountains on the atmosphere

If the earth were shrunk to a similar size, its surface would be smoother than that of a varnished billiard ball. Yet the influence of mountains on the atmosphere is profound (Smith, 1979). The billiard ball model illustrates that variation in the elevation of the earth's surface is insignificant relative to the earth's diameter. Yet at the same scale the atmosphere is but a thin layer surrounding the earth. So, whilst insignificant relative to the earth's diameter, the planet's larger mountains occupy a considerable proportion of the atmosphere's depth; Mount Everest extends almost all the way to the tropopause.

The manner in which a mountain or mountain range affects atmospheric flow is dependent on its size and shape. The along-wind length of the mountain relative to appropriate atmospheric length scales, particularly those of the turning of flow

(apparent in the non-inertial frame of reference) due to the rotation of the earth and the wavelength of internal buoyancy waves, is significant. The height of the mountain is important, insomuch as the potential energy required to surmount an obstacle relative to the kinetic energy possessed by the approaching flow determines how much air is able to pass over the obstacle. The shape of the obstacle, for example whether an isolated dome or an elongated ridge, is another key consideration, as is the vertical structure (in wind velocity and stability) of the atmosphere.

1.2 The effect of rotation on the atmosphere at planetary scales

1.2.1 Importance of rotation for flow across the Antarctic Peninsula

The horizontal equations of motion in cartesian coordinates are

$$\frac{Du}{Dt} - fv = -\frac{1}{\rho}\frac{\partial p}{\partial x}$$

$$\frac{Dv}{Dt} + fu = -\frac{1}{\rho}\frac{\partial p}{\partial y},$$

where u and v are horizontal velocity components, p is pressure, ρ is density and $f(y) = 2\Omega \sin(\phi)$ is the Coriolis parameter (where Ω is the angular velocity of earth's rotation and ϕ is the latitude) and $\frac{D}{Dt} = \frac{\partial}{\partial t} + u\frac{\partial}{\partial x} + v\frac{\partial}{\partial y}$ is the horizontal material derivative (after Holton, 2004). Assuming geostrophic equilibrium, the Coriolis and pressure gradient terms cancel out ($-fv = -\frac{1}{\rho}\frac{\partial p}{\partial x}$ and $fu = -\frac{1}{\rho}\frac{\partial p}{\partial y}$) and there is no horizontal Lagrangian acceleration.

The Rossby number is a measure of the validity of the geostrophic approximation, being the ratio of inertial to Coriolis forces:

$$R_0 = \frac{(U^2/L)}{f_0 U} = \frac{U}{f_0 L},$$

where L is mountain length (in the along-flow direction) and U is wind speed. In the case of flow defined by small $R_0 (\approx 0)$, the Coriolis term dominates and the geostrophic approximation holds. Taking $L \approx 80$ km, ϕ of 67°S, Coriolis parameter $f_0 = 2\Omega \sin(\phi) \approx -1.3 \times 10^{-4}$ s^{-1} and $U = 10$ ms^{-1} as representative of westerly flow speed approaching the roughly north-south orientated Antarctic Peninsula (of crest height generally between 1500 and 2000 m above mean sea level) in the region of study, we find $R_0 \approx 1$. The high latitude and relatively large obstacle along-wind

length dictates that the Coriolis term is non-negligible relative to the acceleration term, and hence the affects of rotation cannot be ignored in the consideration of flow over the AP.

1.2.2 Effect of rotation on flow across the Antarctic Peninsula

With rotation, the problem of flow over a mountain must be considered as a 3-dimensional one. Let us consider a homogenous incompressible fluid extending eastwards (x) and northwards (y) of thickness dz bounded by the surface topography ($z = h'(x, y)$) and tropopause ($z = H = constant$) approaching an infinite ridge. Flow is assumed to be geostrophic and defined by mean zonal and meridional components of flow $\bar{u} = constant$ and $\bar{v} = 0$ respectively (see Figure 1.1). The barotropic potential vorticity equation provides a useful framework and can be written as

$$\frac{1}{\xi + f}\frac{D}{Dt}(\xi + f) = \frac{1}{dz}\frac{Ddz}{Dt}$$

[1.1]

where ξ is relative vorticity (after Holton, 2004). The components of flow are considered as the sum of the mean (bar) and perturbation (prime) components, such that $u = \bar{u} + u'(x, y)$ and $v = v'(x, y)$. Since $\bar{\bar{\xi}} = \frac{\partial \bar{v}}{\partial x} - \frac{\partial \bar{u}}{\partial y} = 0$, it follows that $\xi = \xi'(x, y)$. Hence, equation [1.1] is linearised, terms which are quadratic in perturbation quantities are ignored, h' is considered to be small relative to H and the steady-state nature of a mountain induced disturbance is considered to give:

$$\frac{\partial \xi'}{\partial t} = -\bar{u}\frac{\partial \xi'}{\partial x} - v'\frac{\partial f}{\partial y} - \frac{f_0}{H}\bar{u}\frac{\partial h'}{\partial x} = 0,$$

[1.2]

where f_0 denotes constant f along lines of latitude (after Holton, 2004). The $-\bar{u}\frac{\partial \xi'}{\partial x}$ term (*term A*) in the above can be interpreted physically to represent zonal advection of perturbation vorticity, the $-v'\frac{\partial f}{\partial y}$ (*term B*) represents meridional advection of planetary vorticity and the $-\frac{f_0}{H}\bar{u}\frac{\partial h'}{\partial x}$ (*term C*) represents vortex stretching due to changes in the height of underlying topography. Where flow encounters the mountain and $\frac{\partial h'}{\partial x} > 0$ a positive vorticity tendency will be imparted by *term C* (note that f is negative in the Southern Hemisphere) due to vortex compression in the vertical

(Figure 1.1). In order to maintain the steady state of equation [1.2], the other 2 terms

must contribute a net negative quantity.
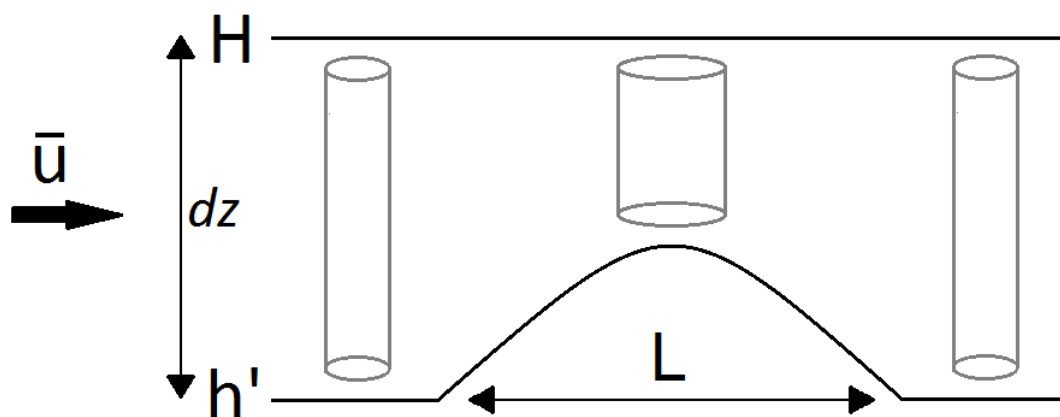
Figure 1.1: Schematic illustrating vortex compression over a mountain of along-wind length *L*. The cylinders represent a set volume of air bounded vertically by the surface topography h', and a free surface (say, the tropopause) H, as flow passes over the mountain.

If *term A* dominates over *term B*, then the relative vorticity balance is achieved

with $-\bar{u}\frac{\partial\xi'}{\partial x} < 0$ and hence $\frac{\partial\xi'}{\partial x} > 0$ above the windward slope, and, conversely $\frac{\partial\xi'}{\partial x} < 0$

on the lee slope. This results in a positive vorticity anomaly and hence an anticyclone

(anticlockwise circulation in the Southern Hemisphere) centred over the mountain

(Figure 1.2). If *term B* dominates, then the balance is achieved with $-v'\frac{\partial f}{\partial y} < 0$, and

hence $v' > 0$ above the windward slope, and poleward air with greater planetary

vorticity (relatively high-f air) is advected in (from the south in the Southern

Hemisphere). Conversely $v' < 0$ on the lee slope, bringing in relatively low-f air from

the north. This results in cyclonic (clockwise in the Southern Hemisphere) circulation

over the mountain.
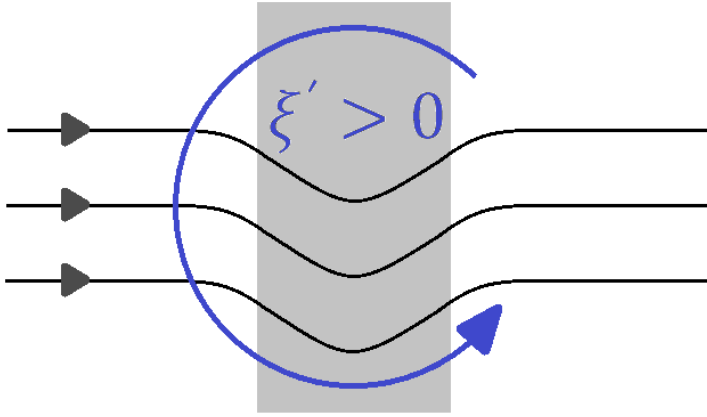
Figure 1.2: Schematic showing streamlines across a mountain ridge (shaded grey) in the southern hemisphere, demonstrating the effect of vortex compression in the vertical in the case where *term A* dominates over *term B* in equation [1.2]. Zonal advection of perturbation relative vorticity (ξ') induces anticyclonic circulation above the ridge.

Whether *term A* or *term B* dominates is dependent on the mountain's along-wind length, L. The disturbance in the flow caused by a mountain can be thought of as a forced stationary Rossby wave. Free Rossby waves are dispersive (larger wavelengths travel faster) and always propagate westward relative to the mean flow, as pertained to by the definition of their phase speed (assuming a westerly mean flow);

$$c = \bar{u} - \frac{1}{K^2}\frac{\partial}{\partial y}\left(f + \bar{\xi}\right),$$

[1.3]

where $K = \frac{2\pi}{\lambda}$ (where λ is wavelength) is the horizontal wavenumber. Usually, for synoptic-scale (horizontal length scale of the order of 1000 km or more) Rossby waves *term A* dominates over *term B*. Since *term A* (*term B*) imparts an eastward (a westward) tendency to wave propagation, whilst propagating westward relative to the mean flow, such waves propagate eastward relative to the earth. For large enough waves, however, *term B* balances *term A* and the wave is stationary. This occurs at stationary wavenumber K_s, which is given by equation [1.3] as

$$K_s = \left(\frac{1}{\bar{u}}\frac{\partial}{\partial y}\left(f + \bar{\xi}\right)\right)^{1/2}$$

(after Holton, 2004). For constant mean westerly flow across the AP, $\frac{\partial f}{\partial y} \approx 9 \times 10^{-12}$ s^{-1} m^{-1}, $\frac{\partial \bar{\xi}}{\partial y} = 0$ and wind speed $\bar{u} = 10$ m s^{-1}, giving stationary wavelength

$$\lambda_s = \frac{2\pi}{K_s} \approx 6200 \text{ km.}$$

For weaker flow, $\bar{u} = 5 \text{ ms}^{-1}$ we find $\lambda_s \approx 4700$ km. Since $L \approx 80$ km (as defined in Section 1.2.1) $\ll \lambda_s$ defines the wavelength of a forced Rossby wave over the AP, *term A* is deemed to dominate *term B*. Hence the net effect of rotation on the large scale flow across the AP is expected to be that of anticyclonic circulation over the ridge (as shown in Figure 1.2). Rotation has other affects on the mesoscale characteristics of flow over a mountain, which will be discussed later in this chapter.

1.3 Response of the atmosphere to flow over a mountain at the mesoscale

Having dealt with the synoptic-scale (horizontal length scale of the order of 1000 km or more) horizontal effect of rotation, we will now explore the response of the atmosphere at the mesoscale (horizontal length scale in the order of 10s to a few 100s of km) to flow over an obstacle such as the AP. We will start by focusing on the effect of a low level perturbation associated with flow over a mountain on the atmosphere above.

1.3.1 Mountain waves

The flow of air over a mountain creates a disturbance whereby, in a stably stratified atmosphere, potentially cool dense air is forced to rise above its environmental equilibrium level. Such a disturbance generates internal gravity waves, for which the restoring force is buoyancy. The highest frequency which such buoyancy-driven vertical oscillations may have is defined by the Brunt Väisälä frequency,

$$N = \left(\frac{g}{\theta} \frac{d\theta}{dz} \right)^{1/2}.$$

Gravity waves may propagate vertically (e.g. the hydrostatic mountain wave shown in Figure 1.3a) or horizontally (e.g. the trapped lee waves shown in Figure 1.3b) depending on the vertical structure of the atmosphere (Smith, 1979). In a continuously stratified atmosphere where N and u are constant with height, wave energy propagates in the same direction as the near surface disturbance, i.e. upwards,

and, so long as the mountain is of sufficient along-wind length (as explained below),

vertically propagating waves are generated.
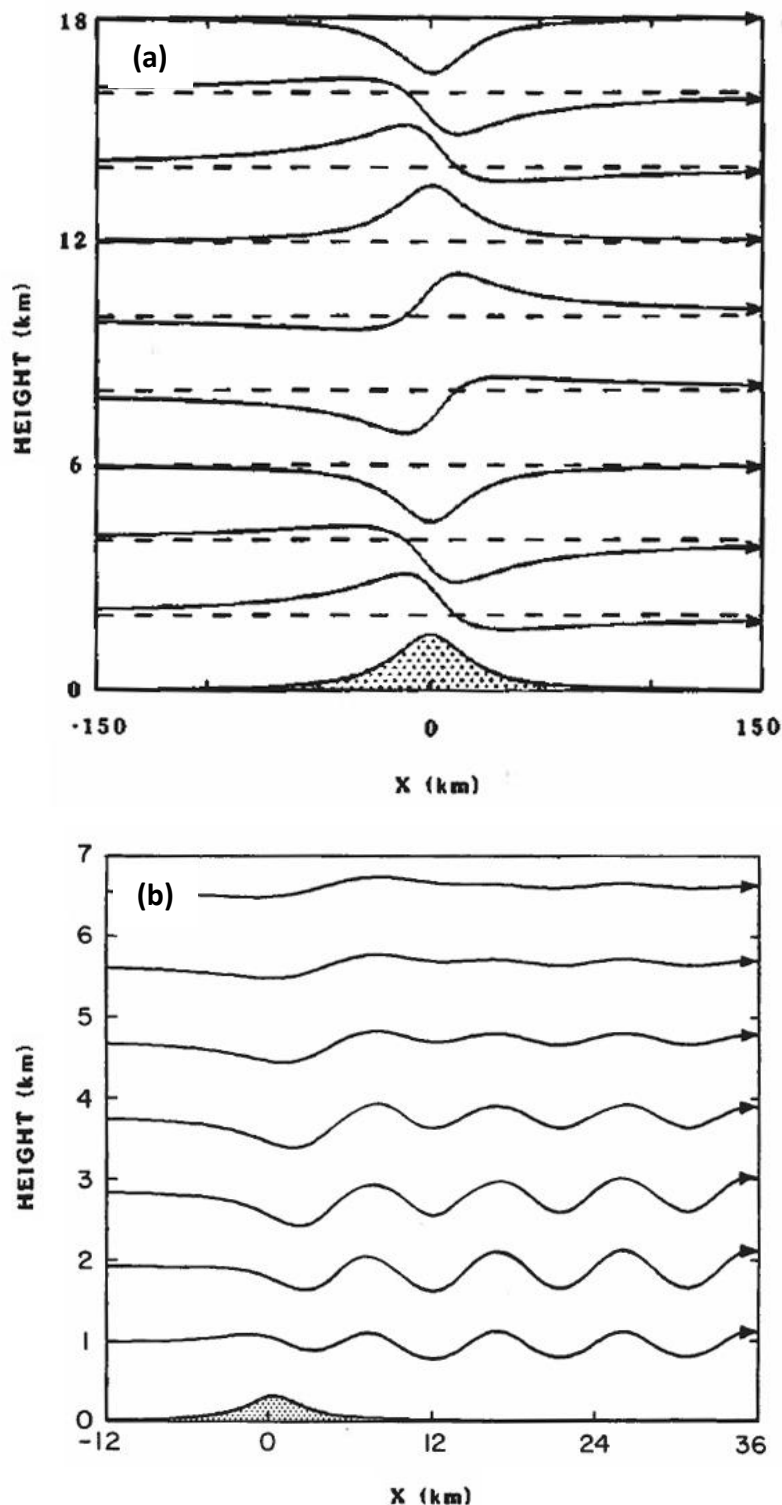
Figure 1.3: Streamlines defined by linear theory for steady flow across a bell-shaped mountain in 2-dimensions where upwind conditions promote a) vertically propagating hydrostatic mountain waves; b) trapped lee waves (due to vertical variation in Scorer parameter). After Durran (1990).

In this section we consider 2-dimensional mountain waves (in the x, z plane) propagating in an inviscid, stably stratified, non-rotating atmosphere. The Boussinesq approximation is made, assuming the atmosphere to be incompressible and local density variations to be sufficiently small perturbations from a mean basic state to be neglected except when they appear in terms multiplied by the acceleration due to gravity. Employing these assumptions, the analytical description of mountain waves begins with the following equations:

horizontal momentum conservation;

$$\frac{\partial u}{\partial t} + u\frac{\partial u}{\partial x} + w\frac{\partial u}{\partial z} + \frac{1}{\rho}\frac{\partial p}{\partial x} = 0\,,$$

[1.4]

vertical momentum conservation;

$$\frac{\partial w}{\partial t} + u\frac{\partial w}{\partial x} + w\frac{\partial w}{\partial z} + \frac{1}{\rho}\frac{\partial p}{\partial z} + g = 0\,,$$

[1.5]

mass conservation;

$$\frac{\partial u}{\partial x} + \frac{\partial w}{\partial z} = 0\,,$$

[1.6]

energy conservation;

$$\frac{\partial \theta}{\partial t} + u\frac{\partial \theta}{\partial x} + w\frac{\partial \theta}{\partial z} = 0\,,$$

[1.7]

where potential temperature θ can be written as a function of pressure and density:

$$\theta = T\left(\frac{p_s}{p}\right)^{R/c_p} = \frac{p}{\rho R}\left(\frac{p_s}{p}\right)^{R/c_p}\,,$$

[1.8]

where T is temperature, p_s is a reference pressure (usually taken to be surface pressure), R is the gas constant and c_p is the specific heat of dry air at constant pressure (after Holton, 2004).

The next step involves linearising these equations [1.4 - 1.7] by letting

$$u = \bar{u} + u'(x, y)\,,$$

$$w = w'(x, y)\,,$$

$$\rho = \rho_0 + \rho'(x, y)\,,$$

$$p = \bar{p}(z) + p'(x, y)\,,$$

$$\theta = \bar{\theta}(z) + \theta'(x, y),$$

where ρ_0 is basic state density, which, along with basic state zonal flow $\bar{u}$ are assumed to be constant,

$$\frac{d\bar{p}}{dz} = -\rho_0 g,$$

After taking logarithms from both sides, equation [1.8] becomes

$$\ln \bar{\theta} = \frac{c_v}{c_p} \ln \bar{p} - \ln \rho_0 + \text{constant},$$

where c_v is the specific heat of dry air at constant volume. The resulting equations, after ignoring terms which are quadratic in perturbation quantities, are as follows:

$$\left(\frac{\partial}{\partial t} + \bar{u} \frac{\partial}{\partial x} \right) u' + \frac{1}{\rho_0} \frac{\partial p'}{\partial x} = 0,$$

$$\left(\frac{\partial}{\partial t} + \bar{u} \frac{\partial}{\partial x} \right) w' + \frac{1}{\rho_0} \frac{\partial p'}{\partial z} - \frac{\theta'}{\bar{\theta}} g = 0,$$

$$\frac{\partial u'}{\partial x} + \frac{\partial w'}{\partial z} = 0,$$

$$\left(\frac{\partial}{\partial t} + \bar{u} \frac{\partial}{\partial x} \right) \theta' + w' \frac{\partial \bar{\theta}}{\partial z} = 0.$$

Eliminating p', u' and θ' by reducing these equations simultaneously we obtain a single equation for w':

$$\left(\frac{\partial}{\partial t} + \bar{u} \frac{\partial}{\partial x} \right)^2 \left(\frac{\partial^2 w'}{\partial x^2} + \frac{\partial^2 w'}{\partial z^2} \right) + N^2 \frac{\partial^2 w'}{\partial x^2} = 0.$$

[1.9]

It is assumed the solution to equation [1.9], defining the vertical perturbations of internal gravity waves, is (excluding imaginary terms) of the form:

$$w' = \hat{w} \cos(kx - mz + vt),$$

where $\hat{w}$ is wave amplitude and $kx - mz + vt$ is the wave phase (with k and m denoting the horizontal and vertical wave numbers, and v the angular frequency). Substituting the assumed solution into equation [1.9] yields the dispersion relationship

$$(v - \bar{u}k)(k^2 + m^2) - N^2 k^2 = 0$$

(Holton, 2004). The intrinsic frequency (frequency observed in the frame moving with the background flow) is then given by

$$\hat{v} = v - \bar{u}k = \pm \frac{Nk}{(k^2 + m^2)^{1/2}} = \pm \frac{Nk}{|\kappa|},$$

where $\boldsymbol{\kappa} \equiv (k, m)$. Horizontal and vertical intrinsic phase speeds (rates at which the phase of the wave propagates in space, relative to the mean flow) are $c_x = \hat{v}/k$ and $c_z = \hat{v}/m$ respectively, whilst the components of the intrinsic group velocity (velocity of the wave packet or of energy propagation, relative to the mean flow) are

$$c_{gx} = \frac{\partial \hat{v}}{\partial k} = \pm \frac{Nm^2}{(k^2 + m^2)^{3/2}},$$

$$c_{gz} = \frac{\partial \hat{v}}{\partial m} = \pm \frac{-Nkm}{(k^2 + m^2)^{3/2}}.$$

It is evident that energy propagation in the vertical is in the opposite z-direction to phase propagation (c_{gz} and c_z have opposite signs), and that the group velocity vector ($\boldsymbol{c}_g$) is perpendicular to the direction of phase propagation (since $\boldsymbol{c}_g \cdot \boldsymbol{\kappa} = \pm \frac{Nkm^2}{(k^2+m^2)^{3/2}} - \frac{Nkm^2}{(k^2+m^2)^{3/2}} = 0$). Hence, energy propagates parallel to the wave crests and troughs, unlike in acoustic or shallow water gravity waves. Figure 1.4 is a schematic diagram of the perturbation fields in an internal gravity wave at an instantaneous point in time. Study of this diagram affords physical insight into why phase propagation is directed perpendicular to wave fronts. For instance, the phase line labelled 'most buoyant fluid' must move down and to the left as the air in the shaded region (which is gaining buoyancy; i.e. $w' < 0$) reaches its lowest elevation (i.e. forms the wave trough).
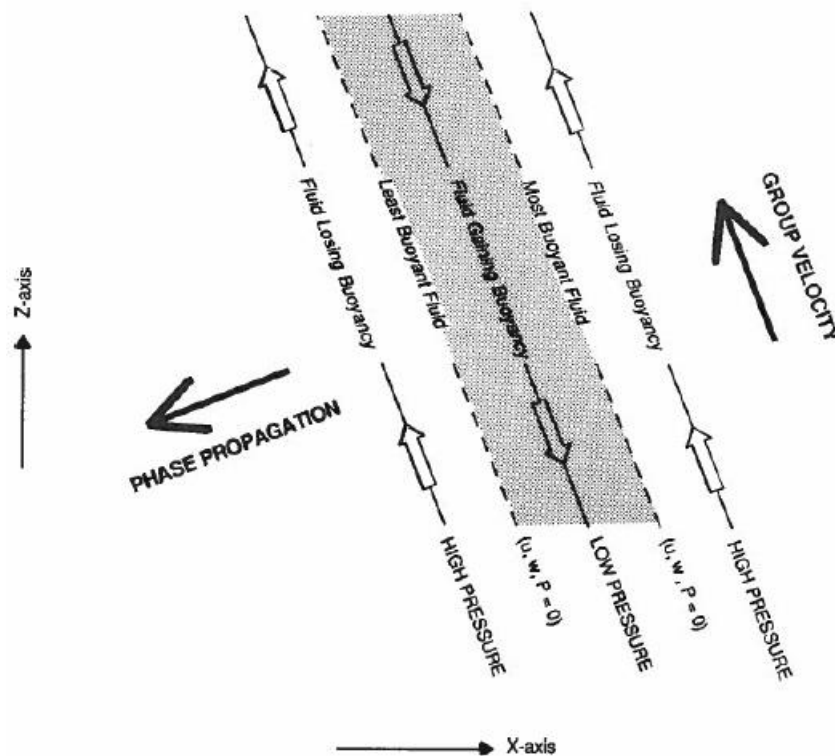
Figure 1.4: Schematic describing instantaneous perturbation fields (x-direction wind speed u, vertical velocity w, pressure P) in an internal gravity wave in the x-z plane. Open arrows along phase lines indicate the direction of air movement. After Durran (1990).

Queney (1947) considered waves above an infinite series of periodic ridges defined by a sinusoidal function. In this case the waves excited are stationary relative to the ground (so that phase velocity, $c = 0$), and the time derivative in equation [1.9] disappears to leave

$$\left(\frac{\partial^2 w'}{\partial x^2} + \frac{\partial^2 w'}{\partial z^2}\right) + \frac{N^2}{\bar{u}^2} w' = 0.$$

[1.10]

Substituting [1.9] into the above we find the dispersion relationship

$$m^2 = \frac{N^2}{\bar{u}^2} - k^2.$$

It follows that m is real if $\bar{u} < N/k$. Hence, if the buoyancy frequency N exceeds the intrinsic frequency $\bar{u}k$, vertical propagation of hydrostatic mountain waves is supported by wave crests being tilted upstream at an angle of $\alpha = \cos^{-1} \bar{u}k/N$ from the vertical (Durran, 1990) (Figure 1.3a and Figure 1.5b). Since the energy source for these waves is at the surface, energy propagation (and the group velocity vector) must be directed upwards and phase propagation must have a downwards component. As $\bar{u}k$ increases (i.e. the horizontal wavelength or the along-wind length of the mountain decreases, assuming constant $\bar{u}$), the vertical wavelength will increase until m becomes imaginary where $\bar{u}k > N$. In this case there is no way for buoyancy forces to support such a small disturbance and the resulting waves are evanescent (decay exponentially with height) with wave crests and troughs aligned vertically (Figure 1.5a). Waves defined by $\bar{u}k$ only marginally less than N may be non-hydrostatic where energy propagates both vertically and horizontally. In the case of real mountains, complexities in orography define a wide spectrum of length scales, giving rise to a variety of propagation modes, and the resultant wave field can be expected to radiate energy both vertically and horizontally.
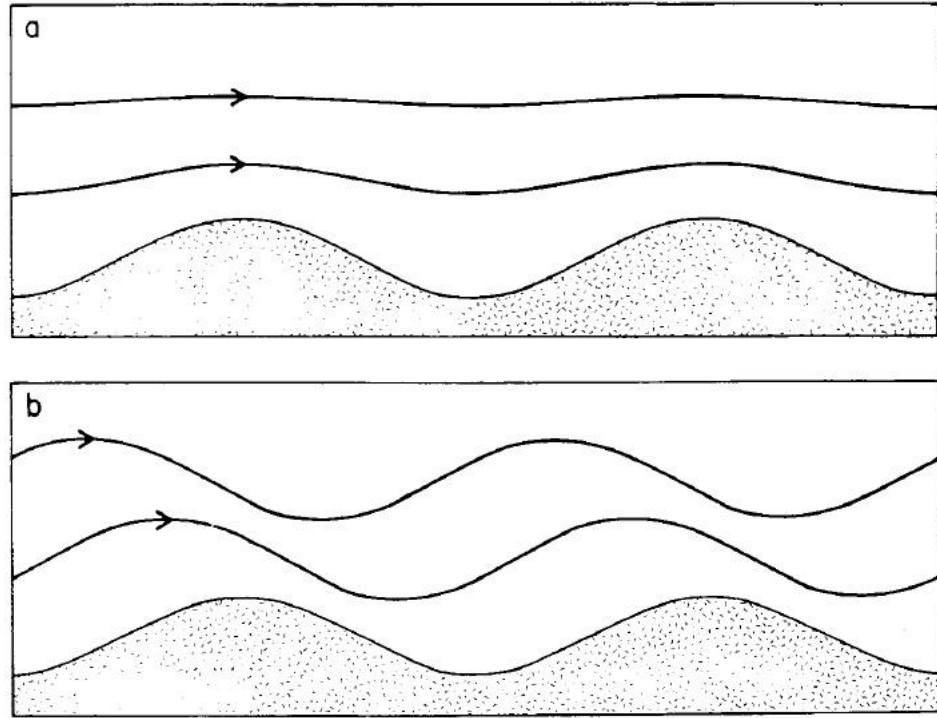
Figure 1.5: Streamlines in steady flow across an infinite series of sinusoidal ridges where a) N exceeds the intrinsic frequency $\bar{u}k$ (narrow ridge case); b) the intrinsic frequency $\bar{u}k$ exceeds N (wide ridge case). After Smith (1979).

The horizontal wavenumber is, in our idealised model, identical to the wavenumber of the sinusoidal terrain. In the case of the AP – an isolated ridge – k may be approximated by $\frac{2\pi}{L}$, where L is the ridge's along-wind length. Using typical values for $\bar{u}$ and N (10 ms^{-1} and 0.012 s^{-1}; the latter value averaged from measurements from radiosondes launched to the west of the AP at British Antarctic Survey's Rothera Research Station) for westerly flow approaching the AP, the critical value of L defining whether vertical propagation is supported is ~2.6 km. Given that $L \gg 2.6$ km, the AP is easily able to force the vertical propagation of hydrostatic mountain waves (such as the idealised example in Figure 1.3a).

If $\bar{u}$ and N are allowed to vary with height, equation [1.10] becomes

$$\left(\frac{\partial^2 w^{'}}{\partial x^2} + \frac{\partial^2 w^{'}}{\partial z^2} \right) + l^2 w^{'} = 0 \, ,$$

where l, the Scorer parameter is described by

$$l^2 = \frac{N^2}{\bar{u}^2} - \frac{1}{\bar{u}} \frac{\partial^2 \bar{u}}{\partial z^2}$$

(Holton, 2004). Vertical propagation will now be supported if $k^2 < l^2$. Scorer (1949) showed, using a 2-layer atmospheric model, that the vertical variation in l can be used to forecast the nature of wave propagation. Scorer's study implied that where

a lower layer of air defined by values of sufficiently large l to support vertical propagation is capped by an upper layer of lower stability and/or stronger cross-mountain winds in which waves will decay with height, wave energy can be reflected without loss of amplitude between the layer transition and the surface, leading to the generation of horizontally propagating trapped lee waves (Figure 1.3b; Durran, 1990). Vertical variation in l can also be diagnostic of vertical variation in the amplitude of vertically propagating waves (as discussed in Section 1.3.1).

1.3.2 Mountain wave, mean flow interaction

It has been established that energy within a hydrostatic wave propagates upwards through the atmosphere. At some level wave energy must be dissipated and transferred back to the mean flow. Mountain waves are dissipated where $\bar{u} = 0$; a condition satisfied in real atmospheric flows at a mean state critical level, where the mean flow direction rotates by at least 90° with height. Durran and Klemp (1987) and Bacmeister and Pierrehumbert (1988) found that where a mountain wave interacts with a mean state critical level, a local region of turbulence usually forms. Alternatively, if a mountain wave's amplitude becomes large relative to its vertical wavelength, wave limbs steepen to such an extent that overturning occurs and the wave breaks at what is known as a wave-induced critical level. Such overturning can occur at low level above the mountain if $\hat{h}$ is sufficiently large (discussed further in Section 1.4.1.4) or higher in the atmosphere where the wave encounters a local increase in $N/\bar{u}$ with height (such as at the tropopause). The decrease in air density with height also encourages wave breaking (the 'bullwhip effect'). Ultimately, any small amplitude mountain waves which propagate into the mesosphere will disperse via radiative damping (Durran, 2003).

In the case of the AP and the mountains of the Southern Andes, the deep propagation of hydrostatic waves to heights above the tropopause is thought to occur more frequently than above most other major mountainous regions on earth. Satellite observations (e.g. Preusse et al., 2006 and Wu and Eckermann, 2008) appear to back up this theory. When flow is westerly within the troposphere, the tendency for circumpolar westerlies associated with the polar vortex in this region increases the likelihood of mean westerly flow extending aloft (with no mean state critical level). Additionally, the relatively simple ridge-like topography of the AP and Southern Andes

discourage the low level deflection of flow. Wu and Eckermann (2008) presented stratospheric saturated microwave radiance data acquired from the Microwave Limb Sounder on the *Aura* satellite. Fluctuations in the saturated radiances are due to air temperature fluctuations, so can be used to derive gravity wave-induced temperature variance. Figure 1.6 shows mean global radiance variances at 37 km above mean sea level (AMSL) for the month of July 2005. The highest variance values appear in the region occupied by the polar vortex, especially downwind (assuming westerly flow) of the AP and the Southern tip of South America.
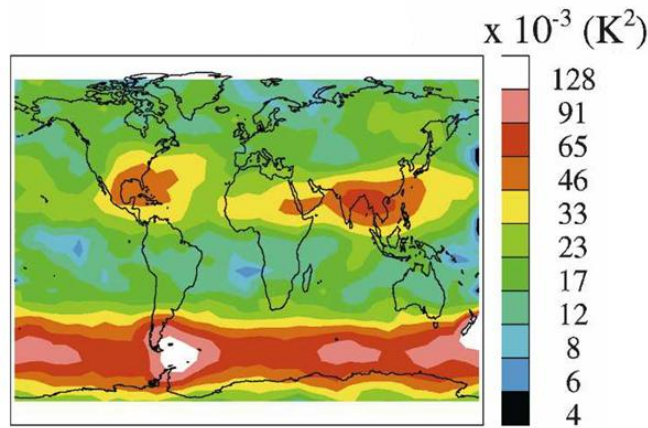
Figure 1.6: Mean global thermal radiance variances at 37 km above sea level for the month of July 2005, ascertained from the Microwave Limb Sounder on the Aura satellite during an ascending orbit. After Wu and Eckermann (2008).

When air flows across a mountain, a region of high (low) pressure forms on the windward (leeward) side of the mountain in association with the deceleration (acceleration) of mean flow (as described by linear theory of hydrostatic mountain waves: Smith (1980) and supported by observations: Colle and Mass (1998) and Pan and Smith (1999)). The resulting pressure gradient exerts a downwind-directed force on the mountain. The mountain must in turn exert an equal and opposite force (or drag) on the atmospheric mean flow. Hence mountains have a decelerative effect on flow. The horizontal momentum equation for 2-dimensional inviscid Boussinesq flow where $\overline{w} = 0$ can be expressed

$$\frac{\partial \rho_0 \overline{u}}{\partial t} = -\frac{\partial}{\partial z} \left(\rho_0 \overline{u'w'} \right).$$

Flow will be decelerated where the mountain wave induced momentum flux is divergent (i.e. $\frac{\partial}{\partial z} \left(\rho_0 \overline{u'w'} \right) > 0$) (Durran, 2003). Eliassen and Palm (1961) found that momentum flux is, in fact, non-divergent except at critical levels (Dunkerton, 1980). Hence, a hydrostatic mountain wave will have no effect on the mean zonal velocity

and temperature fields except where it breaks. This is known as 'nonacceleration theorem' (first considered in the work of Eliassen and Palm, 1961). Where the wave breaks, nonlinear processes convert wave energy to turbulent kinetic energy (Andreassen et al., 1994) and deposit wave momentum to the mean state flow (Fritts et al., 2006; Woods and Smith, 2010). Since the drag exerted on the flow is in the upwind direction here, whereas the force exerted on the mountain is in the downwind direction, the consequent momentum flux is downwards. So, hydrostatic mountain waves act to transport horizontal momentum vertically such that the drag exerted by the mountain on the flow is not felt at mountain level, but aloft where the wave is dissipated in the form of turbulence incurred by wave breaking.

1.3.3 The breakdown of mountain wave linear theory

ALPEX (the ALPine EXperiment) was one of the first major field campaigns in the field of orographic flow. Prior to this campaign in 1982, and the development of high-speed computers, much of the research had focussed on 2-dimensional linear theory. However, within the observations from ALPEX, few examples of simple vertically propagating mountain waves were found (Smith, 1989b). Smith (1989b) describes; "instead, complicated flow phenomena such as flow splitting, shallow föhn, and bora with wind reversal aloft were more commonly seen". Clearly, in appreciation of the 3-dimensional complexities of real world cases of orographic flow, linear theory alone is insufficient.

Long (1955) developed a finite-amplitude wave model (termed "Long's Model") to approximate nonlinear flow and considered the onset of isentropic overturning as flow aloft neared stagnation (at which point linear theory becomes invalid), implying the significance of a parameter describing the vertical displacement of streamlines above a mountain; the non-dimensional mountain height,

$$\hat{h} = \frac{Nh}{U},$$

where h is the height of the mountain.

Subsequently, further work using Long's model (Huppert and Miles, 1969), linear theory (Smith, 1979), towing tank experiments (Snyder, 1985 and Hunt and Snyder, 1980) and rawinsonde observations (Trombetti and Tampieri, 1987) have confirmed the non-dimensional mountain height to be a vital diagnostic in the assessment of flow over mountains. Since the wavelength of vertically propagating

mountain waves is proportional to $\frac{U}{N}$, $\hat{h}$ can be thought of as a ratio of the vertical wavelength to the height of the mountain (Smith, 1979). In the case of a continuously stratified atmosphere, for $\hat{h} \ll 1$, solutions obtained from linear theory are qualitatively similar to those obtained from nonlinear numerical models (Durran, 2003). But linear theory begins to break down as the height of the mountain becomes comparable to the vertical wavelength of hydrostatic disturbance. Consequently, low mean flow speed, low mean static stability and a large mountain will encourage nonlinear phenomena. Huppert and Miles (1969) progressed Long's (1955) work, employing $\hat{h}$ as a measure of nonlinearity to determine critical values of $\hat{h}$ for which static instability first occurs. Apart from mountain height, this value is also dependent on the mountain shape and aspect ratio (Smith, 1979).

In consideration of a vertically non-continuous fluid, the presence of a roughly crest-level inversion can also encourage nonlinear flow characteristics (Brinkmann, 1974; Smith, 1979; Mass and Albright, 1985; Durran, 1986). The breakdown of linear theory is associated with:

a) flow splitting, whereby low-level flow ceases to follow the terrain, compromising the linear boundary condition;

b) flow stagnation, implying $u' = -\bar{u}$ (linear theory assumes $u' \ll \bar{u}$);

c) turbulence induced by gravity wave breaking above the mountain.

1.3.4 Flow stagnation

According to linear theory, as $\hat{h}$ is increased towards unity, two regions of flow approach stagnation: some distance above the mountain within the hydrostatic wave, and at relatively low levels (within the first vertical wavelength) above the windward slope (Smith and Grønås, 1993). The former is associated with low level wave breaking. This occurs as streamlines within the wave become locally vertical or overturn, i.e. $\bar{u} + u' \leq 0$. Overturning implies $\frac{\partial \theta}{\partial z} < 0$, such that the wave becomes statically unstable and breaks, inducing unsteady, turbulent flow.

The second incipient stagnation region is at the lower boundary on the windward slope, and its occurrence is the result of flow blocking. Flow blocking refers to the deceleration of flow upwind of a mountain, sometimes to such an extent that it stagnates or reverses. Flow across the central streamline of an isolated mountain may

then be redirected to either side of the mountain without flowing directly over (see Figure 1.7). Isentropes will intersect the terrain, with flow being tangent to both the terrain and the dissecting potential temperature surface (Smith, 1989b). Only at regions of stagnation may flow splitting occur as only here may flow have two directions at one point.
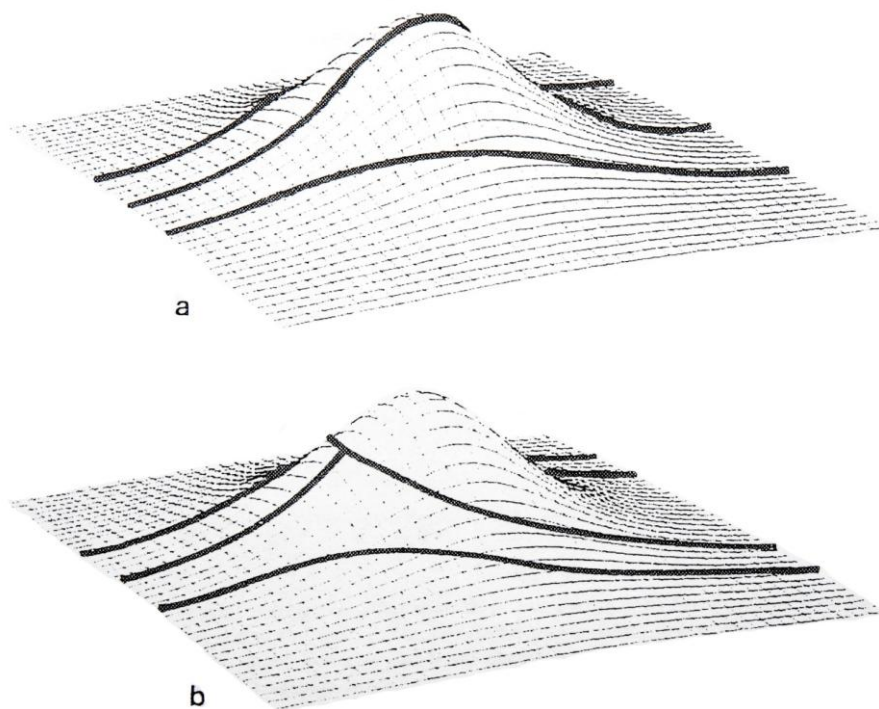
Figure 1.7: Hypothetical streamlines for near surface flow over an isolated mountain in the case of a) laminar flow across the mountain and b) upstream stagnation and flow splitting along the central streamline. After Smith (1989b).

Flow blocking propagates as a wave phenomenon. These waves `propagate upstream as "columnar" motions, meaning that they permanently alter the density and horizontal velocity profiles (Baines, 1987). Pierrehumbert and Wyman (1985) used a 2-dimensional numerical model to investigate, among other things, the upstream extent of flow blocking. Whilst for non-rotating flow waves would propagate arbitrarily upstream, the inclusion of the Coriolis force in the model was found to limit the upstream extent of the decelerated layer to a maximum horizontal length of the order of the mountain's Rossby radius of deformation, $\lambda_R = Nh/f$.

Sheppard (1956) provided the first estimate for the dividing streamline height (z_d), defined as the streamline that touches the summit of the mountain (Baines, 1995). Air below z_d is blocked, whilst air above it flows over the mountain. Using the argument that an air parcel will flow over a mountain if the kinetic energy it possesses is greater than the potential energy required to overcome stratification and surmount

the obstacle, Sheppard assumed that the pressure of a rising parcel is equal to the unperturbed pressure far from the mountain and used Bernoulli's equation to find

$$\frac{z_d}{h} = 1 - \frac{U}{Nh} = 1 - \frac{1}{\hat{h}}.$$

[1.11]

Smith (1979) and Smith and Grønås (1993) disputed the validity of this approximation, arguing that Sheppard's pressure assumption was false. However, large eddy simulation work by Ding et al. (2003), and laboratory experiments by Snyder et al. (1985) showed good agreement with Sheppard's formula. Ding et al. (2003) indicates that the success of Sheppard's formula is largely coincidental; suggesting that, for air flowing over an obstacle, the energy loss due to friction and turbulence compensates the energy gained from the pressure field. Hence Sheppard's (1956) disregard of the mountain top pressure anomaly is considered to be, indirectly, a reasonable assumption.

Hunt and Snyder (1980) extended Sheppard's (1956) formula to 3 dimensions, showing that the streamline dividing height could be approximated by $z_d/h = 1 - \alpha/\hat{h}$ for isolated mountains, where α is a constant of order 1. In a model study of air flow over a ridge-like barrier with aspect ratio $r = a_y/a_x = 5$ (where a_x (a_y) is along-flow (cross-flow) mountain length), Ólafsson and Bougeault (1996) confirmed that most simulations displayed a good fit to this formula when $\alpha = 1.2$.

Smith (1989a) proposed an alternative method of estimating z_d, using linear theory to derive a formula for the height of the onset of upslope stagnation considering the balance of kinetic energy of fluid parcels, the potential energy barrier posed by the obstacle, and the cross-mountain pressure gradient. It should be noted that, as stagnation approaches, the linear solution becomes increasingly invalid, and so must be considered a first approximation only. Despite this, the nonlinear numerical simulations of Smolarkiewicz and Rotunno (1990), Bauer et al. (2000) and Ólafsson and Bougeault (1996) verify the linear approach.

Using Smith's formula, one is also able to estimate the value of $\hat{h}$ at which stagnation appears in the incipient stagnation regions. Figure 1.8 – adapted from a figure appearing in Ólafsson and Bougeault, 1996, which in term was adapted from Smith, 1989b – shows the onset of stagnation as a function of r and $\hat{h}$. The figure should be interpreted by setting an aspect ratio, then tracing along a line of increasing

$\hat{h}$ from a small value. Below both curves A and B, mountain waves propagate linearly.

Above curve A (B), wave breaking (flow splitting) is predicted. The critical curves above

either curve A and B (i.e. the continuation of curve A above B, or curve B above A;

shown in Figure 1.8 as dotted lines) are unrealistic as linear theory does not account

for wave breaking or the reduction in wave amplitude due to flow splitting (Smith,

1989b). Indeed, laboratory experiments by Castro (1987) suggested that windward

flow splitting limited wave amplitude to such an extent that wave breaking may not be

supported when flow splitting occurs first. The boundaries defining a final regime –

simultaneous wave breaking and flow splitting – are not known (the dashed lines in

Figure 1.8 are Smith's (1989b) suggestions).
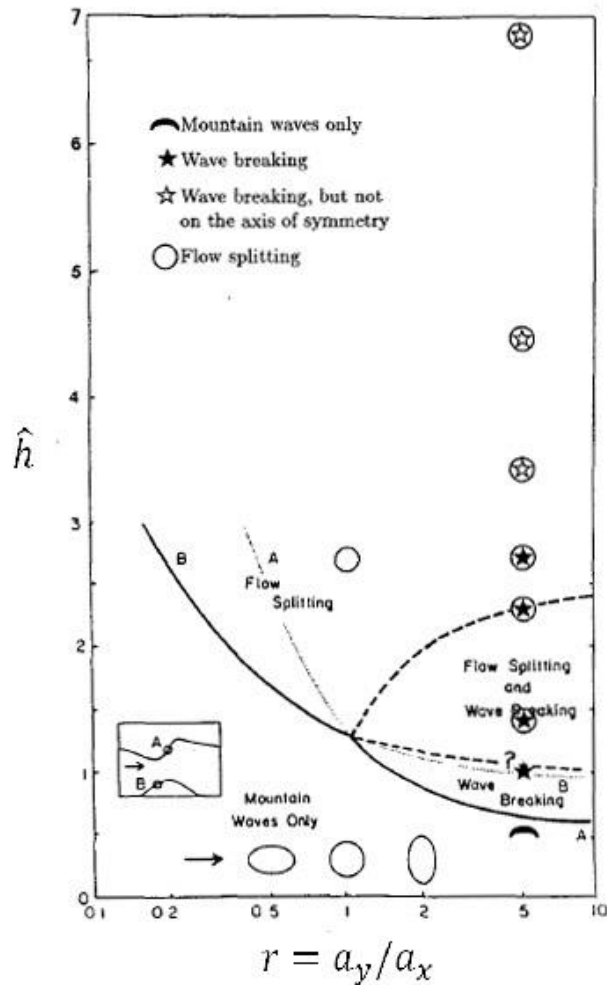
Figure 1.8: Regime diagram for hydrostatic flow over mountains as a function of aspect ratio r and non-dimensional mountain height $\hat{h}$. Where solid, curve A defines the onset of wave breaking due to stagnation (according to linear theory) above the mountain (location A in the inset box) if $\hat{h}$ is increased from a small initial value. Where solid, curve B defines the onset of upwind flow splitting associated with stagnation (according to linear theory) upwind of the mountain (location B in the inset box) if $\hat{h}$ is increased from a small initial value. Where dotted, the critical curves are unrealistic. The real location of these curves (which define a final regime; simultaneous wave breaking and flow splitting) are speculated upon as the dashed curves. Also plotted are the results of Ólafsson and Bougeault's (1996) idealised nonlinear hydrostatic numerical model experiments. After Ólafsson and Bougeault (1996), and originally Smith (1989).

For ridges aligned parallel to the flow, with increasing values of $\hat{h}$, mountain waves propagate linearly initially, until flow splitting occurs. Wave breaking is not thought to occur at any value of $\hat{h}$ (as discussed above). For ridges aligned perpendicular to flow the first stagnation point to appear is above the mountain (denoting wave breaking), initiated at smaller values of $\hat{h}$ the longer the ridge is. Upstream stagnation and flow splitting is then thought to be initiated at greater $\hat{h}$.

Also plotted on Figure 1.8 are the results of Ólafsson and Bougeault's (1996) idealised nonlinear hydrostatic numerical model experiments, which coincide well with Smith's (1989b) regime diagram. Their findings suggest that the upper dashed line may require revision. Numerous other numerical modelling studies have largely supported Smith's regime diagram (e.g. Smolarkiewicz and Rotunno, 1990; Smith and Grønås, 1993; Schär and Durran, 1995; Bauer et al., 2000).

Smith's (1989b) regime diagram appears then to provide a useful diagnostic tool for predicting and understanding the nature of flow over a mountain, given the upstream profile. In the real world complexities such as heterogeneous orography comprising a range of length and height scales, vertical wind shear and stability gradients complicate matters, shifting the regime boundaries. Smith (1989a) found that, in the case of forward wind shear, flow stagnation and wave breaking aloft is discouraged (i.e. occurs first at higher $\hat{h}$) relative to windward stagnation and blocking. The qualitatively opposite case is true for reverse wind shear.

As determined in Section 1.2.1, rotation is non-negligible for flow over the AP. The effect of rotation upstream of an obstacle the size of the AP (see Section 1.2.2) is that decelerated air is deflected in the opposite direction to the Coriolis force (i.e. to the right in the southern hemisphere) due to geostrophic imbalance. If the obstacle is long in the cross-flow direction, the diverted air may accelerate along the length of the ridge to form a barrier wind (Smith, 1982). The acceleration of flow within the barrier jet is associated with a relative increase in the Coriolis force, deflecting flow towards the ridge and encouraging enhanced flow over. Consequently, for a north-south oriented ridge of uniform shape and finite length in homogenous westerly flow in the southern hemisphere, z_d will vary along the length of the ridge; the lowest values being found south of the mid-point (in the North-South direction) of the ridge, in association with an accelerating northerly barrier jet (Ólafsson and Bougeault, 1997; Wells et al., 2005). Hence, under the influence of rotation, wave breaking may occur at one end of the ridge, but not the other. Ólafsson and Bougeault (1997) made use of a 3-dimensional model to show that the Coriolis force acts to inhibit blocking since air is encouraged to deflect around the obstacle rather than 'pile up' against it. Ólafsson and Bougeault also found that the inclusion of surface friction suppresses wave amplitude and breaking above an obstacle.

1.3.5 Mesoscale flow over the Antarctic Peninsula

It has been mentioned that observations in the Alps revealed the prevalence of nonlinear-dominated over pseudo-linear flow-over regimes. As explained in Section 1.3.2, because of its synoptic setting (within the polar vortex) the AP is more likely to force the deep propagation of vertically propagating waves than the Alps (the mountain range of concern for ALPEX) because of the reduced possibility of a mean state critical level. However, its shape – a high level ridge with steep slopes forming a sharp barrier and no major cross-ridge valleys / gaps – will encourage the onset of stagnation and nonlinear phenomena at lower $\hat{h}$ than would isolated mountains (Figure 1.8). For reference, assuming values of N and h of 0.012 s^{-1} and 1500 m respectively (characteristic values for the AP and approaching flow), $\hat{h} = 1$ is satisfied when $U = 18$ ms^{-1}.

The large Coriolis force due to the AP's high latitude means that barrier flows are commonly observed in association with blocked winds (e.g. Schwerdtfeger, 1975; Parish, 1983). Simulations by Orr et al. (2008) revealed deflected flow accelerating past the northern tip of the Peninsula as tip jets similar to the tip jets found off Cape Farewell, Greenland (e.g. Doyle and Shapiro, 1999; Moore and Renfrew, 2005). Assuming westerly flow, an accelerating northerly barrier wind may enhance flow-over due to Coriolis deflection towards the ridge.

Following Pierrehumbert and Wyman (1985), the maximum distance upstream of the AP for which approaching flow may 'feel' the Peninsula's orography is the Rossby radius of deformation, $\lambda_R = Nh/f \approx 150$ km for the AP.

Surface friction should be expected to play a diminished role relative to mountain ranges in more temperate and continental regions; the ocean surface and ice possessing low coefficients of friction.

1.4 Downwind effects

1.4.1 Downslope windstorms

1.4.1.1 Background

Downslope windstorms are strong, potentially damaging, low level winds which form on the lee side of mountains under certain conditions. Such winds have

been observed in many regions, but the most well known case study is that of the Boulder windstorm, due "in part to the strength of the phenomenon there and in part to the concentration of atmospheric scientists in that city" (Smith, 1985). Lilly (1978) presents observations of a major westerly Boulder windstorm in January, 1972, during which winds were found to surpass 60 ms^{-1}. In the immediate lee a large amplitude quasi-hydrostatic mountain wave was observed above the Colorado Front range (part of the Rocky Mountains) west of Boulder. Severe to extreme aircraft turbulence was detected in 2 regions: within the boundary layer in the lee, and in the mid-troposphere, originating from a region of strong wave-generated shear (Figure 1.9a and b).

Presumably due to the impact of such events on communities, severe downslope windstorms often have local names. Those induced by flow over the Rockies are known as Chinook winds. Others include the Alpine föhn (e.g. Seibert, 1990), the Southeast European bora (e.g. Smith 1987) and the Southern Californian Santa Ana (e.g. Svejkovsky, 1985). Colle and Mass (1998) studied 55 cases of westerly downslope windstorms generated by flow over the Cascade Mountains of Washington State, identifying four common features:

1) strong cross-barrier winds extending above mountain summit level,

2) a critical level above the mountains,

3) an inversion near mountain summit level, with less stable air above,

4) a strong cross-barrier pressure gradient.

These features reflect the findings of theoretical studies into the causes of downslope windstorms, as discussed further below.
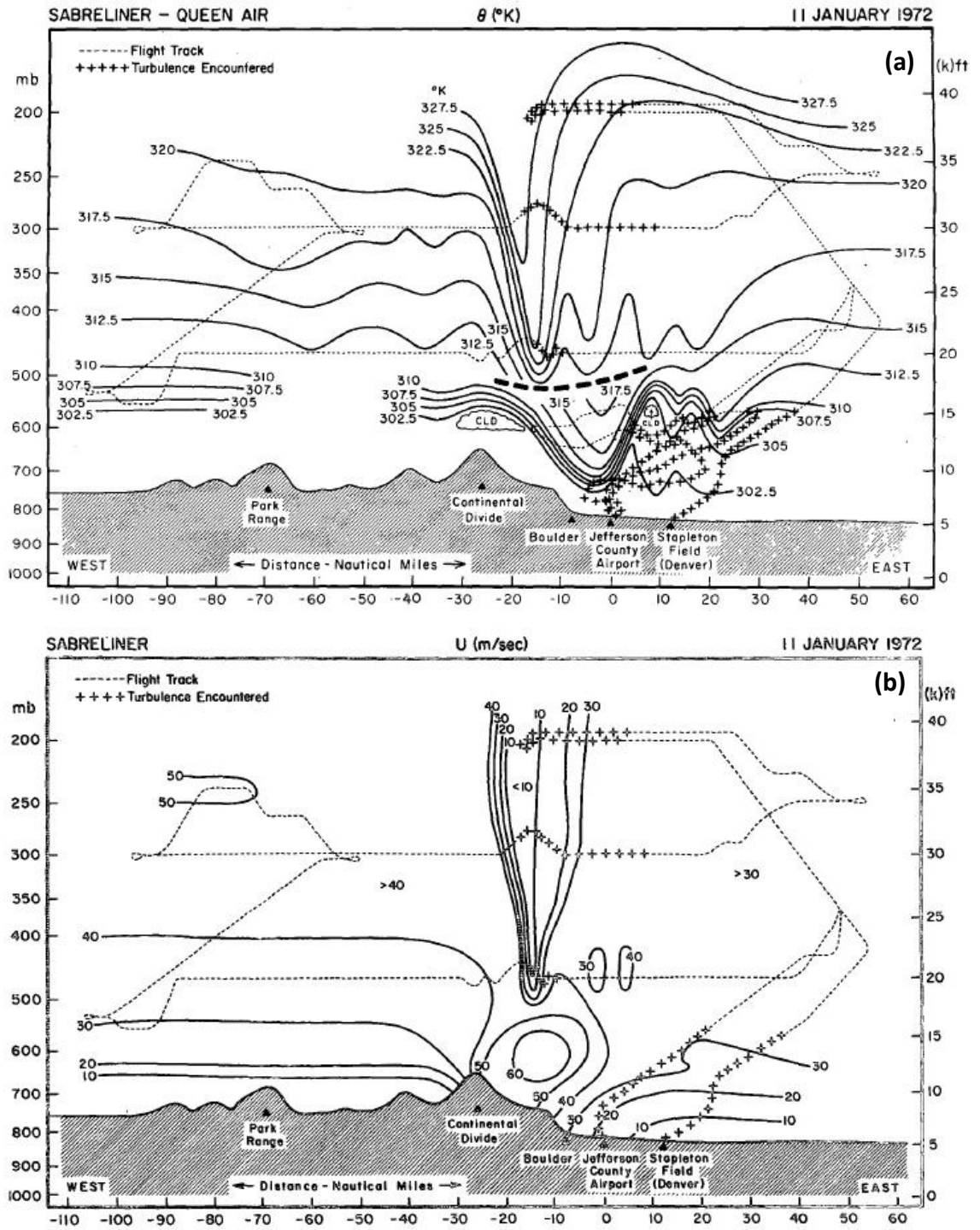
Figure 1.9: a) Isentropes (solid contours; labels in °C) and b) westerly component of flow (solid contours; labels in ms-1) derived from flight and sonde data describing the Boulder downslope windstorm of 11 January 1972. Aircraft path is shown by dotted lines, whilst plus symbols indicate periods of significant aircraft turbulence. In the case of a), data was sourced from two separate flights, whereas data for b) was sourced from just one flight. The heavy dashed line in a) separates data taken from each flight. After Lilly, 1978.

1.4.1.2 Hydraulic theory

Long (1953) was first to identify the similarity between hydraulic theory applied to the flow of an immiscible fluid over an object immersed in the liquid, and the characteristics of flow over a mountain where a downslope windstorm is present.

To assess Long's hypothesis we will consider homogenous hydrostatic flow of depth D over an infinite ridge. The fluid is bounded below by surface topography ($h(x)$) and above by a free surface ($D(x) + h(x)$). The shallow water momentum and continuity equations for steady state are

$$u\frac{\partial u}{\partial x} + g\frac{\partial D}{\partial x} + g\frac{\partial h}{\partial x} = 0 \,,$$

[1.12]

$$\frac{\partial uD}{\partial x} = 0$$

and reduce to

$$(1 - Fr^{-2})\frac{\partial(D + h)}{dx} = \frac{\partial h}{dx},$$

[1.13]

where the Froude number Fr is the ratio of the mean flow velocity to the velocity of shallow-water gravity wave propagation, given by

$$Fr = \sqrt{\frac{u^2}{gD}}$$

[1.14]

(after Durran, 1990).

Equation [1.13] describes a fluid whose depth will vary as it encounters sloping topography in a manner dependant on the value of Fr. It is apparent that where $Fr > 1$ (supercritical flow), if the fluid encounters rising topography ($\frac{\partial h}{\partial x} > 0$), the elevation of the free surface will increase ($\frac{\partial(D+h)}{\partial x} > 0$). In this case $g\frac{\partial D}{\partial x} + g\frac{\partial h}{\partial x} > 0$ and it follows from equation [1.12] that $\frac{\partial u}{\partial x} < 0$, i.e. the flow decelerates. As supercritical flow decelerates upwind of a mountain crest, kinetic energy is converted to potential energy above the hill, and then converted back to kinetic energy in the lee as flow reaccelerates.

Where $Fr < 1$ (subcritical flow), the elevation of the free surface will decrease with rising topography in association with flow acceleration. In this case upwind

potential energy is converted to kinetic energy above the hill and back to potential energy in the lee. Supercritical and subcritical flows are illustrated in Figure 1.10a and b).
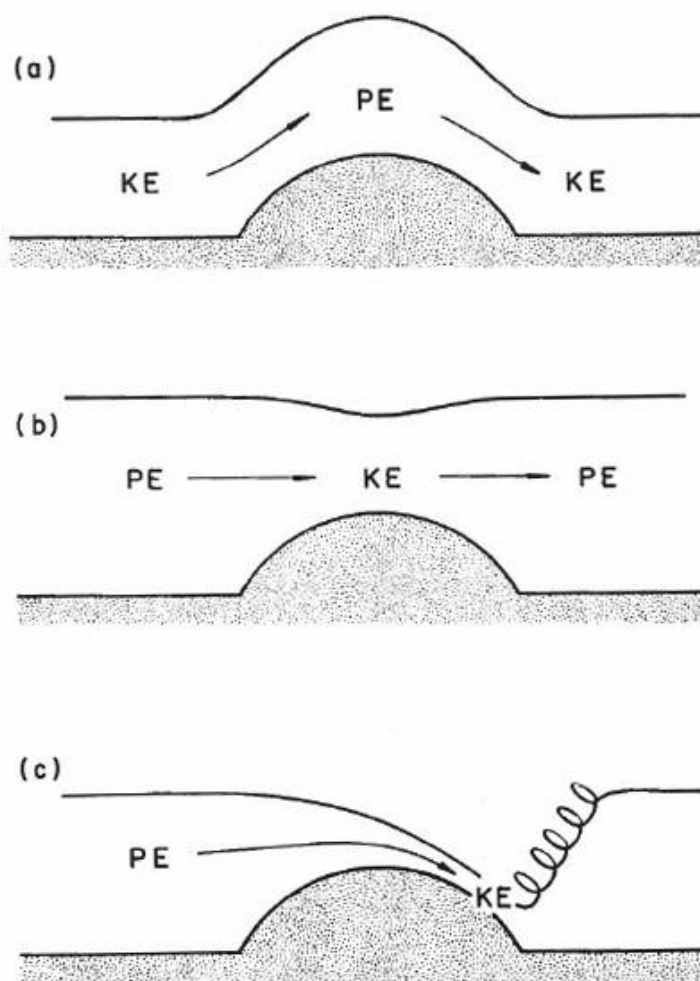
Figure 1.10: Shallow water flow over an obstacle; a) supercritical regime, b) subcritical regime, c) hydraulic jump regime. After Durran (1990).

Long (1953 and 1954) proposed that a third regime may be responsible for the formation of downslope windstorms. In this case, mean flow is weakly subcritical. Upon encountering the windward slope, the fluid accelerates. Above the obstacle a transition from subcritical to supercritical flow occurs so that as the fluid descends the lee slope, it continues to accelerate. Readjustment to ambient conditions then occurs abruptly at some point above the lee slope in the form of a turbulent hydraulic jump. Since potential energy is converted to kinetic energy for the duration of the fluid's advection over the mountain, particularly strong winds develop above the lee slope (Figure 1.10c).

The obvious caveat to the hydraulic theory is that it considers an atmosphere which is bounded by a free surface, in which energy cannot escape upwards (Durran,

1990). As described in section 1.3.2, in the real unbounded atmosphere energy may be transported vertically to great heights by internal gravity waves.

1.4.1.3 Linear amplification of lee slope winds

The distribution of wind speeds within hydrostatic waves in linear theory is asymmetrical across the mountain, with maximum speeds appearing above the lee slope (Durran, 1990). This is illustrated in Figure 1.3a; note the relative closeness of streamlines above the lee slope. Indeed, Lilly and Klemp (1979) showed that, for a homogenous atmosphere (constant u and N with height), solutions derived from Long's finite-amplitude equation compared well with small amplitude linear theory. Eliassen and Palm (1961) showed that sharp gradients in the Scorer parameter with height can bring about a reflection of wave energy. Klemp and Lilly (1975) used linear theory applied to a layered atmosphere in which wind speed and stability are constant in each layer. They found that under certain layering configurations, partial reflection of wave energy could become resonant, resulting in amplification of the lee slope wind maximum. The optimal configuration for downslope winds in their results for the Boulder windstorm was where the tropopause (associated with a sudden increase in static stability) was at a level one half vertical wavelength above the mountain.

Durran (1986) performed nonlinear numerical modelling studies of non-hydrostatic flows within a 2-layer atmosphere. He found that the effect of a discontinuous stability profile strongly influenced the sensitivity of the model output to nonlinear processes. Figure 1.11 illustrates isentropes for four flow-over configurations modelled by Durran, in which the elevation of the layer interface varies (cases *a* and *c* ¼ vertical wavelength; cases *b* and *d* ½ vertical wavelength), as does the relative stability of each layer (cases *a* and *b* have $N_L = 2N_U$; cases *c* and *d* have $N_L = 1/2N_U$, where N_L (N_U) is the stability of the lower (upper) layer). The value of $\hat{h}$ associated with the most stable layer is fixed at 0.6. In this case of hydrostatic, adiabatic flow, the isentropes are considered to represent streamlines. Linear theory predicts the pressure drag (normalised against the drag generated by linear hydrostatic waves over a Witch of Agnesi mountain) exerted on the mountain to be 4 times greater in cases *a* and *d* than in cases *b* and *c* (Durran, 1986). Though qualitatively accurate relative to the nonlinear simulations for cases *a*, *c*, and *d*, linear theory greatly underestimates pressure drag for case *b*. This simulation exhibits the

most drag (associated with a large lee surface wind perturbation) of the four cases,

and a downwind feature which resembles a hydraulic jump.
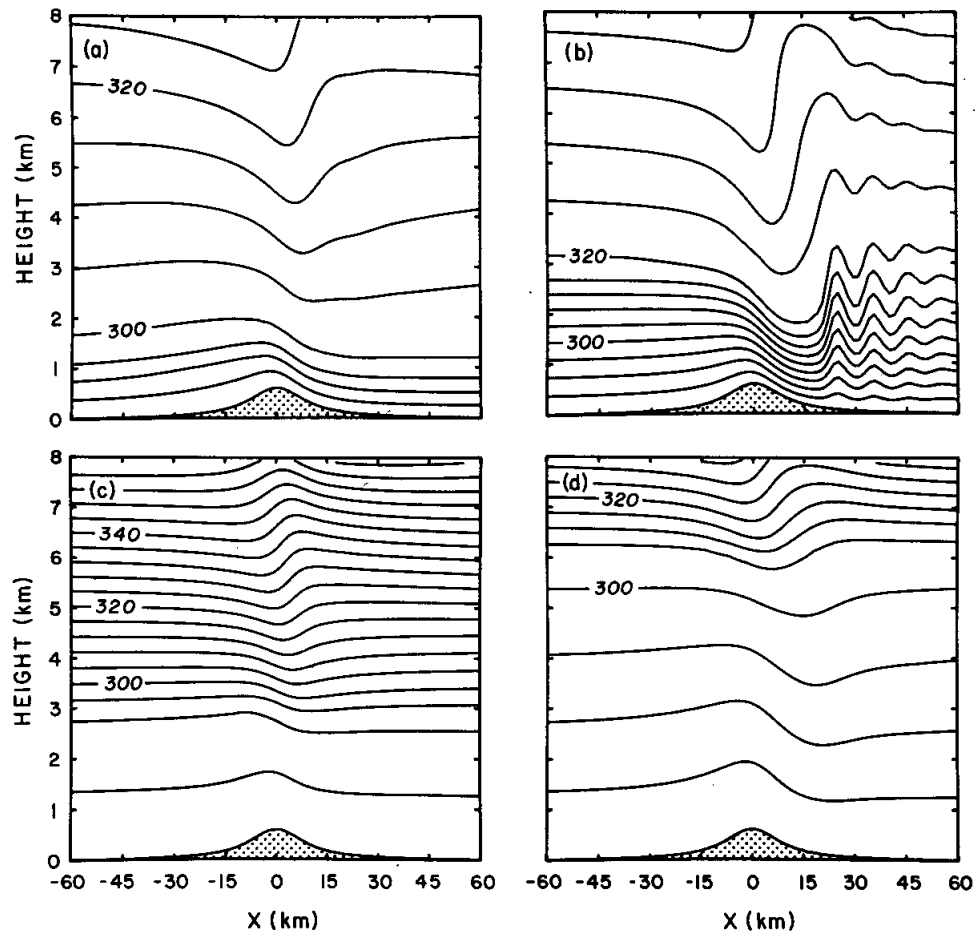
Figure 1.11: Isentropes defined by flow over a bell-shaped ridge in 2-dimensions, derived from a non-linear numerical model after a fixed runtime. The idealised atmosphere has two layers: a lower (an upper) layer defined by stability N_U (N_L). In all four scenarios the value of $\hat{h}$ associated with the most stable layer is 0.6. The layer interface is at ¼ vertical wavelength above the surface in a) and c) and ½ vertical wavelength above the surface in b) and c). The ratio N_U / N_L = ½ in a) and b), whilst N_U / N_L = 2 in c) and d). After Durran (1986).

Figure 1.12 illustrates the effect of the degree of nonlinearity on pressure drag

and surface wind speed. Whilst linear theory predicts that the strength of the

horizontal surface wind perturbation will scale linearly with h (Durran, 1990), the

wave-amplitude dependence apparent in Figure 1.12 lends itself better to comparison

with hydraulic theory; specifically the transition between the low drag supercritical

everywhere regime, to the high drag subcritical everywhere regime, via the

particularly high drag hydraulic jump (cross-mountain transition from subcritical to

supercritical) regime (as described in Figure 1.10). Furthermore, Durran (1986) also

performed simulations testing the sensitivity of the flow characteristics to the

thickness of a lower stable layer below an upper less stable layer. Four configurations were considered; the interface placed at elevations of (case *a*) $\bar{u}/N_L$, (case *b*) $2.5\bar{u}/N_L$, (case *c*) $3.5\bar{u}/N_L$ and (case *d*) $4\bar{u}/N_L$ (Figure 1.13). Once again, Durran's results reflect the implications of hydraulic theory. Assuming the layer interface to act as a free surface bounding the lower level, a greater layer depth D will invoke smaller Fr (see equation [1.14]). Upholding the hydraulic theory comparison, case *a* (*d*) resembles a supercritical (subcritical) regime, whilst cases *b* and *c* resemble the hydraulic jump regime, exhibiting the strongest lee side winds and downwind jumps (stationary in case *b*, horizontally propagating to form lee waves in case *c*).
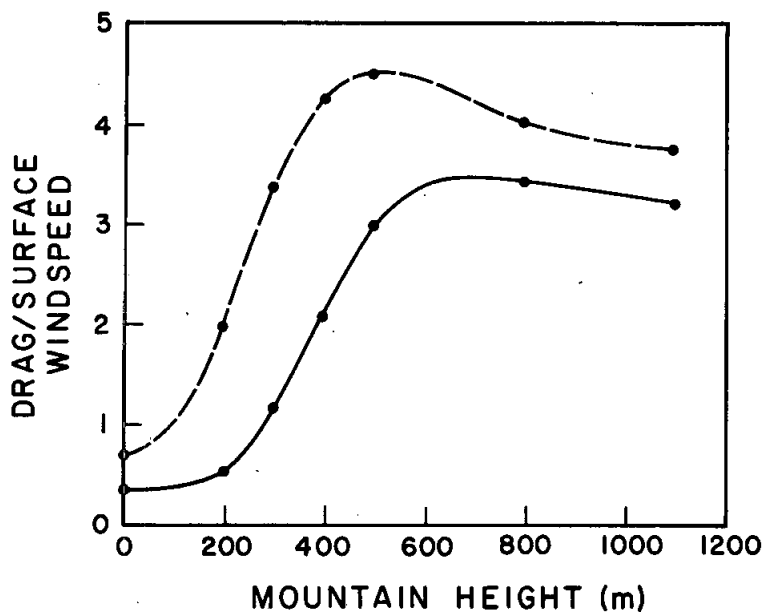
Figure 1.12: Normalised pressure drag (solid curve) and peak surface wind speed perturbation (dashed curve) as a function of mountain height for a two-layer atmosphere (defined by stabilities N_L for the lower layer and N_U for the upper layer) where the interface is at an elevation of 3000m and N_L = 2.5 N_U. Data are derived from a non-linear numerical model after a sufficient spin-up period. Note that N_L / U = 0.001, so $\hat{h}_L = h/1000$. After Durran, 1986.
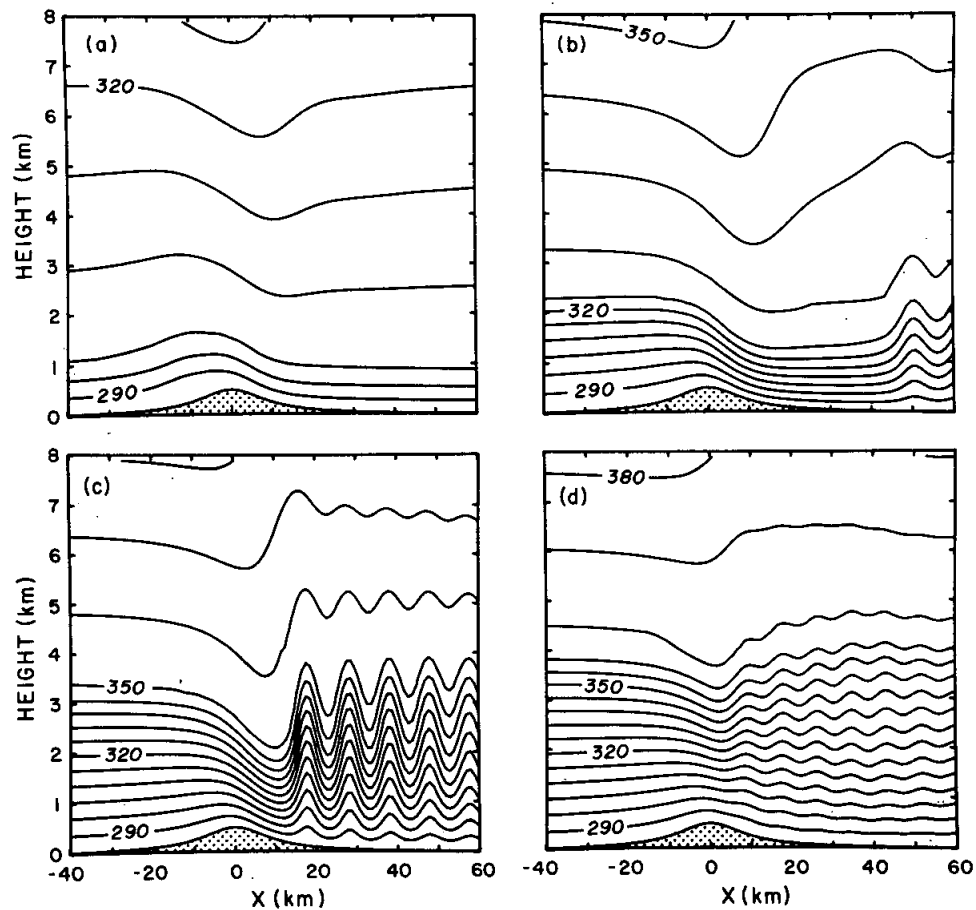
Figure 1.13: Isentropes defined by flow over a bell-shaped ridge in 2-dimensions, derived from a non-linear numerical model after a fixed runtime. The idealised atmosphere has two layers: a lower (an upper) layer defined by stability N_U (N_L). Note that $N_L \gg N_U$. In all four scenarios $\hat{h}$ for the lower layer is 0.5. The layer interface is found at elevations a) $\bar{u}$ / N_U, b) 2.5 $\bar{u}$ / N_L, c) 3.5 $\bar{u}$ / N_L and d) 4 $\bar{u}$ / N_L. After Durran (1986).

In conclusion, though linear theory has some power in predicting enhanced surface winds under some conditions, nonlinear processes appear to be essential in the development of downslope windstorms (Holton, 2004). Durran (1986) found that, in a layered atmosphere, an interface between a lower stable layer and an upper less stable layer may act as a free surface such that transitions between drag regimes may be qualitatively approximated by hydraulic theory.

1.4.1.4 Wave breaking theory

A succession of papers by Clark and Peltier (1977, 1984) and Peltier and Clark (1979, 1983) identified that low-level wave breaking (as discussed in Section 1.3.4) may encourage the development of downslope windstorms. With the aid of numerical simulations of idealised flow, Clark and Peltier (1977) observed that, if upstream $\bar{u}$ and N are fixed to define a value of $\hat{h}$ which encourages stagnation and wind breaking

above a mountain, flow would evolve in time towards a new high drag / severe wind regime. In their simulations wave amplitude appeared to subside dramatically above the level of wave breaking. Clark and Peltier proposed that when the stagnant mixing region associated with the breaking wave possesses a Richardson number of less that ¼, it acts as a reflective surface (known as a 'wave-induced critical level') for mountain waves. Similar to the reflection of waves in association with a steep gradient in Scorer parameter considered by Klemp and Lilly (1975), such reflection may incur a resonant response, leading to wave amplification in the lower troposphere.

Durran and Klemp (1987) and Bacmeister and Pierrehumbert (1988) performed numerical experiments to find that a mean state critical level defined by a Richardson number of less that ¼ can incur a similar resonant response as a wave-induced critical level.

Smith (1985) developed a revised mathematical model to that of Peltier and Clark (1983), in which he found that a severe wind response could be obtained if the critical level was positioned anywhere between ¼ and ¾ vertical hydrostatic wavelengths above the mountain. Durran and Klemp (1987) found Smith's model to be more satisfactory than Peltier and Clark's, since it's results exhibited a similar dependence on mountain height (i.e. $\hat{h}$) as those exhibited by their simulations. Hence, wave amplification in association with a critical level will only occur if $\hat{h} > \hat{h}_{critical}$, even if the critical level is of the mean-state variety (Durran, 1990). Durran (1990) points out that Smith's model closely, though not exactly resembles the shallow water hydraulic model, whereby the streamline dividing laminar flow beneath the critical level from turbulent flow above is analogous to the free surface in hydraulic theory.

Smith and Skyllingstad (2011) performed Large Eddy Simulation experiments to find that in the presence of wave breaking, the stability profile above the wave-induced critical level had little effect on the resulting downslope winds. This conforms to the theory of a wave-induced critical level forming a reflective surface.

1.4.1.5 Three-dimensional theory

Very little theoretical work has considered the triggering mechanisms of downslope wind storms in three-dimensions. Phillips (1984) formulated an analytical solution for surface pressure drag across an elliptical mountain. He found that the

maximum pressure perturbation in two-dimensional flow was only 10% larger than in three-dimensional flow where the aspect ratio a_y/a_x is 3 or 4. Phillips therefore maintains that the 2-dimensional consideration of downslope windstorms is an adequate approximation of the 3-dimensional problem, especially in the consideration of a long ridge.

1.4.1.6 Downslope windstorms in the real world

Observational studies of downslope windstorms largely substantiate the suitability of the internal hydraulic mechanism to describe their occurrence. Smith (1987) used aircraft data to examine the nature of the Yugoslavian Bora. Investigating five case studies, some common features were identified. The air rising over the topography appeared to accelerate as it ascended – consistent with hydraulic theory whereby air flow is initially subcritical – with streamlines converging and accelerating upslope. A narrow turbulent region was observed immediately downwind of the mountains, deduced to be shear driven. The shear is associated with the downslope bora and a sloping updraft just downwind. The updraft resembles a hydraulic jump and in some cases was associated with 'jump' or 'rotor' clouds. Above the turbulent zone a region of low stability (isentrope spreading) and near stagnation was observed in all five cases, seemingly filling the gap between the bora wind and the relatively undisturbed air above (Smith, 1987). Most of these features were also observed in the structure of the Boulder windstorm of January 1972 (Lilly, 1978) and are evident in Figure 1.9a and b. In Smith's study, four of the five cases exhibited a mean state critical level. In the final case, there was little directional wind shear but large $\hat{h}$ (due to weak approaching flow) and possible wave breaking (associated with a wave-induced critical level) gave rise to a similar downwind response as in the other four cases. Brinkmann (1974) examined twenty Boulder windstorms with weather station and radiosonde data, in which maximum leeside surface winds were observed to surpass 36 ms^{-1}. A stable layer at mountain top level with less stable air above was found to be a condition favourable for the formation of a downslope windstorm. Analogous to hydraulic theory, strong cross-barrier winds above the inversion were not found to be necessary. Mass and Albright (1985) also observed a crest-level inversion in associated with a windstorm across the Cascade Mountains of Washington State.

Durran (1986) performed simulations of the January 1972 Boulder windstorm using real upwind conditions observed in a sounding to test the sensitivity of the downwind response to the existence of an elevated inversion. In the absence of the inversion no downwind windstorm was simulated. Observational analysis of a westerly flow event across the Colorado Rockies in Bower and Durran (1986) further attest to the vital role of elevated inversions in the generation of strong downslope winds. No inversion was observed, and, despite all other factors seemingly favouring downslope windstorm development, no downslope winds were registered at Boulder.

Smith and Skyllingstad (2011) found that the presence of an elevated inversion encouraged the greater downwind extent of downslope windstorms observed over the Falkland Islands.

As illustrated in Figure 1.9b, the maximum downslope winds for the January 1972 Boulder windstorm were observed above the lee slope, with winds weakening rapidly further downwind (Lilly, 1978). Brinkmann (1974) observed that changes in the upstream wind and stability profile affected the position of a deep lee trough (associated with the drawdown of warm air from above), but that maximum windspeeds occurred when the trough was located at the foot of the lee slope.

Forecasting downslope windstorms is a challenge due to the complex nonlinear interactions between various atmospheric processes and the underlying topography (Colle and Mass, 1998). However, hydraulic theory has been found to provide a relatively robust framework for their understanding. A mean state or wind-induced critical level, or an inversion are considered the upper bound of the hydraulic flow.

Other features thought to encourage the development of downslope windstorms are gentle windward slopes and steep lee slopes, and low relative humidity in the lower troposphere (Durran, 1990).

1.4.2 Effect of non-linear phenomena on mean flow

As discussed in Section 1.3.2, a linear hydrostatic mountain wave has no direct effect on the mean zonal velocity and temperature fields (Eliassen and Palm, 1961). Only dissipative phenomena may alter these fields. In a non-linear regime, dissipative processes such as low-level wave breaking and shear-generated turbulence related to a hydraulic jump are confined close to the mountain (Schär & Smith, 1993). Here,

viscous dissipation leads to a loss of kinetic energy to internal energy and hence Bernoulli function loss. The flow decelerates and a wake is formed in the lee of the mountain.

For isolated, circular topography the presence of wave breaking is assumed to signal a high drag state (Epifanio and Durran, 2001). The flow decelerates to form a wake in the lee. Upstream stagnation incurs flow splitting so that flow navigates around rather than over the mountain, resulting in reduced wave amplitude, downslope winds and drag. Where $\hat{h}$ is large enough to cause flow splitting, a pair of recirculating vortices are produced in the lee.

In the case of a ridge of varying height along its crest, alternating flow regimes can give rise to downslope flow defined by a series of jets and wakes (potential vorticity banners; Grubišíc, 2004). For example, Jiang and Doyle (2005) found that, for a Croatian Bora event, in the lee of high topography, the presence of wave breaking helped generate a thin, more supercritical downslope flow, associated with the generation of a hydraulic jump and hence an extensive near-surface wake. Meanwhile, in the lee of passes, deeper, less supercritical flow is able to maintain its speed in the absence of a hydraulic jump (Jiang and Doyle, 2005).

1.4.3 Gap winds

Gaps winds are strong gusty winds in the lee of mountain passes or valleys. Air accelerates from the gap exit in association with a decrease in pressure to form a jet downwind. In relation to large scale flow, two types of gap flow are observed; those where the gap or valley is aligned parallel (*type A*; Figure 1.14a), and those where the gap or valley is aligned perpendicular to the large-scale flow (*type B*; Figure 1.14b) (Zängl, 2002). The latter has been observed across the Strait of Juan de Fuca (Reed, 1931; Overland and Walter, 1981) and the Cascade Mountains of Washington State (Mass and Albright, 1985; Jackson and Steyn, 1994). Such flows are characterised by a cross-mountain pressure gradient which drives air ageostrophically through the gap. This idea can be adequately represented by considering the acceleration of a surface layer through a channel due to a pressure gradient (Overland and Walter, 1981). An appropriate form of the equation of motion for scale analysis is

$$\frac{du}{dt} - fv = -\frac{1}{\rho}\frac{\partial p}{\partial x} + K\frac{\partial^2 u}{\partial z^2}.$$

For typical mesoscale gaps in topography, the Coriolis and viscosity terms become small relative to the other terms, giving

$$\frac{du}{dt} = \frac{d}{dx}\left(\frac{u^2}{2}\right) = -\frac{1}{\rho}\frac{\partial p}{\partial x}.$$

Hence, inertial acceleration provides the balance for the pressure gradient term, such that the flow is in approximate ageostrophic equilibrium with the surface pressure gradient imposed both synoptically and locally due to the orography (Overland and Walter, 1981).
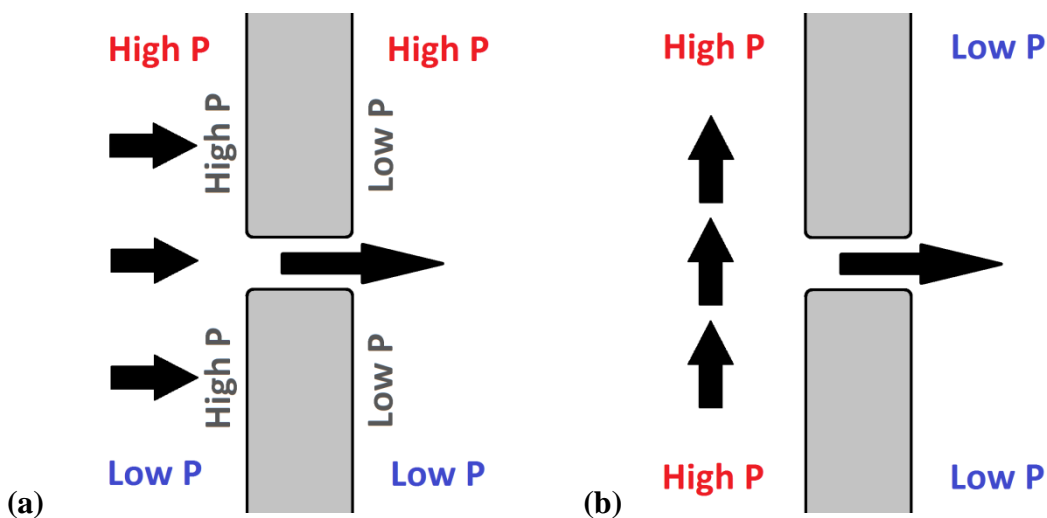
Figure 1.14: Schematics of a) type A and b) type B gap flows through a gap in a ridge. Synoptic pressure gradient is insinuated by red 'High P' and blue 'Low P' labels. In a), grey 'High P' and 'Low P' labels indicate perturbations to the mean state pressure field due to the effect of the topography.

Examples of locations of *type A* gap flow observations include the Aleutian Islands (Pan and Smith, 1999), various sites in Japan (Arakawa, 1969 and Saito, 1993) and The Cascade Mountains (Colle and Mass, 1998).

Zängl (2002) performed non-linear simulations with idealised terrain to show that *type A* gap flows appear in fact to be primarily forced by the same mechanism as *type B* gap flows; a cross barrier pressure gradient. In this case the pressure gradient is not due to synoptic conditions but related to the high drag state incurred by flow over the adjacent higher topography (Figure 1.14a).

Colle and Mass (1998), however, made use of model and observational data for windstorms downwind of passes in the Cascade Mountains to show that leeside winds are highly sensitive to features associated with mountain wave flow accelerations; such as the strength of the cross-barrier flow, the presence of a critical level, and vertical Scorer parameter variability. They conclude that the windstorms are

generated by acceleration due to both the cross-gap pressure-gradient and wave/hydraulic effects.

Pan and Smith (1999) use the shallow water model for flow over idealised terrain to examine the nature of gap winds and lee wakes. Upwind inversions – a common feature of non-linear flow over orography – may provide the upper free surface assumed to exist by the shallow water model (Flamant et al., 2002). Flamant et al. (2002) showed using a numerical model that gap flow through the Wipp Valley in Austria during a föhn event can be well reproduced with a 2-dimensional shallow water model.

Where $Fr > 1$, linear vertically propagating gravity waves are encouraged with no low level wave breaking (Saito, 1993). According to linear theory the strength of the lee slope wind speed anomaly increases with increasing mountain height (Pan and Smith, 1999). Accordingly, winds in the lee of a gap will be weaker than those downwind of higher topography in a linear flow regime (assuming that confluence and diffluence is negligible such that flow is considered to behave in a locally 2-dimensional manner across the topography). Theory would suggest then that non-linear processes are required to promote gap jets. Hence, only flows in which upstream flow is subcritical ($Fr < 1$) are considered in Pan and Smith's study.

They found that flow over high terrain was accelerated more than flow through gaps. This is associated with a transition from subcritical to supercritical flow, resulting in the generation of a hydraulic jump further down the lee slope. Above gaps, the flow is more likely to be subcritical or only weakly supercritical, and a hydraulic jump does not form. As a result of Bernoulli loss due to dispersion related to the hydraulic jump (as discussed in Section 1.4.2), a wake will be formed downwind of the hydraulic jump. Hence, the downslope windstorm will constitute stronger flow than the gap jet, but the gap jet will extend further downstream. In Pan and Smith's paper, these conclusions are validated by surface wind observations gathered from synthetic aperture radar from the vicinity of the Aleutian Islands.

Other observations of strong winds associated with gap jets extending downstream for a long distance include those in the Strait of Juan de Fuca (Overland and Walter, 1981), west of the Cascade Mountains (Mass and Albright, 1985) , the German Alps (Jaubert and Stein, 2003) and the Austrian Alps (Flamant et al., 2002).

Pan and Smith's conclusions also reflect those drawn by Saito (1993), who modelled a fully non-linear flow over idealised terrain. The terrain was modulated by a cosine function to simulate a ridge defined by a series of peaks and cols. In addition to the linear regime (flow in the immediate lee of peaks stronger than in the immediate lee of gaps), and the hydraulic regime (gap jets continuing far further downwind but weaker than downslope windstorms in the immediate lee of peaks upwind of the hydraulic jump), they noted a third 'blocked' regime (Table 1.1). In this regime the barrier is too high for a transition to supercritical flow, and lower $\hat{h}$ upstream of the gaps discourages blocking and promotes stronger winds in the lee of gaps than in the lee of the peaks.

Regime	Peak		Gap		Strongest winds	Gap jet downwind?
	Upwind	*Above ridge*	*Upwind*	*Above ridge*		
Linear	↑	↑	↑	↑	Lee of peak	No
HJ (peak and gap)	↓	↑	↓	↑	Lee of peak	No
HJ (peak only)	↓	↑	↓	↓	Lee of peak	Yes
Blocked	↓	↓	↓	↓	Lee of gap	Yes

Table 1.1: Flow characteristics across an undulating (i.e. with peaks and gaps) ridge. ↑ = supercritical, ↓ = subcritical, HJ = Hydraulic Jump.

Zängl (2002) performed non-linear simulations with idealised terrain to find that wave breaking above 2 peaks separated by a gap is generally associated with wave breaking above the gap axis. He found, however, that the wave breaking within the gap takes significantly longer to initiate. The wave breaking may then encourage the development of a hydraulic jump regime across the gap axis.

Pan and Smith (1999) assessed the relative important of confluence on flow regimes across topography with gaps. The effect of acceleration due to confluence (within gaps) and deceleration due to difluence (above peaks) is a lower (higher) critical height for gaps (peaks). In both modelled and real cases, the change from subcritical to supercritical conditions always occurred first (with decreasing $\hat{h}$) above peaks. Hence, although significant, the effect of confluence was found *not* to dominate over the effect of enhanced vertical displacement on the acceleration of flow.

Gaberšek and Durran (2004) assessed mass and momentum budgets of flow through a gap similar to that of Pan and Smith (1999) using idealised simulations,

identifying three distinct regimes; a linear regime with almost no enhancement of flow through the gap, a mountain wave regime with strong flow acceleration in the gap exit (downwind portion) due to the downward transport by the mountain wave above the lee slopes, and a blocked regime in which weak (relative to that in the mountain wave regime) acceleration is simulated in the gap entrance (upwind portion) due to lateral convergence and pressure gradient forces. These results agree with those of Pan and Smith (1999) and Zängl (2002). The strongest winds and greatest accelerations were simulated in the mountain wave regime, highlighting once again the importance of vertical transport in the generation of strong gap winds. The lateral convergence-induced blocked regime gap winds are considerably weaker due to weaker flow enhancement and a weak (hence blocked) mean-state flow.

1.4.4 The föhn effect

1.4.4.1 Background

Although described in Section 1.4.1.1 as a local name for downslope windstorms the definition of *föhn* is historically ambiguous. Yoshino (1975) suggested that it should simply describe a scenario where air flowing down a mountain is warmer than the air it is displacing. This definition is endorsed by Smith (1979) and appears to be widely accepted.

The *Bora* is a similar downslope wind to the föhn, but is distinguished by a cooling of lee side conditions, due to the source air upwind of the obstacle being particularly cool (Hoinka, 1985). The *Chinook* describes föhn-type downslope winds descending the eastern slopes of the Rocky Mountains (e.g. Beran, 1967). To avoid confusion, "föhn" will, from here onwards, be used as an umbrella term for any downslope wind which induces lee side warming (including the Alpine föhn and the Chinook).

The occurrence of the Alpine föhn had been recognised since the 19th century, with northern Europe experiencing warmer spells when the south föhn blows. Hann (1866) hypothesised that the causal mechanism for the föhn was the adiabatic compression heating of descending air, rather than the advection of warm dry air from the Sahara, as had previously been surmised. He also discussed the effect of latent heat release during condensation above the windward slopes. This mechanism is illustrated in Figure 1.15a. As air rises above the windward slope of the mountain, it

cools and becomes saturated. Condensation occurs, releasing latent heat to the ascending air. So long as some of the water is lost through precipitation above the windward slopes, after the air has descended the lee slopes, it will be warmer and drier than at the same level upwind. However, Hann, in the first edition of his textbook (Hann, 1901), states that precipitation on the windward side is not a necessary condition for föhn – that the drawdown of air from above is sufficient to bring about leeside warming. Ficker (1920) described the föhn effect in similar terms, whereby low level approaching flow is blocked (i.e. unable to pass over the mountain) and föhn air is derived from higher, potentially warmer altitudes upwind (this mechanism, named subsequently the 'isentropic drawdown' mechanism, is illustrated in Figure 1.15b and, as it appears in Ficker (1920), in Figure 1.16). However, in subsequent textbooks and in popular science a paradigm shift occurred whereby the isentropic drawdown mechanism was dropped, and latent heat above the windward slopes became labelled *the* causal mechanism of the föhn effect. A 'text book' definition developed in which only the latent heat mechanism was considered (Seibert, 1990). Whilst this oversimplified explanation persists in the sphere of popular science (a search for 'the föhn effect' on internet search engines will attest to this), rebukes against the paradigm in the scientific literature have ensured a more considered understanding.
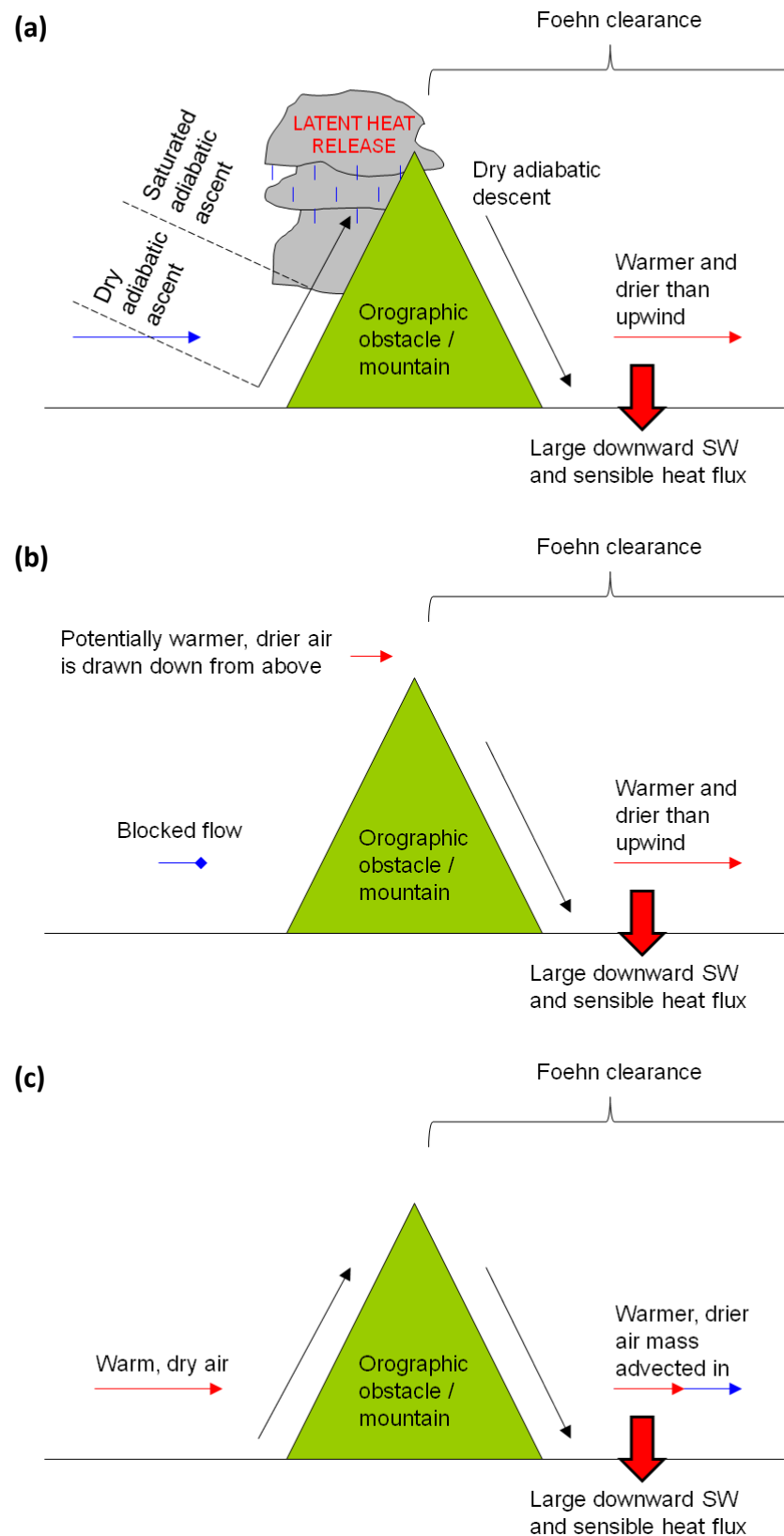
Figure 1.15: Illustrations of a) the latent heating mechanism, b) the upwind blocking / isentropic drawdown mechanism, and c) the warm source region mechanism for the föhn effect. Narrow red (blue) arrows denote relatively warm (cool) flows. The warm, dry, cloudless air constituting the föhn clearance leads to large downward solar shortwave and sensible heat fluxes.

Figure 1.16: The isentropic drawdown mechanism as it appears in Ficker (1920). 'Luft in Ruhe' translates from German to 'calm air', referring here to the blocked flow below mountain crest level. 'Erwärmung' translates to 'warming'.

Following Yoshino (1975), a revised description of the mechanisms responsible for föhn warming is found in Smith (1979). He pointed out that downstream warming may be caused by the latent heat mechanism (Figure 1.15a), the low-level blocking mechanism (Figure 1.15b), or due to a warmer source region (Figure 1.15c). This implies that föhn flow may take many forms; synoptically forced flow over a mountain, gap winds, and density-driven katabatic winds (which, through adiabatic compression heating and/or mixing may induce a near surface warming to the lee of a mountain).

Based on observations from various föhn cases since the ALPEX Experiment in 1982, Seibert (1990) contested the plausibility of latent heat being the primary föhn warming mechanism. Her objections included 1) sometimes föhn events are not associated with cloud formation upwind; 2) in the vast majority of cases there is no heavy rain fall (assuming cloud mass is in steady state, precipitation is required to induce a warming; otherwise water will re-evaporate as it descends the lee slope); 3) the quantitative effect of latent heat gain due to precipitation on the energy budget is too small to account for the temperature gradients associated with most föhn events.

Due to its mesoscale irregularities, the Alpine föhn is a highly three-dimensional phenomenon (Hoinka, 1985; Zängl et al., 2004). The Alps form an east-west barrier to flow, with alpine valleys largely aligned north-south. The föhn is, with very few exceptions, confined to valleys aligned north-south, originating from mountain passes (Zängl et al., 2004). Thus, it can be considered a type of gap flow. Two types of Alpine föhn have been identified in the literature; *shallow föhn* and *deep föhn*. Shallow föhn describes a föhn event where the synoptic pressure gradient is aligned north-south, promoting large scale easterly or westerly flow (corresponding to the *type B* gap flow described in Section 1.4.3) (*Zängl*, 2003)*.* In this case, the major mechanism for the generation of downslope winds is gap flow through mountain passes (Sprenger and Schär, 2001; Zängl, 2002). Deep (or 'classical') föhn occurs where

large scale flow is aligned predominantly north-south, i.e. cross-barrier (corresponding to the *type A* gap flow described in Section 1.4.3). In this case, gravity waves may develop and the mechanism for downslope winds in the lee of passes becomes more analogous to those discussed in relation to downslope windstorms in Section 1.4.1.

Föhn winds provide a highly proficient mechanism for the melting of snow (the Chinook is commonly known as "the snow-eater"; Hoinka, 1985). Hamann (1943) assigned the Chinook to be largely responsible for a temperature rise of 64°C in 14 hours east of the Black Hills in South Dakota. Math (1934) described a southwest Pacific-derived Chinook displacing polar air, to drive a 27°C temperature increase in just 5 minutes in the city of Havre, Montana. Not only are they warm, föhn winds are also characteristically dry (low relative humidity). This is because föhn air is sourced from regions aloft where the specific humidity is low, warmer air has a higher saturation vapour pressure (i.e. can hold more water), and because of the 'washout' effect of any precipitation which may occur upwind. Such dry air leads to clear, cloudless conditions (the "föhn clearance", or "föhn gap") in the lee of mountains, which in turn allows strong solar radiation to reach surface levels (Hoinka, 1985). Downwards sensible heat flux from the warm föhn air to a surface of snow or ice, together with enhanced incoming solar radiation leads to highly effective melting conditions (Figure 1.15). Sublimation rates are also likely to be high, due to the surface level advection of warm, dry, fast flowing air.

Föhn flow has also been found to prohibit the formation of the nocturnal stable boundary layer, due to turbulent mixing and advection at low levels (Beran, 1967).

Where föhn flows are associated with a hydraulic jump, the downwind extent of strong winds is limited, but the föhn effect (warming and drying) can extend further downstream (up to 100km away from the barrier in Southern Bavaria north of the Alps, according to Hoinka, 1985).

1.4.4.2 Modelling of real föhn events

As computer capabilities have improved, numerical modelling has played an ever increasingly important role in the study of flow over mountains. Numerical Weather Prediction Models (NWPs) have proved capable of simulating linear flow over mountains quite well (e.g. Shutts, 1992; Shutts and Broad, 1993), providing that

the model resolution is small relative to horizontal and vertical wavelength of mountain waves (Smith, 2004).

Modelling non-linear features of flow over mountains represents a greater challenge due to the sensitivity of lee-side flow to the height of the upwind dividing streamline; a difficult feature to reproduce accurately (Smith, 2004). Nevertheless, improved computer power, enabling advances such as 3-dimensional boundary conditions which evolve in time (e.g. Clark et al., 2000), smaller time steps and higher horizontal and vertical resolution, has accompanied an improvement in NWP simulations of realistic airflow over mountains.

The Mesoscale Alpine Programme (MAP) of 1999 aimed to improve the predictability and understanding of severe Alpine weather events (see Bougeault et al., 2001 for an overview). The availability of extensive validation data in the form of airborne and surface observations encouraged a series of modelling studies examining MAP föhn events (e.g. Zängl et al., 2004; Jaubert and Stein, 2003; Drobinski et al., 2003; Smith, 2004).

Zängl et al. (2004) provided surface and radiosonde observations, as well as high resolution (mesh size 800 m) simulations using the Penn State/NCAR mesoscale model MM5, for a case of deep föhn in the Wipp Valley in West Austria. The model simulated a highly non-linear southerly flow-over regime, with potentially cool air 'piling up' south of the alps. A strong pressure gradient was found to develop, with surface pressure 8 to 12 hPa higher upwind than downwind. The resulting föhn flow through the Wipp Valley is consistent with a *type A* gap flow. The föhn drives an increase in lee side temperatures of order 10°C.

Zängl et al. find that the high resolution simulation reproduced most of the observed features very well. The model is found to predict the onset of föhn within an hour for almost all regions, and simulated temperatures rarely stray outside 2K of observed temperatures. They deduce that the minor discrepancies between observations and model are mainly due to small scale orographic irregularities which are not fully resolved by the model. Finally, Zängl et al. showed that decreasing the model resolution to 1.4km had only weak detrimental effects on the accuracy of the simulation.

Jaubert and Stein (2003) modelled a strong deep föhn flow through the Rhine Valley. Despite strong approaching winds (>20 ms^{-1}, corresponding to an estimated $\hat{h}$

of ~1), non-linear phenomena such as wave breaking and blocking were evident. Hydraulic jumps in the lee of higher terrain limited the downwind extend of downslope windstorms, whilst gap winds extended downwind as jets.

Jaubert and Stein showed that the ability of their model (Meso-NH) to reproduce the local flow features strongly depended on the resolution. At 2.5km grid spacing, although the general characteristics were present, an increase in resolution to 0.625km was accompanied with a better representation of near surface winds and of mixing due to small scale wave breaking.

Drobinski et al. (2003) used the Meso-NH (at a finest mesh spacing of 2km) to investigate the characteristics of a föhn flow through the Rhine Valley as it evolved from a shallow to deep event. They found that the channelling efficiency of the valleys was enhanced and föhn flow was intensified as the föhn 'deepened' (i.e. the cross-barrier component of synoptic flow increased).

Smith (2004) used aircraft and radiosonde data to validate results gathered from the Met Office UM (Met UM), nested down to 1km, for a föhn event across the Swiss Alps. She found that the model reproduced the large-scale flow very well. Upstream wind and stability profiles are accurately simulated, and upstream flow splitting, a lee-side cold pool and the föhn flow are captured. Whilst the wavelengths were accurately simulated, gravity wave amplitudes were underpredicted. Smith suggests this is due in part to model smoothing of the strong inversion at the tropopause. This is a common NWP problem, and is attributable to limited vertical resolution and diffusion effects (Zängl et al., 2004).

Despite not gaining a great deal of attention, the field of föhn flow in the polar regions has been discussed in the literature. The region of the McMurdo Dry Valleys (MDVs) is the largest ice-free region in Antarctica, located between McMurdo Sound and the East Antarctic Ice Sheet. From the analysis of meteorological records in the area, westerly föhn has been identified to be responsible for near surface warming of >40°C (Speirs et al., 2010). The unique landscape of the MDVs is suspected to be due in part to ice melt caused by such events.

Speirs et al. (2010) coin the term 'polar föhn' for such events; one of which lasted 5 days during May 2007 and is discussed in their paper. Gusts were observed up to nearly 40 ms^{-1} and surface warming of 48.5°C is detected. The föhn event is associated with large-amplitude vertically propagating mountain waves. Previously,

such strong warm wind events have been attributed to a katabatic mechanism (initially proposed by Bull, 1966, according to Speirs et al., 2010). Subsequently, the föhn mechanism became more popular amongst those studying the region (Speirs et al., 2010). For example, Clow et al. (1988) noted that the MDVs do not lie within the katabatic confluence zone. Speirs et al. (2010) make use of model trajectory analysis to confirm the hypothesis put forward by previous studies that the warming due to the föhn mechanism dominates over warming due to katabatic flows from the polar plateau.

Chapter 2

Motivation and methods

Contents

List of figures

List of tables

2.1 Climate change in the vicinity of the Antarctic Peninsula

2.1.1 Recent climate change on the Antarctic Peninsula

The Antarctic Peninsula (AP) (Figure 2.1a) has been identified as one of the fastest warming regions on earth during the past 50 years (Vaughan et al., 2001). Station records reveal a warming rate of 3.7 ± 1.6 °C per century; several times the mean rate of 'global warming' (Figure 2.2a) (Vaughan et al., 2003). Furthermore, Vaughan et al. (2003) argue that evidence from ice core derived oxygen isotope records, marine sediments and the recent vacation of penguin rookeries suggests that such warming is unprecedented during at least the past 1800 years.

Until recently it was thought the degree of warming observed on the Peninsula during the last few decades may be unique on the Antarctic continent (e.g. Figure 2.2b). Vaughan et al. (2003) suggested that AP warming may be a regional amplification of 'global warming', but, regarding the trend across the entire Antarctic continent, described a locally variable pattern with mean warming close to the global mean (Figure 2.2a). King and Comiso (2003) identified a disassociation in climate regimes between the AP and the rest of continental Antarctica, reflected in a lack of correlation in satellite-derived surface temperatures. Furthermore, surface temperature records from stations reveal far greater interannual climate variability on the west coast of the AP than elsewhere in Antarctica, leading King (1994) to surmise that the region may exhibit stronger coupling between temperatures and regional sea-ice extent than elsewhere on the continent.

More recently, however, Steig et al. (2009) performed a study making use of not just the records provided by manned station data (as many of the previous studies – including that of Vaughan et al. (2003) – had confined their analysis to), but also records from automatic weather station (AWS) measurements, as well as satellite thermal infrared observations, to produce a more comprehensive documentation of Antarctic temperature trends than previously presented. Additional data points located in continental West Antarctica reveal a warming trend between 1979 and 2003 in this region greater than that found on the Antarctic Peninsula (Figure 2.3). Meanwhile, East Antarctic temperatures are also shown on the whole to have increased, though to a far lesser extent. Notable is the occurrence of anomalous sea ice losses in the West Antarctic sector, relative to small gains around the rest of the

continent. It would appear from Steig et al.'s (2009) results then that the major

climatic divide in the past few decades has been between East and West Antarctica,

rather than between the AP and continental Antarctica.
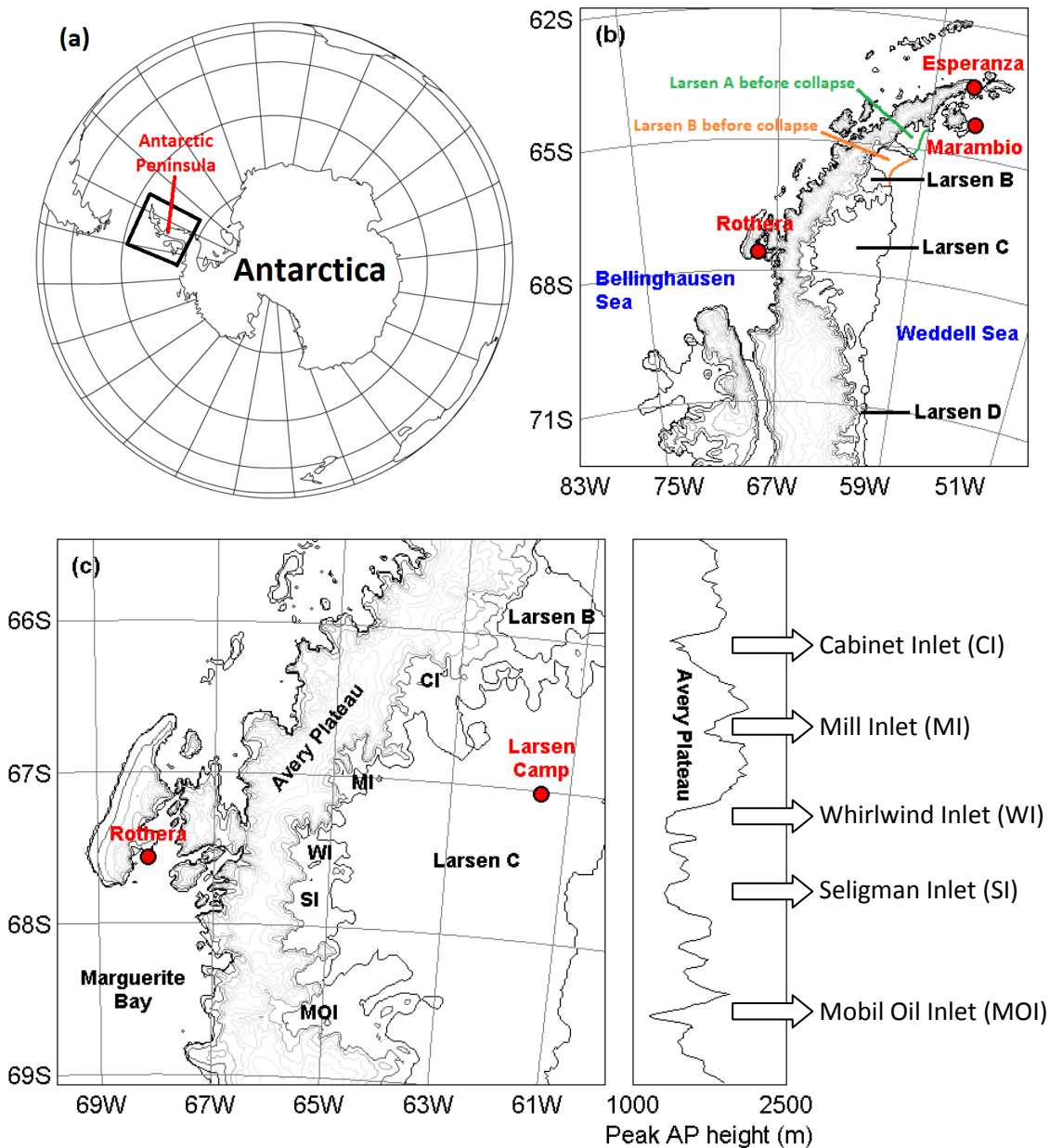
Figure 2.1: Maps showing the location of the Antarctic Peninsula and other important
locations. The black box in (a) marks roughly the outline of map (b). Also plotted (to the right
of the map) in (c) is peak orographic height for each model grid increment along the y-axis
(roughly N-S) along the crest of the AP. Passes / depressions in the crest line generally
coincide with the positions of inlets (marked) on the eastern slopes of the AP.
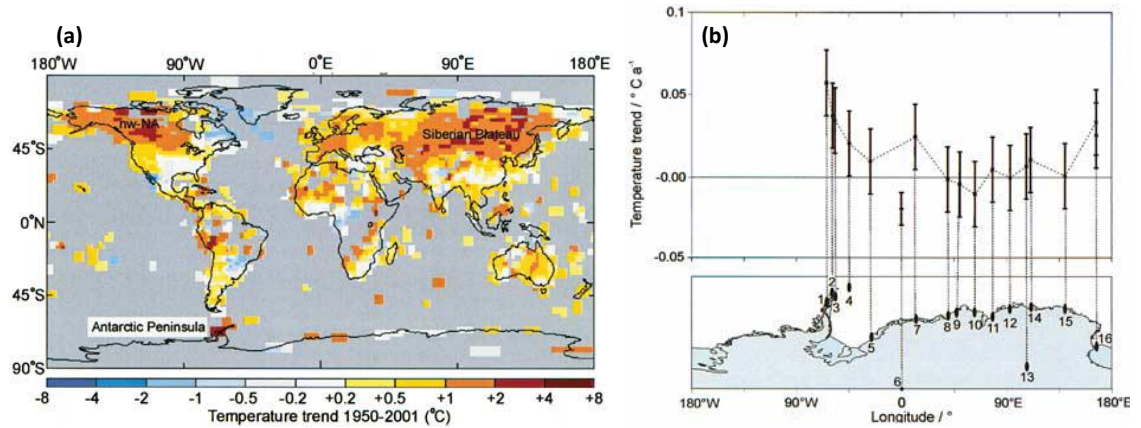
Figure 2.2: (a) Trends in surface mean annual air temperature for 1950-2001 as derived from weather stations; grey shading denotes areas of no data. (b) Variations in meridional temperature trends calculated for 16 Antarctic stations. Stations 1, 2 and 3 (Faraday/Vernadsky, Bellingshausen and Esperanza respectively) are located on the AP and exhibit the greatest warming trend. Error bars are given at the 1-sigma (68%) level. After Vaughan et al. (2003).
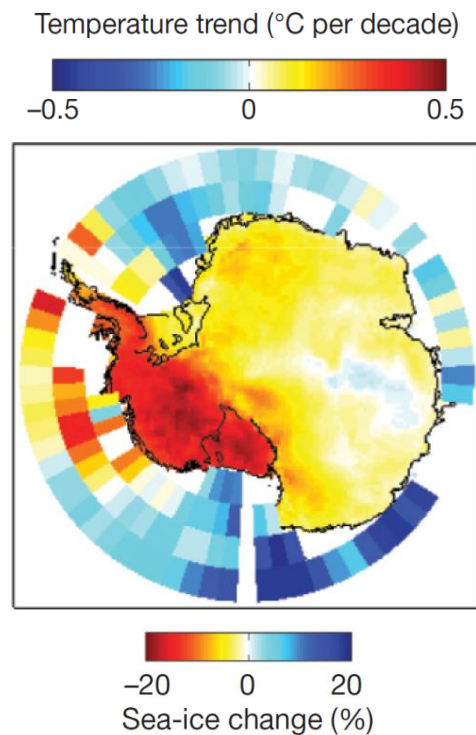
Figure 2.3: Reconstruction of trends in temperature and sea-ice concentration between 1979 and 2003 from both manned and automatic weather station measurements, as well as satellite thermal infrared observations. From Steig et al. (2009).

On the AP the majority of climate records, including the longest ones, are located on the northwest side of the Peninsula. However, shorter records point towards similar warming to the east and south (Vaughan et al., 2001). Moreover, records from Esperanza and Marambio research stations in the far northeast of the AP suggest that the warming may have even been stronger than on the west (Marshall et al., 2006). Whilst to the west of the Peninsula the warming has been strongest during

the austral autumn and winter (Meredith and King, 2005), the east side has experienced enhanced warming during the summer and autumn (King, 1994).

At a local level, the warming of the AP has brought about changes to terrestrial flora, seasonal snow cover, lake ecology, penguin distribution, ice-shelf distribution, glacier thickness and sea-ice duration (Vaughan et al., 2003). Eastern AP warming is also thought to be partly responsible for the collapse of 7 ice shelves in the past 50 years, associated with minor sea level rise and potentially affecting Weddell Sea deep water production (Vaughan et al., 2001). Meltwater ponds have increasingly been observed on the surface of AP Ice Shelves during the melt season (Van den Broeke, 2005). It has been suggested that the action of such meltwater ponds in the propagation of fractures and crevasses in the ice helps to accelerate ice-shelf disintegration (Van der Veen, 2007; Glasser and Scambos, 2008).

East of the Peninsula, the Larsen Ice Shelf reaches over 200km across the Weddell Sea as a floating extension of the glaciers originating in the mountains of the AP (Figure 2.1b). Over the past few decades, seven of the twelve ice shelves around the AP have either retreated significantly or been lost altogether (Cook and Vaughan, 2010). The collapse of ice shelves can indirectly bring about sea level rise by causing the glaciers that feed them to accelerate (Cook et al., 2005). Cook et al. (2005) establish that 87% of AP glaciers have retreated since their earliest known positions.

Morris and Vaughan (2003) constructed a map of mean near-surface air temperature for the AP region for the year 2000, using measurements of snow depth and air temperature from meteorological stations and AWSs. They found that the spatial extent of AP ice shelves closely follows the -9°C isotherm (Figure 2.4 and Table 2.1). The limit of the ice shelves which have exhibited considerable ice loss over the past few decades is bounded by the -5°C and -9°C isotherms (except for one anomaly; the southern ice front of the George VI Ice Shelf has retreated, yet is located south (the cooler side) of the -9°C isotherm; Figure 2.4), consistent with a warming of around 4°C (Morris and Vaughan, 2003).

(a)   **(b)**
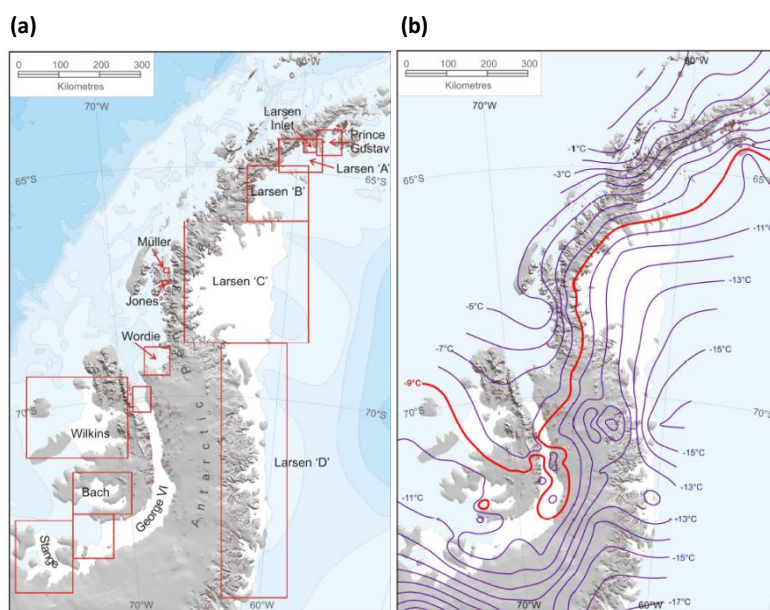
Figure 2.4: (a) Location of ice shelves in the vicinity of the AP. (b) Mean annual temperature during 2000 (contours), as compiled by Morris and Vaughan (2003). From Cook and Vaughan (2010).

Ice Shelf	Total change (km^2)	% remaining
Müller	-38	51
Jones	-29	0
Wordie	-1281	10
Wilkins	-5434	67
George VI	-1939	93
Bach	-311	94
Stange	-264	97
Prince Gustav	-1621	1
Larsen A	-3624	10
Larsen B	-9166	21
Larsen C	-5295	91
Larsen D	886	104
All	-28117	82

Table 2.1: Change in surface area of ice shelves in the vicinity of the AP between the earliest records and the most recent observations (2008/2009). See Figure 2.4 for ice shelf locations. From Cook and Vaughan (2010).

The two northernmost sections of the Larsen collapsed in January 1995 (Larsen A; Figure 2.5) and February-March 2002 (Larsen B; Figure 2.6). These collapses define the two most spectacular ice shelf retreats documented on the AP. The Larsen A lost almost 2000 km^2 of ice within a few weeks, and the Larsen B lost ~3250 km^2 within a few days (Cook and Vaughan, 2010). Images taken from NASA's Terra satellite illustrate the dramatic nature of the Larsen B collapse (Figure 2.8).
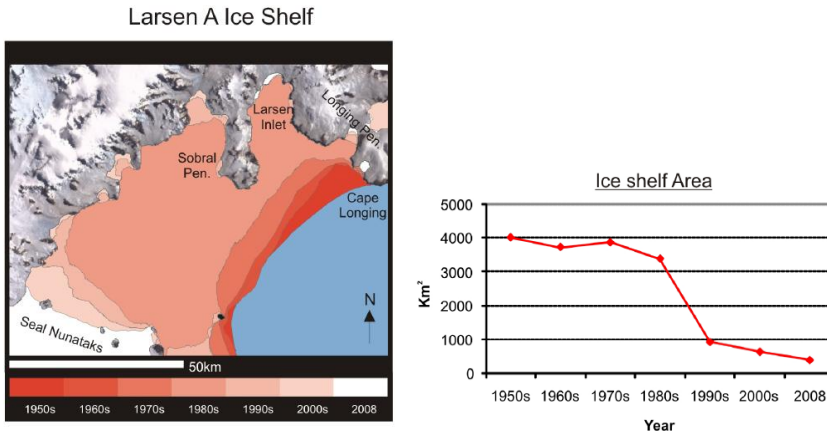
Figure 2.5: Change in spatial extent and surface area of the Larsen A Ice Shelf. From Cook and Vaughan (2010).
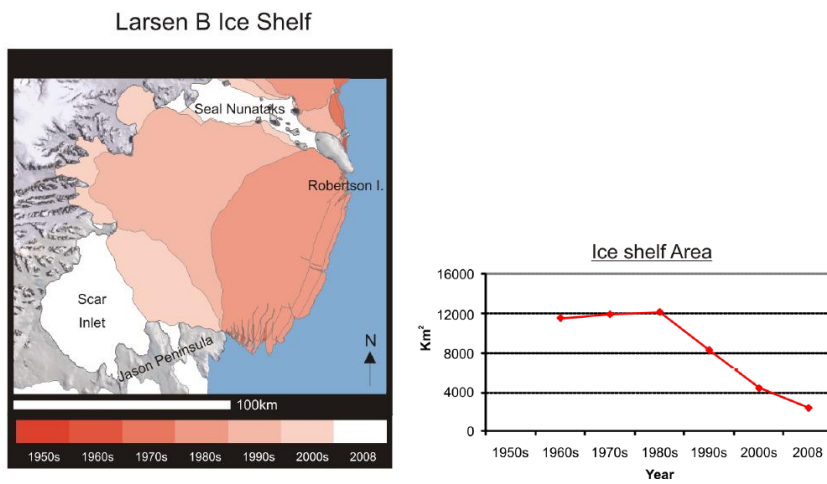
Figure 2.6: Change in spatial extent and surface area of the Larsen B Ice Shelf. From Cook and Vaughan (2010).
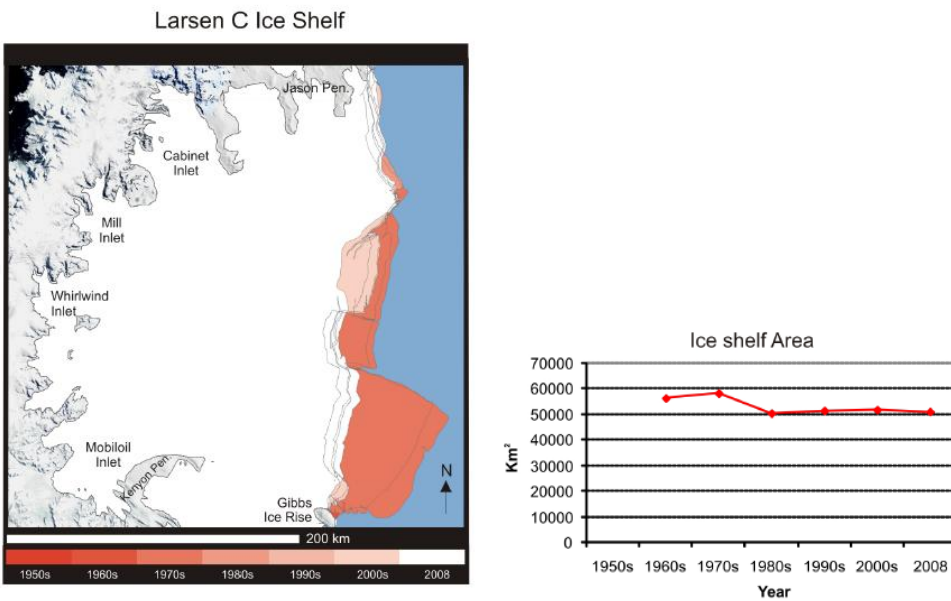
Figure 2.7: Change in spatial extent and surface area of the Larsen C Ice Shelf. From Cook and Vaughan (2010).

(a)

(b)

Detached ice / icebergs
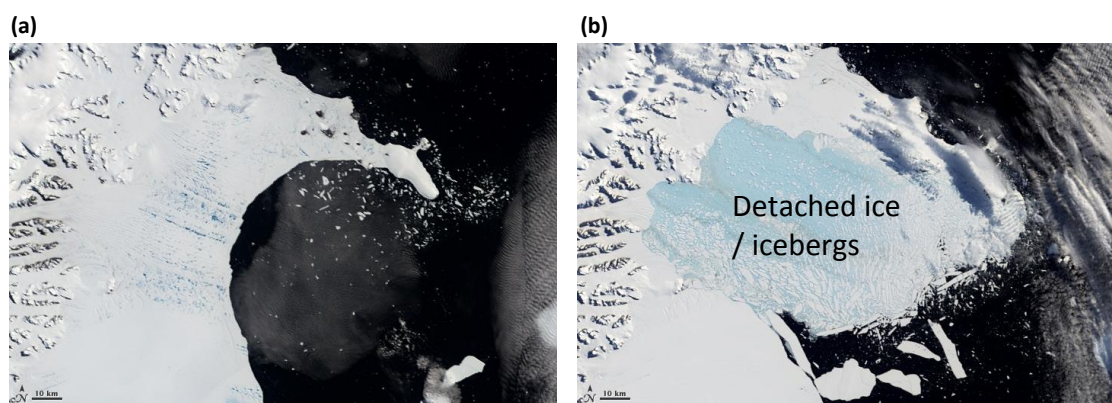
Figure 2.8: Satellite images of the Larsen B Ice Shelf (a) on 31 Jan 2002 before its collapse and (b) on 7 March 2002 after its collapse, from the Moderate Resolution Imaging Spectroradiometer (MODIS) on NASA's Terra satellite.

Marshall et al. (2006) examined surface data to find that the two summer seasons during which the Larsen A and B collapses occurred coincided with the two warmest summers on record (between 1959 and 2005) at Esperanza. Immediately before the collapse, a large amount of meltwater was observed on the ice sheet surface (Van der Broeke, 2005). Many theories have been postulated for the breakup of the two ice shelves, the majority of which define warming atmospheric temperatures as the underlying cause (Cook and Vaughan, 2010). Glasser and Scambos (2008) made use of satellite data to conclude that, as well as the atmospheric mechanism, increasing ocean temperatures due to the intrusion of Circumpolar Deep Water onto the continental shelf (Vaughan et al., 2003) leading to enhanced bottom melting and the recession of the ice-shelf front is likely to have played a role in the collapse. However, Nicholls et al. (2004) used conductivity-temperature-depth observations to deduce that regional changes in ocean temperature are unlikely to have a major effect on basal melting of the Larsen, though they highlight the urgent need for further oceanographic observations in the region to improve understanding.

This study will focus geographically on the vicinity of the largest remaining section of the Larsen Ice Shelf, Larsen C (Figure 2.1b). In contrast to Larsen A and Larsen B, Larsen C has been relatively stable in recent decades, with no large calving events (Figure 2.7). It currently lies immediately to the south and east (the cooler side) of the -9°C near-surface temperature isotherm, as determined in Morris and Vaughan's (2003) study (Figure 2.4).

2.1.2 Changing Antarctic atmospheric circulation in association with warming on the Antarctic Peninsula

At a maximum height of over 2000 m, length of ~1500 km and width of ~200 km, the AP is a significant promontory and obstacle to flow (Orr et al., 2008). The circumpolar vortex defines a mean westerly flow regime around the South Pole, bringing warm, moist air from across the Southern Ocean and Bellinghausen Sea to impinge on the Peninsula (Marshall et al., 2006). For the most part, the low level westerly transport of these (commonly) stably stratified air masses is halted by the AP, especially to the south where the Peninsula is bounded by the high mountains of West Antarctica (Orr et al., 2008). For this reason, the east side of the AP is commonly cooler than that of the west, being strongly influenced by equator-ward winds bringing cold air from the continent. This cold and highly statically stable air tends to dam up against the east side of the AP which can result in the formation of strong southerly barrier winds (Schwerdtfeger, 1974; Parish, 1983). Such cool pools are encouraged by heat loss to the cool ice surface of the Larsen (the temperature of which is capped at 0°C), with a deep near-surface inversion a common feature. In the vicinity of the Larsen C, the AP's west coast is thus on average 3-5°C warmer at near-surface level than its east coast (the western extent of the Larsen Ice Shelf) at the same latitude (Morris and Vaughan, 2003). Further east across the Larsen Ice Shelf, near-surface temperatures are considerably cooler still (Figure 2.4).

A few theories have been postulated for the AP warming trend, with Vaughan et al. (2003) proposing three mechanisms: changing ocean circulation, local greenhouse warming amplified by sea-ice processes, and changing atmospheric circulation. Within the context of atmospheric circulation, consideration has been given to the possibility of increasing northerly winds bringing in warm South Pacific air (King and Harangozo, 1998; Van den Broeke, 2000). Thompson and Solomon (2002) went on to investigate the relationship between rising AP temperatures and a recent strengthening of the mean westerly winds that circumnavigate the pole. They propose that the enhanced westerly winds act to replace the incidence of cool continental outbreaks onto the AP from the south with relatively warm maritime air from the Bellingshausen Sea.

The strengthening circumpolar vortex is associated with a positive shift towards the high-polarity index of the Southern Annular Mode (SAM) since

approximately 1965 (Marshall, 2002), a shift which has been attributed largely to human activity. Thompson and Solomon (2002) provide evidence that the trends in tropospheric circulation in the Southern Hemisphere can be traced to changes in lower stratospheric circulation brought about largely by photochemical ozone losses (the Antarctic ozone "hole"), and to a lesser extent by increases in well-mixed greenhouse gases and stratospheric water vapour.

Marshall et al. (2002) found that surface AP warming was substantially greater than that higher in the troposphere, casting doubt on the theory that large scale atmospheric circulation changes could be responsible. However, Orr et al. (2004) proposed a "low level" orographic explanation for the western AP warming, whereby the oncoming westerlies are blocked by the AP and deflected southwards, giving rise to increased northerlies and enhanced advection of warm air into the area.

Marshall et al. (2006) went on to find that fluctuations in the recent surface warming trend on the east side of the AP (at Esperanza Research Station) showed considerable similarity to temperature variability explained by the trend in the SAM (Figure 2.9). They suggest that warming to the east of the AP during westerly flow may not only be due to the advection of warm westerly winds replacing cooler continental air masses, but also to the regional effect of föhn warming associated with cross-Peninsula flow. The positive trend in the SAM is most apparent during summer seasons (Marshall, 2003), which, assuming there does exist a connection between the SAM and east AP warming, could explain the (previously discussed) enhanced summer season warming to the east relative to the west of the AP.
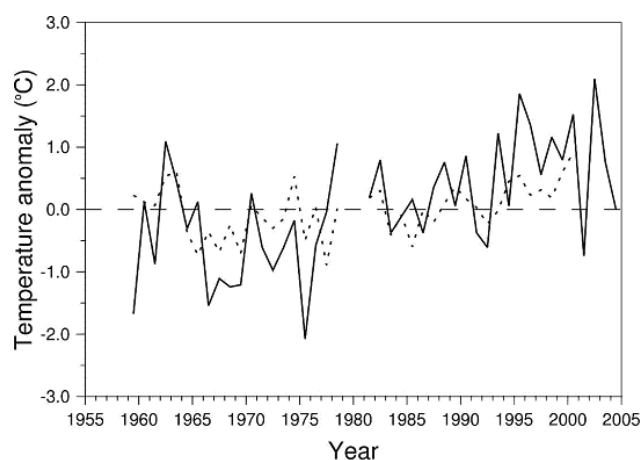
Figure 2.9: Variation in summer temperatures at Esperanza Research Station (solid line) and variations explained by the trend in SAM (dotted line) based on detrended data between 1965 and 2000. The correlation is 0.46, significant at the <1% level. After Marshall et al. (2006).

At the AP, based on composite ERA-40 reanalysis data between the years 1958 and 2000 used by Marshall et al. (2006), negative polarity SAM (SAM-) summers are found to be characterized by mean upstream westerly flow at a geopotential height of 850 hPa of $\bar{u}$ ~5ms^{-1} and hence $\hat{h}_{SAM-}$ ~3.00 and positive polarity SAM (SAM+) summers by $\bar{u}$ ~8ms^{-1} and $\hat{h}_{SAM+}$ ~1.88 (Orr et al, 2008).

Building upon Marshall's work, Van Lipzig et al. (2008) performed composite comparisons of SAM+ and SAM- using the regional atmospheric climate model (RACM014) to demonstrate the enhanced flow-over conditions during SAM+ and its effects on temperature and weather. Their results show increased (decreased) cloud cover and precipitation to the west (east) of the AP during SAM+ conditions. These findings are indicative of the föhn mechanism. As illustrated in Figure 2.10, the temperature difference between SAM+ and SAM- is greatest above the AP's east slope and the Larsen along a cross section passing through Larsen B Ice Shelf (Van Lipzig et al., 2008). Towards the north at Esperanza, despite very low $\hat{h}$ encouraging enhanced flow-over, the relatively low altitude of the AP here diminishes the degree of warming associated with the föhn (Van Lipzig et al. 2008). Towards the south at Alexander Island, AP altitude is too high for extensive flow-over even during SAM+ conditions and no east side warming is observed.

Whilst the trend in the SAM has been much discussed in the literature in relation to enhanced westerly flow and AP warming, Thompson and Solomon (2002) find that in fact only 50% of the warming is accounted for by the coincident trend in the SAM. This highlights the importance of other climate change mechanisms in the region. Steig et al. (2009) found that the observed temperature trends in their reconstruction combining manned and unmanned stations closely resembles the pattern of temperature anomalies induced by the zonal wavenumber-3 pattern in atmospheric circulation. Observations suggest a shift towards the positive phase in the wavenumber-3 pattern since about 1979 (Holland and Raphael, 2006), which, according to model work carried out by Steig et al. (2009), is associated with greater cyclonic flow in the Amundsen Sea region, bringing warm, moist northerly winds to West Antarctica and the AP. This mechanism is likely associated with the recent loss of sea ice in this region (Figure 2.3), and to north westerly föhn across the Antarctic Peninsula (Steig et al., 2009).
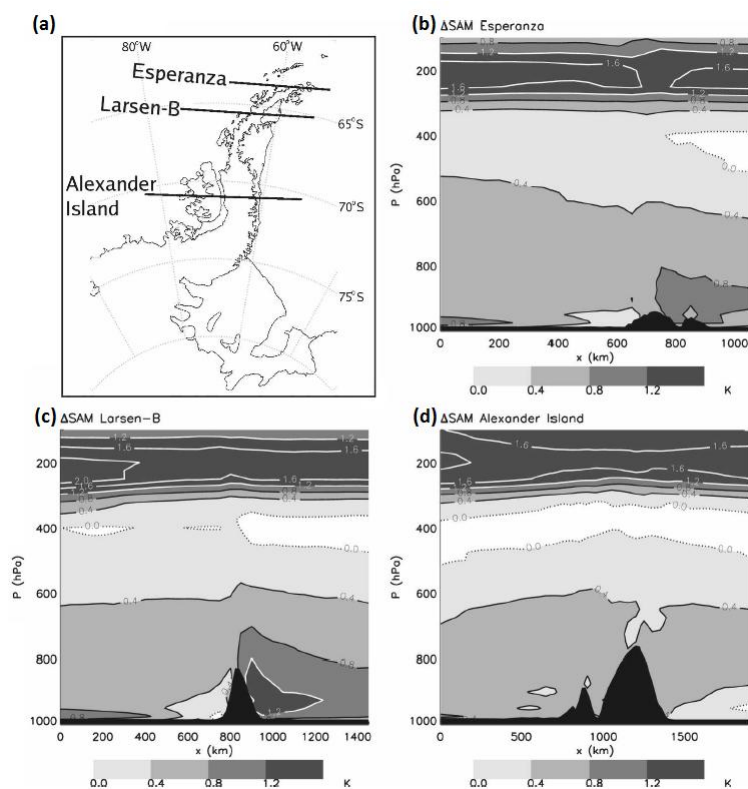
Figure 2.10: Difference in potential temperature between summer SAM+ and SAM- conditions for cross sections passing above (b) Esperanza Research Station, (c) the Larsen-B Ice Shelf and (d) Alexander Island. Cross sections transects are marked in (a). After Van Lipzig et al. (2008).

2.2 The effect of westerly flow on glacio-meteorological conditions in the vicinity of the Antarctic Peninsula

2.2.1 The effect of the Antarctic Peninsula and the Larsen C Ice Shelf on the lower atmosphere during westerly flow

In the vicinity of the Larsen C Ice Shelf the Antarctic Peninsula is a continuous high level ridge (Figure 2.1c). Despite there being no major cross-ridge valleys, there are lower sections of the ridge and passes between peaks which provide an 'easier' route for air to cross the AP. Large glacial valleys to the east of the AP provide conduits through which downslope flows may be channelled (note that gap flows in the Rhine Valley, Germany have been observed to keep within the width of the valley they flow through, rather than the much narrower pass they breach; Jaubert and Stein, 2003). The deepest of the passes is located upslope of Mobil Oil Inlet, towards the south of the region of interest. North of about 67.2°S, the ridge bends from being aligned roughly north-south to become aligned roughly northeast-southwest, widens

and rises in altitude as the Avery Plateau is encountered. A notable pass is encountered towards the northern extreme of the region of study, upslope of Cabinet Inlet. Other major inlets include Whirlwind Inlet and Mill Inlet.

As a long high-level ridge with few gaps, it follows that the AP has a strong blocking effect on approaching flow, i.e. the critical $\hat{h}$ defining the transition from non-linear to linear flow will be low (see Figure 1.8). Through the passes, one would expect gap flows and, under suitable conditions, potential vorticity banners downwind. It should be expected that, during periods of southerly to south westerly synoptic flow, *type B* westerly gap winds may develop across the AP due to a west-east pressure gradient. Such flows cannot occur when geostrophic flow is north to northeasterly, though *type A* westerly gap flows may.

The long straight nature of the obstacle has also been observed to promote the formation of barrier winds (southerly barrier flows have been observed to the east of the AP by Parish, 1983). A north westerly barrier flow may encourage more flow over the AP due to Coriolis deflection to the left associated with barrier flow acceleration.

The AP is bounded to the south by the Antarctic continent, but air is free to flow around the northern tip. However, Coriolis acceleration is more likely to encourage westerly flow to be diverted to the right and flow southwards. Upstream blocking and a wake induced vortex in the lee caused by flow around the northern tip may lead to lee cyclogenesis, bringing warm westerly air to the Larsen Ice Shelf (though these maritime air masses tend to be relatively moist and therefore unlikely to possess the melting potential of the dry, cloudless föhn air).

The first mention in the literature of föhn warming on the Larsen C is found in Schwerdtfeger (1984). Schwerdtfeger discusses 20 months-worth of measurements from a meteorological station at Snow Hill Island (on the east side of the AP towards its northern-most extent, at a latitude of ~64.5 °S), erected as part of the Swedish South Polar Expedition of 1901-1903. The coolest temperature detected during this period was -41.4 °C on 6 August 1902, whilst the warmest temperature detected was 9.3 °C on 5 August 1903. Schwerdtfeger attributes such anomalously warm winter-season conditions to the föhn effect.

Orr et al. (2008) performed rotating tank experiments to examine the changeover in conditions from blocked to flow-over regimes over a model of the AP.

In the blocked regime, as the air beneath z_d approaches the ridge it begins to slow down and is deflected to the right (south) due to the decrease in Coriolis force, forming a barrier jet. Some air (above z_d) does flow over the ridge, accelerating and hence being deflected to the left/north. In the flow-over regime, enhanced flow-over promotes strong downslope winds on the Leeside and a subsequent hydraulic jump (Orr et al., 2008). Laboratory models such as this one are valuable in assessing the underlying processes, but in reality the idealized flow and terrain is unrepresentative of real flow (Orr et al., 2004).

To accompany their laboratory findings, Orr et al. (2008) used the MetUM at 12km horizontal resolution to simulate 2 real cases characterised by 1) a blocked regime and 2) a flow over regime. The model clearly reproduced the differences in air flow and west-east temperature gradient between the two regimes across the AP, with east side warming only present in the flow-over case. However, in the flow-over case a relatively deep cool pool remained above the Larsen, the föhn air unable to penetrate to near-surface level. Orr et al. suggests this may be due to the use of climatological (monthly) rather than daily sea ice fields. They argue that as a consequence sea ice coverage in the north-east Weddell Sea was exaggerated, incurring a highly stratified lower atmosphere through which the descending föhn could not penetrate. However, modelling work carried out in association with this study suggests it is more likely due to their model not being high enough resolution to resolve the magnitude of vertical motions in the vicinity of steep, complex terrain.

King et al. (2008) analyse observational data acquired from aircraft measurements over the Larsen Ice Shelf on 6 January 2006. These measurements document a föhn event with significantly higher temperatures and lower humidity apparent on the east coast relative to the west coast (Figure 2.11). From low level flight measurements over the Larsen, strongly stable air was observed to extend up to an elevation of ~250m. However, the depth of the stable boundary layer as implied by the turbulence kinetic energy profile was over 600m. King et al. (2008) deduced that turbulence at such high levels was a result of the presence of strong vertical shear in the horizontal wind vector associated with a low level southerly to southwesterly jet of peak speed (15ms^{-1}).
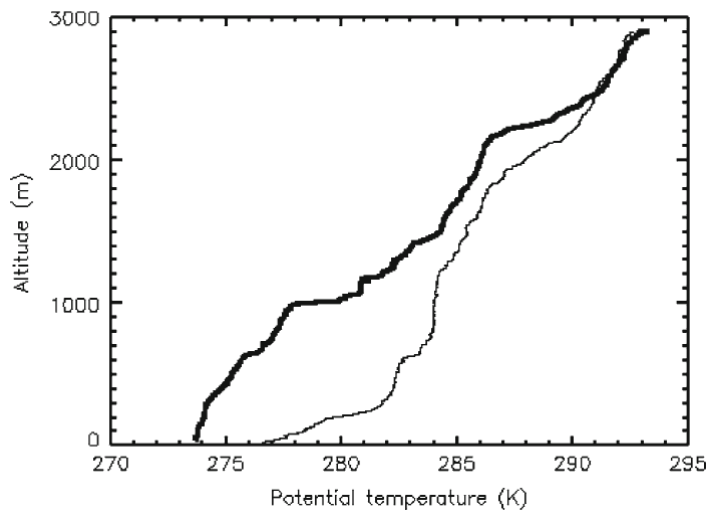
Figure 2.11: Vertical profiles of potential temperature during aircraft ascent from Rothera Research Station upwind (west) of the AP (thick line) and initial descent towards the Larsen Ice Shelf near Larsen Camp (for location see Figure 2.1c) downwind (east) of the AP (thin line), on 6 January 2006. After King et al. (2008).

The case study work of Orr et al. (2008) and King et al. (2008) confirms that westerly flow of suitable strength incident on the AP brings about cross-Peninsula flow and an east side warming due to the föhn effect.

The presence of the Larsen C to the east of the AP has a major effect on boundary layer flow and conditions. In contrast to observations of Alpine föhn the Larsen C Ice Shelf provides a flat, low friction surface comprising very few orographic complexities. As such, once clear of the orography of the Peninsula, downslope flows are not confined to valleys, as is often the case in the Alps.

As described in Section 2.1.2, cool air often pools to the east of the AP above the Larsen C, due to continental southerlies and heat loss to the ice surface of the Larsen. The boundary layer is particularly stable during the winter months (King et al., 2008). Lee et al (1989) used a 2-dimensional hydrostatic model with idealised terrain to show that the presence of a cool pool in the lee of a mountain can curtail the generation of large amplitude mountain waves. They found that under such conditions, a downslope windstorm struggles to penetrate through the cool pool to flush away the cool air. In their simulations, the cool pool would eventually erode away by strong mixing at the leading edge, after which the mountain wave was able to develop to the point of breaking and stronger downslope winds would appear.

During the summer season near-surface conditions become less stable and convective boundary layers are commonly observed on the Larsen (Kuipers Munneke

et al., 2012). This diminished stratification enables the deeper penetration of descending warm föhn flow towards the surface (Orr et al., 2008). Since surface temperatures over the ice sheets on the east side of the AP cannot exceed 0°C, such near-surface warming can lead to the formation of a strongly stable boundary layer (King et al., 2008).

As explained in Section 1.4.4.1, the föhn effect may be experienced a long way downwind of a hydraulic jump. However, in the case of the Larsen, the presence of a cool pool and continued surface cooling due to the ice surface may prevent such extensive warming in the absence of advected föhn surface winds.

Consequently it is hypothesised that, in the case of the AP, a highly non-linear flow-over regime may induce strong warming at the base of the lee slope, but that the warming may not extend far downwind as a hydraulic jump acts to 'pump' the föhn air back upwards. In the case of a more linear flow-over regime, it might be expected that a) the cool pool takes longer to be flushed away because of weaker, less erosive downslope winds; b) föhn warming in the immediate lee is less intense as air is derived from lower altitudes upwind; and c) once the cool pool is eroded away, föhn air is more likely to advect eastwards at near-surface level above the ice in the absence of (or the presence of a less pronounced) hydraulic jump.

Theoretically (as described in Section 1.3.2), in the case of completely linear ($\hat{h} \ll 1$) flow where there is no low level wave breaking or windward flow splitting, the upwind and downwind atmospheric profiles are identical, since air on the leeside will have been derived from the same height upwind and no dissipative effects will be present across the obstacle. Of course, a completely linear scenario is impossible in nature, and, as previously mentioned, observations would suggest that pseudo-linear vertically propagating mountain waves are a relatively rare occurrence (though more common across the AP than across other mountain ranges; see Figure 1.6). Furthermore, since the maritime westerlies are generally warmer than the air above the Larsen, even linear advection of westerly flow across the AP is likely to bring about a leeside warming.

It should be expected that, during non-linear flow regimes, gap jets – extending as they do further downwind than adjacent hydraulic windstorms – may also help to advect föhn air across the Larsen.

Although there has been much research into föhn, there has been little study on the extent of leeside warming and the sensitivity of such warming to upstream conditions, as discussed above. Often the focus appears to be on the strength of downslope flow, presumably considering the potential for wind damage.

2.2.2 The föhn effect on the Larsen C Ice Shelf

As stated previously, the Larsen C currently lies to the south and east (the cooler side) of the -9°C isotherm in Morris and Vaughan's (2003) map of estimated mean near-surface temperatures in the vicinity of the AP (Figure 2.4), and has been relatively stable in recent decades with no major calving events (Figure 2.7). Although not in danger from collapse in the immediate future, Cook and Vaughan (2010) assert that, should AP warming continue, the Larsen C may soon succumb to a similar pattern of retreat.

In a study using data from the British Antarctic Survey (BAS) AWS at Larsen Camp (named AWS Larsen; the location of Larsen Camp is shown in Figure 2.1c) recorded between March 1995 and March 2003, Van den Broeke (2005) determined a strong dependence of ice melt rates on wind direction. The highest ice melt rates (average of ~4 mm per day) were observed when wind was from the northwest (coincident with conditions likely to promote the advection of warm föhn flow across the AP), whilst the lowest rates were accompanied by southerly flow (likely consisting of air of continental origin).

King et al.'s (2008) aircraft measurements of surface heat fluxes on the Larsen in westerly föhn conditions during the afternoon revealed a mean net energy flux of 52 Wm^{-2} available for melting the ice shelf. They found that the net radiative flux made the largest contribution (92%) to the melt, whilst the contribution made by sensible heat flux (25%) was largely offset by latent heat flux, which was found to remove heat from the surface via sublimation equivalent to 17% of the melt rate. Comparing their values with the work of Van den Broeke (2005), King et al. (2008) found that their observed mean melt rate was similar to climatological estimates at the same time of day measured at a nearby AWS.

Kuipers Munneke et al. (2012) analyse data sourced from two AWSs on the Larsen C for the period between 22 January 2009 and 1 February 2011. The primary AWS (IMAU AWS 14) used for the study was located within close proximity of Larsen

Camp (Figure 2.1c). During the summer (DJF) at IMAU AWS 14, net shortwave radiation provided a large source of energy (mean of 38 Wm^{-2}) to the ice surface, while energy was removed by net longwave cooling (mean of -21.1 Wm^{-2}), latent heat flux (mean of -9.6 Wm^{-2}) via sublimation and sensible heat flux (mean of -5 Wm^{-2}) owing to the commonly convective nature of the summer surface layer. A considerable amount of energy (mean of 8.6 Wm^{-2}) is consumed by melting.

The summer convective boundary layer is caused by the large downward shortwave radiative flux warming the surface. Conversely, during nighttime in the summer and during the entire winter season, a surface inversion exists above the Larsen and the flux of sensible heat is positive towards the surface (Kuipers Munneke et al., 2012).

A surface inversion can also be formed when warm air is advected above the cool ice surface. Kuipers Munneke et al. (2012) identified such an episode in their AWS observations during November 2010. During this time, winds observed at IMAU AWS 14 had a strong westerly component, and, with the use of a NWP model, Kuipers Munneke et al. (2012) are able to confirm that the period documents a föhn event associated with strong westerly flow across the AP. The resultant föhn clearance is reflected in strong net shortwave radiation and low net longwave radiation for the period 10-18 November (Figure 2.12 and Table 2.2). The warm (>0°C) föhn air induces a positive sensible heat flux, but this is largely offset (as in the case studied by King et al., 2008) by a large negative latent heat flux due to sublimation (encouraged also by the warmth, and the dryness of the föhn air). The combination of a large shortwave flux and positive sensible heat flux counterbalances energy lost through longwave and latent heat fluxes, leaving a mean value of 29.6 Wm^{-2} for the period (Figure 2.12 and Table 2.2).
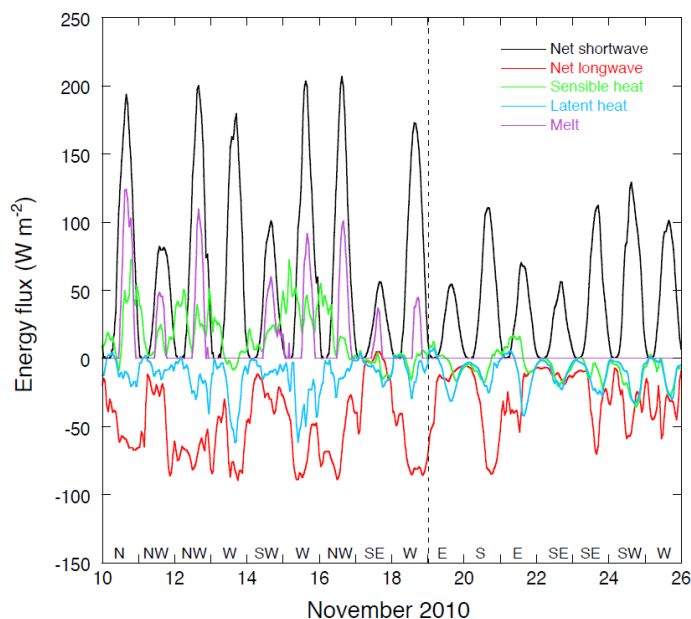
Figure 2.12: Surface energy balance components during the period 10-26 November 2010. Daily mean wind direction is shown at the bottom of the panel. Data is from measurements at IMAU AWS 14 near Larsen Camp. From Kuipers Munneke et al. (2012).

Field	Unit	10-18 Nov	19-25 Nov
Air temperature (2m)	°C	-0.4	-5.6
Relative humidity (2m)	%	79	92
Net shortwave flux	Wm^{-2}	63.1	37.8
Net longwave flux	Wm^{-2}	-49.9	-25
Sensible heat flux	Wm^{-2}	16.5	-6.8
Latent heat flux	Wm^{-2}	-13	-11.1
Melt energy	Wm^{-2}	29.6	0.9

Table 2.2: Mean surface energy balance components (positive downwards) and meteorological fields for the period of broadly westerly near-surface flow of 10-18 November 2010 and the subsequent period of largely southerly to easterly near-surface flow of 19-25 November.

After the föhn episode, winds at IMAU AWS 14 turn to become largely easterly to southerly, advecting cooler, moister air into the region. During this period (19-25 November), the mean net shortwave flux decreases considerably, the sensible heat flux becomes negative (convective), and very little energy is made available for melt (Figure 2.12 and Table 2.2). The negative sensible heat flux is explained by the advection of cool air above a wet snowpack which must refreeze before cooling below 0°C (Kuipers Munneke et al., 2012). Comparing the two periods serves to highlight the exceptionally large surface energy fluxes and melt rates present during föhn conditions.

2.3 Thesis aims

In an attempt to explain the recent rapid regional warming observed on the AP's eastern coast, the föhn warming hypothesis developed in a series of papers between 2006 and 2008 (Marshall et al., 2006; Orr et al, 2008; Van Lipzig et al., 2008; King et al., 2008; see Section 2.2). This thesis is motivated by this hypothesis and contributes to a major NERC-funded research project (Orographic Flows and Climate of the Antarctic Peninsula; OFCAP) which is investigating various aspects of this hypothesis.

The case of warming temperatures to the east of the AP illustrates the potential impact of regional climate change on both local and global scales, as well as the importance of mesoscale processes in shaping regional climate. Simulations of real föhn flow over the Alps (as part of the MAP project) using high-resolution (below 2km mesh spacing) models have shown excellent correlation with observations (Drobinski et al., 2003; Jaubert and Stein, 2003; Zängl et al., 2004; Smith, 2004; see Section 1.4.4.2). However, due to the lack of observational data such studies have been, up until now, impossible to emulate over Antarctica.

As part of the OFCAP project, an intensive field campaign took place in the vicinity of the AP (based at BAS's Rothera Research Station; Figure 2.1b) between January and February 2011. During the campaign, aircraft, AWS and radiosonde observations were gathered to document (amongst other objectives) two westerly föhn events across the AP. Such an abundance of observational data far improves upon previous attempts at observing such events. In Section 2.4 the methods of observational data capture are discussed.

Most of the previous model studies within the field of orographic flow over the AP have suffered from a common shortcoming; insufficient resolution. Climate model or (re)analysis studies (e.g. Marshall et al., 2006; Van den Broeke and Van Lipzig, 2004; Van Lipzig et al., 2004) have generally used horizontal resolutions over 50km, tending to yield an underestimate of the height of the AP (Van Lipzig et al., 2008), preventing accurate analysis of the influence of the complex topography on the flow. Even at the relatively high horizontal resolution of 14km, Van Lipzig et al. (2008) found that their RACM014 simulations overestimated many sea surface temperature anomalies. In Orr el al. (2008) downslope winds were unable to penetrate through the cool pool capping

the Larsen C in their model simulation of a real föhn case. Although largely attributed
to the use of monthly sea ice fields in their model runs, it is suspected that insufficient
resolution was at least partly responsible. Their model had a grid spacing of 12 km; a
considerably coarser resolution than those employed for the MAP model studies of
Alpine föhn described above. In the present study, it is hoped that by running a model
at considerably higher resolution than in any previous model study of flow in the
vicinity of the AP (1.5 km grid spacing and 70 vertical levels), new insight will be
afforded into the dynamics of flow over the Peninsula and the föhn effect on the
Larsen Ice Shelf.

Numerous previous studies have undertaken to investigate in detail downslope
windstorms during föhn events and the mechanisms which cause an amplification in
such winds (e.g. Brinkmann, 1974; Lilly, 1978; Durran, 1986; Smith, 1987; Jones et al.,
2002). Other focuses of study regarding the consequences of cross-mountain flow
include the deep propagation of hydrostatic mountain waves and the formation of
polar stratospheric clouds during cross-mountain flow (Dörnbrack and Leutbecher,
2001; Voigt et al., 2003), leeside turbulence and the development of rotors due to
leeside boundary layer separation as a hazard to aviation (Doyle and Durran, 2002;
Hertenstein and Kuettner, 2005; Gohm et al., 2008) and the perpetuation of gap
flows through leeside valleys during föhn events (e.g. Zängl et al., 2004; Drobinski et
al., 2003). However, there have been very few quantitative studies on the degree
and/or spatial distribution of leeside warming or the relative importance of the
various mechanisms responsible. Consequently, the sensitivity of leeside warming to
upwind conditions / varying flow regimes is an area of study in need of further
investigation. The context of the present study into the impact of westerly föhn events
across the AP on Larsen Ice Shelf melt rates ensures an emphasis on the warming
effect of föhn events. Hence, it is hoped that new insights regarding this little studied
though well known aspect of föhn theory will be afforded. Moreover, due to its
relatively simple, comparatively 2-dimensional, isolated nature as a long narrow
relatively straight ridge of high topography surrounded by ocean and a smooth ice
surface to the leeside, the Antarctic Peninsula provides a good 'natural laboratory' for
the problem of flow over a mountain, affording easier investigation of the
fundamental dynamics in the absence of many of the orographic complexities which

characterise other more extensively studies mountain ranges, for example the Alps or the Rockies.

It is hoped that the results discussed within this project will improve understanding of the conditions which characterise warming on the east side of the AP, and suggest whether evidence at the mesoscale supports the hypothesis for the föhn effect as a mechanism for the recent rapid warming in the vicinity of the Larsen Ice Shelf.

2.4 Observational data capture

2.4.1 Observational data sources

The OFCAP field campaign took place between early January and early February 2011. Personnel were based at Rothera Research Station and at Larsen Camp (Figure 2.1c). Upper air measurements were made by an instrumented BAS De Havilland Canada Twin Otter aircraft (Figure 2.13), which was stationed at Rothera. The aircraft was equipped with the Meteorological Airborne Science INstrumentation (MASIN). For more details on aircraft data capture see Section 2.4.2.

Additional upper air measurements were made during radiosondes flights launched from both Rothera and Larsen Camp. The radiosondes were attached to helium-filled latex weather balloons and measured various atmospheric parameters, the data from which was transmitted to a fixed receiver at the surface. Finally, new AWSs were erected on Adelaide Island, the Antarctic Peninsula's crest on the Avery Plateau (Figure 2.14), and on the Larsen C Ice Shelf (Figure 2.14). Due to limited data coverage as a result of mast collapses and/or simply the preferential use of other observational data sources, data from these particular AWSs are not used in the current study. The additional observational data made available as a result of the OFCAP field campaign is a valuable resource in the documentation of two föhn events and for model validation purposes.

One source of observational data used in this study did not herald from the OFCAP campaign. Data from two AWSs positioned on the Larsen C (one at Larsen Camp; Figure 2.1c, the other ~70 km to the southwest towards the centre of the Ice Shelf) are used in Chapter 5. These AWSs are owned by the Institute for Marine and Atmospheric Research Utrecht (IMAU) and incorporate radiation sensors for the

measurement of shortwave (SWF) and longwave (LWF) radiative fluxes. Using the AWS measurements as input, a surface energy budget (SEB) model has been employed (for details, see Kuipers Munneke et al., 2012) to ascertain turbulent heat fluxes as well as sub-surface heat fluxes.

2.4.2 Aircraft measurements

The Twin Otter aircraft was equipped with various instrumentation with which the key meteorological variables were measured (as summarised in Table 2.3). A common time base was provided for all sensors by the GPS system, and data was recorded using an onboard computer system. The aircraft's twin turbo-prop engines, 'Short Take off and Landing' (STOL) capability and fitted skis allow it to be used from small remote unpaved airstrips such as that at Rothera, and also from snow, such as at Larsen Camp. Its range is 1000 km on a full tank of fuel, has a typical data collection speed of 60 ms^{-1} and is capable of attaining an altitude of 5000 m.

In this study altitude measured by the aircraft's Geographic Positioning System (GPS) is used to determine the aircraft's height above mean sea level. In some cases these heights are then adjusted using data from the radar altimeter (which measures height above the underlying surface, though has a maximum vertical range of only 800-1000 m) to give an approximate height above the surface for a continuous section of a flight (even where the aircraft exceeds the height of the radar altimeter's range). Note that this method is only used for aircraft data above the relatively homogenous, smooth orography of the Larsen Ice Shelf.

Figure 2.13: Photographs of the BAS De Havilland Canada Twin Otter aircraft in the hangar at Rothera being fitted with MASIN instrumentation and (inset, bottom right) in flight.

Figure 2.14: Photograph of an AWS being erected on the Avery Plateau (a high section of the AP ridge; for location see Figure 2.1c).

Total Temperature	Total Temperature is measured by two Goodrich Rosemount Probes mounted on the nose. A non de-iced model 102E4AL shown on the left of the image and a de-iced model 102AU1AG shown on the right. These are logged at 0.7Hz.	
Altitude and Air Speed	Static and Dynamic pressure are measured from the aircraft static ports and heated pitot tube on the co-pilot's side. These are on the left of the photo. Honeywell HPA sensors are used. The two pressures are logged at 5 Hz.	
Cooled-Mirror Hygrometer	A Buck 1011C cooled mirror hygrometer is fitted on the aircraft nose on the co-pilot's side. This is the small inlet at bottom right of the photo. The chamber is directly behind the inlet with a control unit in the main rack. The mirror temperature is recorded at 1Hz. The chamber pressure is also recorded.	
Radar Altimeter	Data are recorded from the aircraft's two radar altimeters fitted in the tail section at around 10Hz. These have a range of around 800-1000m and a wider beam compared to the laser altimeter.	
Turbulence Probe	A NOAA/ARA BAT 'Best Aircraft Turbulence' is fitted on a boom extending out from the roof of the aircraft on the co-pilot's side. This 9 hole probe records pressures and exposed thermocouple temperatures for measuring turbulence by eddy covariance in conjunction with attitude measurements. 3-axis accelerometer data are also recorded from the BAT Probe at 50 Hz. Heaters are fitted inside the hemisphere to enable the instrument to be usable even after encountering icing.	

GPS Position	Around 5m position accuracy is recorded at 10 Hz from the JAVAD 4-antenna GPS attitude system. For greater accuracy this is supplemented by a Trimble 5700 survey system using an antenna mounted above the laser altimeter and processed in kinematic mode with a second ground based unit.	
GPS Attitude and Reference System	A JAVAD AT4 4-antenna GPS system records heading, pitch and roll at 20 Hz and velocites at 10 Hz. Antennas are permanently fitted to each wing and fore and aft of the fuselage.	
Central Logging System	All instruments apart from the CAPS probe are logged to a single Siemens Simatic rack PC using Labview and associated National Instruments hardware including networked compact Fieldpoint modules in the roof and floor. The logging can be monitored and controlled from the main rack in the cabin as well as a remote touchscreen in the co-pilot's seat.	

Table 2.3 [from previous page]: A summary of the instrumentation forming MASIN relevant to the OFCAP field campaign. Adapted from Ladkin (n.d.).

2.5 Modelling

2.5.1 Numerical Weather Prediction model

The UK Meteorological Office Unified Model (MetUM; Cullen, 1993 and Cullen et al., 1997) is an umbrella term for the suite of numerical modelling software developed at the UK Met Office. In this study version 7.6 (at the time the most recent) of the atmosphere-only component of the MetUM is used. This Numerical Weather Prediction (NWP) model uses a set of equations to determine the time-evolution of the atmosphere. The main prognostic variables defined are the 3-dimensional wind components, potential temperature, exner pressure, density and components of moisture (Greed, 2010). The MetUM's dynamical core employs a non-hydrostatic (allowing for vertical accelerations which enables relatively accurate simulations at high-resolution), fully compressible, deep atmosphere with a semi-implicit, semi-Lagrangian, predictor-corrector scheme to solve the equations. The predictor part of the scheme incorporates all the processes but approximates some of the non-linear

terms. The corrector step goes on to readjust the approximated terms towards a more accurate solution. Despite all other prognostic variables being treated in the semi-Lagrangian sense, density (as defined by the continuity equation for mass conservation) is given an Eulerian treatment (Davies et al., 2005). The MetUM employs Arakawa C-grid staggering in the horizontal and a Charney-Phillips grid in the vertical. The model levels are terrain following near the surface, but become increasingly level with height (Davies et al., 2005).

A global model run was performed on a horizontal grid 1024 by 769 (~25 km resolution) to generate boundary conditions for a limited area model (LAM) at ~4 km resolution (MetUM 4km) over the Antarctic Peninsula. This LAM was conducted on a 288 by 360 horizontal grid using 70 levels in the vertical (reaching a height of 40 km) and a 30 second timestep. The MetUM 4km runs were initiated using the UK Met Office operational analysis (which includes daily sea ice and sea surface temperature fields) and a high resolution (200 m in the horizontal) digital elevation model of Antarctica provided by the British Antarctic Survey.

Within this domain a higher resolution (~1.5 km in the horizontal) LAM (MetUM 1.5 km) was nested, initialised using a dump of prognostic fields from the 4 km-resolution model after 6 hours run-time. This is the highest resolution model used in this study, consisting of a horizontal grid 270 by 270 and, as in the 4 km-resolution LAM, 70 levels in the vertical and a time step of 30 seconds. This relatively short time step together with the implementation of a fully three-dimensional potential temperature advection scheme and significantly reduced temporal off-centering in the advection scheme has been shown to more accurately resolve gravity waves in regions of complex topography (Webster et al., 2008). For both the MetUM 4 km and MetUM 1.5 km simulations, a detailed set of physics packages for boundary layer, surface exchange, radiation, cloud, convection and sub-grid scale orography were included.

For the purpose of showing synoptic-scale circulation, a final LAM was run at a horizontal resolution of 12 km (the boundary conditions for which were, as in the MetUM 4 km, provided by the global model run).

Tests were performed to assess the sensitivity of the MetUM 1.5 km simulations to changes in the initiation time of the MetUM suite of nested models. Comparisons (not shown) of key diagnostic fields on model levels and for cross

sections across the AP for simulations initiated 12 hours apart revealed no significant sensitivity for two westerly föhn events across the AP. There were some slight differences in the timing of föhn incursion.

2.5.2 Meteorological reanalysis

To assess the performance of the MetUM in its reproduction of free atmospheric conditions upwind of the Antarctic Peninsula, simulations were compared to data derived from the European Centre for Medium-Range Weather Forecasts (ECMWF) ERA-Interim reanalysis (Berrisford et al., 2009). Additionally, ERA-Interim was used to illustrate the evolution of synoptic-scale circulation during föhn events across the AP.

ERA-Interim is a global reanalysis product covering the observational-data-rich period since 1979 based on cycle 31r2 of ECMWF's Integrated Forecasting System (Dee and Uppala, 2009). It uses a reduced Gaussian grid with a horizontal resolution of ~0.7 degrees or ~80 km, a time resolution of 6 hours, and employs a four-dimensional variational data assimilation process (Rabier et al., 1998).

Although of considerably coarser resolution than the MetUM LAMs and consequently less accurate in its resolution of mesoscale meteorological phenomena in regions of complex topography such as the AP, for synoptic free-atmospheric circulation, meteorological analysis products such as ERA-Interim directly assimilates observational data into model forecasts and thus produces an accurate and independent benchmark at the synoptic scale.

The results of comparisons of mean sea level pressure and pressure and wind velocity at the 850 hPa and 500 hPa levels (not shown) reveal that all MetUM LAMs perform well in their reproduction of conditions upwind (west) of the AP during westerly föhn flow. No significant discrepancies are found and the three LAMs (MetUM 12 km, 4 km and 1.5 km) produce very similar upwind simulations.

2.5.3 Trajectory model

To investigate the Lagrangian evolution of föhn flow across the AP, the trajectory model Lagranto (Wernli and Davies, 1996) is used. This model calculates a large number of trajectories for a certain period of time. In this study the MetUM 1.5 km data is used as input for the model, and initiation regions are specified within

which backward trajectories start from every model gridpoint at a specified pressure level (in our case, 950 hPa). Being backward trajectories, the model works backwards in time (with trajectory paths proceeding upwind with each timestep), in this case for a period of 24 hours (more than sufficient considering the size of the MetUM 1.5 km domain) and with a time resolution of 3 minutes (each time step equating to 6 MetUM time steps). The Lagrangian time-trace of physical variables along these paths are then evaluated, providing a description of the physical evolution of air parcels as they cross the AP.

In Lagranto the kinematic evaluation of the trajectories are calculated using a variant of Petterssen's (1956) method (Wernli and Davies, 1996). The position vector, r, of a trajectory is evaluated using a predictor-corrector scheme. The predictor step involves a forward time step;

$$r^{n+1} = r^n + v(r^n).\Delta t,$$

where v is 3-dimensional velocity, whilst the corrector step is defined by successive (order of 3) iterations performed with an adjusted mean wind;

$$v^{i+1} = \frac{1}{2}\{v^i(r^n) + v^i(r^{n+1})\}$$

(Wernli and Davies, 1996). The off-grid wind components are calculated by linear interpolation of the gridded values.

Lagranto has been used extensively in the investigation of synoptic atmospheric air flows (e.g. Sprenger et al., 2003; Hegglin et al., 2004; Campana et al., 2005; Gray, 2006). Fueglistaler et al. (2003) successfully employed Lagranto to investigate polar stratospheric clouds caused by mountain waves using a moderately high resolution (0.125° or ~14 km horizontal grid spacing and with 60 levels up to 4 hPa in the vertical) mesoscale NWP model. However, there is no evidence in the literature (according to this author's search) that it has been used in conjunction with such a high resolution (~1.5 km horizontal grid spacing and with 70 levels in the vertical up to 40 km) NWP model as is employed in the current study.

2.6 Summary

In this chapter a review of climate change in the vicinity of the AP has been presented in order to give context to the background theory covered in Chapter 1, and to highlight the objectives and potential implications of this study. The initial

motivation for the study is presented: to test the plausibility of the hypothesis that an enhancement of föhn warming to the east of the AP is at least partly responsible for the recent large amplitude climatic warming observed here. The study's aims have been discussed, highlighting the dual purpose of the study. On the one hand the study has a regional context, aiming to improve our understanding of föhn over the Antarctic Peninsula and its potential for causing leeside warming and ice shelf melting. On the other hand, it hopes to provide broader insight into the non-case-specific nature of föhn flows with an emphasis on the causes of leeside warming and its sensitivity to upwind conditions – a relatively understudied aspect of the föhn. The availability of large amounts of observational data from different sources together with the high resolution of the NWP model used allows for a level of analytical detail that has not previously been possible in the study of the föhn.

Chapter 3

A westerly föhn event across the Antarctic Peninsula: flow dynamics and downwind response

Contents

List of figures

3.1 Introduction

During the period 4 to 5 February 2011 a westerly föhn event (in subsequent chapters to be referred to as *Case A*) was observed across the Antarctic Peninsula (AP). In this chapter MASIN aircraft measurements are interpreted together with MetUM simulations to provide a detailed description of the event's key features and an understanding of the governing dynamics. Synoptic scale meteorological conditions will be summarised before examining the characteristics of the downwind response with reference to the upwind forcing.
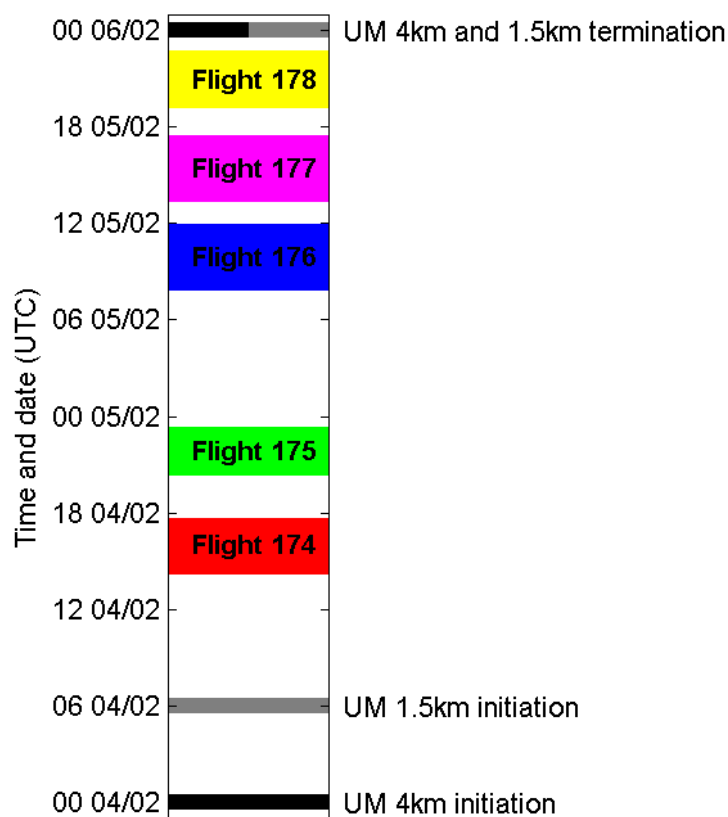
Figure 3.1: Timeline showing timing and duration of flights (174-178) and UM simulation periods for 4-5 February 2011.

Five MASIN flights documented the föhn event during the period of study (Figure 3.1). Each flight embarked from and ended at Rothera Research Station (Figure 3.2a). With the exception of flight 177, the aircraft observations incorporated a leg deemed suitable for the documentation of conditions to the west (upwind) of the AP. Flight 177's western ascent and descent were deemed unsuitable since they took place to the east (in the lee) of the high orography of Adelaide Island. During the flight 176 upwind profile (within Marguerite Bay) the aircraft's humicap malfunctioned. For

this reason, where relevant, specific humidity (q) is derived from flight 176's other upwind profile. This profile is otherwise deemed to be a less suitable leg for the documentation of upwind conditions, as it is once again located between Adelaide Island and the AP's main ridge (Figure 3.2a).

On a number of occasions the aircraft flew straight legs whilst performing a series of manoeuvres whereby it would ascend to some level subsequent/antecedent to descending to near-surface level. Such a flight pattern is herein referred to as a *sawtooth* leg (ST leg).
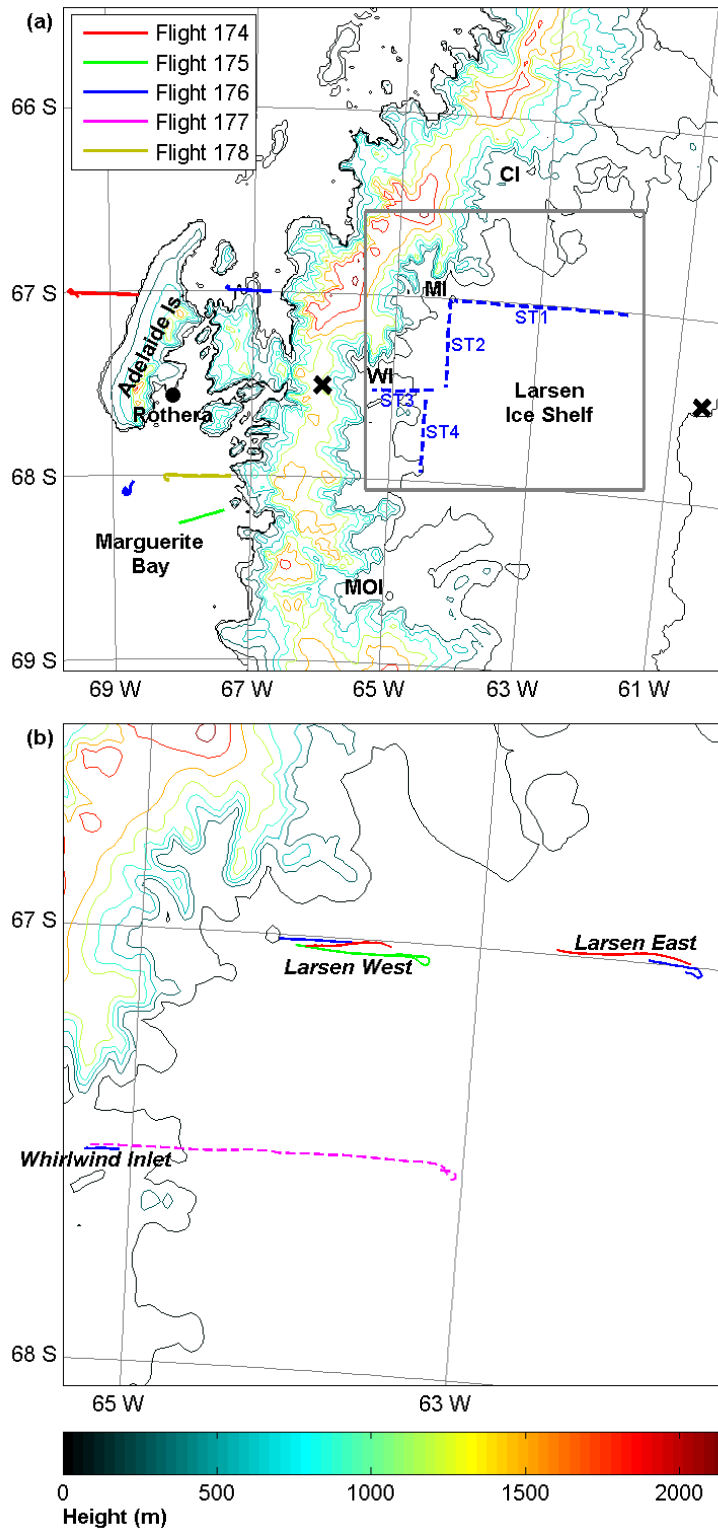
Figure 3.2: (a) Topographic map (derived from MetUM 1.5 km orography data) of the section of the AP relevant to this study, showing the flight tracks of the upwind profile legs (solid lines to the west of the AP), the flight 176 *sawtooth* legs (dashed lines) and important locations. Note that two flight 176 upwind profiles are marked. The profile to the north is used in this study only due to humicap malfunction during the otherwise more useful (less influenced by AP orography) southern profile. Coloured contours give topographic height. The grey square marks the lateral boundaries of the map shown in (b). (b) Map of the northwest region of the Larsen C Ice Shelf, showing the tracks of the *Larsen East* and *Larsen West* region profiles, the flight 176 Whirlwind Inlet profile, and the flight 177 ST leg (dashed line). MOI = Mobil Oil Inlet, WI = Whirlwind Inlet, MI = Mill Inlet, CI = Cabinet Inlet.

3.2 Synoptic conditions and upwind flow

ECMWF ERA-Interim re-analysis simulates a mesoscale low pressure system to the east of the Antarctic Peninsula, deepening between mid afternoon 4 February 2011 and early morning on 5 February 2011 (Figure 3.3ai). Meanwhile a ridge of high pressure to the west of the AP proceeds east in front of a new trough to the west, bringing about a change from southerlies on both sides of the Peninsula to a southwesterly cross-barrier flow in the vicinity of the Larsen C (N of ~70°S) (Figure 3.3aii). Flow with a significant westerly component is simulated to approach the Peninsula until about 16 UTC 5 February; initially southwesterly, becoming westerly and eventually northwesterly as a new low pressure system moves in from the west (Figure 3.3aiii). Comparison of Figure 3.3aii and b (equivalent plot derived from MetUM 12 km data) reveals good synoptic scale agreement between the two models. A MetUM 4 km simulation is used for a more detailed illustration of the pressure patterns in the vicinity of the AP at 4 UTC on 5 February; approximately the time of strongest westerly flow above the Peninsula (Figure 3.4).

The föhn event is associated with a strong cross-Peninsula pressure gradient (Figure 3.4), peaking at ~8.5 hPa/100 km at mean sea level at 4 UTC on 5 February (approximately midway through the föhn event, when cross-Peninsula flow is at its strongest). Climatic pressure gradients for Alpine föhn and Chinook in the Rockies are 2.1 hPa/100 km (Hoinka, 1980) and 4.7 hPa/100 km (Brinkmann, 1974) respectively, suggesting that the present case is one associated with relatively high drag. For context, the case of Alpine föhn documented in Hoinka (1985) exhibited a slightly higher cross-barrier pressure gradient (~10 hPa/100 km).
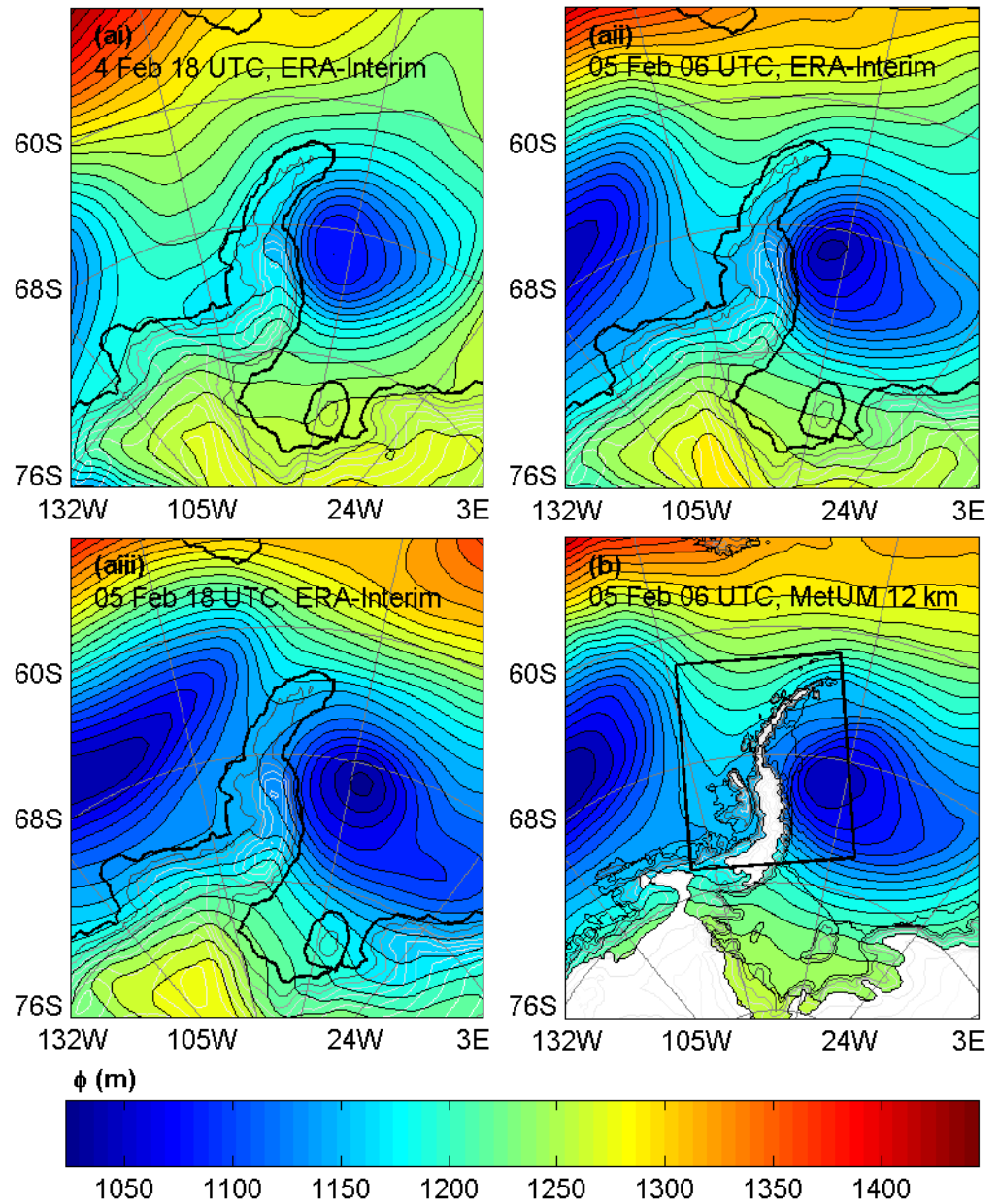
Figure 3.3: Geopotential height (contours, spaced at 15 m) at the 850hPa level, from (a) ECMWF ERA-Interim at (i) 18 UTC 4 February, (ii) 06 UTC 5 February, (iii) 18 UTC 5 February, and (b) the MetUM 12 km simulation at 06 UTC 5 February 2011. The land-sea mask and surface height contours are also plotted. The black square in (b) encloses the domain used for the MetUM 4 km simulation.
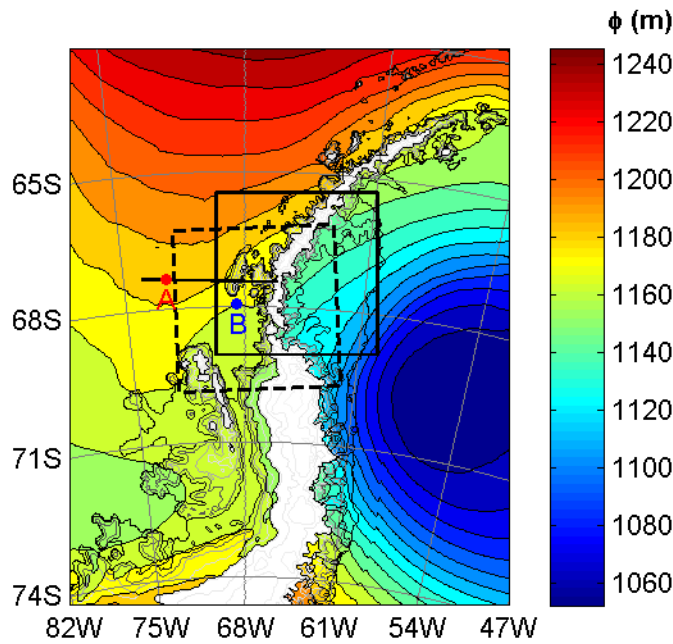
Figure 3.4: Geopotential height (contours, spaced at 10 m) at the 850hPa level, from the MetUM 4 km simulation at 4 UTC on 5 February. The red dot (labelled A) marks the position of *Location A* (the red vertical line in Figure 3.5), which is 150 km roughly west (along the transect shown as the black line) of the west coast of Adelaide Island. The blue dot (labelled B) marks the position of location *B*, which is roughly 50 km west of the AP along a different transect to the south of Adelaide Island. The solid (dashed) black square in (a) marks the boundary of the *standard* (*SW*) MetUM 1.5 km domain.

Figure 3.5 comprises cross-sections (the transect for which is marked on Figure 3.4) describing upwind conditions (potential temperature and wind component). Figure 3.6a is a time series of observed and simulated wind speed and direction at two locations, *A* and *B* (both marked on Figure 3.4). *Location A* is 150 km roughly west of Adelaide Island along the transect marked on Figure 3.4 and used for cross sections of simulated wind velocity and potential temperature (θ) in Figure 3.5. Location *B* is ~50 km west of the main AP ridge, south of Adelaide Island in Marguerite Bay. The model data plotted in Figure 3.6a is averaged between 200 and 2000 metres AMSL (this range is illustrated by the vertical red lines in Figure 3.5) and derived from the MetUM 4 km and 1.5 km simulations respectively for locations *A* and *B*. Also shown are four measurements, averaged between 200 and 2000 metres AMSL, of wind speed and direction from aircraft measurements, and the corresponding values simulated by the MetUM 1.5 km (interpolated to the flight track in time and space). Figure 3.6b is analogous to Figure 3.6a, but shows values of N for the same data sources, as well as simulated westerly and non-directional $\hat{h}$ at *Location A*. Non-directional $\hat{h}$ uses the magnitude of the vertically averaged wind velocity, and westerly $\hat{h}$ uses the vertically

averaged westerly component of flow, in their respective derivation. The height range (between 200 and 2000 m) was chosen as it is considered to be representative of the flow impinging on the AP.
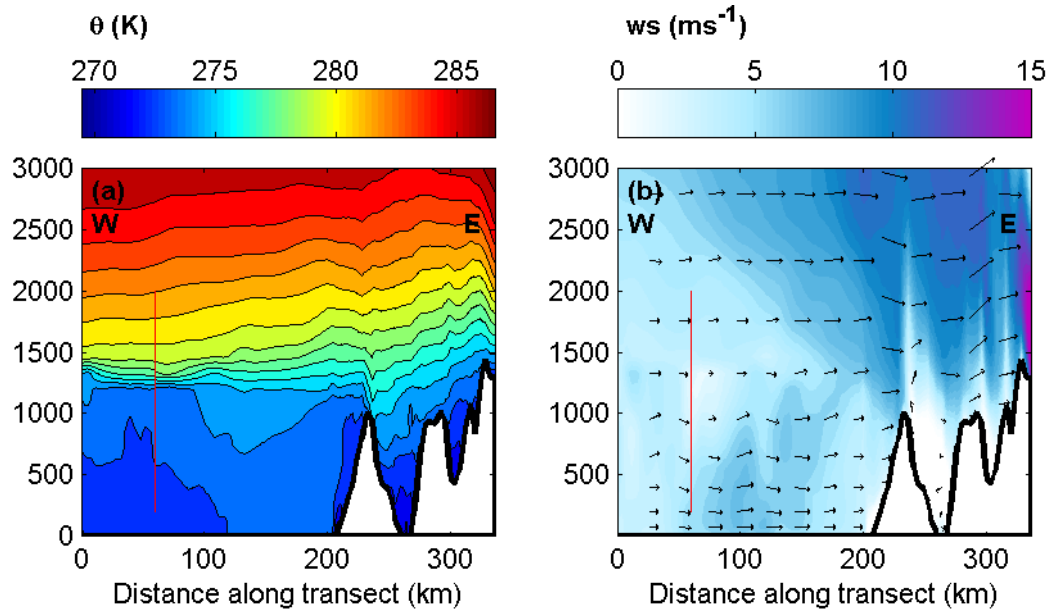
Figure 3.5: Cross sections of (a) potential temperature (contours, spaced at 1 K) and (b) along-transect wind component (colour) and vectors (arrows) at 4 UTC on 5 February along the transect marked in Figure 3.4 by the solid black line from the MetUM 4 km simulation. The red vertical line marks the position of *Location A* and the depth over which fields illustrated in Figure 3.6 were averaged. Vertical to horizontal scale of axes = 1:100.

Figure 3.6a and b illustrate the evolution of upwind conditions. The mean flow direction is approximately south-southwesterly ~150 km (the approximate Rossby radius of deformation, as defined in Section 1.3.5) west of the AP on the morning of 4 February, becoming increasingly westerly such that at 04 UTC 5 February, the mean wind bearing is ~270°. After this time, the migration of the ridge eastwards (Figure 3.3a) brings about a rapid transition in wind direction towards northerly, before approaching easterly by the end of the simulation. Strongest mean wind speeds are simulated near the beginning of the model run at just over 15 ms^{-1}, coinciding with the smallest non-directional $\hat{h}$ values (~1.4). Wind speed declines (and non-directional $\hat{h}$ increases) as flow becomes more westerly, reaching ~3.7 ms^{-1} at 04 UTC 5 February (when flow direction is closest to being directly westerly). Westerly $\hat{h}$ reaches a minimum value of ~2.7 at 22 UTC 4 February. The relatively unchanging mean stability of the profile indicates that changes in wind velocities are largely responsible for variability in $\hat{h}$.
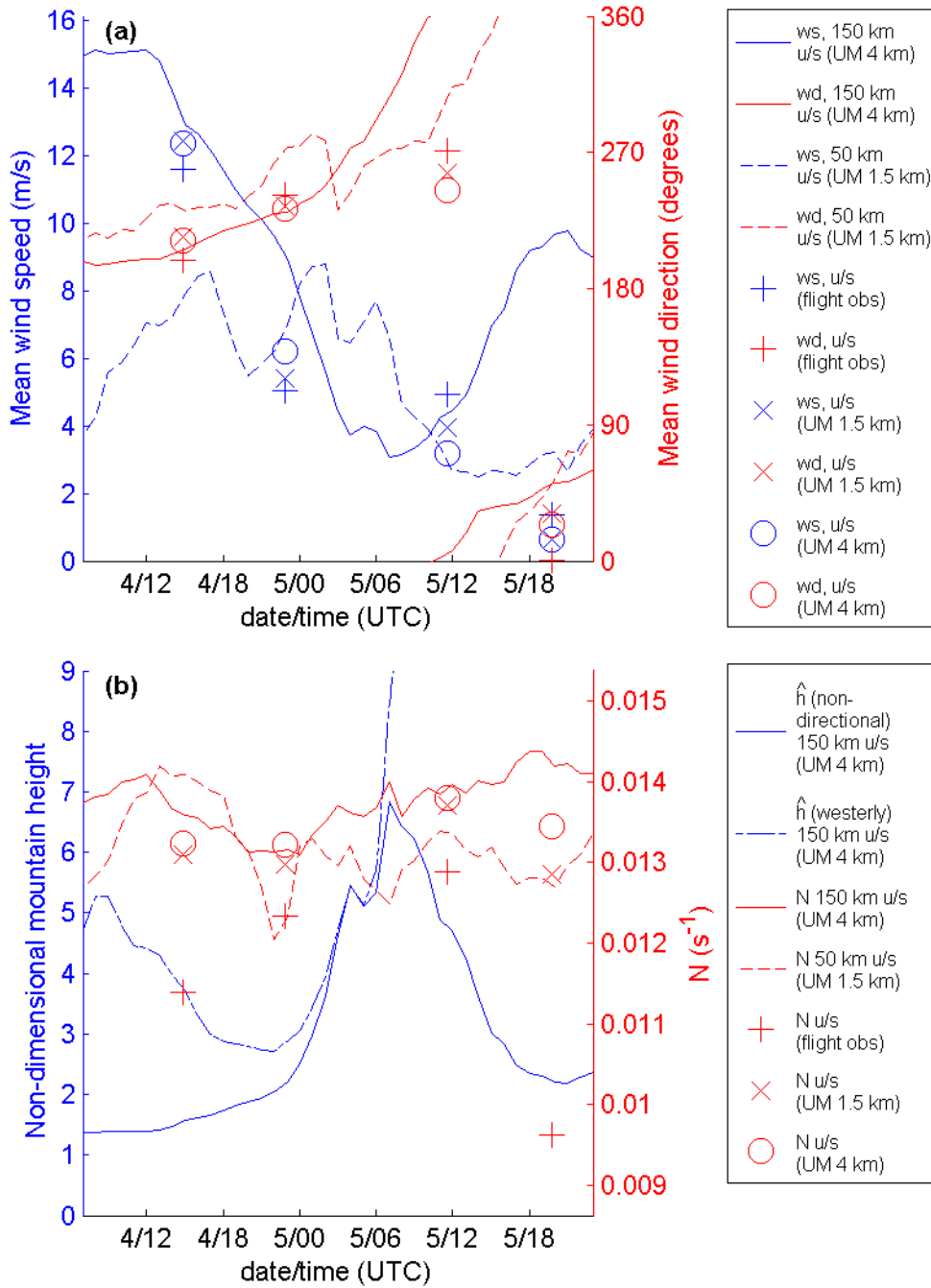
Figure 3.6: Plots of (a) wind speed and direction and (b) Brunt Väisälä frequency and non-dimensional mountain height ($\hat{h}$). All values are vertical averages (between 200-2000 m) from (i) aircraft data for the upwind profiles (the flight tracks of which are illustrated in Figure 3.2a) of flights 174, 175, 176 and 178 ('+' symbols); (ii) MetUM 4 km and 1.5 km data interpolated in 4-dimensions to the flight tracks of the four upwind profiles ('o' and 'x' symbols); (iii) a vertical profile of MetUM 4 km data roughly 150 km west of the AP (location given by the blue dot in Figure 3.4 and defined by the red line in Figure 3.5; solid lines) and (iv) a vertical profile of MetUM 1.5 km data roughly 50 km west of the AP (location given by the red dot in Figure 3.4; dashed line). Note that no value of $\hat{h}$ is presented for (iv) since, being only 50 km upwind of the AP (within the Rossby radius of deformation) such a value would be meaningless. Both westerly (solid/dashed line) and non-directional (solid line) $\hat{h}$ are shown. In the figure legends, ws = wind speed, wd = wind direction, u/s = upstream.

Zängl (2003) found that large amplitude mountain waves are excited only when flow is roughly perpendicular to the ridgeline, whilst Durran (1990) reported

that the generation of downslope winds requires that flow is directed within 30° of perpendicular to the ridgeline. The orientation of the AP (aligned roughly north-south to the south of ~67.5°S but extending in an increasingly northeasterly direction north of ~67.5°S) is such that, in the vicinity of the Larsen C Ice Shelf, any approaching flow between westerly and northwesterly will be directed perpendicular to some portion of the Peninsula. The strongest mean winds for *Location A* during the period of interest are characterised by southwesterly directions. Despite this, the south-migrating low pressure system to the east of the AP acts increasingly throughout this period to divert flow to the right as it approaches the AP. Additionally, the high orography of Adelaide Island appears to deflect the southwesterly flow to the right to pass south of the island (this effect is evident in the back trajectories shown later in Figure 3.18). Indeed, at location *B* (located to the south of Adelaide Island), flow is largely more westerly than for *Location A* (Figure 3.6a). Winds at location *B* are also predominantly weaker. However, being well within the Rossby radius of deformation of the AP during westerly winds, the flow here is expected to be heavily influenced (with low-level blocking predicted by the magnitude of $\hat{h}$) by the orography.

Determining representative values of upwind $\hat{h}$ is evidently a complex problem. However, bearing the above arguments in mind it seems reasonable to propose the non-directional and westerly values of $\hat{h}$ represent lower and upper bounds respectively in consideration of the section of the AP south of the Avery Plateau (see Figure 2.1 for location) during the period of southwesterly to westerly flow. At 22 UTC 4 February – the time of minimum westerly $\hat{h}$ – westerly $\hat{h}$ (non-direction westerly $\hat{h}$) ≈ 2.7 (2.0), corresponding to a dividing streamline height (using α = 1.2 (see Section 1.3.4) and h = 1500 m) of z_d = 833 m (600 m) AMSL, using Sheppard's (1956) formulation. Furthermore, according to Ólafsson and Bougeault's (1996) version of Smith's (1989) regime diagram (Figure 1.8) such values of $\hat{h}$ are expected to be associated with low-level flow blocking and are towards the upper limit of the range expected to support wave breaking above the AP's crest. As discussed in Sections 1.3.3 and 1.4.1, non-linear phenomena and downslope windstorms are encouraged by the occurrence of an elevated upwind inversion (Durran, 1986). A weak inversion (~1.7 K) is observed at ~900 m (see later: Figure 3.8a) and modelled at ~750 m (not illustrated here) AMSL in the flight 174 upwind profile to the west of Adelaide Island. The inversion rises and strengthens in the model,

simulated at an elevation of ~1300 m at a distance of 150 km upwind of Adelaide Island at 04 UTC 4 February (Figure 3.5a). To the south of Adelaide Island an elevated inversion is also apparent in both observational data (at ~1250 m; see later: Figure 3.9a) and model data, the air above which is markedly more stable than that below.

The four upwind flight profiles (see Figure 3.2a for flight tracks) are too close to the Peninsula to afford worthwhile diagnosis for the undisturbed upwind flow. Nevertheless they provide our best validation data with which to test the model's upwind performance. Data gathered for these profiles largely confirm the model's representation of upwind conditions. A roughly south-southwesterly mean flow between 200 and 2000 m AMSL during flight 174 weakens and develops an increasingly westerly component through flights 175 and 176, before becoming a very weak northerly during flight 178 (Figure 3.6a). Equivalent mean wind vector velocities derived from both the MetUM 1.5 km and MetUM 4 km simulations compare well with the aircraft data.

The UM overestimates N for all 4 upwind profiles (Figure 3.6b). The discrepancy is relatively minor for the profiles of flights 175 and 176, and greatest for the profile of flight 178. Since the latter captured upwind conditions subsequent to the period of approaching westerly flow, this is of minor concern for this study. In the case of the flight 174 upwind profile, the major source of the discrepancy is in the temperature at 2000 m; the simulated temperature at 200 m is relatively accurate. Such a discrepancy is arguably unreflective of the model's performance in capturing the undisturbed upwind profile since lower atmospheric stability in this region is sensitive to the effect of the orography on the flow.

Upwind wind velocity and stability values generated by the two models (the 4 km and 1.5 km) are very similar. It would appear that in this case the reproduction of upwind conditions is relatively insensitive to model resolution. This gives credence to the use of the MetUM 4 km's orographically undisturbed upwind conditions (*Location A*, which is outside the MetUM 1.5 km's domain) to relate to the MetUM 1.5 km simulation's downwind response.

Analysis not presented herein reveals good agreement between observed and MetUM 1.5 km simulated upwind specific humidities.

3.3 Leeside response in observations and MetUM validation

3.3.1 Development of föhn conditions above the Larsen C Ice Shelf

Analysis of aircraft data from successive downwind flight profiles along ~67°S above the Larsen C and towards the base of the AP's eastern slope downwind of Mill Inlet (this location is hereafter referred to as *Larsen West*; see Figure 3.2b) reveals a warming and drying trend associated with the incursion of westerly winds typical of a westerly föhn event (Figure 3.7). For the flight 174 *Larsen West* profile southeasterly winds are observed at near-surface level, weakening upwards to become principally westerly above ~1100 m AMSL (Figure 3.7ai). At approximately this height an inversion is found, capping the relatively cool and moist southeasterlies (Figure 3.7aii). By the time of the next flight profile (Flight 175; ~5 hours later), the body of warm westerly flow has strengthened and now extends to a lower altitude; the inversion now residing between 400 and 700 m AMSL. The westerlies continue to penetrate downwards, extending to surface level by the time of the next flight profile (flight 176; ~12 hours later). θ at the base of the aircraft's descent was observed at ~275.1 K, which amounts to a ~3.5 K near-surface warming over ~17 hours.

It is pertinent to consider the times of the flights. Flight 174 occurred during daytime (the mean observation time for the profile under discussion being 17:31 UTC), whereas flight 176 took place in the early morning (profile mean time of 9:43 UTC, a little over 2 hours after sunrise). So the warming is coincident with, and in spite of, night time radiative cooling. The flight 176 profile is associated with the lowest specific humidities (Figure 3.7aiii).

The MetUM 1.5 km performs well, capturing the overall evolution of the föhn event at *Larsen West*; the encroachment of westerly flow to low levels and the pronounced warming and drying (Figure 3.7bi). During flight 174, as in the observations, moderate southwesterlies are simulated towards the top of the profile. Below ~1200 m AMSL flow becomes very weak. The near-surface flow field comprises relatively weak westerlies to northwesterlies, in contrast to the relatively strong southeasterlies observed. Although a relatively stable layer is found between ~1300 m and ~1600 m AMSL, no strong inversion (as was observed) is simulated (Figure 3.7bii). Leeside temperatures (humidities) throughout the entire profile are overestimated (underestimated) by the MetUM, especially below the observed inversion where the θ

discrepancy surpasses 4 K. The early incursion of westerly winds to near-surface level, together with overestimated temperature and underestimated humidities suggest the model may be bringing föhn conditions to the region too early. This is investigated further (and confirmed) in the Appendix section.

By the time of flight 175, westerly to southwesterly winds are already simulated throughout the depth of the profile. Peak wind speeds are of a similar intensity and found at a similar level to those observed for both flights 175 and 176. The simulated profile warms and dries with each successive flight (Figure 3.7bii and biii); temperatures (humidities) largely higher (lower) than those observed, likely due again to the model's erroneously early initiation of föhn conditions. The model's representation of surface temperature improves between flights 175 and 176, coincident with the penetration of westerly föhn to surface level in the observations. At the base of the flight 176 profile the discrepancy is only ~1.4 K. Humidities, meanwhile, are still considerably underestimated by the model.
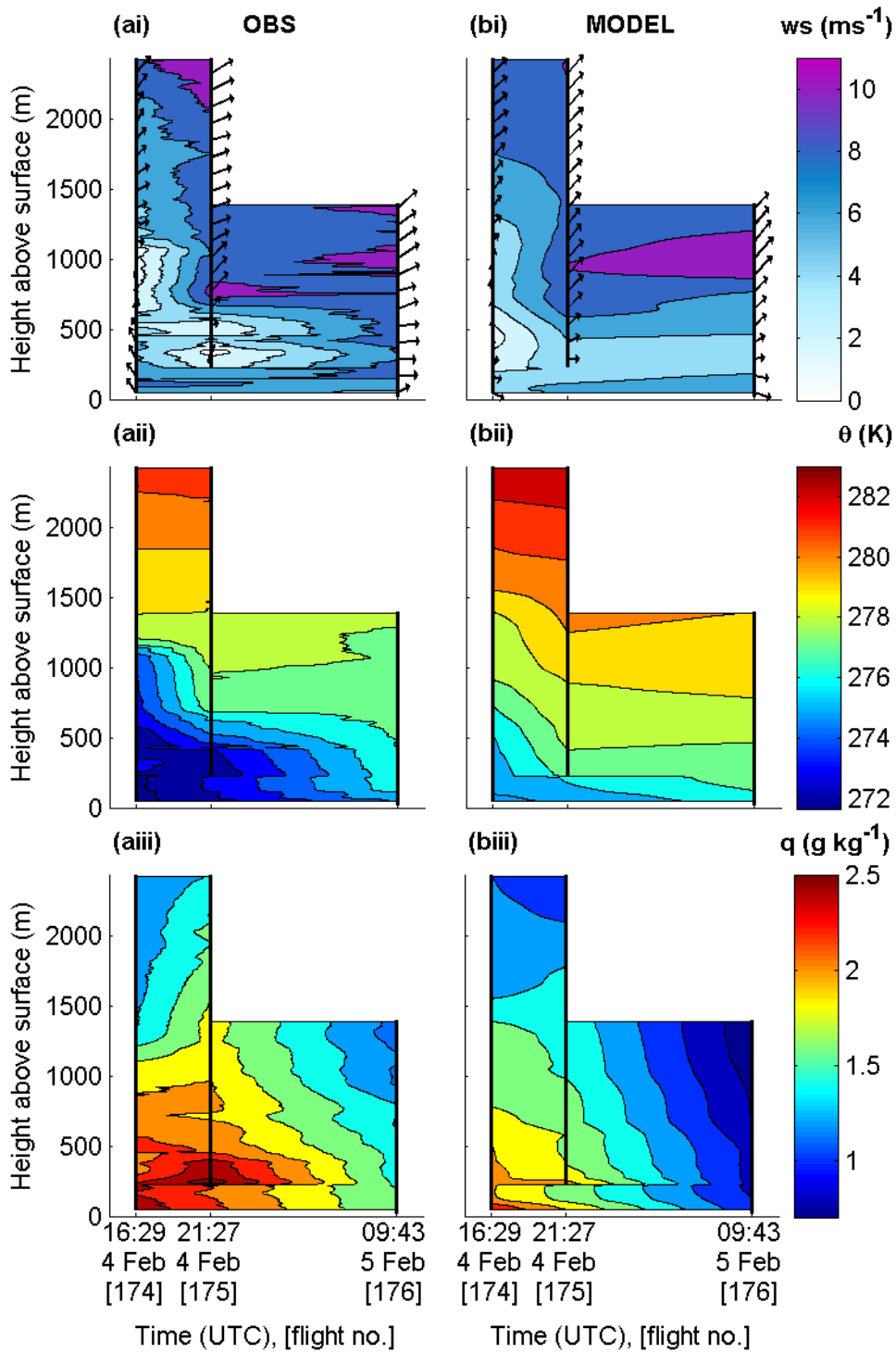
Figure 3.7: Time series of (i) wind speed (contours, spaced at 2 ms^{-1}) and vectors (arrows; the bearing of which denotes the horizontal direction of flow from North), (ii) θ (contours, spaced at 1 K) and (iii) *q* (contours, spaced at 0.2×10^{-3}) with height for data from (a) the *Larsen West* flight profiles (for flights 174, 175 and 176), and (b) the MetUM 1.5 km simulation (interpolated in 4-dimensions to the flight tracks of the *Larsen West* profiles). Contours are interpolated in time using data from each flight profile at a fixed height. The vertical extent of each profile is denoted by a black line. Due to the flight 175 profile not extending below 230 m AMSL, contours below this level are interpolated between data derived from flights 174 and 176 only.

3.3.2 Spatial heterogeneity and diurnal aspects of the föhn

The two downwind profiles – *Larsen West* and *Larsen East* (see Figure 3.2b) – of flight 174 both exhibit, on the whole, cooler signatures than that of the upwind profile (~2.6 K and ~3.4 K cooler respectively at 150 m AMSL; Figure 3.8a shows θ against flight altitude). As discussed previously (see Section 2.1.2), such a west-east temperature gradient is common across the AP (Morris and Vaughan, 2003). Above ~500 m AMSL the downwind profiles are also considerably moister (Figure 3.8b).
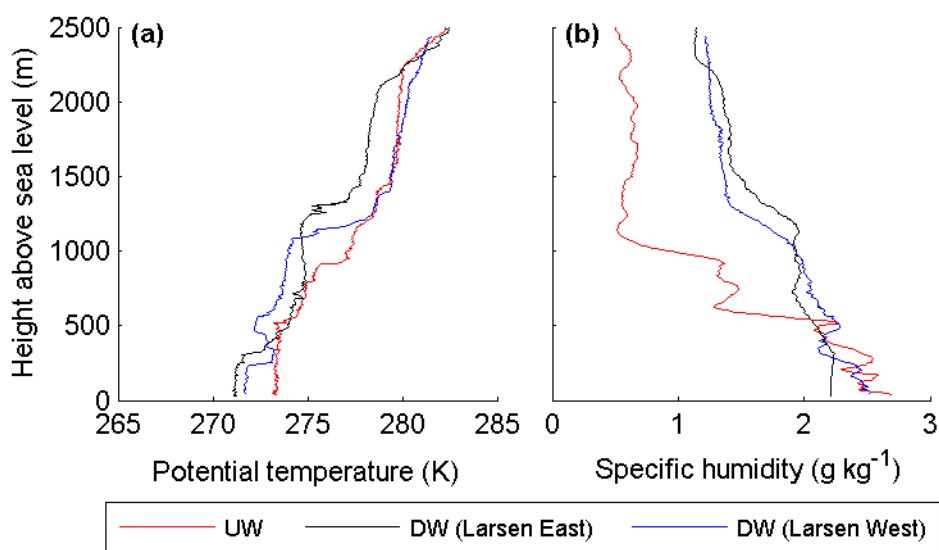
Figure 3.8: (a) θ and (b) *q* derived from upwind (UW) and downwind (DW) flight 174 profiles.

Approximately eighteen hours later the situation has reversed, with föhn conditions characterising the leeside. The equivalent flight 176 downwind profiles comprised of, for the most part, warmer and drier air below 1500 m AMSL than that observed upwind (Figure 3.9a and b; note that although the former is a plot of θ – a function of both temperature and pressure – a similar plot of temperature reveals conditions at 150 m AMSL at *Larsen West*, *Larsen East* and *Whirlwind Inlet* to be warmer than those upwind by 3.6, 1.2 and 2.1 K respectively). The notable exception is the Larsen East profile below ~70 m, due to a deep, very strong inversion (>8 K) extending up to ~150 m; assumed to be the remnants of nocturnal cooling above the ice shelf. Temperatures at *Larsen West* are significantly greater than those at *Larsen East* and, on account of considerably warmer near-surface temperatures (~272.8 K at a height of ~20 m above surface; 1.5 K greater than the observed near-surface temperature upwind), the stability observed in the lower atmosphere is considerably weaker.
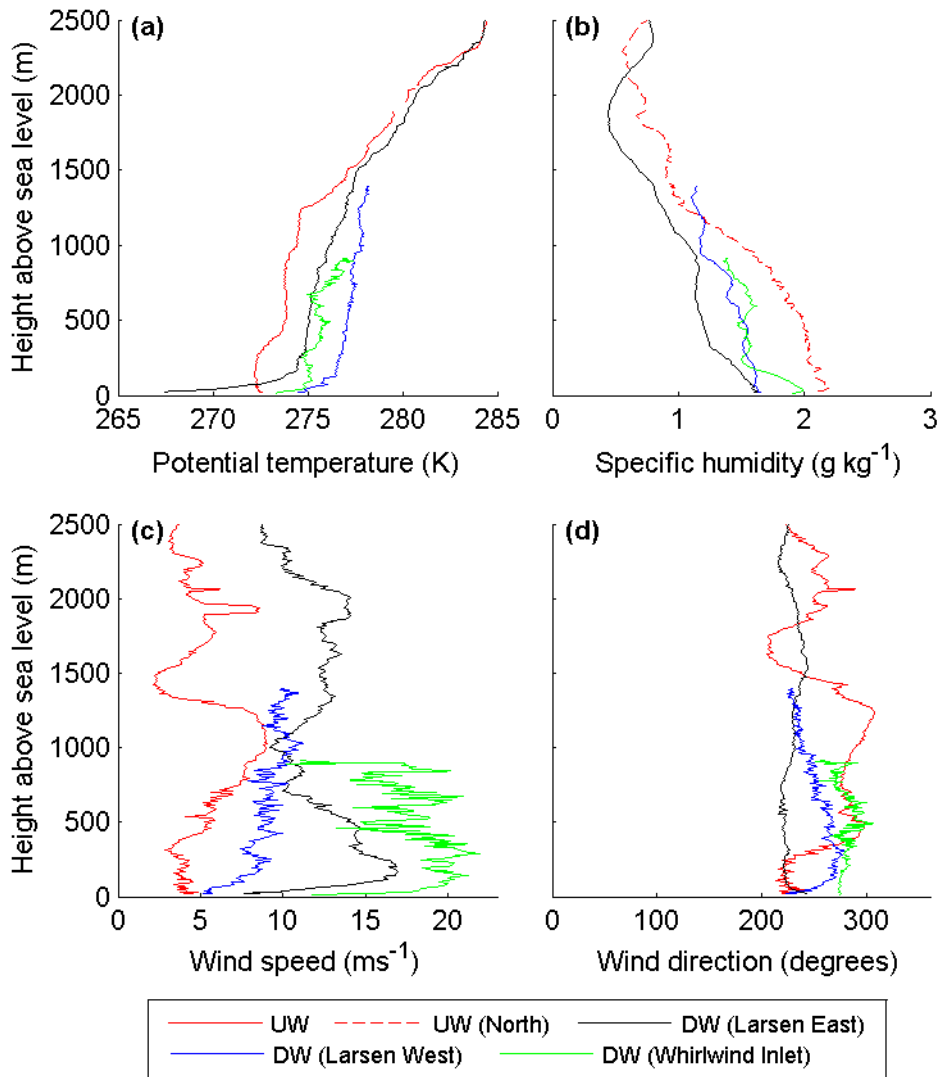
Figure 3.9: (a) θ, (b) *q*, (c) wind speed and (d) wind direction derived from upwind (UW) and downwind (DW) flight 176 profiles. Note that, for *q*, profile 'UW (North)' data is used due to humicap failure during the 'UW' flight 176 profile (see Figure 3.2 for profile flight tracks).

The west-east temperature gradient above the Larsen C is also illustrated in Figure 3.10aii; a cross section of θ interpolated horizontally from data derived from flight 176 ST leg 1 (ST1), during which the aircraft flew westward along 67°S between *Larsen East* and *Larsen West* (see Figure 3.2b for the flight track). The large nocturnal inversion above the ice shelf disappears westwards towards the AP's lee slope, accounting for a gradient in lowest flight level temperature of ~10 K over 60 km. Figure 3.10ai shows that, above the surface inversion across the eastern extent of the transect, winds are considerably stronger than closer to the Peninsula, and are southwesterly as opposed to westerly.

The equivalent transect simulated by the UM 1.5 km generally compares well, capturing the westerly to southwesterly flow transition and cooling (from west to east). However it fails to capture the magnitude of the nocturnal inversion (the

discrepancy in near-surface temperature peaking at ~6 K, towards the eastern extent of the flight leg; Figure 3.10bii). Such a problem is common to NWP modelling (Zängl et al., 2004). The model captures the southwesterly flow above the inversion but wind speeds are generally underestimated (Figure 3.10bi).
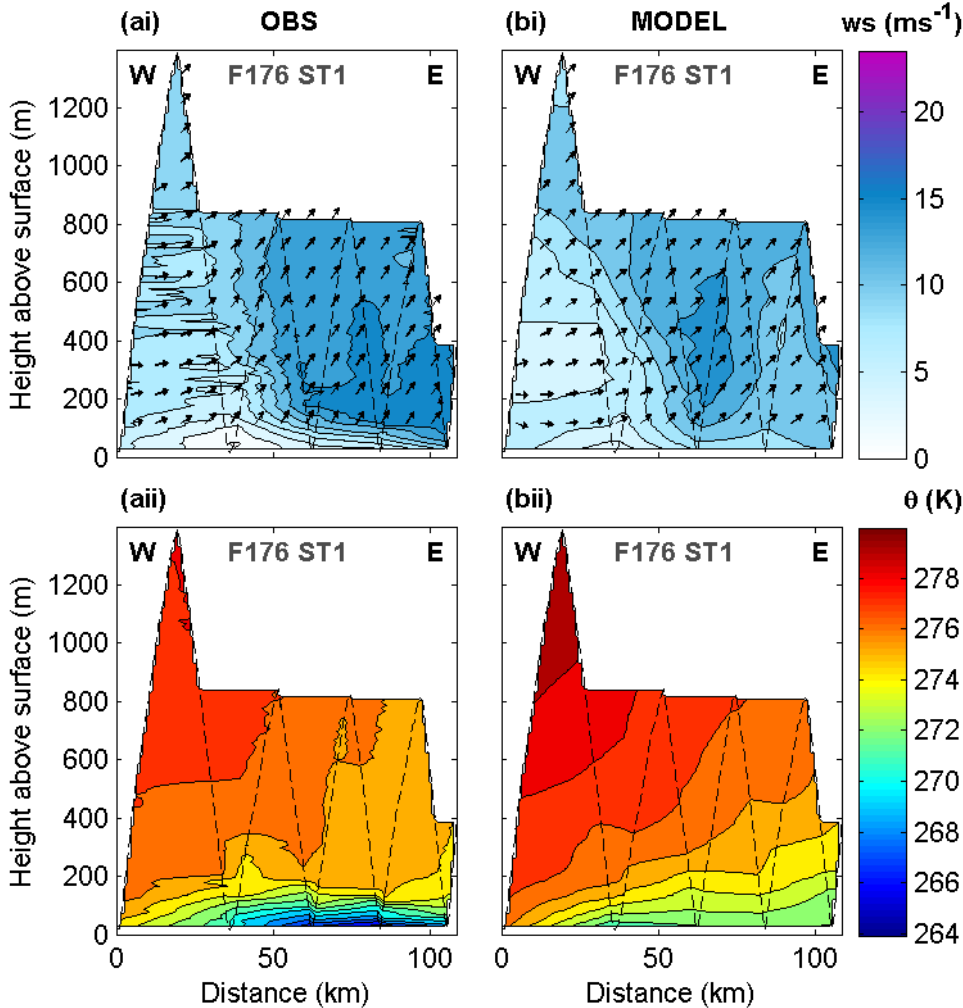

Figure 3.10: (i) Wind speed (contours, spaced at 2 ms^{-1}) and wind direction (arrows; the bearing of which denotes the horizontal direction of flow from North) and (ii) θ (contours, spaced at 1 K) cross sections for the flight 176 ST1 leg during the early morning of 5 February 2011 from (a) aircraft observations, and (b) the MetUM 1.5 km simulation (interpolated in 4-dimensions to the flight track). The x-axis is the distance along the transect (see Figure 3.2a for the flight track) from the most westerly point. For both (a) and (b), data is interpolated horizontally between adjacent profiles along the length of the sawtooth leg. The dashed line denotes the flight path.

Figure 3.11ai and aii are north-south cross-sections of wind speed interpolated from data derived from flight 176 ST2 and ST4 respectively (see Figure 3.2a for location). The two legs are not continuous; the more southerly leg commencing ~13 km to the west and ~30 minutes later than the termination of the more northerly leg. Nevertheless, a low-level jet is evident with peak wind speeds of ~20 ms^{-1} at ~200 m AMSL roughly intersecting (in the meridional sense) the two legs.

The magnitude and position of the jet is captured to a good degree of accuracy in the ST2 profiles simulated by the MetUM 1.5 km (Figure 3.11bii), however a well defined jet is not apparent in the simulated ST4 leg (Figure 3.11bi). Additional model analysis reveals that whilst the model marginally underestimates the cross-sectional area and strength of the jet, it also imprecisely simulates changes in the jet's path – a misrepresentation which happens to be made apparent across the temporally and spatially noncontinuous transition between ST2 and ST4.
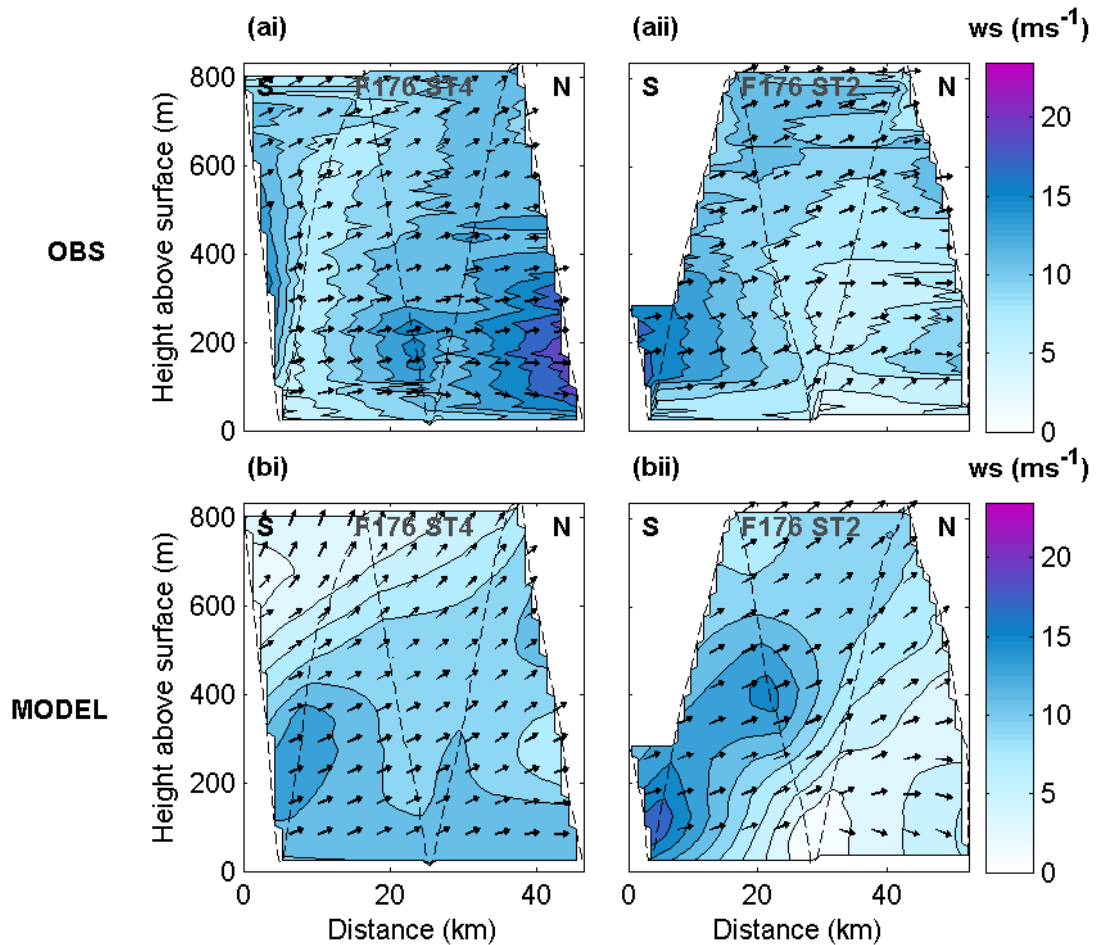
Figure 3.11: Wind speed (contours, spaced at 1.5 ms^{-1}) and wind direction (arrows) cross sections for (i) the flight 176 ST4 leg and (ii) the flight 176 ST2 leg during the early morning of 5 February 2011 from (a) aircraft observations, and (b) the MetUM 1.5 km simulation. The x-axis is the distance along the transects (see Figure 3.2a for flight tracks) from the most southerly points. For further details see the caption for Figure 3.10. Note the colour scale is the same for that used in Figure 3.10.

In the intervening time between negotiating these two legs the aircraft made a westward diversion to fly upwind within the jet into the mouth of Whirlwind Inlet (ST3; see Figure 3.2a). Data pertaining to the location '*Whirlwind Inlet*' in Figure 3.9 was recorded during a period of steep aircraft ascent during this flight leg. Wind speeds at *Larsen West* are considerably weaker and less gusty than those at *Whirlwind Inlet* (Figure 3.9c). Whilst winds veer with height in the boundary layer at *Larsen West*,

very little directional wind shear was observed at *Whirlwind Inlet* (Figure 3.9d)*,* and strong winds extend to near-surface level. Relative to *Larsen West*, the *Whirlwind Inlet* profile exhibits lower temperatures (Figure 3.9a) and, below ~200 m AMSL, higher humidities (Figure 3.9b).

A series of interpolated cross sections for flight 176 ST3 are presented in Figure 3.12. Examination of Figure 3.12a and b reveals a correspondence between wind speed and θ above ~200 m (below this height boundary layer processes – discussed presently – obscure any relationship). Air within the stronger sections of the jet (extending from the surface throughout the profile, the upper margin declining eastwards) is cooler than that in the weaker flow (to the top and east of the profile). A weaker correlation exists between wind speed and *q* (Figure 3.12a and c); regions of stronger winds appearing to exhibit lower humidities.

A stable, moist layer was observed immediately above the ice shelf. As illustrated in Figure 3.12a and verified by observations of windblown snow above the ice and sastrugi (Figure 3.13 is a photograph taken of the surface of the Larsen C within Whirlwind Inlet during flight 178, capturing well-defined sastrugi orientated such as to indicate formation by westerly windblown snow), strong westerly winds extended to near-surface level. This suggests the surface inversion is not due to the remnants of a cool pool. Instead, loss of sensible heat to the ice surface and gain in moisture due to enhanced sublimation rates driven by the strong surface winds provide a plausible mechanism for the moist stable layer (this is investigated in more detail in Chapter 5).

Figure 3.12b and c show that the moist inversion layer deepens and strengthens away from the Peninsula. The enhanced stratification could be due to reduced vertical mixing as a result of a steady transition from turbulent flow at the base of the lee slope towards increasingly laminar flow as air is advected east across the flat, low friction ice surface.
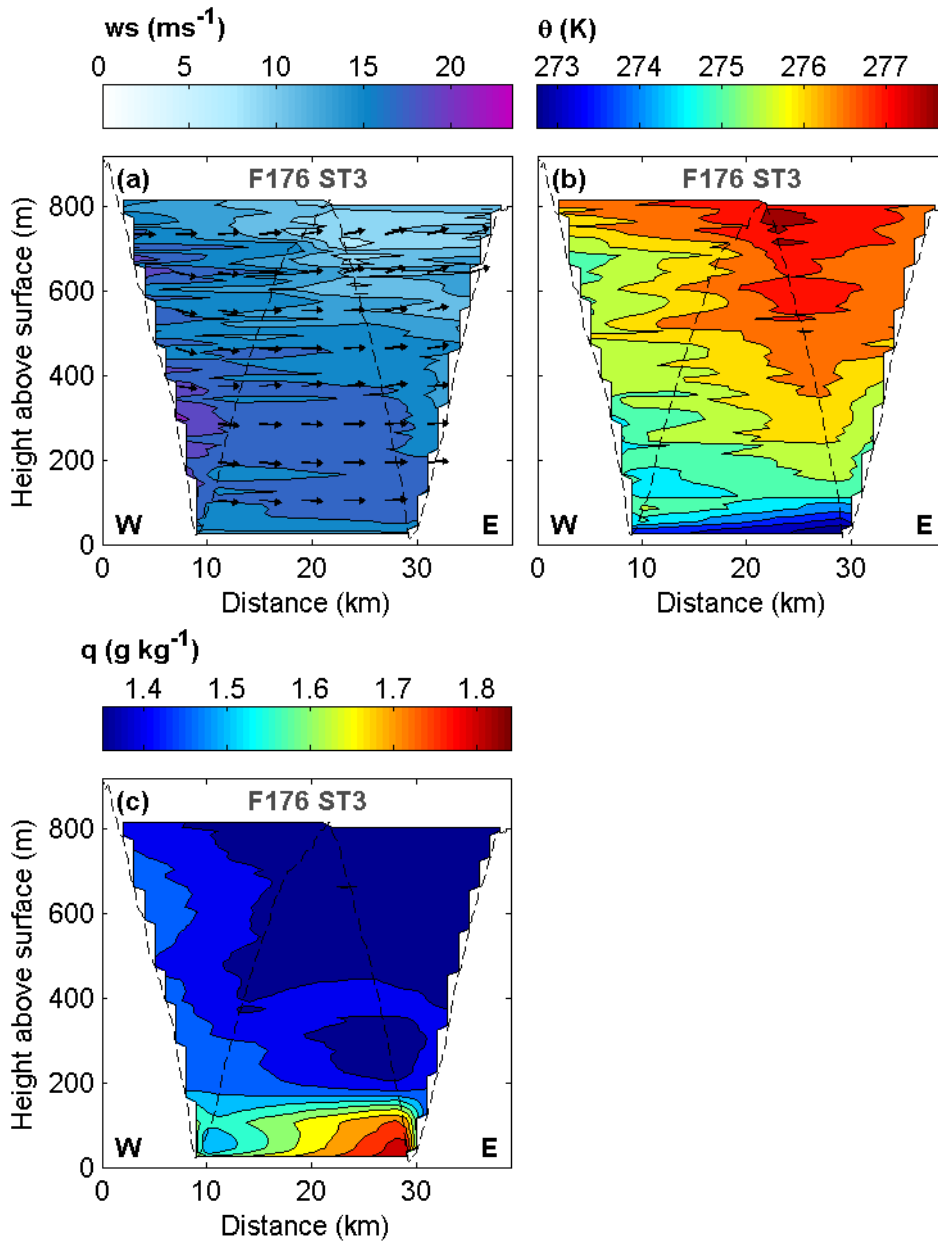
Figure 3.12: (a) Wind speed (contours, spaced at 1.5 ms^{-1}) and wind direction (arrows), (b) θ (contours, spaced at 0.5 K) and (c) *q* (contours, spaced at 5×10^{-5}) cross sections for the flight 176 ST3 leg (see Figure 3.2a for flight track) during the early morning of 5 February 2011 from aircraft data. For further details see the caption for Figure 3.10. Note that whilst the wind speed colour scale is the same, the θ colour scale differs from that used in Figure 3.10.
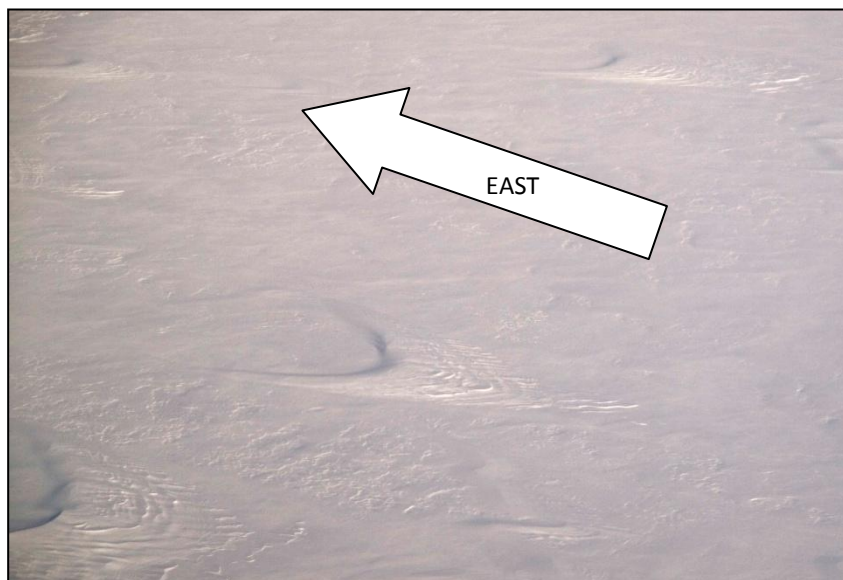
Figure 3.13: Photograph of sastrugi on the Larsen C taken from the aircraft during flight 178 within Whirlwind Inlet. The scale of the features were difficult to judge.

Figure 3.14 illustrates interpolated wind speed and θ fields for a flight 177 sawtooth leg roughly along 67.5°S (refer to Figure 3.2b). The far western portion of this leg shares a similar path to flight 176 ST3, but flight 177 extends considerably further east across the Larsen C and is ~5.5 hours later in the day a little before 18 UTC. Flying deep into the mouth of Whirlwind Inlet, such strong turbulence was encountered that eventually the aircraft was forced to terminate its westerly advance towards the Peninsula. Strong westerly flow observed at the westernmost extent of the flight leg (captured during the aircraft's final ascent of the leg, which was cut short at an elevation of ~290 m; Figure 3.14) weaken abruptly downwind in association with positive (upward) vertical velocities in excess of 4 ms^{-1} (not illustrated). Downwind of this region, near-surface westerly winds strengthen once more. These features resemble a hydraulic jump with a downwind wake, but may also be associated with flow-deflection due to nearby orography.

The UM 1.5 km reproduces the westerly jet (though the low level hydraulic jump and wake is missing) and the transition to more southwesterly flow downwind (Figure 3.14bi). Wind speeds outside the jet are consistently underestimated by 3 to 6 ms^{-1}.
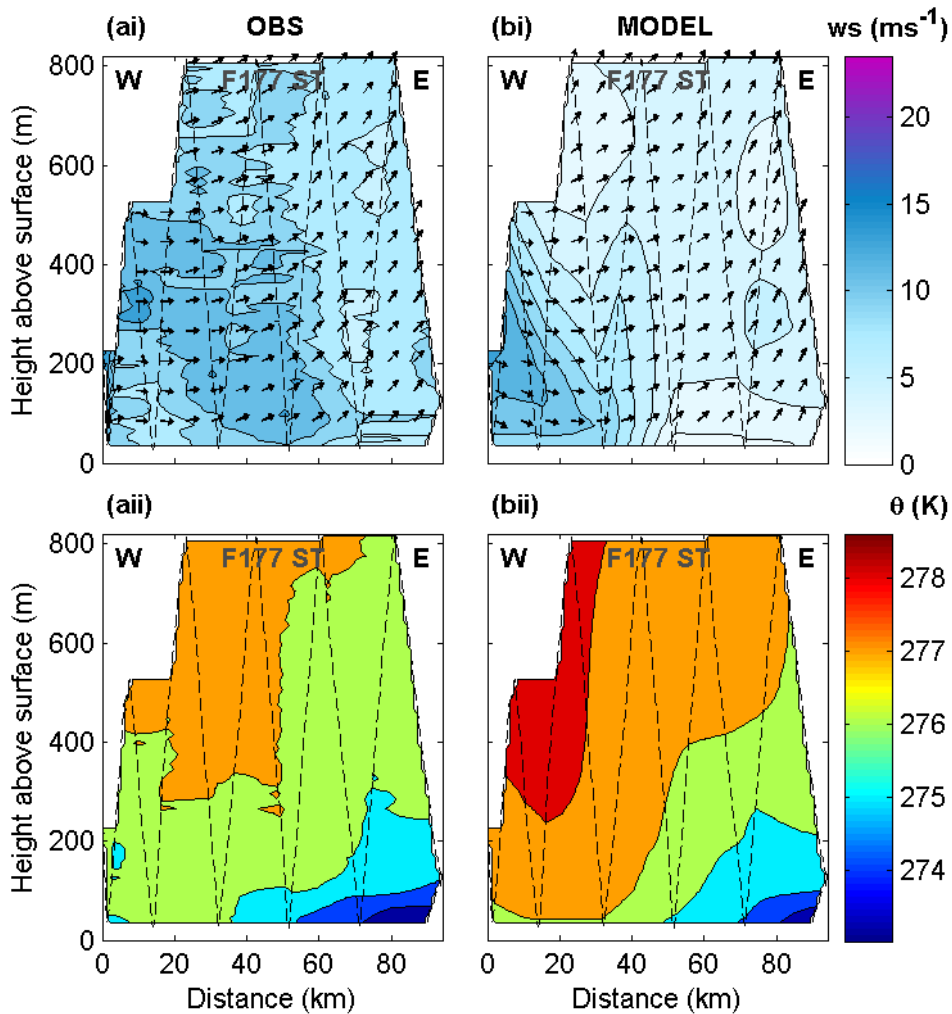
Figure 3.14: (i) Wind speed (contours, spaced at 2 ms^{-1}) and wind direction (arrows) and (ii) θ (contours, spaced at 1 K) cross sections for the flight 177 ST leg (see Figure 3.2b for the flight track) during early afternoon of 5 February 2011 from (a) aircraft observations, and (b) the MetUM 1.5 km simulation (interpolated in 4-dimensions to the flight track). For further details see the caption for Figure 3.10. Note the θ colour scale differs from that used in Figure 3.10. Note that whilst the wind speed colour scale is the same, the θ colour scale differs from that used in Figure 3.10 and Figure 3.12.

Flight 177 documents conditions within and to the east of Whirlwind Inlet a little under 6 hours subsequent to flight 176, during the early afternoon of 5 February. Descending warm föhn air continues to encroach from the west, but, away from the Peninsula, a surface inversion still resides (Figure 3.14aii), above which flow becomes southwesterly. However, this inversion is considerably weaker, owing to higher surface temperatures, than the inversion seen above the Larsen C earlier in the day (compare to Figure 3.10). Note however that this ST leg does not extend as far across the Larsen C as the flight 176 ST1 leg (Figure 3.2b). Although above 0°C for the westerly portion, temperatures at the sawtooth troughs fall below freezing point about half way across the leg and continue to cool eastwards (note that Figure 3.14 shows potential rather than thermodynamic temperature).

Simulated θ is everywhere within ±1.7 K of the observations and surface inversion strength appears at this time to be accurately simulated (Figure 3.14bii), despite being later into the simulation.

The distinct diurnal variation in near-surface temperature observed above the Larsen C (compare Figure 3.10 and Figure 3.14) is encouraged by the dry föhn conditions. Little to no cloud was observed above the ice shelf in the region navigated by the aircraft during the föhn event. Figure 3.15 – a photograph taken above the Larsen C looking west during flight 176 – attests to this fact. The model agrees, simulating cloud only above the southern part of the Larsen C (Figure 3.16a and b) where southwesterly flowing air appears from the MetUM 4 km simulation to be sourced from the east side of the AP and hence not constituting föhn (not illustrated, though discernible in Figure 3.4 from field).

Figure 3.15: Photograph illustrating cloudless föhn clearance conditions above the LIC looking west towards the AP, taken at low level during the flight 176 ST1 leg.

The clear conditions are consistent with the establishment of a leeside 'föhn clearance' (as defined in Section 1.4.4.1). Under such dry conditions one would expect an enhanced diurnal cycle in surface (ice) and near-surface air temperatures as a result of large longwave radiative heat loss at night, contrasting with large shortwave radiative heat gain during the day. Diurnal aspects of this event are discussed further in Chapter 5.
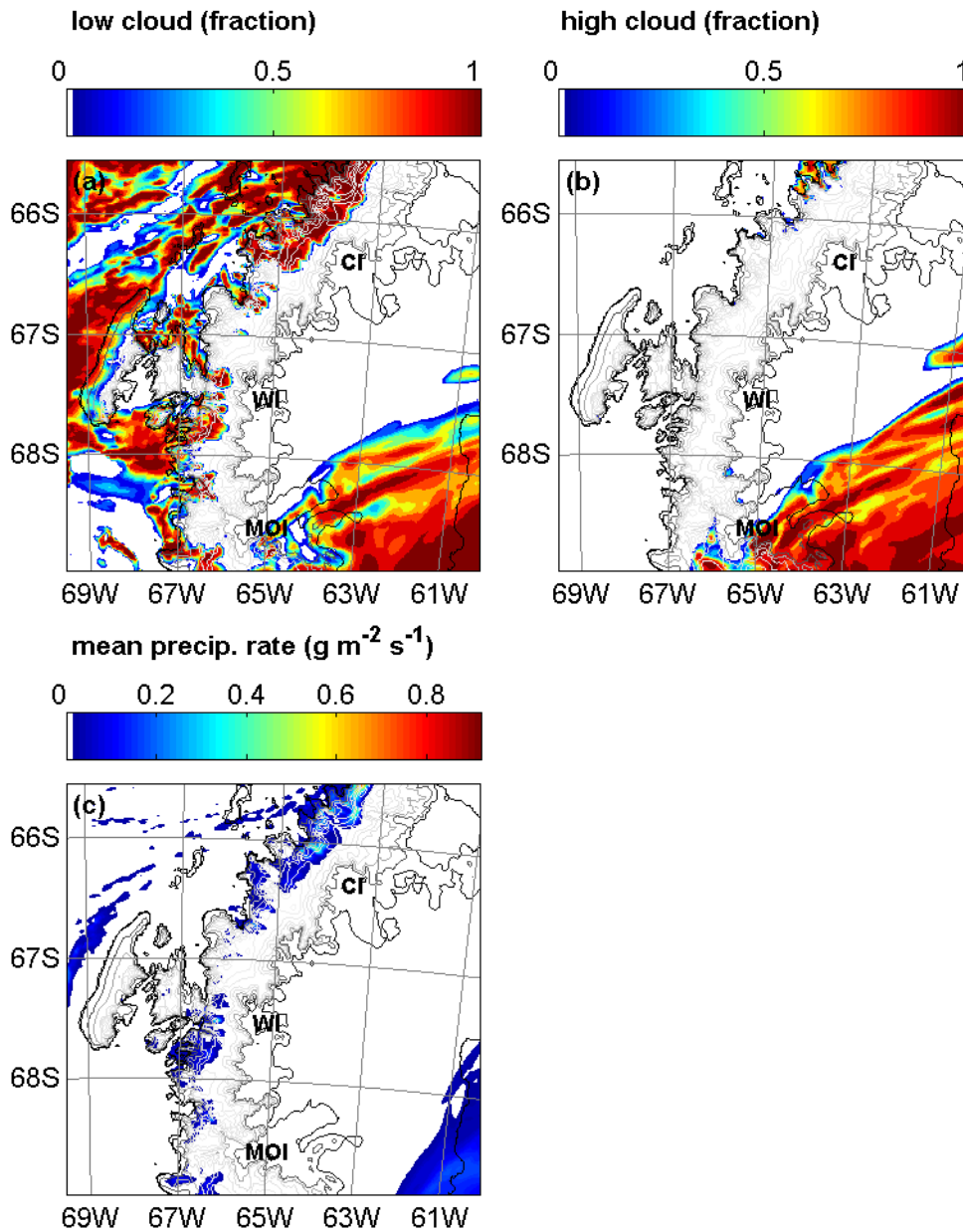
Figure 3.16: (a) Low level (below ~2000 m above the surface) and (b) high level (over ~2000 m above the surface) cloud fraction at 10 UTC 5 February and (c) mean precipitation rate between 22 UTC 4 February and 10 UTC 5 February from the MetUM 1.5 km simulation. Cloud fraction is calculated as the maximum cloud area coverage for all levels between a fixed range of model levels (maximum overlap of cloud is assumed). The boundary separating low and high cloud is ~2000m above sea level. Since the model levels are terrain following, above orography this value will be less.

3.4 Leeside response in the model

3.4.1 Model analysis of broad scale leeside flow features

Observations show that warm, dry föhn air had reached near-surface levels to the east of the AP by the early morning of 5 February. Figure 3.17 illustrates conditions at 10 UTC on 5 February – within the period of time during which the

aircraft navigated east of the AP for flight 176 – as simulated by the MetUM 1.5 km. Figure 3.17ai, bi and ci are *x-y* plots at 150 m AMSL of wind velocity, θ and *q* respectively. The former shows an inhomogeneous flow field characterised by jets emanating from the mouths of inlets separated by regions of calmer flow. Wind direction close to the Peninsula's eastern slopes appears largely to be a function of the orientation of the inlets through which the outflows are funnelled. The major jets include those emanating from Whirlwind Inlet, Mobil Oil Inlet and Cabinet Inlet. Cross sections of cross-transect wind component, θ and *q* through these jets are also presented in Figure 3.17 (ii-iv). It should be noted that Figure 3.17aiii corresponds approximately to Figure 3.11, though the transect used crosses Whirlwind Inlet further west (closer to the AP's eastern slopes) than the aircraft's north-south legs used for the latter.

Away from the Peninsula on the leeside, the flow is largely southwesterly. Examination of Figure 3.17ai affords understanding as to the flow variability observed and simulated along 67°S for flight 176 ST1, as illustrated in Figure 3.10. According to the model, the weak westerlies towards the western end of the ST leg are associated with the relatively weak outflow emanating from Mill Inlet (evident in Figure 3.17ai). On the other hand, the stronger inversion-capping southwesterlies to the east are sourced from the stronger föhn jets to the south.

Figure 3.17b and c illustrate the effect of the westerly föhn; conditions above the Larsen C being predominantly warmer and drier than those to the west of the Peninsula. In agreement with observations, leeside temperatures are considerably higher close to the Peninsula's slopes than they are further east.
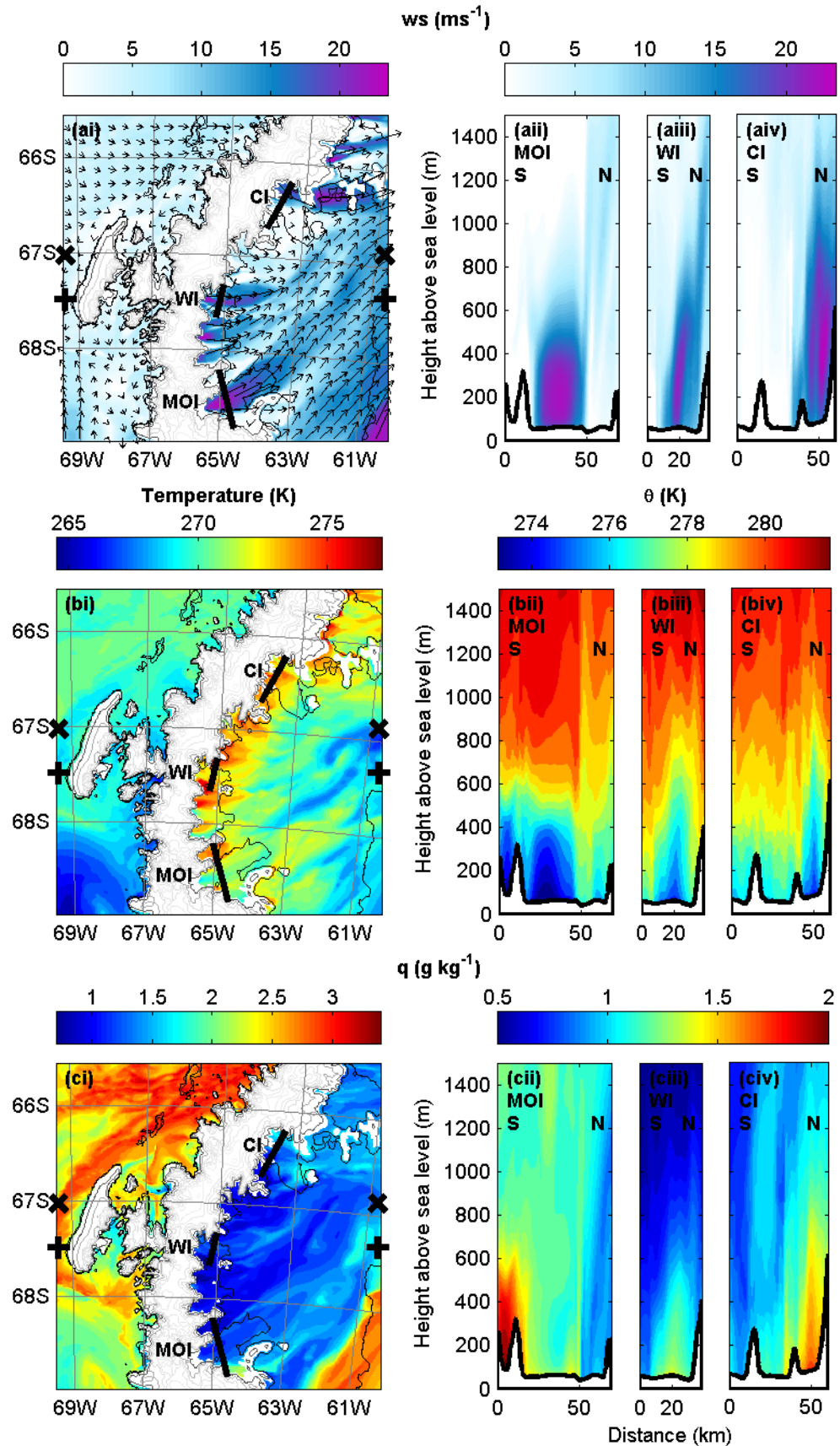
Figure 3.17: (a) Wind speed (contours, in ms^{-1}; transect-normal component in cross sections) and vectors (arrows), (bi) temperature (K), (bii-iv) θ (K), and (c) q in the form of (i) plan (x-y) plots at 150 m AMSL and jet cross sections across (ii) Mobil Oil Inlet (MOI), (iii) Whirlwind Inlet (WI), and (iv) Cabinet Inlet (CI) at 10 UTC on 5 February 2011 from the MetUM 1.5 km simulation. Note that in (aii-aiv) wind speeds are positive in the transect-normal direction closest to westerly (i.e. 'out of the page'), and for reasons of clarity negative values (which

never exceed a magnitude of 5 ms^{-1}) are not shown (white shading indicates speeds ≤ 0 ms^{-1}). Transect lines are marked and labelled on the plan plots. Also marked are the start/end points of *transect gap* ('+'s) and *transect peak* ('x's) used for the cross sections of Figure 3.24. Vertical to horizontal scale of transect plot axes = 1:100.

The jet transect plots of Figure 3.17 show that, close to the mouth of the inlets, the jets are cooler and moister relative to the adjacent wakes (with the exception of the Mobil Oil Inlet jet relative to the wake region to the south; Figure 3.17cii). As previously discussed (see Figure 3.9 and Figure 3.12), this is also apparent in the observations. It is important to note that, as illustrated in Figure 3.17bi and again in agreement with observations (Figure 3.9), whilst generally cooler and moister than the wake regions in the immediate lee of the AP, the air advected onto the Larsen C within the jets is still warm relative to air west of the AP at the same altitude, and the air further east above the ice sheet.

Following the work of Speirs et al. (2010) in the examination of what they refer to as the 'polar föhn' of the McMurdo Dry Valleys, the jets here are termed 'polar föhn jets'. It is believed that this study is the first to document the jets during polar föhn events.

3.4.2 Lagrangian characteristics of the polar föhn jets

The cool, moist nature of the föhn jets relative to adjacent wakes suggests a difference in source region and/or in recent diabatic heat exchange for the constituent air. As discussed in Section 3.3.2, sensible heat loss to the surface and associated sublimation of the ice shelf is likely responsible for the particularly moist, stable near-surface conditions within the jet. To what extent this process affects conditions above near-surface level is touched upon below and investigated further in chapter 5. Firstly we consider the upwind source of leeside air.

Following extensive observational and model studies on gap winds in association with downslope winds and föhn flow (e.g. Colle and Mass, 1998; Pan and Smith, 1999; Flamant et al., 2002; Zängl 2002; Jaubert and Stein, 2003), it is hypothesised that these polar föhn jets are the downwind continuation of gap flows through passes across the AP. As pointed out by Pan and Smith (1999), such gaps are associated with locally smaller $\hat{h}$ than the adjacent higher orography, and hence a lower upwind dividing streamline height (z_d). Consequently, it should be expected that cross-Peninsula gap flows will be comprised of air derived from lower altitudes, where

conditions are generally potentially cooler and moister. Furthermore, it could be that orographic height within the gaps falls below the height of the upwind inversion, encouraging the through-flow of cooler air underlying the inversion.

To test this hypothesis the trajectory model *Lagranto* (see Section 2.5.3) is employed to investigate the source of air parcels residing to the east of the AP and the characteristics of cross-Peninsula flow in Lagrangian space. The trajectories, using output from the MetUM 1.5 km simulation, are initiated at 10 UTC on 5 February (coincident with aircraft observations within Whirlwind Inlet during flight 176) from near the base (950 hPa; ~250 m AMSL in this case) of the lee slope, and run backwards in time for 24 hours using output every 30 minutes. Four diagnostics are examined: the maximum height of the underlying AP orography traversed; the height of the air parcels (as they cross the Peninsula and at predefined distance increments upwind); and the air parcel's θ and q. It should be noted that the accuracy of the maximum orographic height is limited by the fact it is calculated by interpolating between the positions of air parcels at consecutive model outputs (30 minutes apart).

In addition to the model domain used in the analyses presented thus far (hereafter termed the *standard* domain), a second domain for the MetUM 1.5 km model positioned to the southwest (*SW* domain; see Figure 3.4) is used where necessary to avoid the premature departure of trajectories from the model grid to the south and west. Despite the fact the change in domain renders an entirely different simulation, the reproduction of the major features is very similar; with comparable jets and wakes simulated in the immediate lee of the Peninsula (Figure 3.18 and Figure 3.19). So long as caution is applied to quantitative cross-domain comparisons, the results from both domains are of use in testing our hypothesis.
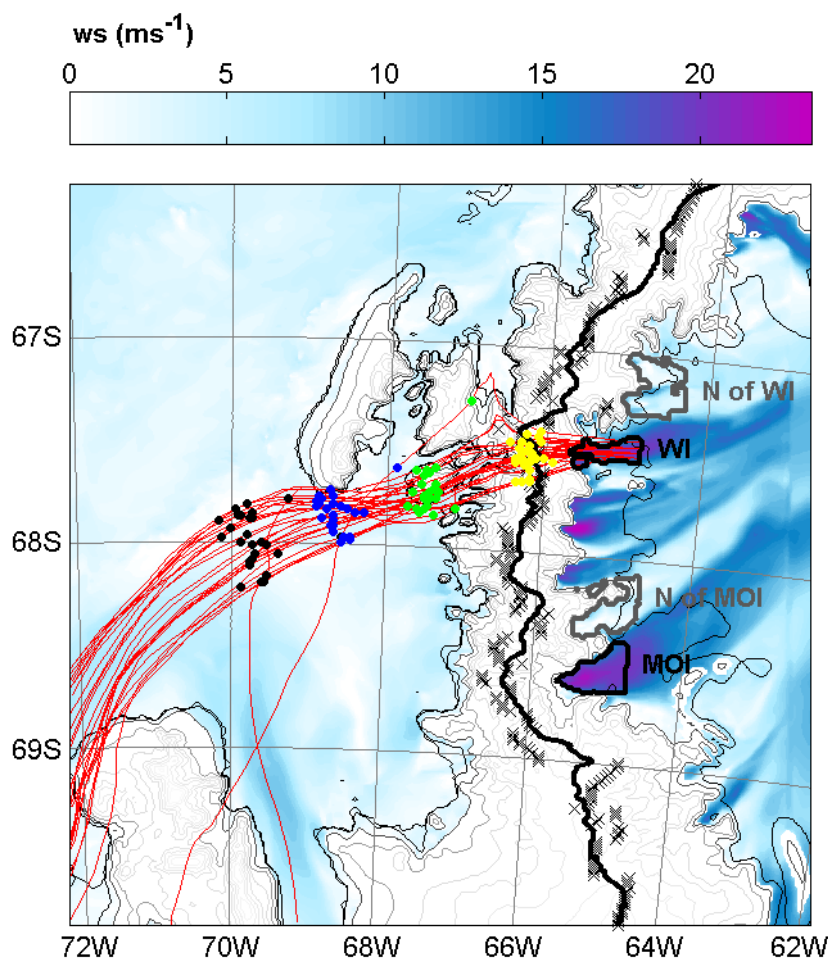
Figure 3.18: Trajectories (red) within the WI region for the *SW* domain, overlaying wind speed at 150 m AMSL at the time of back trajectory initiation (10 UTC 05 February 2011). To enhance legibility only 1 in 6 trajectories are plotted. The yellow, green, blue and black dots indicate the positions of air parcels respectively 0, 50, 100 and 150 km upwind of the AP's crest line (solid black line) for each trajectory. The path of the crest line is determined by connecting the points of peak smoothed AP height for each model grid increment along the y-axis (roughly N-S). The crosses mark the positions of peak unsmoothed AP height for each y-increment. The four *SW* domain trajectory initiation regions are marked and labelled; black boundaries enclose 'jet' regions (associated with wind speeds in excess of 15 ms^{-1}), whilst grey boundaries enclose 'wake' regions (associated with wind speeds less than 5 ms^{-1}).
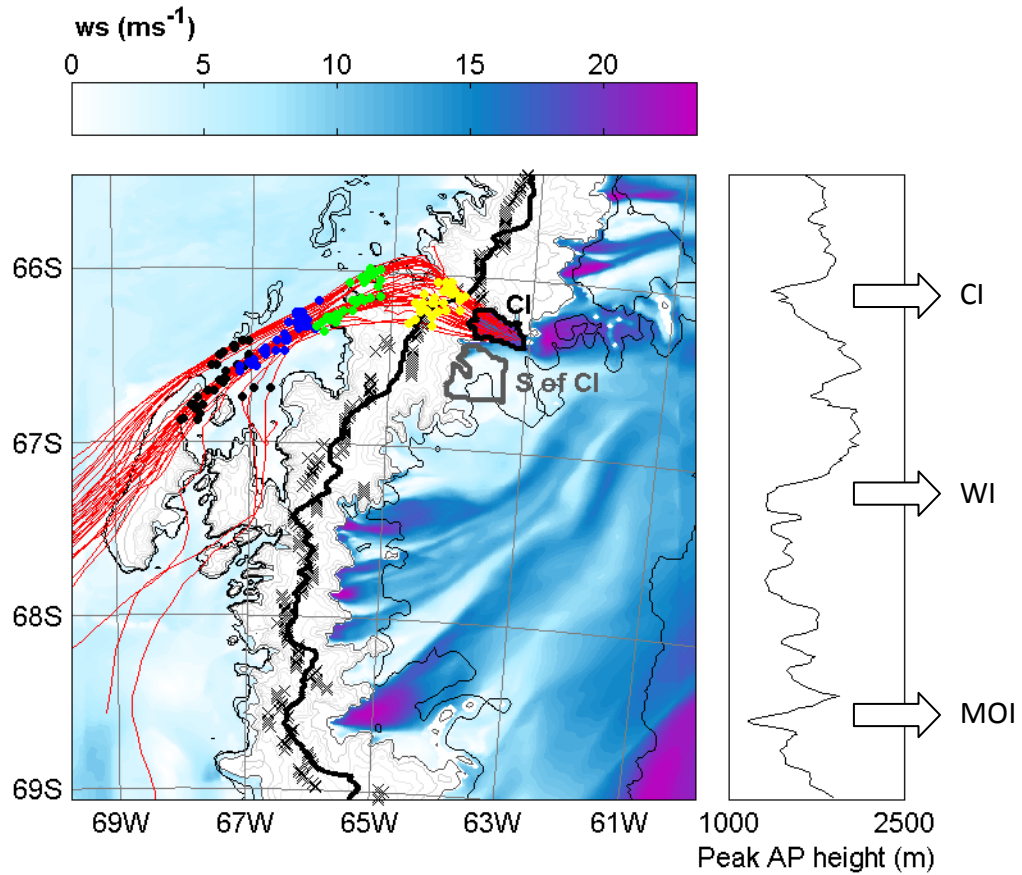
Figure 3.19: As in Figure 3.18, but for trajectories initiated within the CI region of the *standard* domain. Also plotted (right) is peak orographic height for each model grid increment along the y-axis (roughly N-S) along the crest of the AP. Passes / depressions in the crest line generally coincide with the positions of inlets (marked) on the eastern slopes of the AP.

Figure 3.20 presents results from the trajectory analysis. Data in these plots are averaged for multiple trajectories whose initial positions are within predefined sample regions (region boundaries are shown in Figure 3.18 and Figure 3.19), defined as follows:

Full region name	Abbreviation	Type	Domain
Whirlwind Inlet	WI	Jet	SW
North of Whirlwind Inlet	N of WI	Wake	SW
Mobil Oil Inlet	MOI	Jet	SW
North of Mobil Oil Inlet	N of MOI	Wake	SW
Cabinet Inlet	CI	Jet	Standard
South of Cabinet Inlet	S of CI	Wake	Standard

Each region is either associated with strong winds (trajectories with initial flow speed <15 ms^{-1} filtered out) and pertain to jet conditions; or weak winds (trajectories with initial flow speed >5 ms^{-1} filtered out, with the exception of enclosed regions, as explained forthwith) and pertain to wake conditions. Isolated areas of stronger flow

(>5 ms^{-1}) within the wakes are included within the respective sample regions. These westerly flows are weak and quick to disperse relative to the jets but, similarly, originate from the easterly slopes of the AP. Including them avoids sampling bias relative to the jet regions, ensuring that the western boundary of all regions is at the base of the lee slopes.

In all cases, both the mean height of the orography traversed and mean upwind trajectory altitudes are greatest for trajectories originating in wake regions (Figure 3.20ii). The values reveal consistently significant differences in the source altitude between the jet and wake regions, and indicate that the jets appear downwind of flow through passes in the orography (also apparent in Figure 3.19; passes / depressions in the crest line generally coincide with the positions of inlets on the eastern slopes of the AP), i.e. they are gap winds. The CI jet and S of CI wake regions exhibit the greatest jet-wake difference in mean trajectory source altitude; ~1500 m, as opposed to between 400 and 500 m for the other two jet-wake pairs.

There is relatively little deviation in the flow direction of air parcels as they cross the Peninsula upwind of Whirlwind Inlet (Figure 3.18). The gap in this case is aligned close to parallel to the flow approaching the AP. The result is a *type A* gap flow (see Figure 1.14a), whereby the momentum of flow through the gap is due to that transferred from the approaching flow and to that generated by the cross-Peninsula pressure gradient (apparent in Figure 3.4). In contrast, the flow upwind of Cabinet Inlet turns through an angle approaching 90° to cross the AP (Figure 3.19), more closely resembling a *type B* gap flow (see Figure 1.14b), whereby the forcing mechanism is solely the cross-barrier pressure gradient.

The sourcing of near-surface leeside air from significantly higher altitudes upwind is diagnostic of upwind flow blocking, a phenomenon predicted by the relatively large values of $\hat{h}$ associated with the event. Flow is more effectively blocked (associated with a greater dividing streamline height, z_d) by the higher orography upwind of the wakes. Using westerly $\hat{h}$ (considered to be the upper limit of true representative $\hat{h}$ at any given time; see Section 3.2) at *Location A* (position shown in Figure 3.4) and the mean traversed orographic height values derived from analysis of the relevant jet ($h \approx 1400$ m) and wake ($h \approx 1600$) trajectories, z_d is calculated as ~1040 m and ~1190 m for jets and wakes at a time 7 hours prior to trajectory initiation (note that 7 hours is the minimum estimated time given conditions for air to advect

from *Location A* – where the calculation was for (position shown in Figure 3.4) – to the leeside). Despite the jet-wake difference in source altitude being larger than theorised, these values correspond generally quite well with those acquired for the *SW* domain regions shown in Figure 3.20aii, once again (as in many previous studies such as Snyder et al., 1985 and Ding et al., 2003), endorsing Sheppard's (1956) simple but contentious (see Section 1.3.4) formula.

Location A is too far north for flow here to be considered sufficiently representative of flow upwind of the MOI and N of MOI regions. Meanwhile, due to the large non-geostrophic deviation in flow direction across the AP upwind of the CI jet and S of CI wake (Figure 3.19), such theoretical comparison with Figure 3.20cii is inappropriate for these regions. It is of interest however that out of the three jet-wake pairs considered here, it is this set which exhibits the greatest deviation in upwind source altitude.

Figure 3.18 and Figure 3.19 show that upwind of the AP the trajectories are generally tightly clustered in horizontal space, suggesting the föhn jets have a common forcing mechanism, i.e. they are well-defined features. However, Figure 3.21 shows that for each region there is considerable variation in the upwind source altitude, particularly for the wakes. In the case of the CI jet the major bulk of air is derived from altitudes lower than the AP's crest (which is, within the region of study, between ~1100 and ~2200 m AMSL; see the inset altitude profiles of Figure 3.19) and hence any approximately crest-level inversion; indeed a significant quantity of air is simulated to have risen from near-surface level. A far greater proportion of air has been drawn down from high altitudes in the case of the S of CI wake, and comparatively little air is derived from low levels. The same differences are discernible (though considerably smaller) when comparing the WI jet and N of WI wake trajectories. Figure 3.21 confirms that the air is potentially cooler and moister towards the sea surface upwind of the AP, and that the source air for the jet regions is on average cooler and moister than that for the wake regions. Indeed, average θ (q) of air parcels upwind of the AP are, in all cases, lower (higher) for trajectories initiated within the jet regions relative to those initiated within the wake regions (Figure 3.20). The greatest jet-wake discrepancy in θ (q) at the 150 km upwind distance increment is ~6.3 K (~1.1 g kg^{-1}) for the CI and S of CI regions. Note that the largest discrepancy in upwind trajectory source altitude is, as expected due to the drawdown of higher,

potentially warmer air (discussed further in Section 3.4.3), also for this jet-wake pair. The other two jet-wake pairs exhibit θ (q) differences of between 2 and 2.5 K (between 0.25 and 0.29 g kg^{-1}) at the 150 km upwind distance increment.
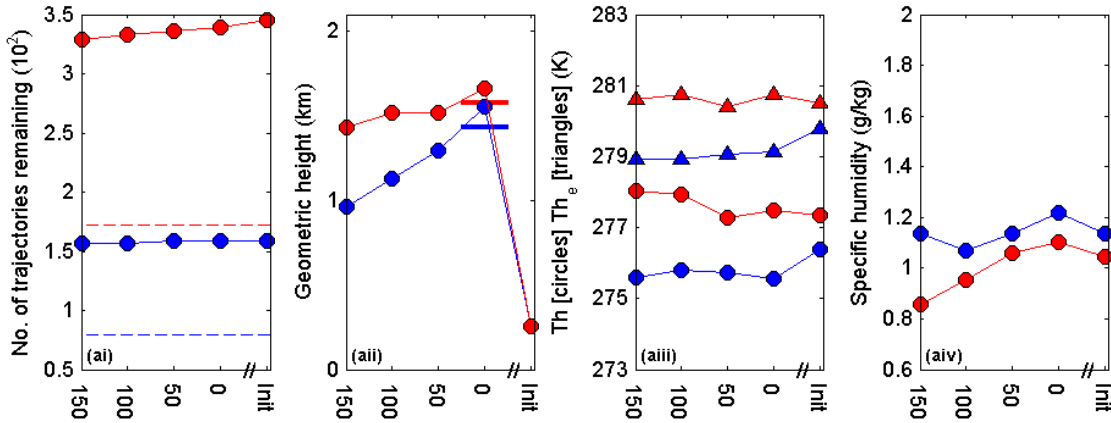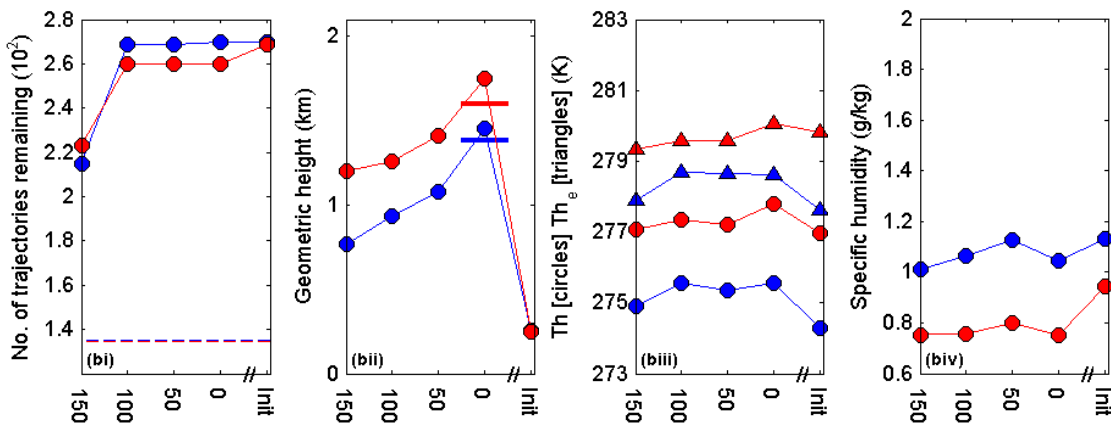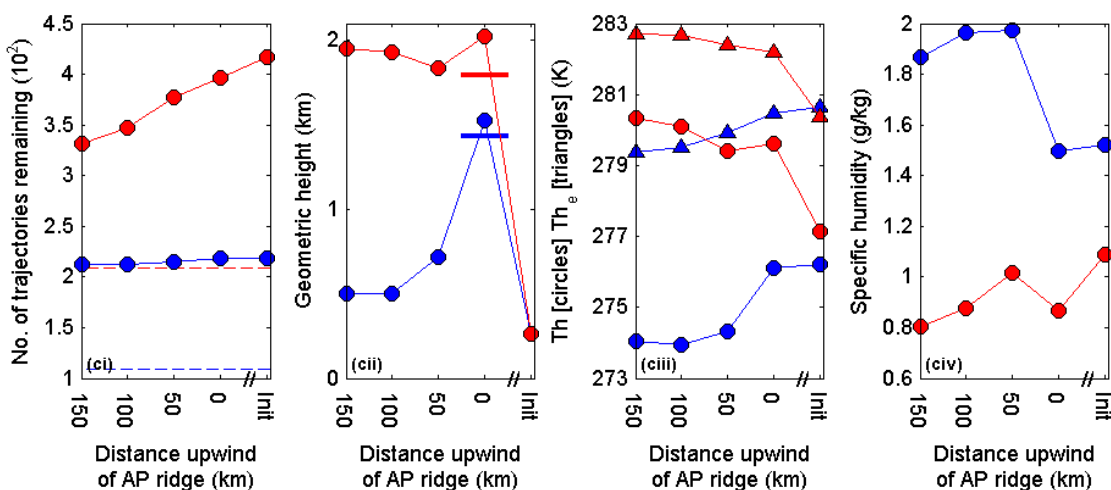
Figure 3.20: Fields for back trajectories initiated at 10 UTC 5 February 2011 at 950 hPa within (a) the Whirlwind Inlet jet (WI) and the wake region north of WI (N of WI), (b) the Mobil Oil Inlet jet (MOI) and the wake region north of MOI (N of MOI), (c) the Cabinet Inlet jet (CI) and the wake region south of CI (S of CI). Trajectories are derived from Lagranto using Met UM data from (a, b) the *SW* domain and (c) the *standard* domain (domains are mapped out in

Figure 3.4). Jet trajectories are classified by wind speeds at initiation of over 15 ms^{-1} (blue), and wake trajectories by wind speeds at initiation of under 5 ms^{-1} (red). The x-axis is trajectory distance upwind of the AP, but also includes an increment for trajectory initiation ('Init') above the Larsen. The distances upwind of the AP are underestimated approximations since corresponding data points are actually the first (as the model progresses backwards in time) for which the distance travelled upwind by each trajectory has surpassed that distance increment. The 'number of trajectories remaining' field (i) is the number of trajectories with valid positional data, i.e. which are not 'lost'. The dashed horizontal lines correspond to half the number of trajectories within the sample at the time of initiation. A back trajectory is deemed to be 'lost' if it does not 'arrive' at an upwind distance increment within the 24 hour period, intersects orography, or leaves the edge of the model domain. The latter is only significant for the 150 km upwind distance increment in the cases of the WI jet, MOI jet and N of MOI wake regions, whilst the number of trajectories intersecting orography is in this case generally insignificant. The horizontal lines in the trajectory height plots (ii) refer to the estimated mean peak height of orography traversed by the relevant trajectories. Note that this line is counter-intuitively sometimes above the mean peak height of the trajectories above the AP. This can be explained by the relatively coarse temporal resolution of the trajectory model matched with the high spatial resolution of the complex AP orography in the MetUM. Trajectory data is output at intervals of 30 minutes, meaning that the data is unlikely to capture the trajectory at the precise moment it reaches its peak altitude above the AP. The location at which a trajectory passes the AP's crest is estimated by linearly interpolating trajectory position between successive data points either side of the ridge. In (iii), Th is mean θ (circular markers) and Th$_e$ is mean equivalent potential temperature (triangular markers).

In discussion of Figure 3.17 (in Section 3.4.1), conditions within the wake region to the south of MOI were highlighted as anomalous, with similar temperatures to and higher humidities than the air making up the MOI jet. Back trajectory analysis explains this anomaly by showing that, despite not being strongly accelerated to form a jet, air within this wake was in fact derived from comparatively low altitudes (mean of ~550 m AMSL at a distance 150 km upwind of the AP's crest) within Marguerite Bay (see Figure 2.1 for the location of Marguerite Bay).
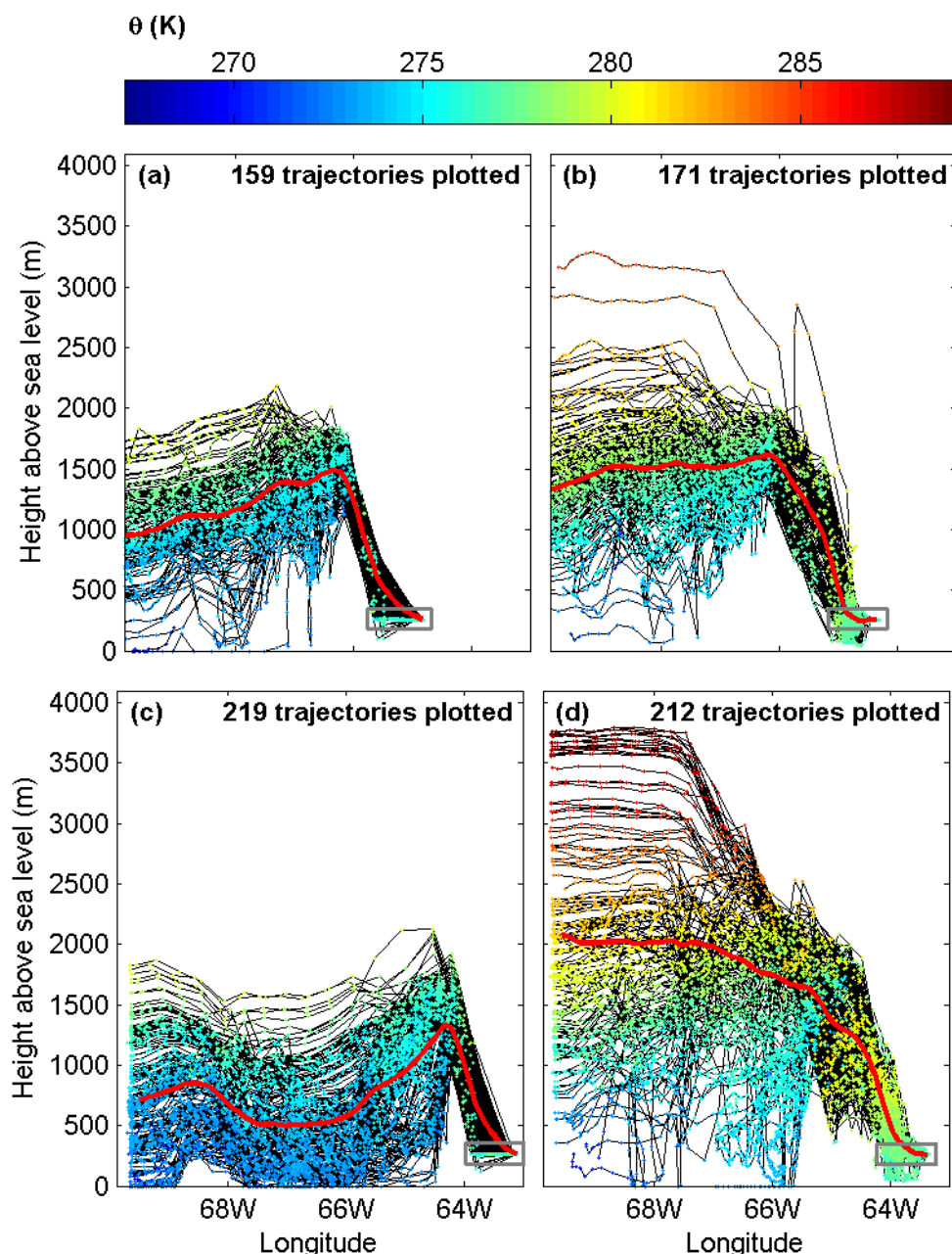
Figure 3.21: Trajectory height with longitude. Dots mark the height of air parcels at each data point (spaced 30 minutes apart). Dot colour denotes θ (K) of the air parcel. The trajectories are initiated at 950 hPa at 10 UTC on 5 February within (a) the WI jet (SW *domain*), (b) N of WI wake (SW *domain*), (c) CI jet (standard *domain*) and (d) S of CI wake (standard *domain*) within the grey rectangles and tend to retreat west and over the AP with successive steps back in time. The red lines give the mean trajectory height. In (a) and (c), all trajectories within each initiation region are plotted, whereas in (b) and (d), due to the larger size of the region, only half the trajectories are plotted (though the mean line is for all trajectories) to improve legibility and aid jet-wake comparison. For (c), following trajectories westward (backwards), the rise in altitude west of about 67.5°W appears largely to be due to the effect of Adelaide Island on the flow field.

3.4.3 Mechanisms responsible for the cross-Peninsula temperature gradient

In Section 1.4.4.1 the mechanisms considered by Smith (1979) to induce föhn warming were listed and illustrated in Figure 1.15. In this section we will consider the

cross-Peninsula temperature gradient as opposed to the magnitude of Leeside warming with time (which is the established definition of föhn warming upheld in Smith, 1979). Consequently the warmer source region mechanism (Figure 1.15c) is irrelevant here as this should eventually (idealistically) affect both upwind and downwind regions equally. The remaining mechanisms include latent heat release (Figure 1.15a) and isentropic drawdown (Figure 1.15b) due to the differential advection of potentially warm air from aloft. In this study another mechanism, not mentioned by Smith (1979), is revealed in the examination of trajectory output. This is a sensible heat exchange mechanism, entailing the exchange of sensible heat related to turbulent mixing of the flow ascending the windward slopes with warmer air above, counteracted by sensible heat loss downwards towards the cool ice surface.

In Figure 3.22 contributions to the mean low-level cross-Peninsula temperature gradient ($\Delta_{LLCP}T$) are illustrated, calculated in accordance with a 3-dimensional model based on trajectory output, the key features and assumptions of which are presented in Figure 3.23. Also plotted is the mean decrease in trajectory height AMSL across the Peninsula (i.e. the mean trajectory descent). The downstream value used to calculate $\Delta_{LLCP}T$ is simply the mean temperature at the leeside trajectory initiation sites (represented by point C in Figure 3.23) at the time of trajectory model initiation. The upstream value used is the mean temperature 150 km (the Rossby radius of deformation, λ_R) traced along the backward trajectories upwind of the AP at the height of trajectory initiation and for the time the trajectories arrive at the 150 km upwind distance increment, and is denoted by point B in Figure 3.23 (note that point B will always be directly above or, more commonly, below point A, which represents the location of trajectories at the 150 km upwind distance increment). Flow should not feel the orographic effect of the AP beyond a distance λ_R upwind of the AP whereas the locations of trajectory initiation are within the region affected by föhn, so any level cross-Peninsula gradient using these limits can also be thought of as the föhn anomaly, i.e. the difference between föhn and background conditions.
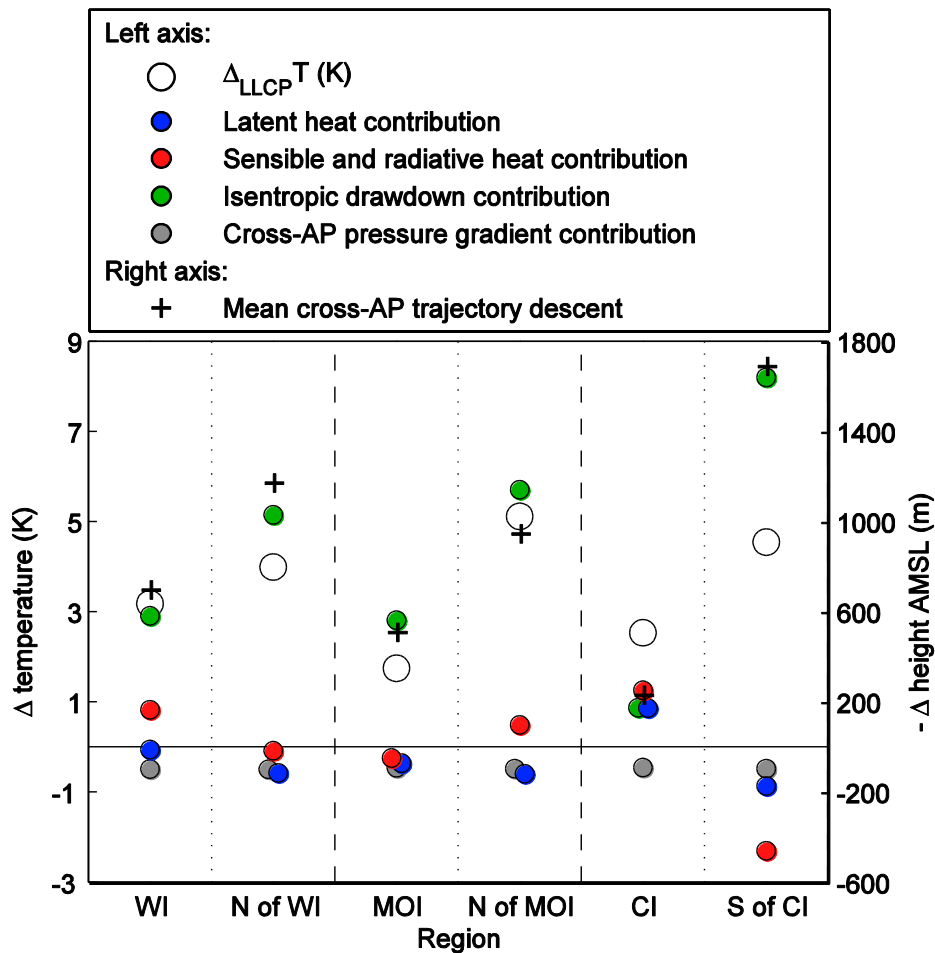
Figure 3.22: Low-level cross-Peninsula temperature gradients ($\Delta_{LLCP}T$) at the mean height of trajectory initiation (~260 m) together with individual contributions to the temperature budget (left axis) and cross-Peninsula descent along trajectories (right axis), for all trajectory initiation regions. All gradients and temperature budget components are calculated using data from the MetUM 1.5 km simulation and Lagranto trajectory model. For the trajectory height gradients, the values used are the mean height of all trajectories at the time of trajectory model initiation and at the 150 km upwind distance increment. For the low level temperature gradients, the downstream value is similarly simply the mean temperature for all trajectories at the time of trajectory model initiation. The upstream temperature used is the trajectory-mean temperature of air 150 km upwind of the AP at the height of initiation (i.e. directly above or, more commonly, below the trajectories at the 150 km upwind distance increment). Note that for ease of visual interpretation, temperature and trajectory height gradients are calculated such that a positive value denotes, respectively, warming (+Δ temperature) and descent (-Δ height AMSL) in the downstream direction.
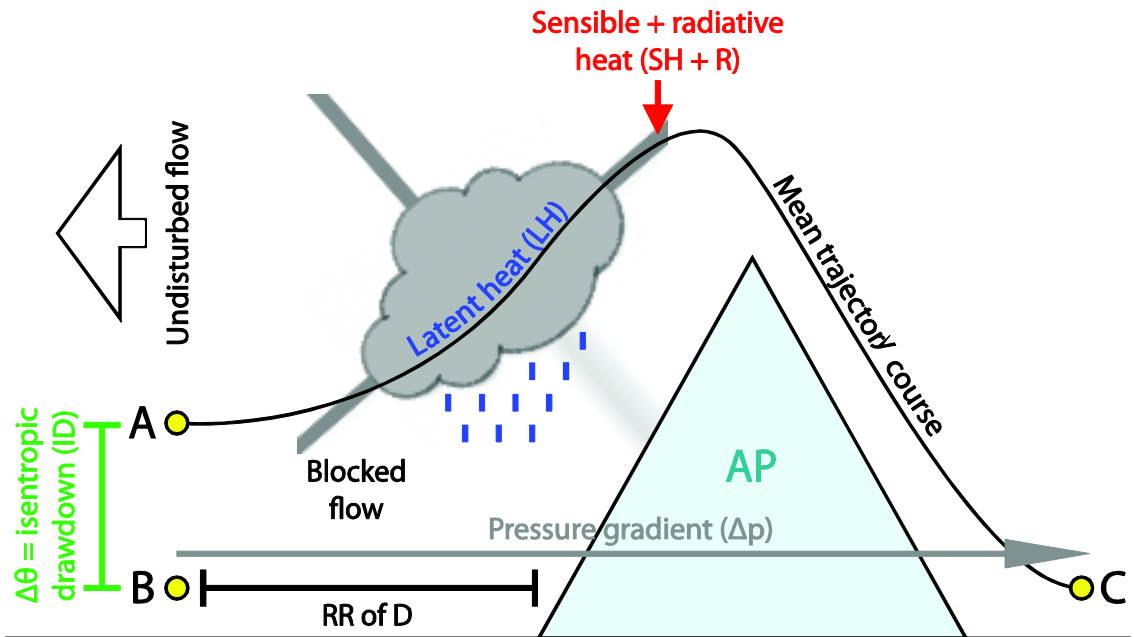
$$\Delta_{LLCP}T = \Delta^{ID}\theta \;\; + \Delta^{LH}\theta \;\;\;\;\;\;\;\;\;\;\;\; + \Delta^{SH+R}\theta \;\;\; + \Delta^{\Delta P}T$$

$$T_C - T_B = \theta_A - T_B + (\theta_C - \theta e_C) - (\theta_A - \theta e_A) + \theta e_C - \theta e_A + T_C - \theta_C$$

Reference pressure for $\theta = p_B$

Figure 3.23: Schematic illustrating the three-dimensional model for describing the key features and assumptions used in the calculation of contributions towards the low-level cross-Peninsula temperature gradient ($\Delta_{LLCP}T$) presented in Figure 3.22. T_X, θ_X and θe_X are the temperature, θ, and equivalent potential temperature, θe, at location X, whilst $\Delta^Y Z$ is the change in Z due to Y.

In all cases, $\Delta_{LLCP}T$ is greater for the wake regions than corresponding jet regions (also evident, though less clearly, in Figure 3.17), due mainly to the relatively warm conditions within the wakes. For all but one of the regions, by far the greatest contribution (peaking at ~+8.2 K for the N of CI wake region) to $\Delta_{LLCP}T$ is that of isentropic drawdown due to differential advection (Figure 3.22). Unsurprisingly these values correlate closely with the magnitude of cross-Peninsula mean trajectory descent, with the largest contributions being for the wake regions. For the CI jet region, mean descent is smallest, and the isentropic drawdown contribution is similar in magnitude to each of the diabatic contributions.

Note that in Figure 3.22 θ is calculated using the pressure at point B as the reference pressure. This way contributions to $\Delta_{LLCP}T$ are relative in magnitude to the temperature at B. Since we are considering a temperature gradient rather than a θ gradient, the effect of the pressure gradient between points B and C (the föhn pressure anomaly) must be taken into account. During a föhn event, due to the

generation of a low pressure anomaly in the lee of the mountains in association with the descent of warm dry air in this region (location C in Figure 3.23), the pressure gradient mechanism ($\Delta^{\Delta P}T$) acts in opposition to the föhn warming effect, having a leeside cooling effect. Figure 3.22 shows that whilst its contribution towards $\Delta_{llcp}T$ is not insignificant, it is never the dominant term and varies little (ranging from -0.5 K to -0.45 K). Wake regions exhibit very marginally smaller (larger negative) $\Delta^{\Delta P}T$ values relative to the adjacent jet regions. The larger amplitude leeside pressure anomalies at the wake locations are in accord with greater mean trajectory descent across the AP.

The contributions of latent and sensible heating towards $\Delta_{LLCP}T$ are quantified using data from the trajectory model. Changes in θ in Lagrangian space are due to diabatic processes. Latent heat exchange can be determined from relative changes in equivalent potential temperature (θ_e) and θ of an air parcel (convergence in θ - θ_e indicating latent heat gain from condensation). Changes in θ_e in Lagrangian space give the remaining diabatic heat exchange, which comprises sensible heat and radiative heat exchanges (the latter presumed to be insignificant in accordance with the analysis of leeside potential temperature budgets in the model). The most significant circumstance of latent heating evident in Figure 3.20iii and iv (convergence of θ and θ_e lines, and decrease in q) is upwind of the CI jet between upwind distance increments 50 and 0 km. Accordingly this segment also exhibits the greatest ascent in the trajectory output – cool, moist air rising from near-surface level up and over the Peninsula (Figure 3.20cii-iv) – and the region has some of the highest simulated upwind time-mean precipitation rates (Figure 3.16c). Indeed the CI jet region is associated with the greatest latent heating contribution towards $\Delta_{LLCP}T$ of all regions (Figure 3.22). Trajectories initiated within the neighbouring S of CI wake region descend from a considerably greater altitude (average of ~1700 m across the AP). Despite moderate latent heat gain allied with ascent between the 50 and 0 km upwind distance increments, steady descent of relatively warm, dry air results in a net negative latent heating contribution (Figure 3.20ii-iv). All other regions exhibit small negative latent heating contributions, the smallest (largest negative) values being attributed to the wake regions in conjunction with greater mean descent of flow across the Peninsula. This gain in moisture may be due to turbulent mixing with

moister air derived from lower altitudes, sublimation at the surface, and evaporation as air descends above the lee slopes.

The low-level humidity gradient across the AP depends upon condensation / evaporation within the cross Peninsula flow, and differential advection. The fact there is generally (with the exception of flow upwind of the CI jet) net gain in moisture across the Peninsula in Lagrangian space (Figure 3.20iv and Figure 3.22) shows that it is the differential advection mechanism which causes the (Eulerian) leeside drying.

The range in sensible and radiative heating contributions across the regions is slightly larger than for latent heating (Figure 3.22). For two of the jet-wake pairs, as with latent heating, larger sensible heating contributions are associated with the greater upwind ascent of the jet trajectories. The exception is with the MOI and N of MOI regions, where the opposite is apparent. A less clear jet-wake relationship might be expected in the case of sensible heating, related to the fact that significant exchanges may be due to warming from above or cooling from the below. The greater windward ascent of air upwind of a jet promotes the former, though the greater wind speeds associated with the jets also encourages the latter due to greater air-ice turbulent exchange (investigated further in Chapter 5). The greatest sensible heating contribution to $\Delta_{LLCP}T$ is for the CI jet, where it constitutes the most significant contribution of all the warming mechanisms.

Siebert (1990), an often cited paper which gives an elegant account of the history of föhn theory in the literature, describes the misinterpretation and alteration over time of Hann's (1901) original theory for the föhn effect. Hann simply stated that föhn warming was due to thermodynamic warming of descending air in a stably stratified atmosphere, and that precipitation was not a necessary condition. The textbook theory which has evolved, however, typically considers exclusively a condensation mechanism. Seibert (1990) presents objections to this theory, rightly pointing out that there are cases of föhn warming without cloud cover upwind and that not just condensation but precipitation is required for a net gain in energy. It should be noted that the content of Seibert's (1990) paper focussed on the Alpine föhn. However, in consideration of föhn as a non-geographically specific term, according to the findings of the present study it could be argued that she overly undervalues the diabatic contribution towards föhn warming. She considers the quantitative effects of precipitation to be too small to explain observed temperature

changes, and dismissed other diabatic effects along a föhn trajectory as insignificant. As mentioned above, however, across the CI jet the combined diabatic effects dominate over the isentropic drawdown contribution to $\Delta_{LLCP}T$, with the sensible heating contribution being the most significant. Moreover, in Chapter 4 two cases are studied where diabatic effects are generally considerably greater than in the presently studied case.

Whilst the contributions presented in Figure 3.22 provide a handle on the relative importance of the various föhn mechanisms, the simplicity of the model and associated assumptions must be taken into account in its application to a real world case. The relevance of the temperature and pressure at point B (which defines the non-Lagrangian elements of the model) requires that conditions at point B are representative of those of the background flow at this height, or more specifically that point B is where flow would be derived in the hypothetical case of linear flow with no low level blocking. However under such circumstances due to vertical wind shear, the 3-dimensional nature of AP terrain, changing pressure gradients associated with the change in flow regime, and/or other orographic obstacles upwind of the AP such as Adelaide Island, for each trajectory the air at C is unlikely to be derived from directly below A.

It is also worth noting the non-linear relationship between the contributions. A smaller isentropic drawdown contribution is likely to be accompanied by larger latent and/or sensible heating contributions due to greater ascent of cooler moister air. Equally, larger latent and sensible heat release over the AP (due to condensation) would be expected to encourage a lower dividing streamline height (and hence a smaller isentropic drawdown contribution) due to lower static stability in the lower atmosphere (Durran and Klemp, 1982; Barstad et al., 2007). The two diabatic heat mechanisms are also mutually dependant, with a greater contribution from one generally encouraging a smaller contribution from the other.

3.4.4 Flow dynamics above and in the lee of the Peninsula

Figure 3.24 consists of cross sections derived from the MetUM 1.5 km simulation for two transects across the AP. *Transect gap* dissects the WI jet roughly along 67.5 °S whilst *Transect peak* dissects the N of WI wake roughly along 67 °S (Figure 3.17). The cross-Peninsula conditions illustrated in these plots should be

(justifiably, given further analysis not presented) regarded as roughly representative of those across other gap and peak sections of the AP.

Cross sections of wind vectors reveal upwind stagnation below AP crest height (Figure 3.24i), demonstrating the effect of flow blocking upwind of the Peninsula. As shown in Section 3.4.3, it is this blocking and the associated drawdown of air from aloft that is largely responsible for the leeside föhn warming and drying, which is once again evident in Figure 3.24iii and v. The cooler, moister nature of flow passing across and downwind of the gap relative to that of the higher orography (peak) is evident. Upwind inversions are apparent in both transects between ~1400 m and ~1800 m AMSL (Figure 3.24aiv and biv). Whereas across *transect peak* the inversion appears to intercept the orography, across *transect gap* it appears to pass just above the orography. Air flowing across the Peninsula at these locations is evidently more likely to be derived from beneath the upwind inversion in the case of the latter. Indeed trajectory analysis reveals that the vast majority of air making up the WI jet is sourced from beneath 1400 m (Figure 3.21a), whereas only about 50 % of trajectories are sourced below this level in the case of the N of WI wake (Figure 3.20aii and Figure 3.21b).

Cross sections of θ reveal the propagation of a hydrostatic mountain wave above the AP (Figure 3.24iii). As discussed in Section 1.3.2, such waves act to transport vertically the horizontal momentum associated with the drag exerted by the mountain on the flow. The wave is also apparent in the large oscillations in temperature and vertical velocity observed during straight and level flight legs across the AP during the event (not shown). The wave signatures apparent in Figure 3.24ii and iii are complex; the high resolution model is able to reproduce small wavelength horizontally propagating waves as well as vertically propagating modes. This is in contrast to the MetUM 4 km model which does not resolve these waves.
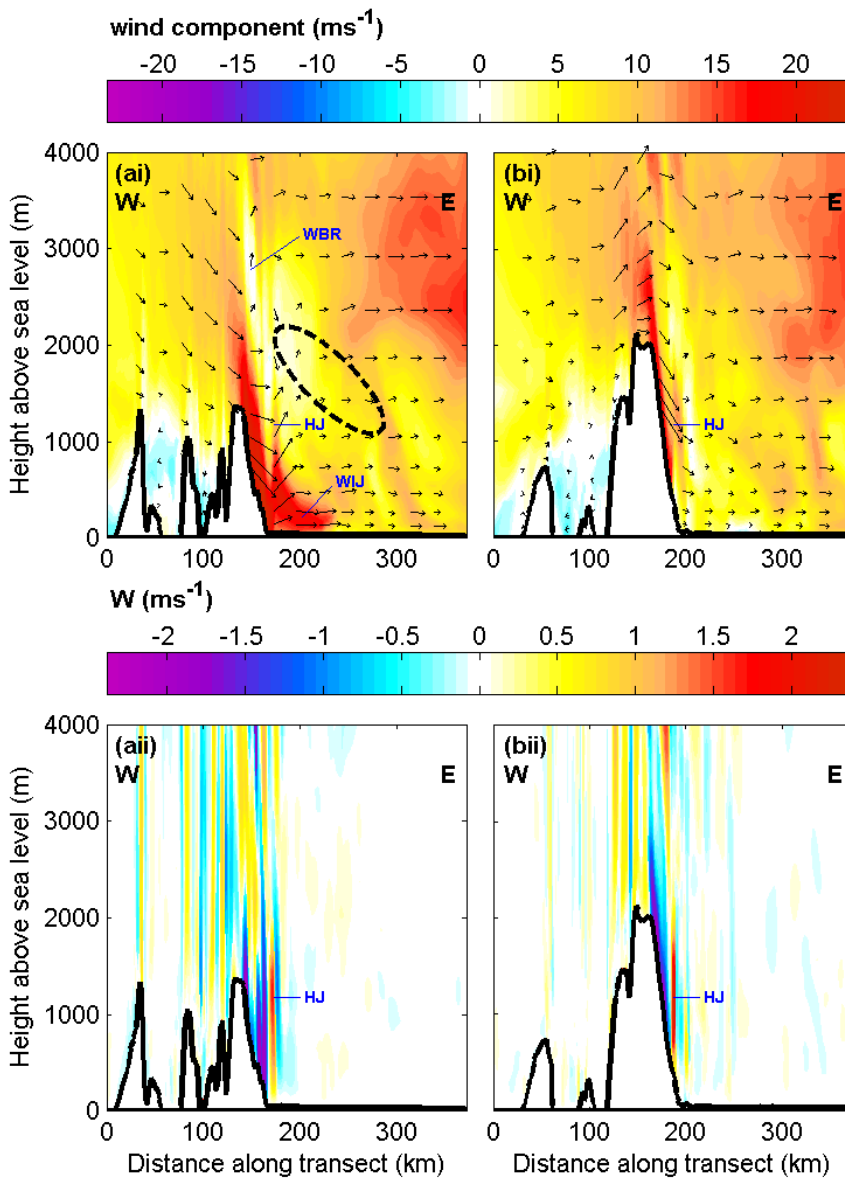
Figure 3.24 [continues to next page]: Cross sections of (i) wind component (colour) and vectors (arrows), (ii) vertical velocity, (iii) θ (contours, spaced at 2 K), (iv) Brunt Väisälä frequency squared (N^2) and TKE (blue contours mark values over 0.1 $m^2 s^{-2}$), and (v) q (contours, spaced at 0.2×10^{-3}) at 10 UTC on 5 February, derived from MetUM 1.5 km data across (a) *transect gap* and (b) *transect peak* (see Figure 3.17 for transect start and end points). HJ = hydraulic jump, WBR = wave braking region, WIJ = Whirlwind Inlet jet. The dashed black ellipse marks the region of isentrope spreading and weak flow discussed in the text. Note that the y-axis in (iii) extends to 6000 m AMSL, whilst all other plots extend to 4000 m. Vertical to horizontal scale of axes = 1:100. Vertical to horizontal scale of arrows in (a) = 1:25.
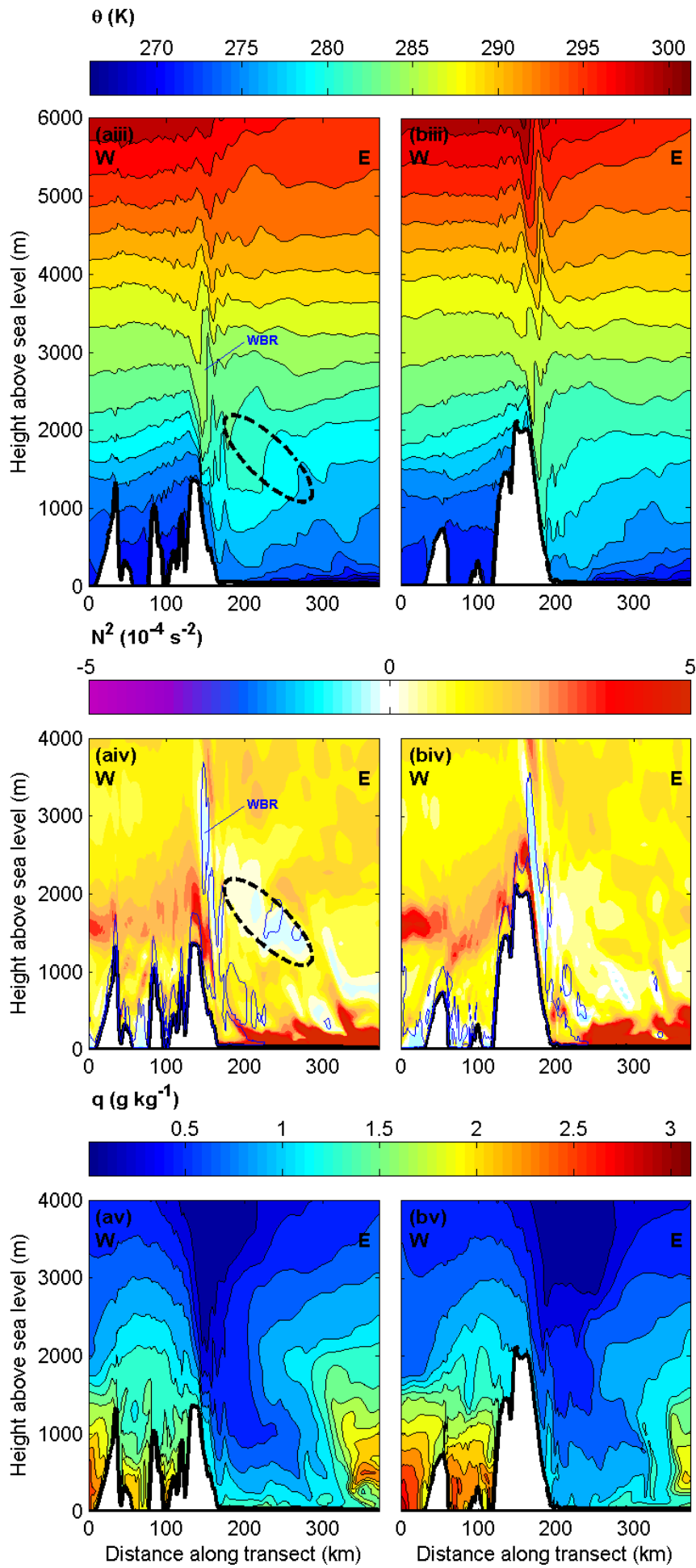
A region of convective instability is simulated in a narrow swath from above the lee slope up to ~3500 m AMSL across both transects (Figure 3.24iv). This region is associated with flow stagnation across *transect gap* and a weakening of horizontal winds across *transect peak* (Figure 3.24i). The stagnation across *transect gap* appears to be associated with wave breaking, implied by the presence of large amounts of TKE (Figure 3.24aiv) and the abrupt decrease in amplitude of the vertically propagating wave apparent in isentrope surfaces above ~3000 m (Figure 3.24aiii). The wave breaking region is marked (WBR) in Figure 3.24i, iii and iv. Along *transect peak* the wave continues to propagate upwards with no clear decrease in amplitude in accordance with the absence of flow stagnation (Figure 3.24biii).

Strong downslope winds (3-dimensional wind vectors reaching speeds in excess of 20 ms^{-1}) are simulated above the lee slope across both transects, though only in the case of *transect gap* does the windstorm reach surface level. In both cases these winds are associated with strongly negative (downward) vertical velocities (w < -2 ms^{-1}).

Along *transect peak*, descending air extends only part way down the lee slope; a vertical band of positive w (> 2 ms^{-1}) prevents downslope flow penetrating further (Figure 3.24bii). This region of ascent resembles a hydraulic jump, associated with a transition from super- to subcritical flow regimes (refer to Section 1.4.1.2). Isentropes are found to incline steeply downwards and then steeply upwards in the downwind direction within the immediate lee of the AP along *transect peak* (Figure 3.24biii); reflecting the descent of potentially warm air from aloft, followed by its subsequent re-ascent. Downwind of the jump the strong downslope winds dissipate, though continued weaker descent acts to transport föhn air towards near-surface level (Figure 3.24bi and bii).

A hydraulic jump is also simulated along *transect gap*, though this time at the base of the lee slope (Figure 3.24aii). According to the magnitude of w and reduced isentropic displacement, this jump is weaker than that across *transect peak*. Furthermore, the downslope jet passes below the region of greatest ascent (Figure 3.24ai). The jump is followed downwind by resumed descent, the flow largely maintaining momentum (due to a preservation of Bernoulli function and/or flow convergence within WI) to culminate in a low level jet above the Larsen C (the WI polar föhn jet; Figure 3.24ai).

Pan and Smith (1999) found that flow over high terrain was accelerated more than flow through gaps, encouraging the transition from subcritical to supercritical flow and so enhancing the likelihood or relative strength of a leeside hydraulic jump. Whilst the stronger hydraulic jump is indeed found along *transect peak*, wind speeds are in fact marginally stronger above the gap. This apparent contradiction may be reconciled by the difference in depth of the downslope flows. Assuming similar flow speed, the greater depth of flow downwind of the gap will, according to equation [1.14], induce a smaller Froude number, resulting in flow less supercritical in nature and consequently (assuming a transition from subcritical to supercritical flow somewhere across the AP) a delayed (further down the lee slope) and weaker hydraulic jump required to return flow to a subcritical state.

Along both transects the most significant low-level leeside warming is, as has been mentioned previously in relation to both model and observational data, located within 50 km east of the base of the AP's lee slope (Figure 3.24iii). Further east a surface inversion resides, strengthening and deepening eastwards. As indicated by the region of TKE at the base of the lee slope (Figure 3.24iv), it would appear that this warm region is kept well mixed by the turbulent föhn, preventing the establishment of the stable boundary layer. Hoinka (1985) described a similar low level turbulence zone in the immediate lee of Alpine mountains during a southerly föhn.

Above the WI jet a region of weak to negative stability (isentrope spreading) and weak flow is found (within the dashed black ellipse marked in Figure 3.24i, iii, and iv). This feature is similar to that observed by Smith (1987) in his study of the Yugoslavian Bora; appearing to 'fill the gap' between the bora wind and the relatively undisturbed air above. Isentrope spreading in the equivalent region has been observed elsewhere, for example in the case of the Boulder Windstorm (Lilly, 1978; see Figure 1.9a). Indeed the interpretation presented here for flow across the AP in the case of *transect gap* i.e. the 'seeping' of relatively cool air derived from low levels beneath an upwind inversion over an obstacle, has some similarities with the bora mechanism. However, in contrast to a typical bora, the flow in our case induces a background leeside warming as it replaces cooler air overlying the ice shelf.

3.5 Synthesis of findings

A westerly föhn event during the period 4 – 5 February 2011 has been documented via aircraft measurements and model output from a MetUM simulation. The event is characterised by predominantly southwesterly to westerly flow with an estimated minimum simulated $\hat{h}$ of between 2.0 and 2.7.

The model analysis of upwind conditions is largely backed up by observations; the wind field appears to have been well captured by both 1.5 and 4 km models, though stability below 2000 m is overestimated. The similarity in the reproduction of upwind conditions by the 1.5 and 4 km models is perhaps unsurprising since the maritime conditions to the west of the AP during westerly flow within the limited 1.5 km domain used here will have experienced little influence by the effects of complex orography (for which the improvement in accuracy attained by the higher resolution model is partly dependent upon).

The ensuing flow regime is characterised by flow blocking, probable mountain wave breaking at relatively low levels above the AP, and strong downslope winds on the leeside. Such non-linear phenomena are consistent with the partially blocked, high-drag flow regime implied by estimations of upwind $\hat{h}$, a strong cross-barrier pressure gradient and the appearance of a weak, roughly crest-level inversion in some regions upwind of the AP. All four 'ingredients' common to the occurrence of downslope windstorms in the lee of the Cascade Mountains according to Colle and Mass (1998) – as discussed in Section 1.4.1.1 – are present in this case.

Observational and model data reveal the encroachment of warm föhn air above the Larsen C from the west, bringing about a reversal in the cross-Peninsula temperature gradient (Figure 3.8a and Figure 3.9a show θ profiles before and during the föhn event). The most significant warming is found at the base of the lee slopes (Figure 3.9a and Figure 3.17bi), where the advective warming and turbulent mixing induced by the föhn dominates over cooling by loss of heat to the ice surface (investigated further in Chapter 5). Indeed, close to the Peninsula's eastern slopes downwind of a high section of the AP, near-surface temperatures (as measured at the lowest flight levels) are found to increase by ~3.5 K during 3 consecutive flights (flights 174, 175 and 176) over an 18 hour period despite the effect of nocturnal cooling amid the latter 2 flights. In contrast, further east across the Larsen C a deep surface

inversion forms during the night, such that a lowest flight level temperature gradient of ~10°C between a point ~30 km east of the base of the AP's eastern slopes and a point ~60 km further east is observed (Figure 3.10aii). As mentioned in Section 1.4.4.1, Hoinka (1985) found that whilst a hydraulic jump downwind of the mountain barrier during an alpine föhn limited the downwind reach of the strong winds, the föhn warming and drying effect extended considerably further downwind; and was detected up to 100 km away from the barrier. A key difference in our case is the presence of the cool ice surface. The weak föhn downwind of the turbulent region appears unable to penetrate through or mix the strongly stable layer generated by nocturnal cooling during the föhn event. It is pertinent to note that whilst at low level in this region no cross-Peninsula θ gradient is apparent, the leeside warming remains apparent higher in the atmosphere where nocturnal cooling is considerably weaker (Figure 3.24iii).

Flight 177 observations together with model analysis show that by early afternoon of 5 February, the stable boundary layer above the Larsen C had weakened considerably. Despite this there remains a west-east temperature gradient (~3°C between a point ~30 km east of the base of the AP's eastern slopes and a point ~60 km further east) above the Larsen C (Figure 3.14aii) and near-surface temperatures remain below 0°C across the majority of the Ice Shelf.

The MetUM 1.5 km generally performs well in its reproduction of leeside conditions during the föhn event, with some caveats. Over the course of the first three flights it overestimates temperatures and underestimates humidities, the discrepancy generally increasing towards the surface. This appears to be at least partly due to the premature incursion of downslope flow across the Larsen C. The model also insufficiently reproduces the strength and depth of the nighttime inversion above the eastern reaches of the Larsen C during flight 176. Otherwise the model reproduces leeside temperatures with reasonable accuracy (within 2 K).

In the immediate lee of the AP a series of jets, here called 'polar föhn jets', are simulated to emerge from the mouths of major Inlets. The approximate position and strength of one of these jets – the Whirlwind Inlet jet – is verified by flight observations (Figure 3.11, Figure 3.12a and Figure 3.14i). The jet was found to extend to near-surface level and be characterised by gusty westerly winds reaching speeds in excess of 20 ms^{-1}.

Conditions within the jets, whilst warmer and drier than those upwind and further east above the Larsen C, are moister and cooler than those in the adjacent wake regions. With the aid of back trajectory analysis using the MetUM 1.5 km data it has been established that air within the jets originates from lower altitudes upwind of the AP and crosses above lower sections of the AP than the air comprising the wake regions. As such, these jets appear to be the downwind continuation of gap winds across the Peninsula. Due to the potentially cooler, moister nature of the maritime air found at lower levels upwind, it is the difference in föhn source altitude that is largely responsible for the cool, moist signature of the jets relative to the wakes (as demonstrated in Figure 3.22), although diabatic processes can also dominate. This finding, together with the appearance in the model of isentrope spreading and near stagnation above the jet provokes comparison to the Bora wind of Eastern Europe; although the analogy does not extent to leeside temperature change (a Bora being defined with leeside cooling rather than warming).

To the south of the Avery Plateau (i.e. south of ~67°S) the Peninsula is aligned largely perpendicular to the approaching southwesterly to westerly flow which dominated during the föhn event. As pointed out by Colle and Mass (1998) in their study of windstorms in the Cascade Mountains, under such circumstances it is difficult to evaluate the relative contributions of the pressure gradient induced gap flow mechanism and the mountain wave induced downslope windstorm mechanism towards the acceleration of flow through the passes. In the case of the pass above Cabinet Inlet to the north, flow was simulated to change direction quite considerably from its upwind trajectory to pass across the AP. In this case the pressure gradient is likely to be the dominant forcing.

Though strong föhn winds persist eastwards above the Larsen C, the jets become less distinct and the flow becomes increasingly geostrophic (turning left to become more southerly; Figure 3.17a) as the influence of the AP's orography subsides. Here the flow tends to rise steadily above the surface inversion, whose strength and depth increases eastwards. The resulting inversion-capping jets resemble the low level jet observed and modelled on the Larsen C during a föhn event in 2006 by King et al. (2008), discussed in Section 2.2.1. With limited available data, King et al. were unable to identify the mechanisms responsible for the jet, though inferred a likely combination of both synoptic and orographic forcing. A model simulation of their case

study revealed a high pressure ridge positioned to the west of the AP and a mesoscale low pressure system centred around 68°S, 55°W, matching closely the positioning of the simulated low pressure system in the present case illustrated in Figure 3.4. The apparent similarity in synoptic pressure patterns between the two cases and the occurrence of analogous inversion-capping southerly to southwesterly jets towards the northeastern reaches of the Larsen C suggest a common mechanism is likely. The account given here of the jet being a result of geostrophic adjustment of westerly föhn jets support King et al.'s inference.

Downwind of higher sections of the AP a downslope windstorm is simulated to extend part way down the lee slope before a strong hydraulic jump returns flow upwards, resulting in near-separation of the boundary layer (Figure 3.24bii). Consistent with energy dissipation and Bernoulli loss imparted by turbulence in the vicinity of the hydraulic jump, the strong winds are considerably weakened in its lee. Weak descending föhn flow continues to the Larsen C at the base of the lee slope, to form the 'wake' regions, advecting in relatively warm and dry air sourced from comparatively high altitudes upwind of the AP. Although hydraulic jumps are also apparent downwind of lower sections of terrain (gaps), here the associated vertical velocities are considerably smaller at low level (within the jet) and the strong winds are able to largely maintain their momentum, becoming evident on the Larsen C as the polar föhn jets.

Using trajectory analysis and a simple 2-dimensional temperature budget model the contributions of the various mechanisms responsible for the föhn warming effect (defined here as the cross-Peninsula temperature gradient) have been quantified. The results show the dominant mechanism to be the drawdown of potentially warm air from aloft, although diabatic processes (in one instance signifiantly) and the cross-Peninsula pressure gradient also make contributions to the temperature budget (Figure 3.22). This is consistent with the nature of the upwind flow; the relatively large upwind $\hat{h}$ and elevated inversion being associated with low-level blocking. Only in the case of the Cabinet Inlet jet is isentropic drawdown not the dominant föhn mechanism. Here the föhn is simulated to have been sourced from lower upwind altitudes than elsewhere. The greater ascent of flow above the windward slopes leads to greater latent heat gain due to condensation leading to orographic precipitation and greater sensible heat gain due to turbulent mixing.

3.6 Summary and implications

- A westerly föhn event, associated with leeside warming and drying, is documented by observational and model data.

- Both MetUM 4 and 1.5 km models reproduce the upwind wind field to a high level of accuracy, whilst overestimating upwind stability.

- In its reproduction of downwind conditions, the MetUM 1.5 km performs sufficiently well to justify the contribution of its results towards the understanding of the dynamics of the föhn event.

- The föhn effect is considerably stronger close to the AP than further east above the Larsen C. This appears (confirmed in Chapter 5) to be due to mixing by the descending föhn close to the Peninsula preventing the formation of a stable boundary layer. Downwind re-ascent of föhn air and increasingly laminar flow encourage stratification and the development of a deep near-surface temperature inversion. For this reason, a high amplitude diurnal temperature cycle is observed and modelled across most of the Larsen C, whereas it is obscured completely close to the base of the lee slope within regions of near-stagnant flow. This characteristic is studied further in Chapter 5.

- The near-surface flow field immediately to the east of the AP consists of jets emanating from the mouths of inlets, separated by regions of calmer flow (wakes). The jets are the downwind continuation of gap flows across lower sections of the AP's ridge and, on account of the constituent air being sourced from lower altitudes upwind of the AP, generally exhibit cooler and moister conditions than the wake regions.

- According to a temperature budget model following trajectories, the dominant mechanism responsible for the föhn warming effect is the differential advection of potentially warm air from high altitude upwind of the AP. Only for one of the sample regions – the Cabinet Inlet jet – is this not the case. Here, sensible heating due to turbulent mixing provides the greatest warming contribution. Up until now in the literature this föhn warming mechanism has either been overlooked or deemed to be insignificant in its contribution towards leeside warming during a föhn event.

Chapter 4

Consistency and variability in leeside response to differing cases of cross-Peninsula westerly flow

Contents

List of figures

List of tables

4.1 Introduction

In chapter 3 a westerly föhn event between 4 and 6 February 2011 (from here on referred to as *Case A*) was examined using data from aircraft observations and MetUM simulations. Warming and drying to the east of the AP was found to be most significant close to the base of the lee slope, whilst a deeper stable layer prevailed above the Larsen C to the east. The case was characterised by non-linear flow features such as upwind blocking, wave breaking and a stationary hydraulic jump. Strong jets emerged from the mouths of inlets as the downwind continuation of gap flows. Being derived from lower altitudes upwind of the AP (above the Bellingshausen Sea), air within these jets was found to be cooler and moister than that within adjacent wake regions. In this chapter these findings and dynamical interpretations will be examined and developed upon via the analysis of two further cases of westerly föhn across the AP. Furthermore, the effect of changes in the value of $\hat{h}$ (the non-dimensional mountain height) and vertical atmospheric structure on downwind conditions will be considered.

The first case dealt with in this chapter (*Case B*) occurred between 26 and 28 January 2011 – a few days prior to *Case A* – and is similarly documented by MASIN aircraft data as part of the OFCAP field campaign, and also by radiosonde data from balloons launched from the Larsen Camp (Figure 4.1). The second case (*Case C*) was far more prolonged than the other cases, occurring earlier during the same summer period, with broadly north-westerly flow for over a month during October – November 2010. With no airborne observational data available for this period, MetUM data alone is used to examine in detail a 2-day long portion towards the end of the period of föhn flow (15 to 17 November 2010). The validation work presented in Sections 3.3 and 4.2.2 for the most part shows that the MetUM 1.5 km performs very well in reproducing the key features of föhn flow across the AP. For this reason, it seems reasonable to draw dynamical conclusions direct from the *Case C* simulation. Some caution should be applied however, since as is revealed below, there are significant differences between all three cases, *Case C* being the most distinct. In Chapter 5 some model validation against AWS observations for *Case C* is presented.
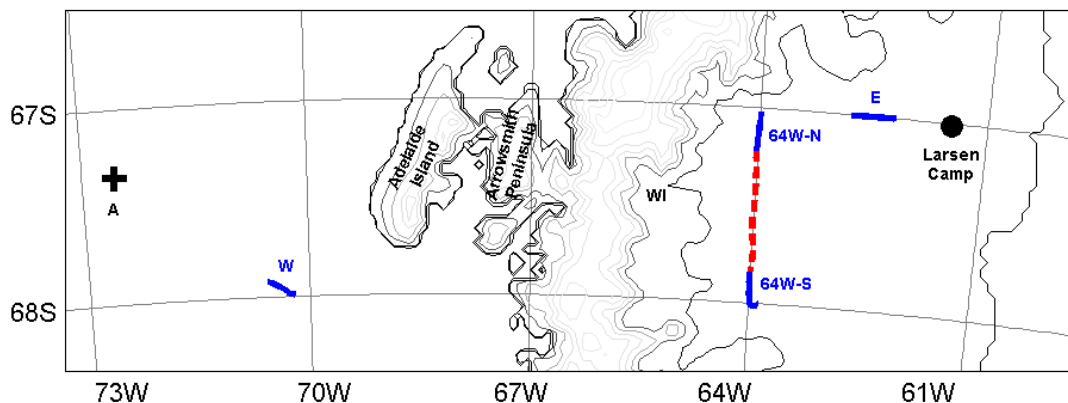
Figure 4.1: Map showing key locations, the relevant flight tracks of MASIN flight 162 during the afternoon of 27 January (including profiles as blue lines and the ST leg as a red dashed line), the location (*Location A*; black cross) 150km roughly west of the west coast of Adelaide Island used to gauge upwind conditions in Figure 4.3 and AP surface height and land-sea mask derived from MetUM 1.5 km orography data. WI = Whirlwind Inlet.

4.2 Case B: 26-28 January 2011

4.2.1 Synoptic conditions and upwind flow

At 12 UTC on 26 January 2011 ECMWF ERA Interim Reanalyses show relatively low pressure to the east and a ridge to the west of the AP bringing southwesterly flow to the Peninsula (Figure 4.2a). As the ridge migrates eastward flow becomes more westerly with a stronger cross-Peninsula component in the vicinity of the Larsen C (Figure 4.2b). By the afternoon of 28 January a new low pressure system has moved in from the west, associated initially with a weakening of westerlies (Figure 4.2c) and eventually the incursion of northerly flow into the region.

A cross-Peninsula pressure gradient is apparent, peaking at ~6.5 hPa/100 km at about 12 UTC on 27 January according to the MetUM 1.5 km. Note this is smaller than the equivalent peak value during *Case A* of ~8.5 hPa/100 km. In both cases these values correspond approximately with peak cross-Peninsula flow.
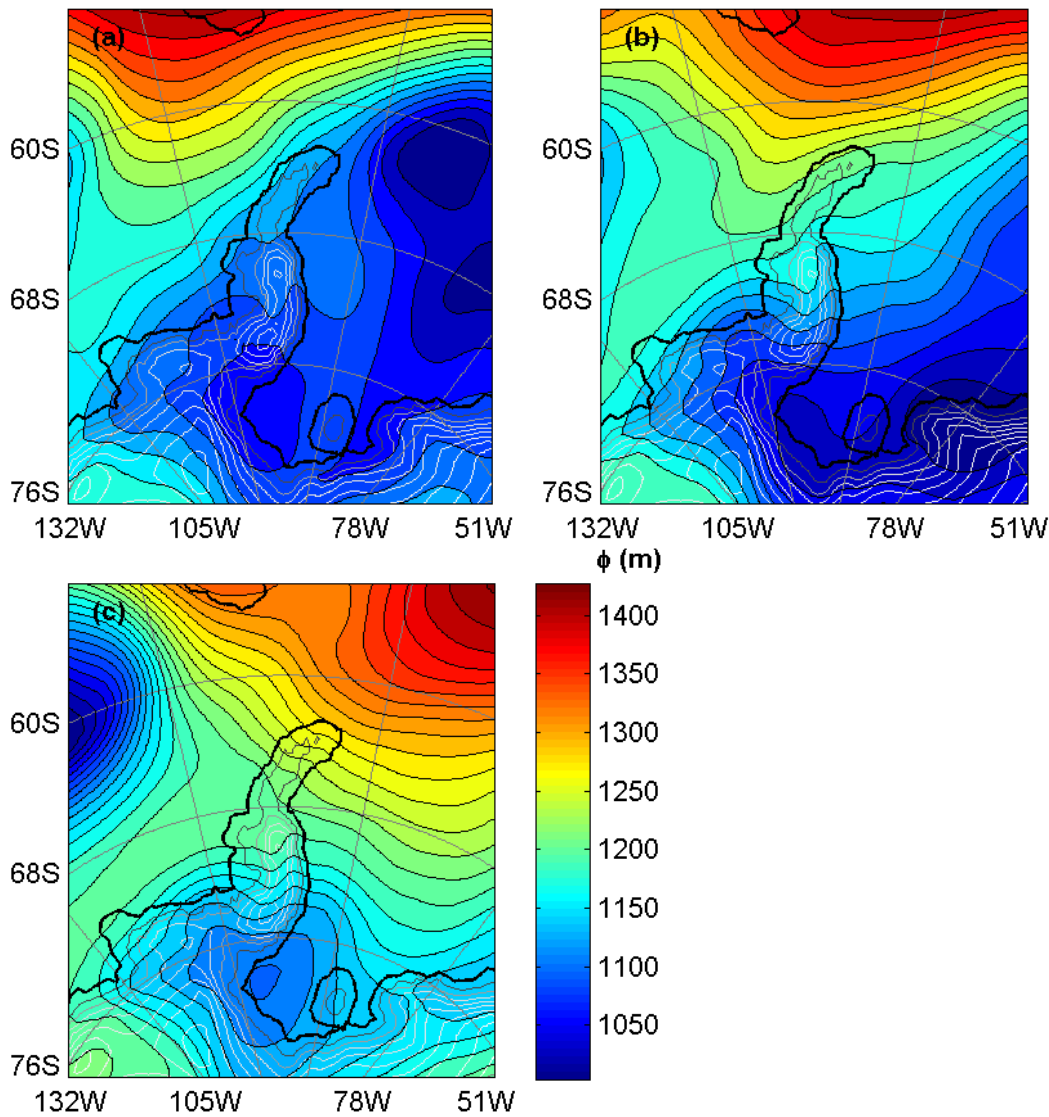
Figure 4.2: Geopotential height (contours, spaced at 15m) at the 850mb level at (a) 12 UTC 26 January, (b) 12 UTC 27 January and (c) 12 UTC 28 January 2011 in the vicinity of the AP during Case B from ECMWF ERA-Interim. The land-sea mask and surface height contours are also plotted.

Figure 4.3 documents upwind conditions for the duration of *Case B* and corresponds to an equivalent plot for *Case A* (Figure 3.6). Figure 4.3a shows that flow direction 150 km upwind is consistently between south westerly and north westerly throughout the simulation period (between 18 UTC on 26 January and 12 UTC on 28 January). Relatively low wind speeds are simulated, peaking at ~8 ms^{-1} at the beginning of the simulation and gradually decreasing thereafter. Westerly $\hat{h}$ reaches a minimum of 3.2 (corresponding to z_d of 938 m) at 6 UTC 27 January when wind direction is south westerly and non-directional $\hat{h}$ is 2.7 (z_d of 833 m) (Figure 4.3b). These values are a little larger than those relating to *Case A*, though cross-Peninsula flow persists for longer with westerly $\hat{h}$ residing below 4 for longer than 24 hours ($\hat{h}$

falls below 4 before the beginning of the simulation), as opposed to just 12 hours in
Case A.
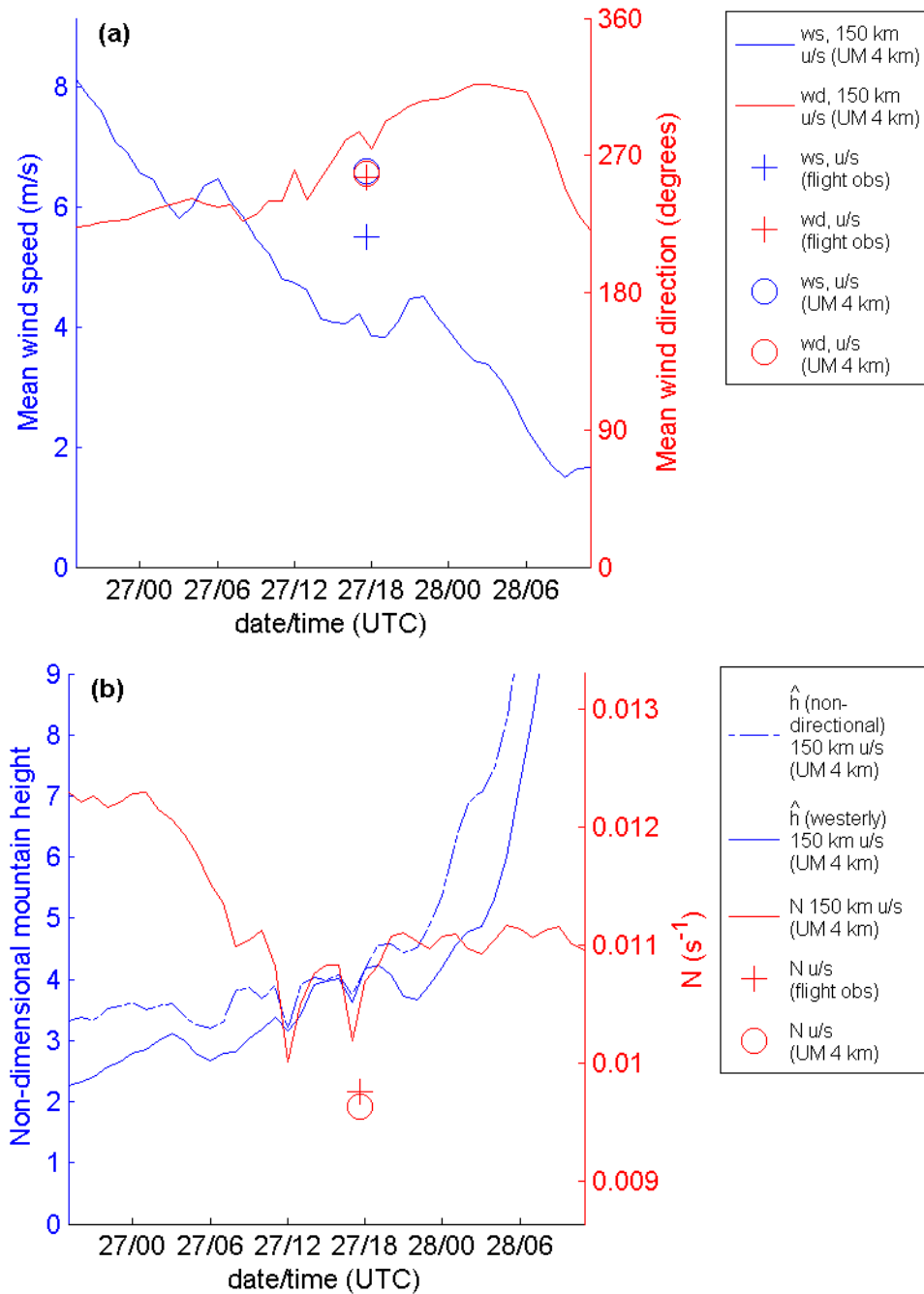
Figure 4.3: Plots of upwind (a) wind speed and direction and (b) Brunt Väisälä frequency and non-dimensional mountain height (ĥ) during Case B. All values are vertical averages (between 200-2000m) from (i) aircraft data for the MASIN flight 162 upwind ('+' symbols); (ii) MetUM 4 km data interpolated to the flight track ('o' symbols) and (iii) a vertical profile of MetUM 4 km data roughly 150km west of the AP (see Figure 4.1; solid lines). Both westerly (solid/dashed line) and non-directional (solid line) ĥ are shown. In the figure legends, ws = wind speed, wd = wind direction, u/s = upstream.

One flight (MASIN flight 162) provides upwind observations within Marguerite Bay on the afternoon of 27 January (see Figure 4.1 for the flight track for this portion of the flight). As in *Case A* equivalent values derived from the MetUM 4 km (the flight leg is outside of the MetUM 1.5 km domain) compare well with the aircraft measurements (Figure 4.3).

4.2.2 Leeside response in observations and MetUM validation

In addition to MASIN aircraft observations, data from radiosondes launched from Larsen Camp (location shown in Figure 4.1) are available for *Case B*. Figure 4.4 consists of a time series from successive radiosonde flights. The development of föhn conditions here reflects the evolution of upwind conditions described in Section 4.2.1.

During the evening of 26 January largely stagnant conditions were observed at low level above Larsen Camp, with moderate westerlies above (Figure 4.4ai). By 12 UTC on 27 January the westerlies have extended to near-surface level, accompanied by warming and drying below ~1300 m. Westerlies persist, as does the warming and drying effect above 100 m, until the morning of 28 January when near-stagnation returns to low levels. Below 100 m the diurnal cycle is evident in temperature and humidity at the lowest levels, with a particularly deep stable boundary layer – common for conditions during weak föhn at night on the Larsen due to longwave radiative heat loss owing to clear skies (as discussed in Chapter 2) – present during the early morning of 28 January. On the evening of 28 January a shift in circulation occurs as the arrival of the new low pressure system illustrated in Figure 4.2c brings in stronger northerly flow associated with warmer and moister air.

The MetUM 1.5km appears to simulate, to a relatively good degree of accuracy, the major developments above Larsen Camp throughout the period of radiosonde measurements (Figure 4.4b). Note that this method of comparison does not account for horizontal drift of the radiosondes during flight, and that the final two radiosonde flights fall outside the time period covered by the simulation.
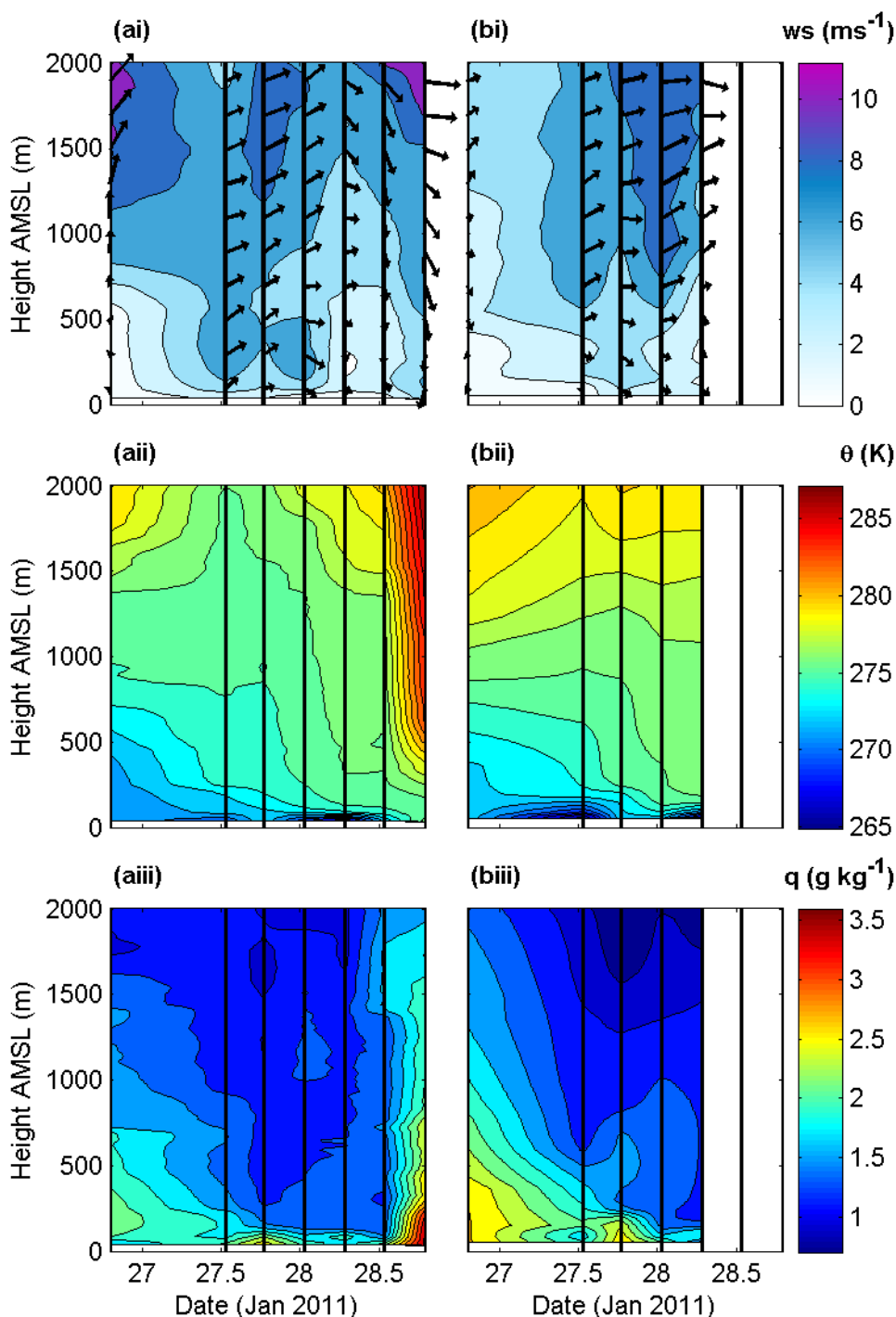
Figure 4.4: Time series of (i) wind speed (contours) and direction (vectors), (ii) potential temperature (θ) and (iii) specific humidity (*q*) constructed from (a) measurements made by radiosondes launched from Larsen Camp during Case B and (b) vertical profiles of MetUM 1.5 km data above Larsen camp at the same time. The vertical black lines indicate the times of radiosonde flights. Data between these times are interpolated between consecutive sets of radiosonde data.

The föhn effect is evident in MASIN Flight 162 profiles, constructed from measurements made on the afternoon of 27 January (see Figure 4.1 for flight tracks). In Figure 4.5 an upwind profile (*profile W*) is presented alongside three downwind profiles: two ~100 km apart along 64 °W (*profiles 64W-S* and *64W-N*) and one further

east a little to the west of Larsen Camp (*profile E*). On both sides of the Peninsula flow has a significant westerly component. Temperatures on the leeside are significantly higher (between ~3.5 and ~6 °C at the same level under 1500 m) than those to the west of the AP. Closer to the Peninsula along 64 °W temperatures are, for the most part, marginally warmer than further east across the Larsen. The exception is below ~300 m in the case of the northern profile on 64°W, where relatively statically stable conditions not found in the southern 64 °W profile are observed. Winds for this portion of the profile are weak and back such that at 300 m flow is westerly whilst at near surface they are northerly, whereas to the south winds are largely stronger and broadly westerly.
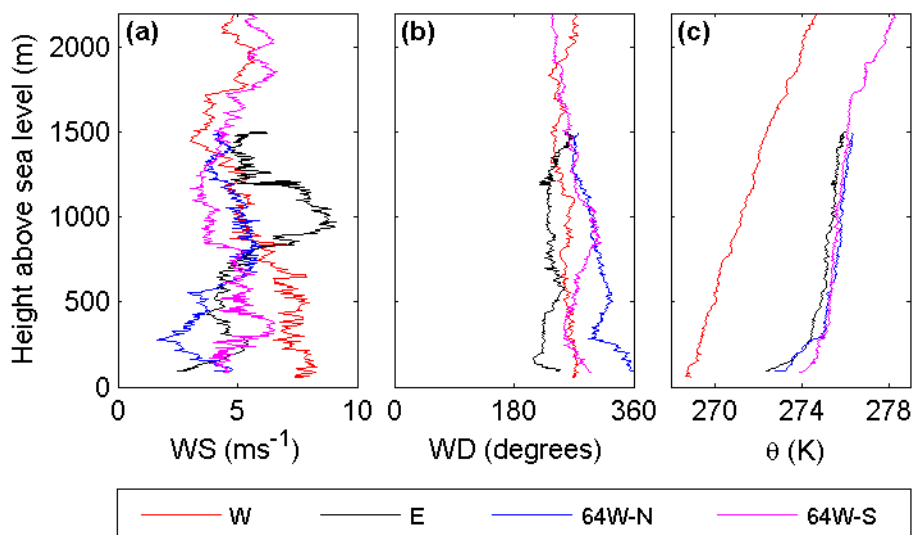
Figure 4.5: (a) Wind speed (WS), (b) wind direction (WD) and (c) θ derived from the four profiles (flight tracks marked on Figure 4.1) of MASIN flight 162: an upwind profile to the west of the AP (W), and three downwind profiles (one roughly midway across the Larsen C on 67 °S (E), and two closer to the Peninsula (64W-N and 64W-S)).

As in *Case A* westerly 'polar föhn' jets were observed close to the base of the AP's eastern slopes. Figure 4.6a shows wind speed interpolated from a saw-tooth leg made during MASIN Flight 162 as the aircraft was flying south along ~64 °W east of Whirlwind Inlet (see Figure 4.1 for flight track). Similar to the jet evident downwind of Whirlwind Inlet during *Case A* (Figure 3.11), peak wind speeds are observed at relatively low level above the ice shelf, below 500 m. The MetUM 1.5 km captures the structure and magnitude of this jet reasonably well, though with peak wind speeds occurring at higher altitude and further south (Figure 4.6b). It should be noted that, in consideration of the weak nature of this föhn event, due to being too far downwind of the AP (where the air to either side of the jet is less warm than close to the Peninsula

within the wakes), the jet does not exhibit a distinct cool and moist signature along this flight transect in either the observations or the model.
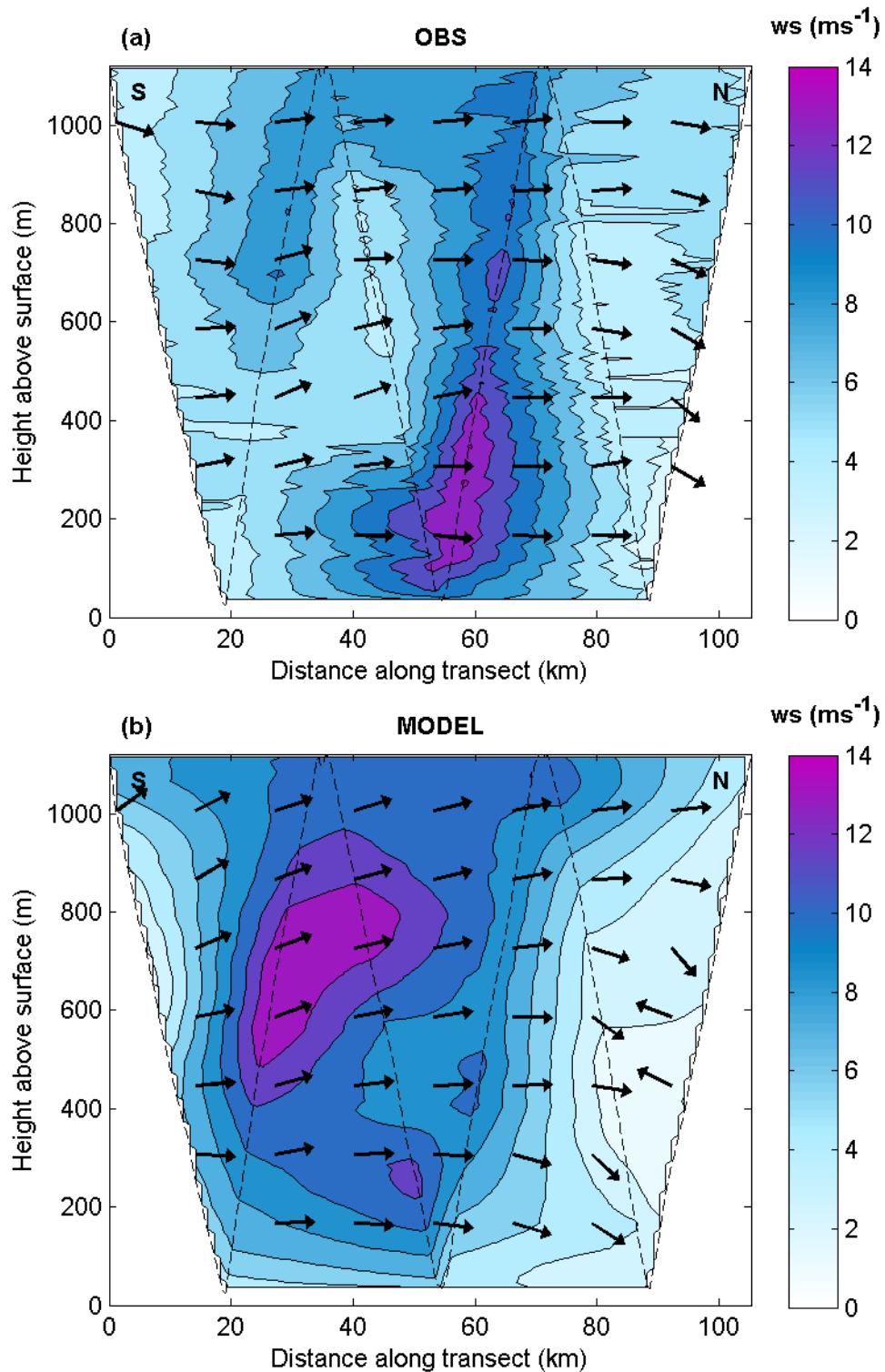
Figure 4.6: Wind speed (contours, spaced at 1.5 ms^{-1}) and wind direction (arrows; the bearing of which denotes the horizontal direction of flow from North) cross sections for the ST leg of flight 162 on the afternoon of 27 January from (a) observations and (b) model. The x-axis is the distance along the transect (see Figure 4.1 for flight tracks) from the most southerly point.

4.2.3 Leeside response in the model

4.2.3.1 Föhn conditions and the wind field above the Larsen C

The key features of the simulated wind field at 150 metres above mean sea level (AMSL) during *Case B* (at 00 UTC 28 January; the end of the first full day föhn) qualitatively resemble those of *Case A*. Distinct, broadly westerly Jets emanate from the mouths of inlets, maintaining momentum for a great distance downwind (Figure 4.7a). The strongest winds are simulated within Cabinet Inlet, whilst the Whirlwind Inlet jet and the other jets south of 67 °S are generally a little weaker than in *Case A*.

Figure 4.7bi and ci illustrate the föhn effect, with temperatures (humidities) higher (lower) downwind of the AP. The föhn clearance is apparent in Figure 4.8a and b. There is no clear west-east temperature gradient apparent in Figure 4.7bi, in contrast to the equivalent plot for *Case A* (Figure 3.17bi), in which temperatures are considerably warmer at the base of the lee slope than further east. This is further investigated in Section 4.2.4. Earlier, during the afternoon of 27 January (~16 UTC), aircraft observations did suggest a west-east temperature gradient, albeit a relatively weak one which was not apparent below 300 m in relation to *profile 64W-N*. Model data (not presented) for this time agrees, revealing a weak and in places indistinct west-east cross-Larsen C temperature gradient not apparent at 00 UTC 28 January.

Cross sections across the same three jets considered for *Case A* reveal a similar pattern; conditions within the jets are for the most part cooler and moister than within neighbouring wake regions (Figure 4.7ii-iv). This is most apparent for the Whirlwind Inlet cross section. Across Mobil Oil Inlet, whilst the coolest moistest air is found distinctly within the jet at near surface level, higher up the relationship is not apparent. Indeed perhaps a more fitting account for the variability in temperature and humidity would be that cooler, moister conditions are simulated downwind of the inlets, but, perhaps as a result of the complex orography, not necessarily directly coincident with the jets.

Although exhibiting a locally distinct cool and moist signature, conditions within the Cabinet Inlet jet are in fact drier than the air within the wake region to the south (Figure 4.7civ). This discrepancy is investigated using back trajectory analysis in the next section.
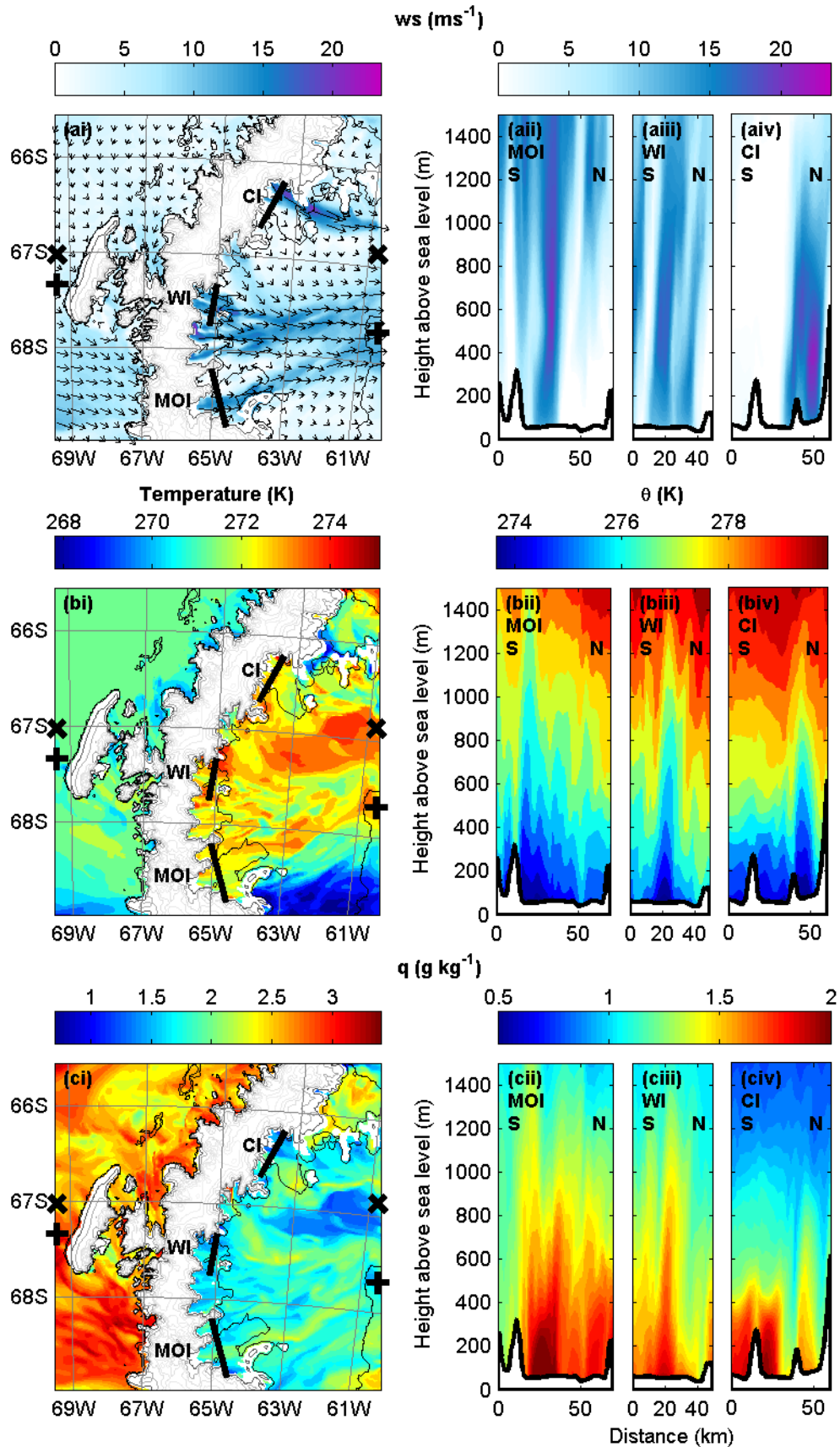
Figure 4.7: (a) Wind speed (contours, in ms^{-1}; transect-normal component in cross sections) and vectors (arrows), (bi) temperature (K), (bii-iv) θ (K), and (c) specific humidity (*q*) in the form of (i) plan plots at 150m above mean sea level and jet cross sections across (ii) Mobil Oil Inlet (MOI), (iii) Whirlwind Inlet (WI), and (iv) Cabinet Inlet (CI) during Case B at 00 UTC on 28 January 2011 from the MetUM 1.5 km simulation. Transect lines are marked and labelled on

the plan plots. Also marked are the start/end points of *transect gap* ('+'s) and *transect peak* ('x's) used for the cross sections of Figure 4.13. Vertical to horizontal scale of transect plot axes = 1:100.
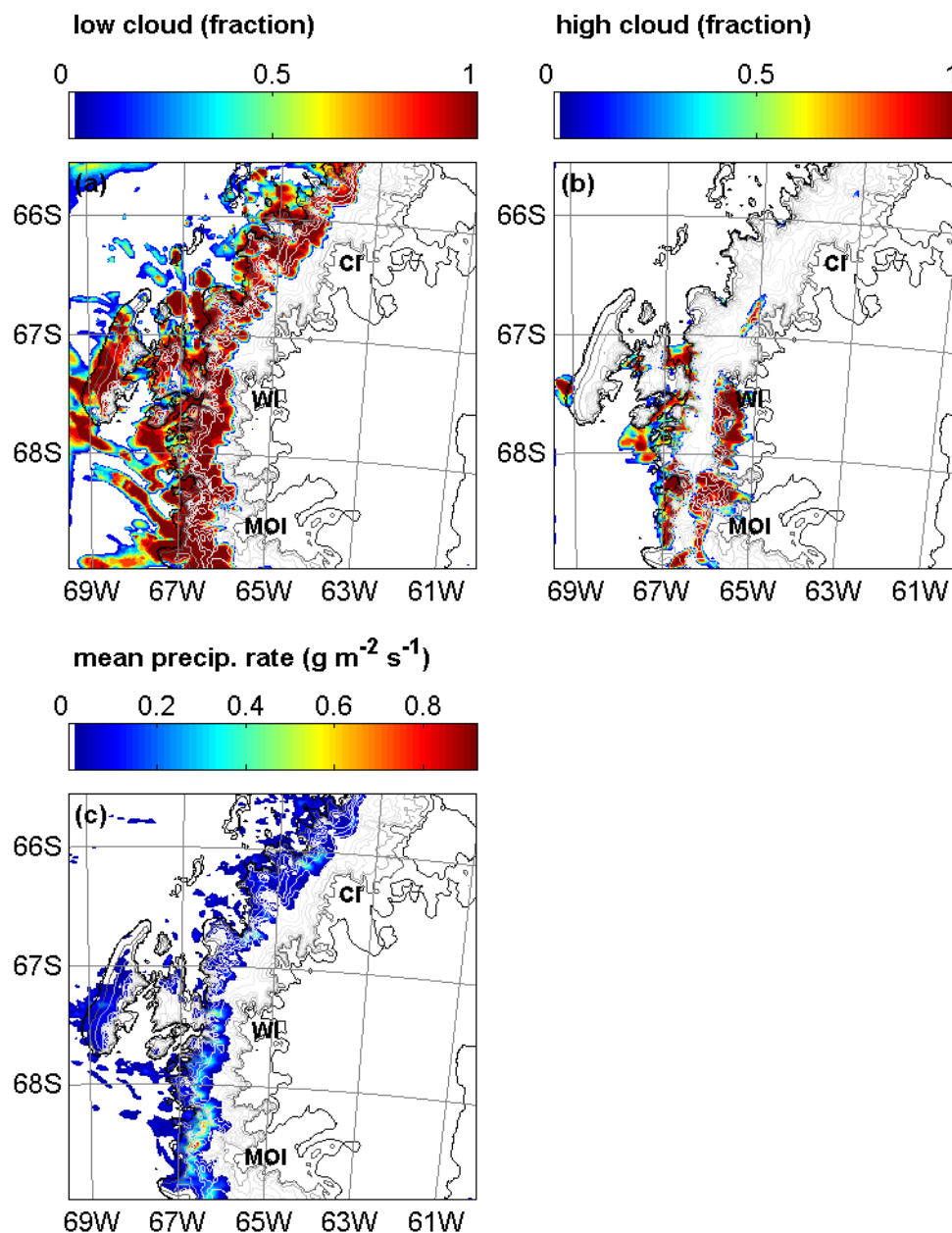
Figure 4.8: (a) Low level (below ~2000 m above the surface) and (b) high level (over ~2000 m above the surface) cloud fraction at 00 UTC 28 January during *Case B*, and (c) mean precipitation rate between 12 UTC 27 January and 00 UTC 28 January from the MetUM 1.5 km simulation (see Figure 3.16's caption for further details).

4.2.3.2 Cross-Peninsula flow

As in Chapter 3, Lagranto is employed to derive flow trajectories across the Peninsula. For *Case B* the trajectories are initiated at 00 UTC 28 January at the 950 hPa level, which matches the time used for the plots of Figure 4.7. Roughly the same sample regions for the initiation of trajectories as those defined for *Case A* are used

here to compare the upwind trajectories of air parcels within jets with those within wakes (Figure 4.9). This figure – equivalent to Figure 4.7a – clearly illustrates the simulated polar föhn jets over the Larsen C. The results, averaged over all relevant trajectories, are illustrated in Figure 4.10. These largely agree with the inference drawn from chapter 3; that the jets are gap winds comprising air which has crossed low sections of the Peninsula and is sourced from low altitudes upwind relative to the air within the wakes. The difference in upwind temperatures is greatest for WI and N of WI.
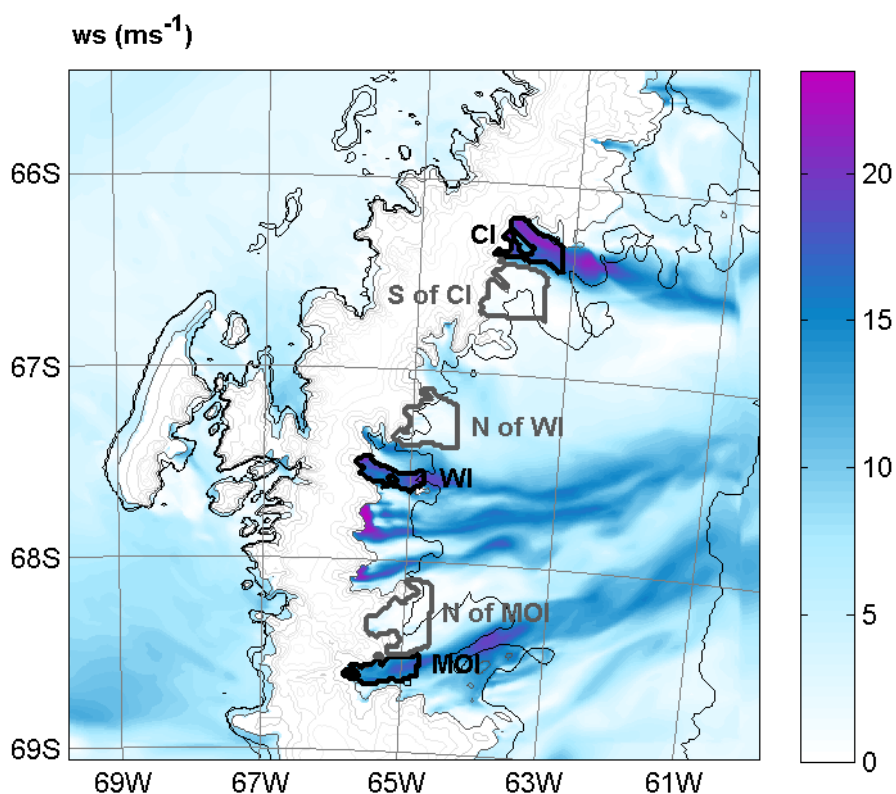
Figure 4.9: Initiation regions for the trajectory analysis of Case B, overlaying a map of wind speed (ms^{-1}) at 150m AMSL at the time of back trajectory initiation (00 UTC 28 January 2011). Black boundaries enclose 'jet' regions (associated with wind speeds in excess of 15ms^{-1}), whilst grey boundaries enclose 'wake' regions (associated with wind speeds less than 5ms^{-1}). MOI = Mobile Oil Inlet, WI = Whirlwind Inlet, CI = Cabinet Inlet.

WI (>15 ms^{-1}) - N of WI (<5 ms^{-1}) | *standard* **domain**
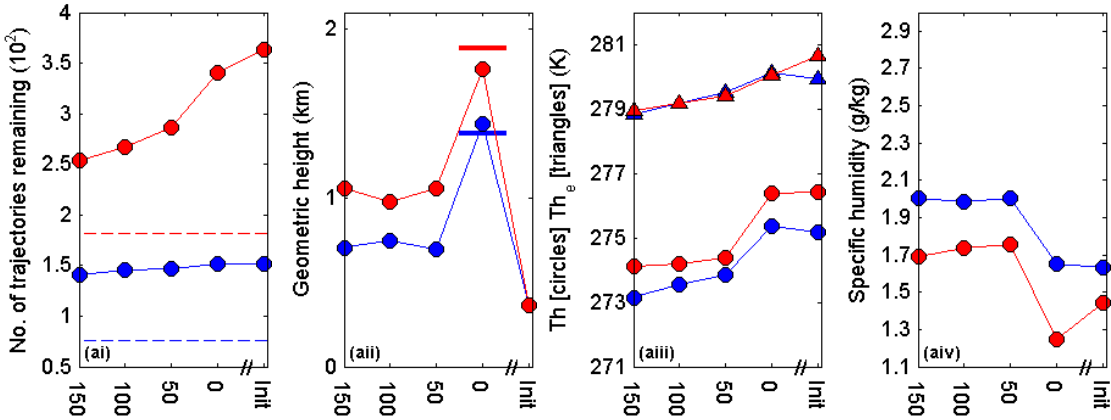
MOI (>15 ms^{-1}) - N of MOI (<5 ms^{-1}) | *standard* **domain**
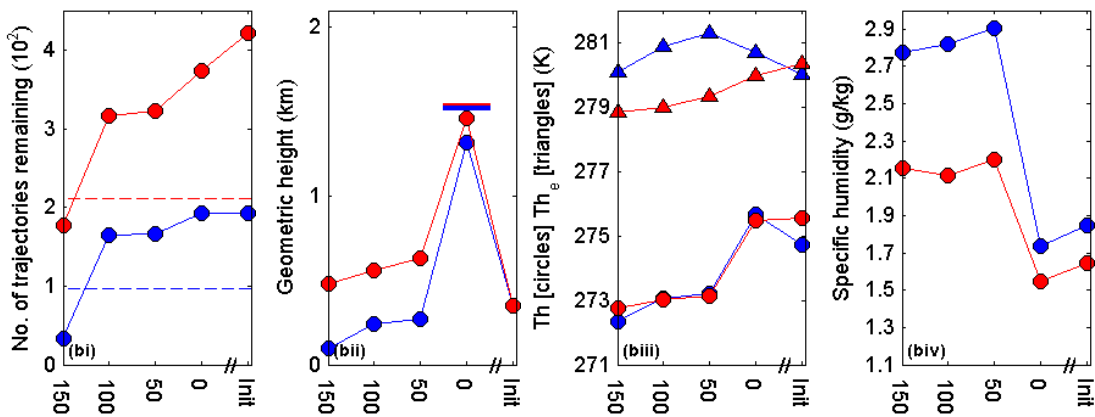
CI (>15 ms^{-1}) - S of CI (<5 ms^{-1}) | *standard* **domain**
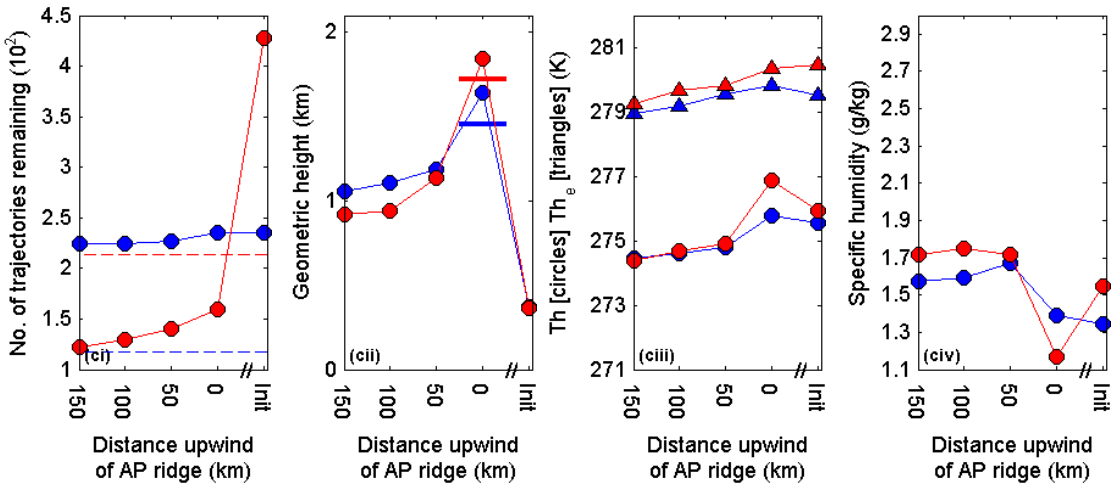
Figure 4.10: Fields for back trajectories initiated at 00 UTC 28 January 2011 during *Case B* within (a) the Whirlwind Inlet jet (WI) and the wake region north of WI (N of WI), (b) the Mobil Oil Inlet jet (MOI) and the wake region north of MOI (N of MOI), (c) the Cabinet Inlet jet (CI) and the wake region south of CI (S of CI). See Figure 3.20's caption for further explanation.

The absence of the usual jet-wake temperature and humidity relationship with regards to the CI jet and S of CI wake has been mentioned in discussion of Figure 4.7. Within the 24 hour duration of the back trajectory model run, only 37 % of the trajectories initiated within the wake region have crossed the Peninsula (Figure 4.10ci

and Table 4.1). The equivalent value for *Case A* was 95 %, and elsewhere for *Case B* the value is never less than 90 % (Table 4.1). Hence it would seem that a) the cross-AP advection of air north of 67 °S is relatively weak and b) a particularly large proportion of the constituent air in the stagnant region south of Cabinet Inlet is not föhn-derived, explaining the relatively cool and moist conditions here. It could be speculated that the relatively cool region with weak northerly flow observed at the base of the flight 162 64W-N profile (Figure 4.5) – which is a little to the south of the prescribed S of CI region – could equally comprise non-föhn air circulated to the east of the Peninsula below the level down to which the föhn has been able to penetrate (indeed warmer westerly flow is observed above ~300 m; Figure 4.5).

An unsurprising trait shown in Table 4.1 is that for all the jet regions, in each of the three cases, all trajectories pass across the Peninsula. For the wake regions, a smaller percentage of trajectories cross the Peninsula in *Case B* than in *Case A*. This supports the notion (predicted by larger $\hat{h}$) that *Case B* is defined by weaker cross-Peninsula advection than *Case A*.

A comparison of trajectory data shows that air was derived from lower altitudes upwind in *Case B* than in *Case A* (Table 4.1), barring one exception (the CI jet region; perhaps an anomaly due to the non-geostrophic nature of the gap flow upwind of this region during *Case A*). On first inspection this seems at odds with the larger $\hat{h}$ found to be associated with *Case B* (larger $\hat{h}$ corresponds theoretically to a larger streamline height, z_d). For both cases *A* and *B* the mean upwind heights of trajectories shown in Table 4.1 are smaller than values of z_d calculated theoretically with Sheppard's (1956) formula (equation [1.11]) using the estimations of model derived $\hat{h}$ at *Location A* (see Figure 4.1 for location) at a suitable time (7 hours previous to trajectory initiation). However, the discrepancy is considerably greater for *Case B* (over 600 m, as opposed to ~200 m for *Case A*). A plausible explanation for this is revealed in differences in upwind stability and wind profiles between the cases, and is discussed later in Section 4.2.4.

It should be noted that the geometric height of trajectory initiation varies across cases, since a pressure level (950 hPa) is used to define this height. However, the difference is such that the initiation height for *Case A* is lower than for *Case B*, so the conclusion that leeside air is derived from higher altitudes in *Case A* is not compromised.

Region	Type	Case	Domain	% of trajectories crossing AP	Height upwind (150, 100 or 50 km) minus initiation height (m)
WI	Jet	A	SW	100	702
		B	Standard	100	344
		C	Standard	100	58
N of WI	Wake	A	SW	98	1176
		B	Standard	94	693
		C	Standard	97	8
MOI	Jet	A	SW	100	675
		B	Standard	100	-112
N of MOI	Wake	A	SW	97	1007
		B	Standard	90	208
CI	Jet	A	Standard	100	236
		B	Standard	100	690
		C	Standard	100	108
S of CI	Wake	A	Standard	95	1693
		B	Standard	37	-
		C	Standard	100	-5
All regions	Both	A	Both	98	915
		B	Standard	90	365
		C	Standard	100	42

Table 4.1: Percentage of trajectories crossing the AP within the 24 hour model run time and mean height (AMSL) of trajectories at a set distance (50 km – red text, 100 km – blue text or 150 km – black text) upwind of the Peninsula for all regions for all three cases. Where 100 km (50 km) is chosen as the upwind distance increment, it is because over 50 % of the backward trajectories have been 'lost' at the 150 km (100 km) increment.

4.2.3.3 Mechanisms responsible for the cross-Peninsula temperature gradient

In *Case A* the dominant mechanism responsible for the föhn warming effect was the drawdown of potentially warm air from high altitudes upwind. In *Case B* the isentropic drawdown mechanism contribution is smaller (less than half, and for the MOI region, negative) and no single mechanism is found to dominate, though all do contribute significantly (Figure 4.11). Figure 4.11 is equivalent to Figure 3.22,

illustrating the contributions by each föhn mechanism towards cross-Peninsula temperature gradients (Δ_{LLCP}T) for all but one of the trajectory initiation regions. The missing region is the S of CI wake region, omitted due to the small proportion (37 %; as documented in Table 4.1) of trajectories crossing the AP. All gradients and temperature budget components are calculated using data from the MetUM 1.5 km simulation and Lagranto trajectory model, according to the model illustrated in Figure 3.23.
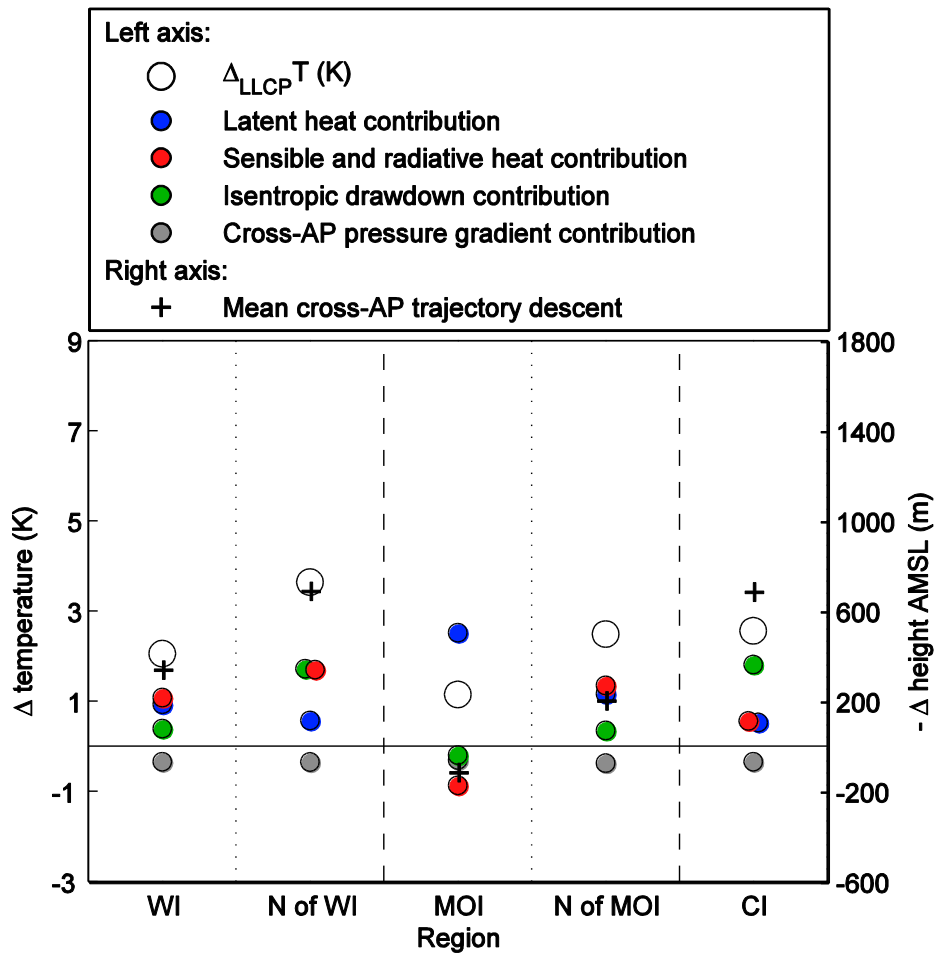
Figure 4.11: Low-level cross-Peninsula temperature gradients (Δ_{LLCP}T) at the mean height of trajectory initiation (~260 m) together with individual contributions to the temperature budget (left axis) and cross-Peninsula descent of flow trajectories (right axis) for *Case B*. Note that the same y-axis ranges are used as in Figure 3.22. For further details refer to the Figure 3.22 caption.

The isentropic drawdown mechanism is, unsurprisingly, correlated with the cross-Peninsula change in trajectory height (the values of which are considerably smaller than in *Case A*) and hence largely responsible for the wake regions exhibiting greater values of Δ_{LLCP}T than the jet regions (Figure 4.11). For the MOI jet region, air is sourced from lower altitudes upwind, resulting in a negative isentropic drawdown

contribution and a large latent heating contribution. Indeed the greatest simulated precipitation rates above the windward slopes of the AP are found upwind of this region (Figure 4.8c).

These findings show that latent heating is able to provide the primary (and in the case of the MOI jet region, the only positive) warming contribution during a föhn event; something not denied, but equally not considered in Seibert's (1990) work on mechanisms responsible for Alpine föhn, where she proposes isentropic drawdown as the primary mechanism. In her paper, she estimates typical Lagrangian warming due to latent heat release of 1.5 to 2 K for moist flow over Alpine mountains. This calculation considers flow of speed 10 ms^{-1} travelling through a 100 km-wide region of precipitation 4000 m deep with a precipitation rate of 1 mm hr^{-1} (0.275 g m^{-2} s^{-1}). Whilst peak precipitation rates shown in Figure 4.8c are considerably greater (reaching ~0.9 g m^{-2} s^{-1} upwind of MOI), the width of the precipitation band is much smaller than 100 km. The latent heating contribution towards the θ budget for the MOI jet trajectories is ~2.5 K.

Moreover, the significance of the combined sensible and radiative heating mechanism (especially for 2 of the regions, where it made the largest contributions) is at odds with Seibert's (1990) assertion that such diabatic warming is 'small' along föhn trajectories. Indeed this result overturns the current paradigm that the sensible and radiative heating contributions are negligible. It would be appropriate therefore to expand Figure 1.15 to include a fourth schematic (Figure 4.12) to illustrate these final important föhn mechanisms.
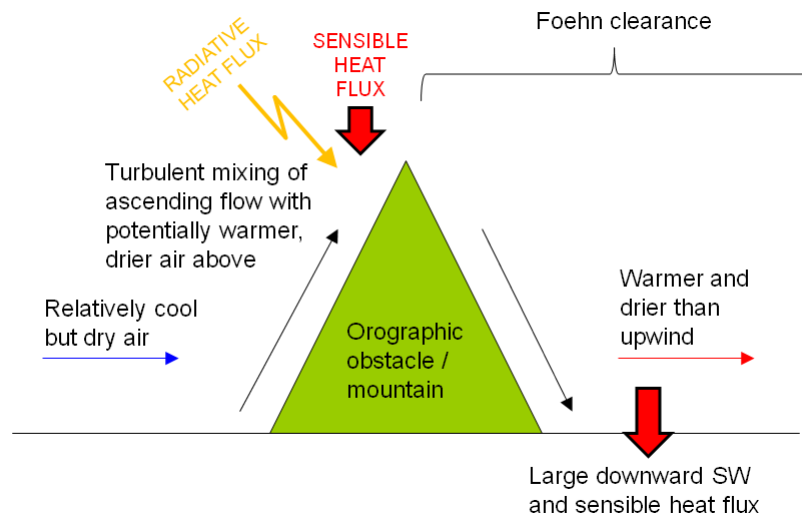
Figure 4.12: Illustration of the sensible and radiative heating mechanisms for the föhn effect. This schematic supplements those shown in Figure 1.15. The narrow red (blue) arrow denotes relatively warm (cool) flow.

4.2.3.4 Flow dynamics above and in the lee of the Peninsula

Transects across the AP of relevant fields during *Case B* (once again at 00 UTC 28 January) help to further illustrate similarities and differences with *Case A*. Figure 4.13 corresponds to figure 3.23, though the transect passing through WI (*transect gap*) has different start and end points (shown in Figure 4.7) to reflect the slight northerly component of flow direction of the WI jet in *Case B*. The transect passing through N of WI (*transect peak*) is identical. Note that whilst this transect crosses a high section of the AP downwind of which there is a hydraulic jump part way down the lee slope (typical of conditions upslope of a wake region), at the base of the lee slope it intersects the northwesterly jet emanating from Mill Inlet (at approximately -64.9 W -67 S; see Figure 4.7ai) before passing across the expansive stagnant region between the WI and CI jets (Figure 4.7ai and Figure 4.13bi).
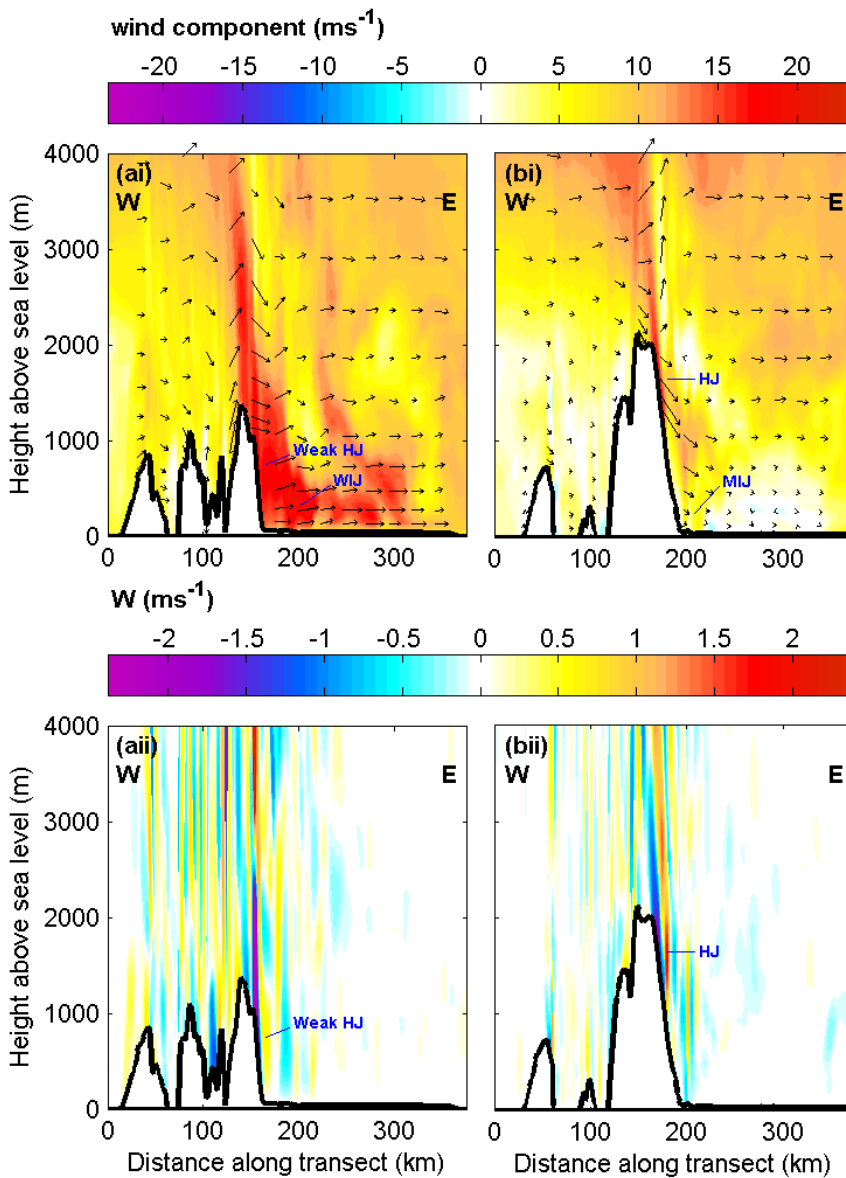
Figure 4.13 [continues to next page]: Cross sections of (i) wind component (colour) and vectors (arrows), (ii) vertical velocity, (iii) θ (contours, spaced at 2 K), (iv) Brunt Väisälä frequency squared (N^2) and Turbulent Kinetic Energy (blue contours mark values over 0.1 m^2 s^{-2}), and (v) q (contours, spaced at 0.2×10^{-3}) at 00 UTC on 28 January, derived from MetUM 1.5 km data across (a) *transect gap* and (b) *transect peak* (see Figure 4.7 for transect start and end locations). Note that the y-axis in (iii) extends to 6000 m AMSL, whilst all other plots extend to 4000m. Vertical to horizontal scale of axes = 1:100. Vertical to horizontal scale of arrows in (a) = 1:25. Note that the colour scales are the same as for the equivalent plots in Figure 3.24.
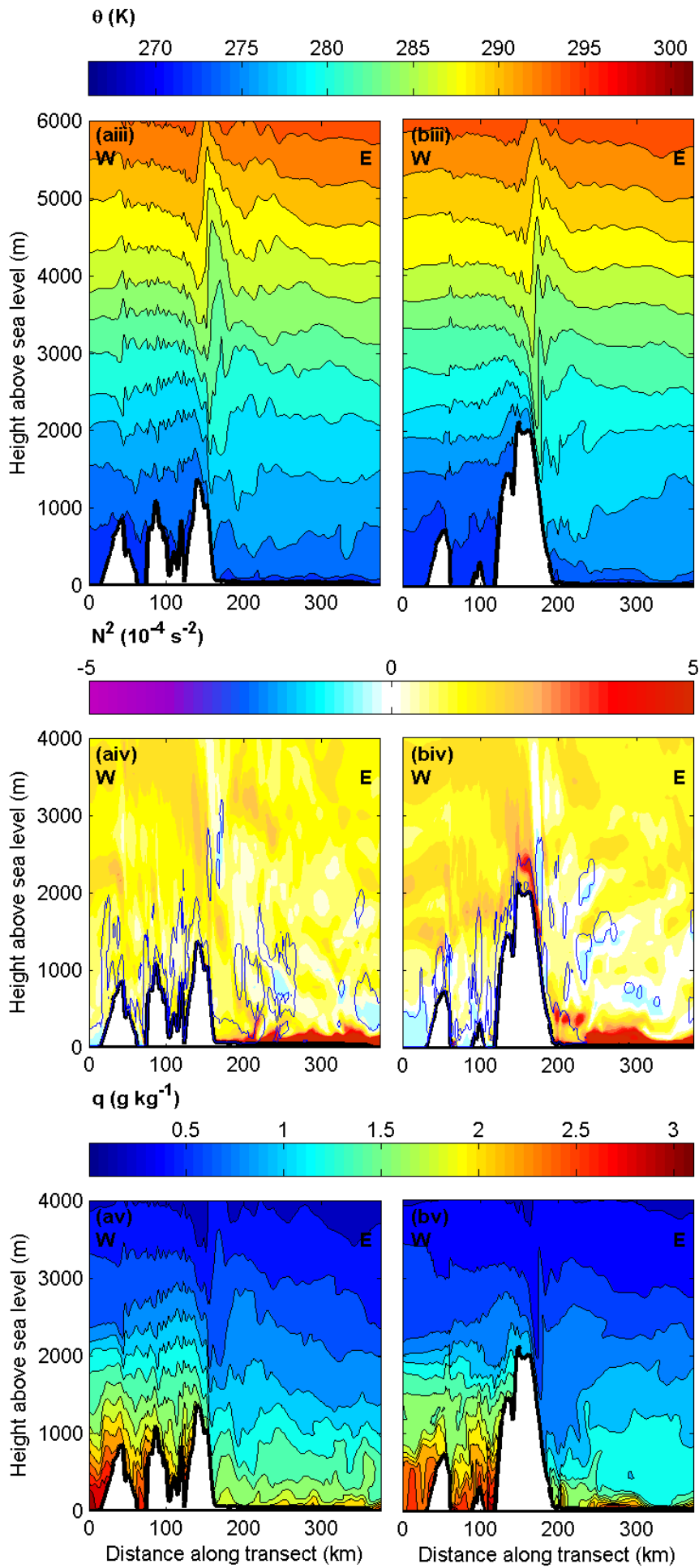
Along *transect gap*, as in *Case A*, strong winds (>20 ms^{-1}) are simulated in the lee of the AP (Figure 4.13ai). The band of strong descending winds extends high above the Peninsula, implicating the likely role of a mountain wave mechanism in addition to the gap flow (cross-mountain pressure gradient) mechanism in the existence of the lee jet. In *Case A* strong winds were confined to near-surface above the lee slopes and the Larsen C, above which weaker (to the point of stagnation), neutrally stratified flow was present (Figures 3.17aii-iv and 3.24ai and aiii). In *Case B* the gap jets are less well defined, extending higher above the surface with no flow stagnation aloft (Figure 4.7aii-iv and Figure 4.13ai). Vertical motions above the lee slope are smaller than in *Case A* with a less severe downslope component of flow and a weaker hydraulic jump in the immediate lee of the AP. In fact, a region of descent immediately downwind is associated with larger amplitude vertical velocities than those of the hydraulic jump.

Whilst descending winds are able to penetrate to near surface along *transect gap*, along *transect peak* – as illustrated in Figure 4.13bii – strong descent is followed downwind by a hydraulic jump high on the AP's lee slopes (higher than in the equivalent *Case A* plot, Figure 3.24bii).

Hydrostatic mountain waves propagate vertically above the AP along both transects (Figure 4.13iii). For *transect peak* the disturbance is relatively minor (as in *Case* A) whilst above *transect gap* a larger amplitude wave is simulated though, in contrast to *Case A*, no wave breaking is apparent in isentrope surfaces. Accordingly there are only small patches of weak TKE above the ridge, and there is little dampening of wave amplitude. Downwind of the Peninsula there is indication of horizontally propagating wave modes along *transect gap* in vertical velocity (Figure 4.13aii) and isentrope surfaces (Figure 4.13aiii).

The advection of warm dry air from above the AP ridge to near surface level above the Larsen C is apparent in Figure 4.13iii and v. The greater drawdown of air from aloft during *Case A* than *Case B* (evident in a comparison of Figures 3.22 and Figure 4.11) is nicely illustrated in a comparison of the specific humidity cross sections for each case (Figures 3.24v and Figure 4.13v). Similar to *Case A*, along both transects a region of TKE in the boundary layer extends from the base of the lee slope eastwards for a few tens of kilometres, east of which flow becomes laminar (Figure 4.13iv).

4.2.4 Evaluation of the dynamical differences between cases *A* and *B*

The differences in downwind conditions for *Case B* and *Case A* appear on first inspection at odds with the differences in upwind conditions. Whilst both cases are characterised by relatively large $\hat{h}$ (> 1), the value is larger in *Case B*. Yet *Case A* exhibits more non-linear flow characteristics, including greater upwind blocking and hydrostatic wave breaking not seen in *Case B*. However, as demonstrated in Durran (1986) and Durran (1992), vertical heterogeneity in the upwind stability profile has a profound effect on the linearity of the ensuing flow regime. In *Case A* a significant feature of the upwind flow is the occurrence of a crest-level inversion. As discussed in Sections 1.3.3 and 1.4.1 such a feature has been found to have considerable influence on the ensuing flow regime, encouraging nonlinear phenomena (Smith, 1979; Durran, 1986; Durran, 1992; Mass and Albright, 1985; Colle and Mass, 1998; Vosper, 2004; Smith and Skyllingstad, 2011). There is no inversion evident in either observational (Figure 4.5) or model (Figure 4.13iii) data for *Case B*. Furthermore, in contrast to *Case A*, the upwind vertical stability profile in *Case B* is such as to discourage non-linear phenomena, with stability increasing upward (see Section 1.4.1.3) (Durran, 1986). The presence of the inversion in *Case A* is likely to prevent the ascent of air from below crest level, whilst the relatively low static stability of the air above the inversion is likely to encourage drawdown from aloft. Conversely, in *Case B* the weaker static stability above crest height is likely to promote the ascent of approaching westerly flow over the AP. This difference seems likely to be responsible for the much lower mean source altitude for *Case B* trajectories than for *Case A* trajectories (as discussed in Section 4.2.3.2 in reference to Table 4.1). Accordingly, the dominance of the isentropic drawdown mechanism towards the föhn warming effect seen for *Case A* is not seen for *Case B*. Instead, in *Case B* the diabatic heat mechanisms provide generally similarly significant contributions.

The absence of a clear west-east (upwind-downwind) temperature gradient in *Case B* (as illustrated in Figure 4.7bi) is now investigated in relation to the flow dynamics. Plots of θ anomaly relative to an upwind value (the mean temperature within a circular area of radius 30 km upwind of the AP) at 150 m and ~2.5 m (model level 1) for cases *A* and *B* are assembled in Figure 4.14a and b. To reduce complications in the comparison of cases, the plots are all for the same time of day

(20 UTC). These plots shall, justifiably (according to further data analysis), be regarded as qualitatively representative of each föhn event.

In both cases *A* and *B* the föhn warming is more pronounced at a height of 150 m than it is at a height of ~2.5 m (model level 1) (Figure 4.14a and b). This is due to the cooling effect of the ice shelf on the air above.

The major distinction between cases *A* and *B* in terms of leeside warming is the temperature difference between air within the immediate lee and that upwind of the AP, a quantity which is greater for *Case A* (5-10 K at a height of 150 m, according to Figure 4.14a) than *Case B* (2-4 K at a height of 150 m, according to Figure 4.14b). This is also evident in a comparison of Figures 3.22 and Figure 4.11, and is in accordance with the dynamical differences already discussed. In *Case A*, relative to *Case B*, the sourcing of air from greater altitude leads to the enhanced drawdown of warm air from aloft. Indeed, whereas in *Case A* the isentropic drawdown mechanism was found to be consistently the dominant föhn warming mechanism, in *Case B* no single mechanism dominates throughout all trajectory initiation regions. Above the Larsen C the stronger hydraulic jump simulated in *Case A* within WI more effectively returns the turbulent föhn air away from the surface, resulting in the near-separation of the boundary layer (according to the MetUM 1.5 km) and the west-east (upwind-downwind) temperature gradient. Conversely, in *Case B* the sourcing of föhn air from lower altitudes upwind together with the weaker hydraulic jump and subsequent continued descent above the Larsen C is associated with a weaker warming effect in the immediate lee, but also a weaker west-east temperature gradient above the Larsen C.
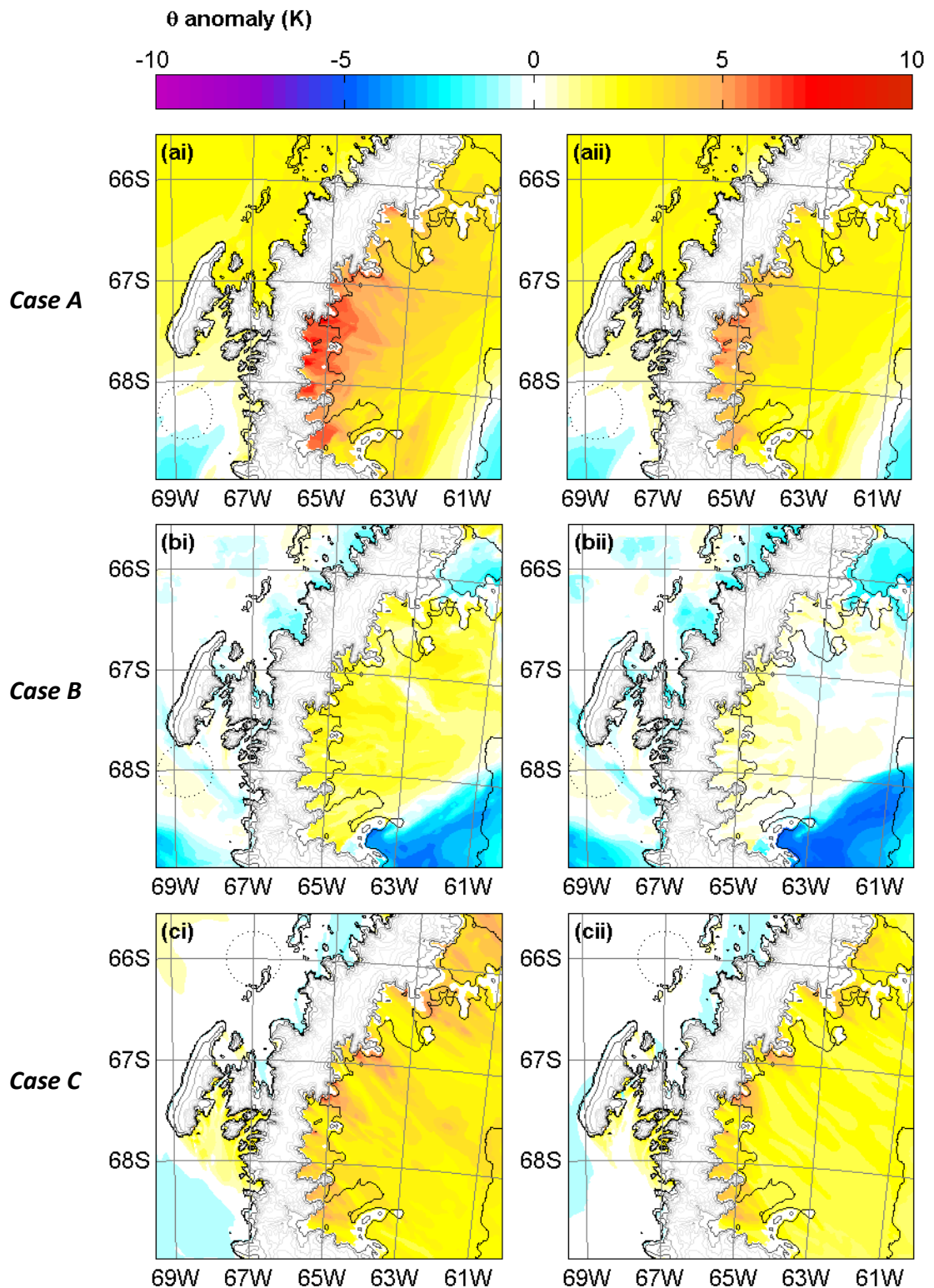
Figure 4.14: θ anomaly at (i) 150 m AMSL and (ii) ~2.5 m (model level 1) at 20 UTC on (a) 4 February 2011 during *Case A*, (b) 27 January 2011 during *Case B* and (c) 15 November 2010 during *Case C* from the MetUM 1.5 km simulation. The anomaly is calculated as the difference from the mean temperature within the dotted black circles of radius 30 km in each plot. The locations of these circles are chosen to represent upwind conditions for each case; reflecting the cross-Peninsula flow direction in each case: roughly (a) southwesterly, (b) westerly and (c) northwesterly. Note that in order to facilitate comparisons between (i) and (ii), data in (ii) is masked where the underlying orography is above 150 m AMSL.

4.3 Case C: 15-16 November 2010

4.3.1 Synoptic conditions and upwind flow

During the early Austral summer of 2010/11, synoptic weather conditions in the vicinity of the AP appeared to be 'locked' in a particular regime associated with strong mean northwesterly flow impingent on the AP. Above the Peninsula at the 850mb level at 66 °S a little to the north of Cabinet Inlet flow directions between westerly and northerly are illustrated for ECMWF ERA-Interim analysis between 7 October and 17 November 2010 in Figure 4.15. In order to relate to the work carried out by Kuipers Munneke et al. (2012) on this föhn event (discussed in Section 2.2.2) this study focuses on the final days of this episode (the yellow shaded region in Figure 4.15).
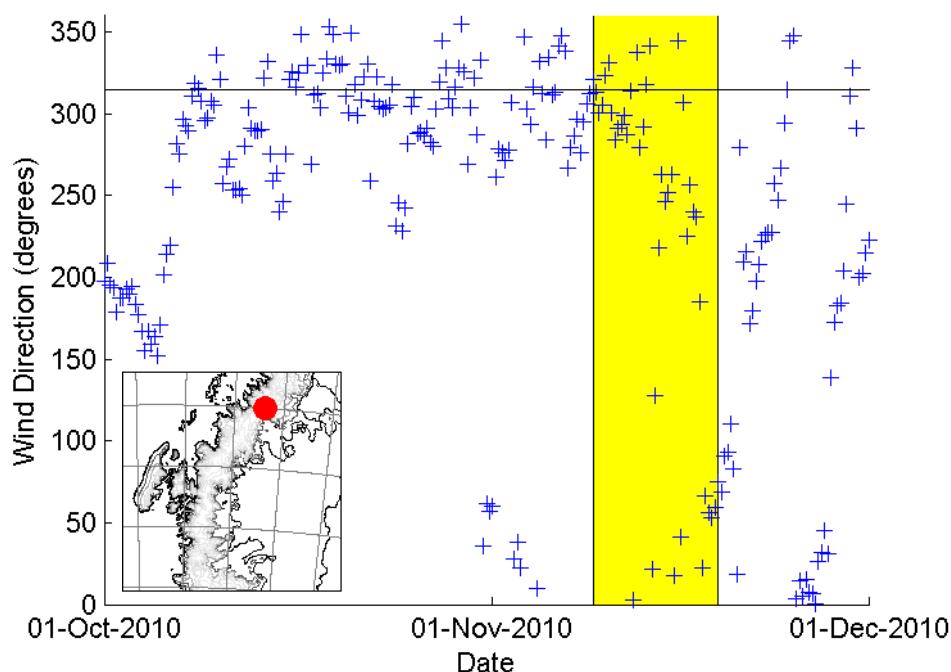
Figure 4.15: Wind direction at 850 hPa above the AP at 66°S (red dot on inset map) between 9 October and 19 November 2010 from ECMWF ERA-Interim data. The horizontal black line is wind direction = 315° (winds directly from the northwest). The yellow shaded region marks the period examined in this study.

This abnormally prolonged period of broadly northwesterly flow is associated with a shrinking of the circumpolar vortex and, specifically in the vicinity of the AP, the presence of persistent high pressure (a blocking high) north of the AP, above and to the east of the southern tip of South America. This results in an enhancement of the meridional pressure gradient and hence the mean westerly component of flow at

higher latitudes (evident from National Centres for Environmental Prediction / National Centre for Atmospheric Research (NCEP/NCAR) reanalysis data not shown here). This can be seen for the period of focus in plots of geopotential height at the 850mb level (Figure 4.16). On 10, 13 and 16 November, low pressure systems are centred at locations south of 68 °S and to the west of the Peninsula, bringing northwesterly flow across the AP. This pattern is typical until 17 November as the high pressure to the north migrates northwards, as does the band of mean northwesterly flow (Figure 4.16d), and synoptic pressure gradients resume a more typical arrangement.
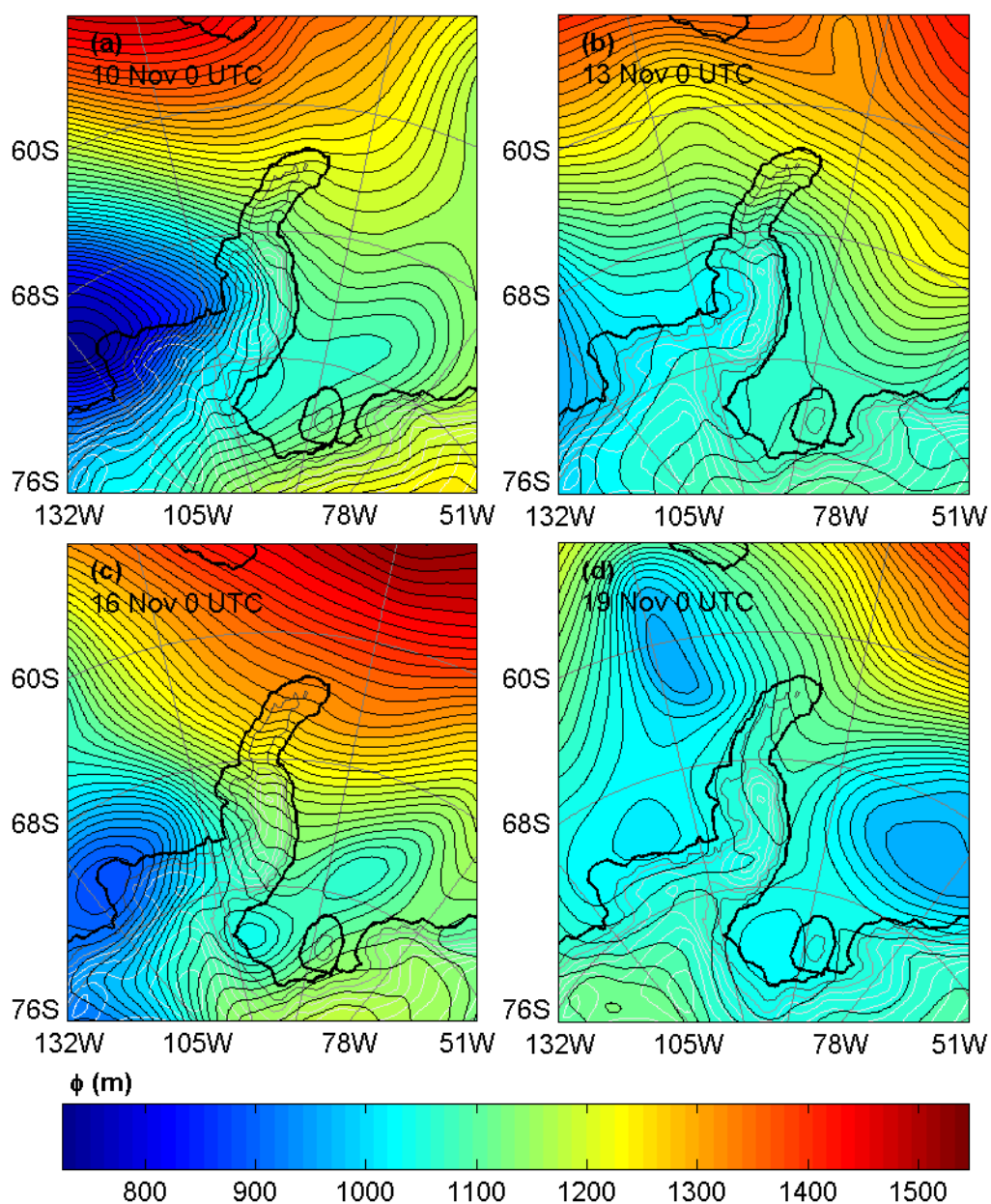
Figure 4.16: Geopotential height (contours, spaced at 15m) at the 850hPa level at 00 UTC on (a) 10, (b) 13, (c) 16, and (d) 19 November 2010 from ECMWF ERA-Interim. The land-sea mask and surface height contours are also plotted.

Five MetUM simulations each of duration 42 hours have been carried out to document the event – with 6 hour gaps between simulations – between 9 and 19 November. Vertically averaged wind speed and direction and non-dimensional mountain height 150 km upwind of the AP are presented in Figure 4.17. Winds are consistently between westerly and northerly between 9 and 16 November and are relatively strong during this period, peaking at over 25 ms^{-1} on 15 November. Such strong approaching flow in addition to comparatively low static stability (see later; Figure 4.23iv), translates to consistently low westerly to northwesterly $\hat{h}$, reaching a minimum of 0.58 on 10 November. The remainder of the discussion regarding this northwesterly event will consider the fourth simulation of the series only (initiated at 6 UTC 15 November). This simulation was chosen for further analysis as it is associated with the longest period of upwind $\hat{h} < 1$ (largely during 15 November), and hence likely providing the greatest contrast in flow characteristics to the highly non-linear *Case A*. The episode of föhn conditions documented by this simulation shall be referred to as *Case C*. The minimum $\hat{h}$ for this simulation is 0.67 during the evening of 15 November. Using Hunt and Snyder's (1980) adjustment for elongated ridges, Sheppard's (1956) formula dictates that, for $\hat{h} < 1.2$, there should be no upwind blocking / flow separation ($z_d < 0$) in an idealised scenario. During 16 November $\hat{h}$ increases significantly as winds weaken and become northerly.

At midday on 15 November, the cross-Peninsula pressure gradient in the vicinity of Cabinet Inlet (where the strongest cross-Peninsula flow is simulated) is ~6 hPa/100 km according to the MetUM 1.5m simulation. This value is smaller than those representative of cases *A* (~8.5 hPa) and *B* (~6.5 hPa), in accordance with the greater linearity of this case. Note however that the *Case C* value is only marginally smaller than the *Case B* value. As illustrated in Figure 1.12, at some value of $\hat{h}$ (the threshold value $\hat{h}_T$), the cross-Peninsula pressure gradient peaks, with further increases in $\hat{h}$ incurring a reduction in atmospheric pressure drag on a mountain. This is intuitive if one considers geostrophic flow directed increasingly parallel to a smooth ridge ($\hat{h} \rightarrow \infty$). *Case B* (*C*), being characterised by the weakest (strongest) cross-Peninsula flow of the three cases, is likely to be associated with $\hat{h}$ greater (smaller) than $\hat{h}_T$, whilst characteristic $\hat{h}$ for *Case A* appears to be closest of the three cases to $\hat{h}_T$.
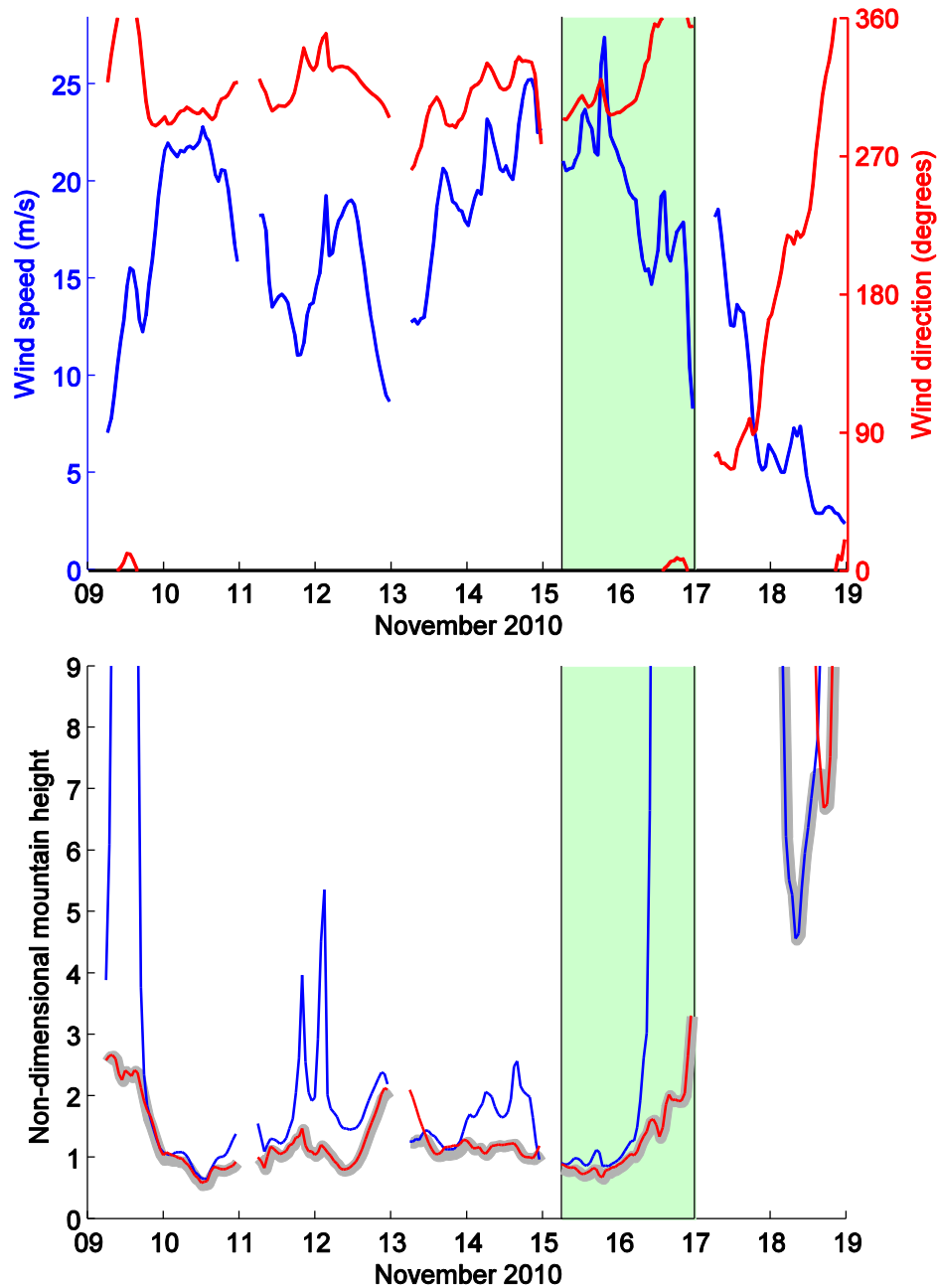
Figure 4.17: Plots of (a) wind speed and direction and (b) non-dimensional mountain height (ĥ) during a portion of November 2010. All values are vertical averages (between 200-2000m) from a vertical profile of MetUM 4 km data roughly 150km west of the AP (location given by the black cross in Figure 4.1). Both westerly (blue line) and northwesterly (red line) ĥ are shown, as is 'west to northwesterly' ĥ (thick grey line), which treats any wind direction between west and northwest as being perpendicular to the AP. The green shaded region marks the period of *Case C* (the fourth simulation).

4.3.2 Leeside response in the model

4.3.2.1 Föhn conditions and the wind field above the Larsen C

Winds above the Larsen C at 150 m AMSL during *Case C* (Figure 4.18ai) are at least as strong close to the Peninsula within certain major inlets, and considerably stronger elsewhere as for cases *A* and *B* (Figures 3.17ai and Figure 4.7ai). In cases *A* and *B* polar föhn jets characterised by similar magnitude wind speeds were found high within the major inlets, but the strength of these flows quickly subsided downwind. In contrast, in *Case C* these jets are broader and persist with little deceleration, extending right across the Larsen C. The northwesterly direction of the background flow is responsible for the major jets emanating from WI, CI and Mill Inlet, whilst there is no jet apparent within the southwesterly oriented MOI. The CI jet is the widest jet, far wider than in cases *A* and *B* (once again presumably due to the northwesterly as opposed to south westerly flow direction in concert with the orientation of the Peninsula here). Between the jets wake regions are again apparent (note that whilst this naming convention is upheld here, the 'wake regions' might now more fittingly be described as 'regions of relatively low wind speed'). Whilst in similar locations (downwind of relatively high orography), these wakes are narrower than those found in cases *A* or *B*, and across the Larsen C regions of stagnation are fewer and less extensive. A cross section through the three major jets (Figure 4.18aii) reveals that strong winds extend over a kilometre above the surface, rather than being confined to relatively low level, as in *Case A*.
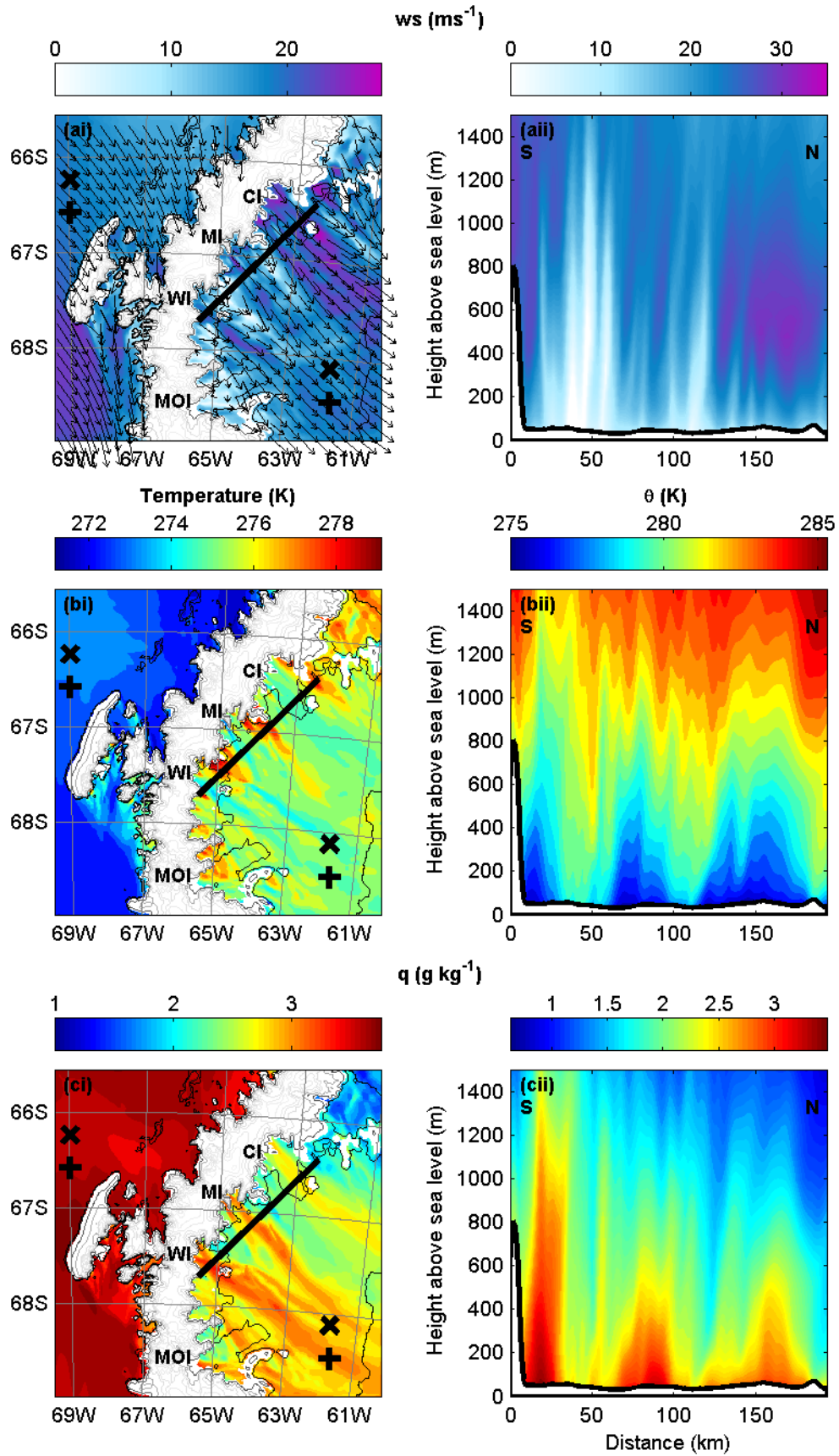
Figure 4.18: As in Figure 4.7 but for Case C at 22 UTC on 15 November 2010 and with cross sections (ii) along a transect passing through Whirlwind Inlet (WI), Mill Inlet (MI) and Cabinet Inlet (CI). Note that transects different to those used for Case B define *transect gap* ('+'s) and *transect peak* ('x's) for the cross sections of Figure 4.23 and Figure 4.24 (though both still pass through WI and N of WI respectively).

The föhn effect is evident in cross-Peninsula gradients in θ and *q* (Figure 4.18bi and ci). A clear distinction between jets and wakes is more apparent than in the other cases, with streams of cool moist air marking the polar föhn jets. This signature is also clearly evident in the cross sections. Temperatures above the far eastern side of the Larsen C are no lower than those within the mouths of the inlets (i.e. in this respect there is no west-east (upwind-downwind) temperature gradient), though are significantly cooler than those at the foot of the lee slope outside of the jets (Figure 4.18bi).

4.3.2.2 Cross-Peninsula flow

For trajectory analysis of *Case C* initiation regions were chosen using different sampling criteria as used previously. For cases *A* and *B* wind speed was used to separate jet and wake regions. Here the large variability in wind speeds close to the Peninsula means this method does not distinguish the jets and wakes cleanly. Instead temperature is used. As established during analysis of cases *A* and *B* (and self evident from Figure 4.18 for *Case C*), polar föhn jets are characterised by relatively cool temperatures. It should be noted that a wind speed criterion was also tested, and was found to produce qualitatively similar sampling regions to those produced using the temperature criteria. Given the absence of the MOI jet in this case only the WI, CI and adjacent wake regions are considered (Figure 4.19).

Figure 4.20 presents the results of the trajectory analysis in the same manner as in Figures 3.20 and Figure 4.10. For the N of WI wake region many trajectories are 'lost' (~28 %) between the 0 and 50 km increments of distance upwind of the AP due to intersection with orography (Figure 4.20ai). Despite this enough remain to provide statistically robust data. For the CI jet region virtually all trajectories are lost at the 100 km (and none remain at the 150 km) increment due to leaving the edge of the domain to the north (Figure 4.20bi). For the same reason S of CI wake region trajectories are gradually lost with increasing upwind distance increments.
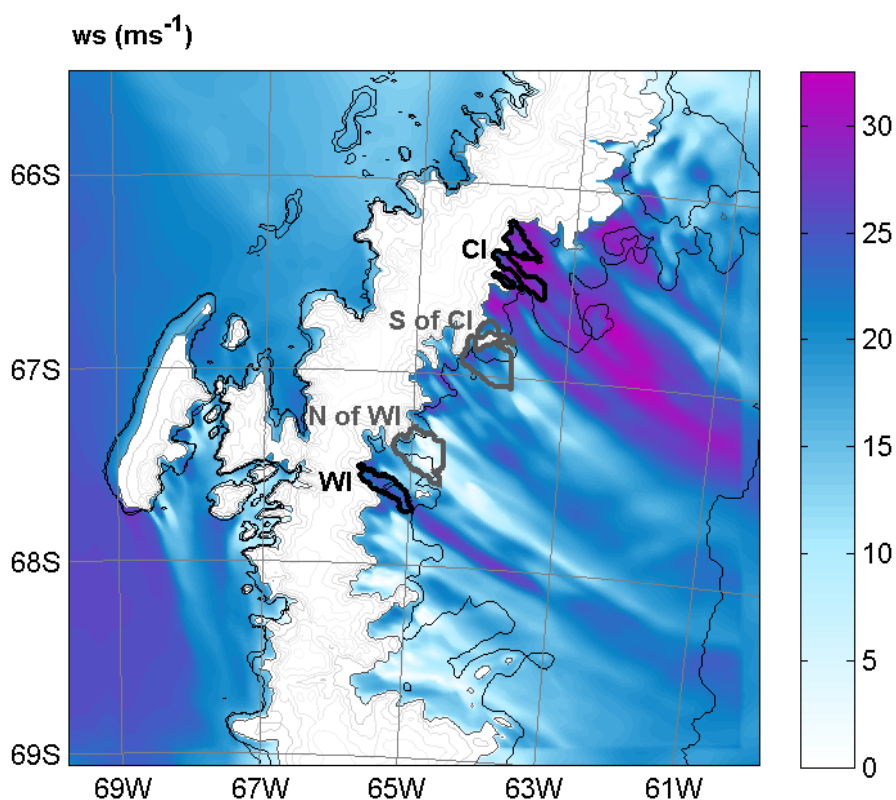
Figure 4.19: As in Figure 4.9 but for Case C trajectories initiated at 22 UTC on 15 November 2011. Also, Jet (wake) regions are now defined by θ at initiation below 278 K (above 280 K).

Due to the strength of flow, virtually all trajectories – initiated above the Larsen again at the 950 mb level – are sourced from upwind of the AP (Table 4.1). Furthermore there is little difference in mean trajectory height between trajectory initiation and 100 km upwind of the AP (Table 4.1). This is in agreement with the small value of $\hat{h}$ calculated for the event (as discussed in Section 4.3.1), and suggests isentropic drawdown in the lee of the AP in this case will be small. The fact the föhn effect is still apparent (there is a cross-Peninsula temperature and moisture gradient) is due to the diabatic heating and moisture loss which occurs as air rises and crosses the AP (this is also once again apparent in changes in mean θ and q as trajectories cross the AP; Figure 4.20). Background humidities are greater than in the two previous cases (compare Figure 4.20iv with Figures 3.18iv and Figure 4.10iv), associated with thick cloud cover upwind and high precipitation rates above the windward slopes of the AP (Figure 4.21).

WI (<278 K) - N of WI (<280 K) | *standard* domain
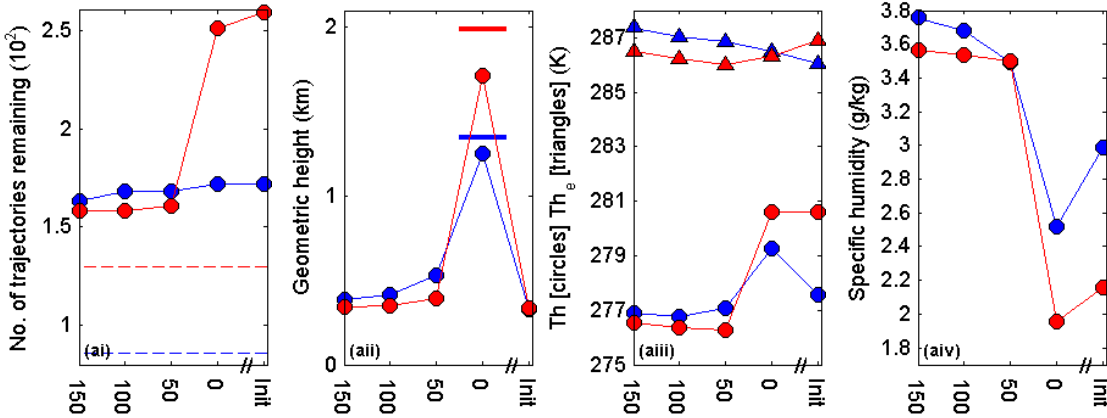
CI (<278 K) - S of CI (>280 K) | *standard* domain
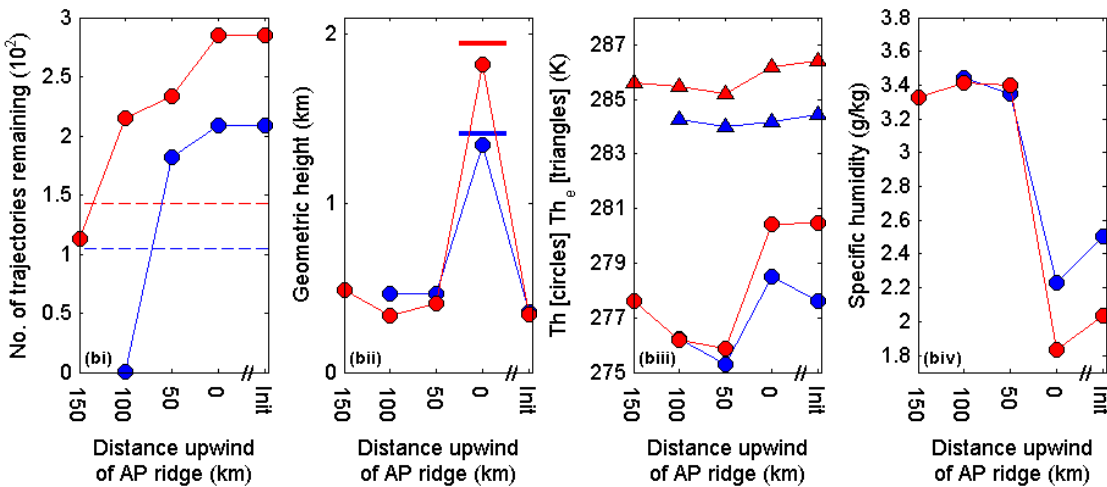
Figure 4.20: As in Figure 4.10, but for back trajectories initiated at 22 UTC 15 November 2010 during Case C within (a) the Whirlwind Inlet jet (WI) and the wake region north of WI (N of WI), (b) the Cabinet Inlet jet (CI) and the wake region north of CI (N of CI). Also in contrast with Figure 4.10, jet trajectories are classified by θ at initiation under 278 K (blue), and wake trajectories by θ at initiation over 280 K (red).

In common with cases *A* and *B* the jet trajectories cross the Peninsula at lower altitudes than the wake trajectories (on average). However, further upwind the jet and wake trajectories reside at approximately the same height, a result which is consistent with the nature of the flow upwind. Though 1500 m is used as a representative height for the AP in the calculation of $\hat{h}$, the mean height of orography upwind of the jet (wake) regions is, according to Figure 4.20ii, lower (higher) than this at ~1370 m (~2000 m). Using these heights instead gives $\hat{h}$ = 0.61 for passes and 0.89 for peaks. Since both values are below 1.2, one would expect no apparent difference in source altitude upwind of the AP between jet and wake regions, as seen in Figure 4.20.

Upwind of the AP, air is warmer and marginally moister for the WI jet trajectories than the N of WI wake trajectories. This is consistent with the lower

altitude of the jet trajectories. Across the AP, this relationship is reversed, with diabatic warming being considerably greater along the wake trajectories than the jet trajectories. Similar cross-Peninsula changes in θ and humidity are seen for the other jet pairing, though CI jet trajectories do exhibit marginally cooler potential temperatures upwind of the AP than S of CI wake trajectories. This indicates a small advective contribution towards explaining the warmth of the air within the S of CI wake region relative to that making up the CI jet.
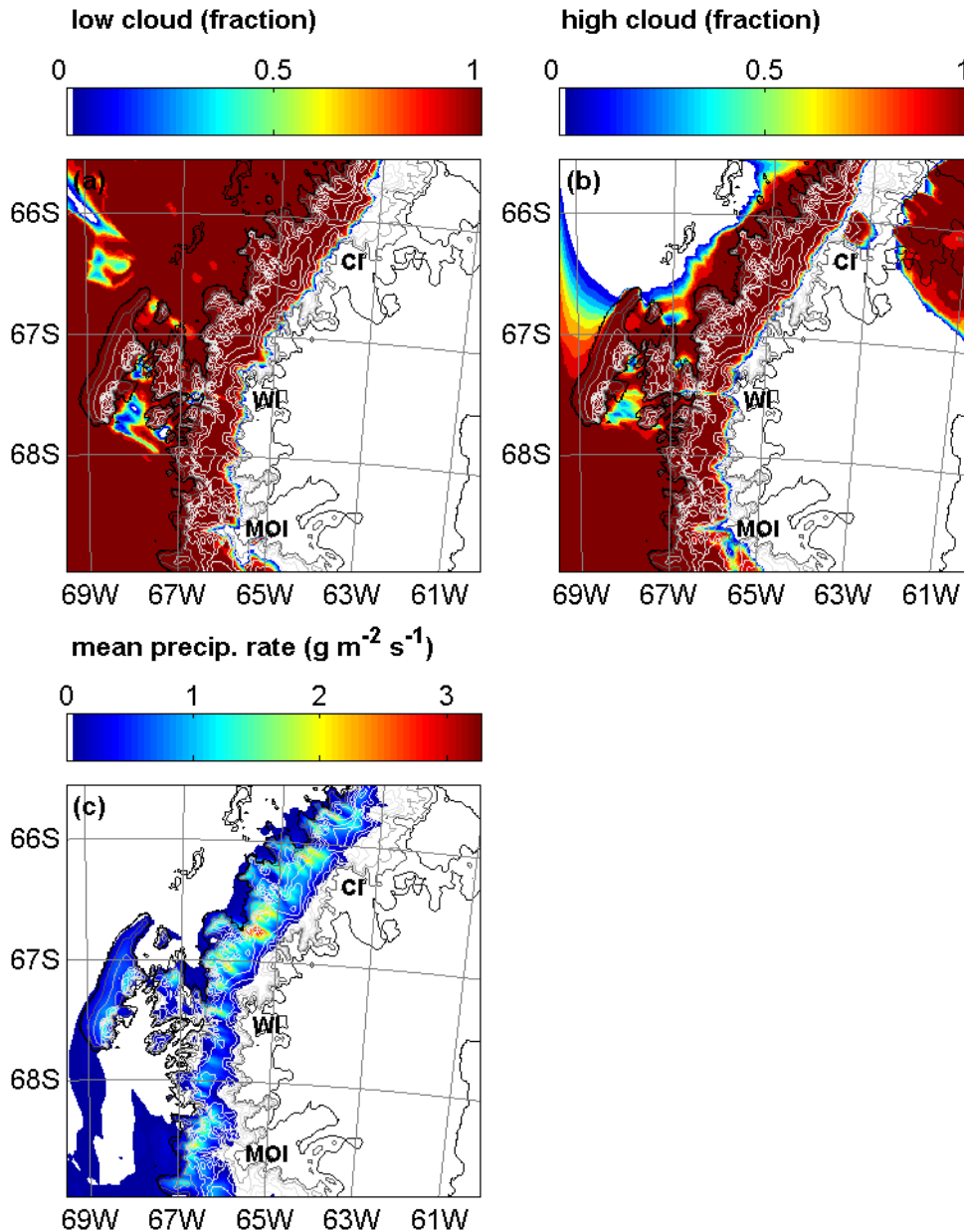
Figure 4.21: (a) Low level (below ~2000 m above the surface) and (b) high level (over ~2000 m above the surface) cloud fraction at 22 UTC 15 November during *Case C*, and (c) mean precipitation rate between 10 UTC 15 November and 22 UTC 15 November from the MetUM 1.5 km simulation. Refer to the Figure 3.16 caption for explanations for the calculation of these diagnostics.

4.3.2.3 Mechanisms responsible for the cross-Peninsula temperature gradient

In *Case C* latent heat release is the primary cross-Peninsula warming mechanism (Figure 4.22). This is consistent with the relatively moist conditions and large vertical displacement of air as flow rises above the windward slopes giving rise to high precipitation rates (Figure 4.21c). The greatest latent heating contribution is 3.6 K for the N of WI wake regions. The other mechanisms offer only small warming contributions. In this case the 'classic' textbook thermodynamic / condensation theory of föhn warming holds.

In cases *A* and *B* differences in the source location of the föhn was largely responsible for the cool, dry nature of the jets relative to the wakes. In *Case C*, however, contributions of the isentropic drawdown mechanism are small positive values for all regions, reflecting the linearity of the event – specifically the small cross-Peninsula change in trajectory height. Instead, it is the greater ascent required for flow to traverse the high sections of the AP ridge which results in greater latent heat release upwind of the wake regions than the jet regions, leading to the cooler drier jets.

As previously mentioned, Seibert (1990) estimates typical warming along air parcel trajectories across Alpine mountains during a moist föhn event due to latent heat release of 1.5 to 2 K. Seibert's calculation considers flow of speed 10 ms^{-1} travelling through a 100 km-wide region of precipitation 4000 m deep with a precipitation rate of 1 mm hr^{-1} (0.275 g m^{-2} s^{-1}). Peak precipitation rates for *Case C* shown in Figure 4.21c are considerably greater (even more so than those for *Case B*) – reaching values of 2 to 3 g m^{-2} s^{-1} above the AP. Whilst the width of the precipitation band in this case is smaller than 100 km at ~60 km, and residency time for cross Peninsula flow within the region of precipitation is smaller due to stronger wind speeds (~20 ms^{-1} as opposed to 10 ms^{-1}), the height of the AP (1500 to 2000 m) is smaller than the Alps so orographic precipitation is likely not to be spread over a vertical range of 4000 m. Using the same method as Seibert (1990), but with these *Case C* values (including a precipitation rate of 4 mm hr^{-1}, which translates to just over 1 g m^{-2} s^{-1}; the estimated mean value across the precipitation band), a latent heating contribution towards Lagrangian cross-Peninsula warming of ~4 K is attained. This value is close to the greatest latent heating contribution towards $\Delta_{LLCP}T$ of all the initiation regions during *Case C*, of 3.6 K for the N of WI region.
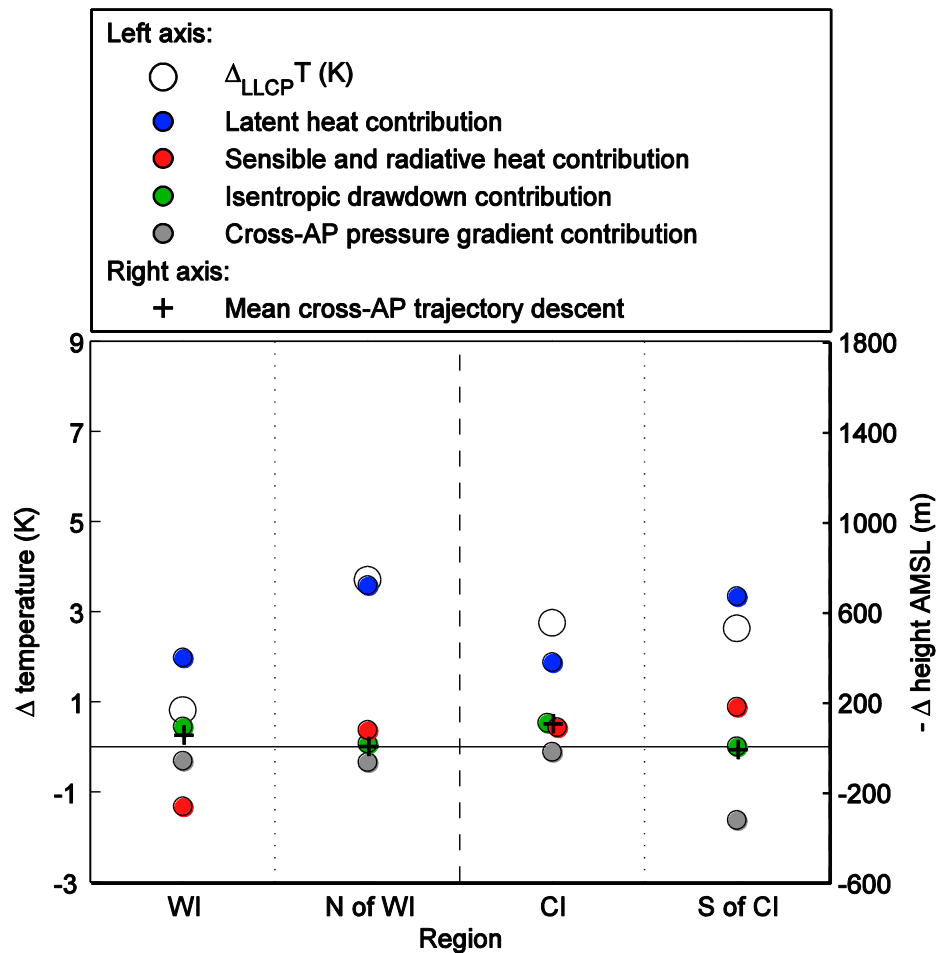
Figure 4.22: Low-level cross-Peninsula temperature gradients (Δ_{LLCP}T) at the mean height of trajectory initiation (~330 m) together with individual contributions to the temperature budget (left axis) and cross-Peninsula descent of flow trajectories (right axis), for all trajectory initiation regions. Note that the same y-axis ranges are used as in Figures 3.22 and Figure 4.11. For further details refer to the Figure 3.22 caption.

4.3.2.3 Flow dynamics above and in the lee of the Peninsula

Figure 4.23 compares *Case A* to *Case C* via cross-sections through the WI jet (*transect gap*). The non-linear phenomena characterising *Case A* and, to some respect, *Case B* are absent in the *Case C* cross sections. Figure 4.23ii shows the normalised streamwise wind anomaly. The wind anomaly is calculated by subtracting the vertically averaged (between 0 and 4000 m AMSL) upwind (at distance = 0 km along the transect) streamwise wind component ($\bar{u}$) from the wind field. The wind anomaly is then normalised by the same value $\bar{u}$.

Minimal upwind blocking and no low-level wave breaking or hydraulic jump is apparent, though small amplitude horizontally-propagating non-hydrostatic lee waves are evident, in the lee of the AP (Figure 4.23bi-bv). The flow field is relatively homogenous in the vertical across the Peninsula, with a column of accelerated flow

above the AP's main ridge (Figure 4.23 bii). This is in contrast to *Case A* (and *Case B*) where the most strongly accelerated flow was above the AP's eastern slopes (Figure 4.23 aii). Nevertheless in *Case C* relatively strong flow is simulated in the lee of the mountains. This positive flow anomaly does not, as in *Case A*, 'hug' the lee slopes to the near-surface level, but is vertically deeper and extends further east (over 100 km downwind of the AP) above the Larsen C. The peak magnitude of the wind speed anomaly relative to the estimated mean background flow field (normalised wind speed anomaly) in the downslope flow is greater (by a factor of over 3) for *Case A* than *Case C*.

The greater upwind ascent of air in *Case C* than *A* is reflected in greater positive vertical velocities above the windward slopes (Figure 4.23iii). Above and in the lee of the mountains larger amplitude vertical velocities are simulated in *Case C* than in *Case A*. However, normalising vertical velocities by horizontal wind speeds (i.e. the flow angle from the horizontal; not presented) gives values for *Case C* which are significantly smaller than *Case A*.

Case A is characterised by the drawdown from aloft of warm föhn air in the immediate lee of the AP, with eastward re-ascent of isentropes and an associated increase in stability above the Larsen C. In *Case C* isentropes to the lee below crest height slant downwards in an easterly direction (a similar pattern is seen in q surfaces; Figure 4.23vi). Boundary layer turbulence associated with vertical wind shear is simulated to extend across the entirety of the Larsen C along *transect gap*. An elevated (~300 m AMSL) inversion above the Larsen C appears likely to be the downwind re-establishment of an inversion upwind (apparent in Figure 4.23bv at ~600m). A near-surface inversion above the Larsen C is thinner and weaker than that in *Case A*.

Cross sections along a transect passing through N of WI (*transect peak*) reveal non-linear characteristics not found along *transect gap*. Similar to *Case A*, the downslope flow is returned upwards in a band of strong ascent (Figure 4.24c), downwind of which there is evidence of boundary layer separation (Figure 4.24a) and a region of decelerated flow is apparent above the Larsen (Figure 4.24b). A warm region at the foot of the lee slope followed downwind by cooler, more stable conditions (Figure 4.24d) mirrors the temperature structure for both jet and wake

cross sections in *Case A*. Due to the smaller vertical wind shear the boundary layer

above the Larsen is less turbulent than in the jet.

 Figure 4.23 [Through next two pages]: Cross sections of (i) wind component (colour) and vectors (arrows), (ii) normalised wind component anomaly (see notes in text), (iii) vertical velocity, (iv) θ (contours, spaced at 2 K), (v) Brunt Väisälä frequency squared (N^2) and TKE (blue contours mark values over 0.1 $m^2 s^{-2}$), and (vi) *q* (contours, spaced at $0.2×10^{-3}$) during (a) Case A at 22 UTC on 4 February 2011 and (b) Case C at 22 UTC on 15 November 2011, derived from MetUM 1.5 km data across *transect gap* (see Figures 3.17 and Figure 4.18 respectively for transect start and end locations). HJ = hydraulic jump, WBR = wave braking region, WIJ = Whirlwind Inlet jet, EUI = elevated upstream inversion, EDI = elevated downstream inversion, NSI = near-surface inversion. Note that the y-axis in (c) extends to 6000m AMSL, whilst all other plots extend to 4000m. Vertical to horizontal scale of axes = 1:100. Vertical to horizontal scale of arrows in (a) = 1:25.

θ (K)
N² (10⁻⁴ s⁻²)
q (g kg⁻¹)
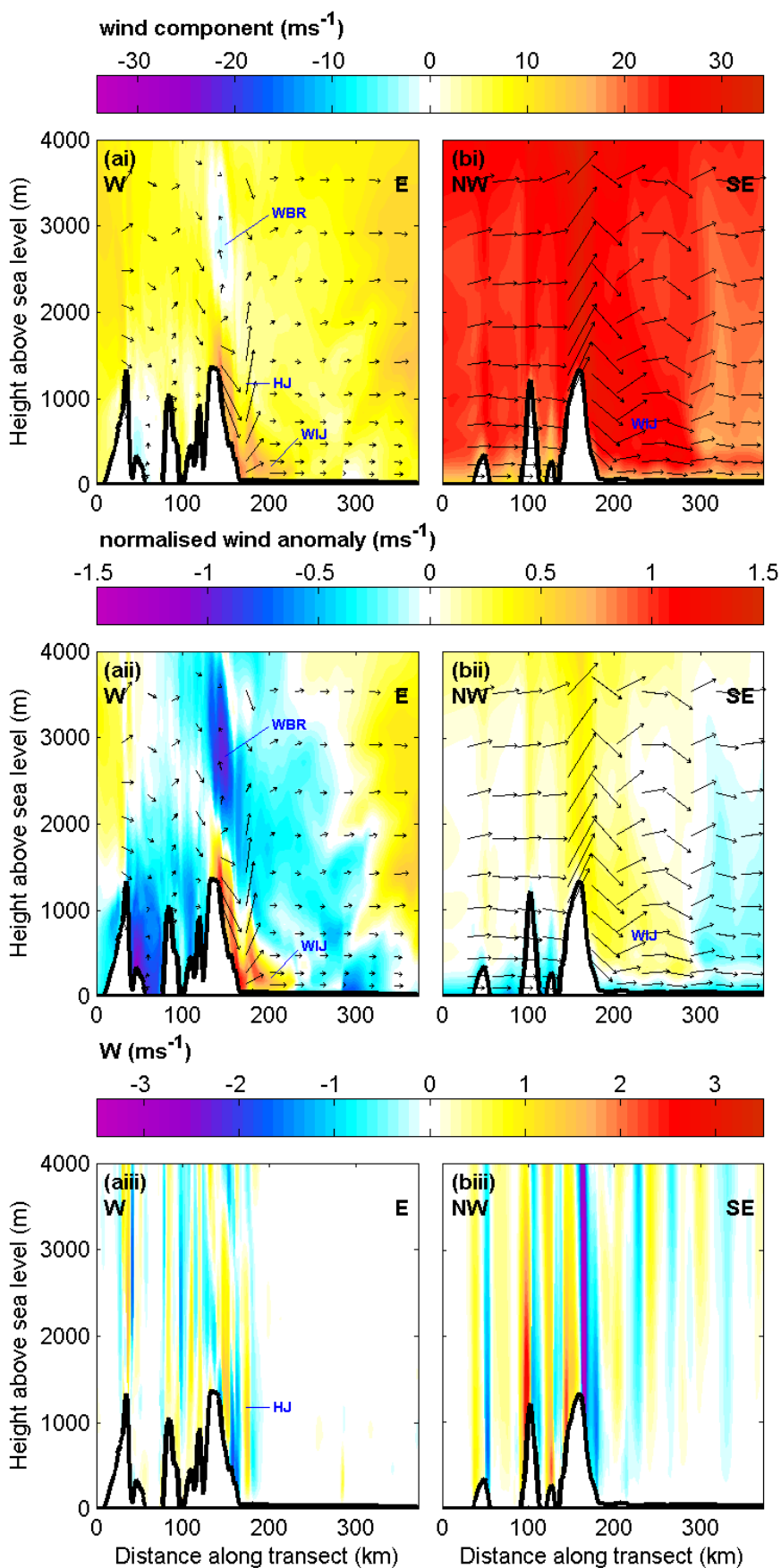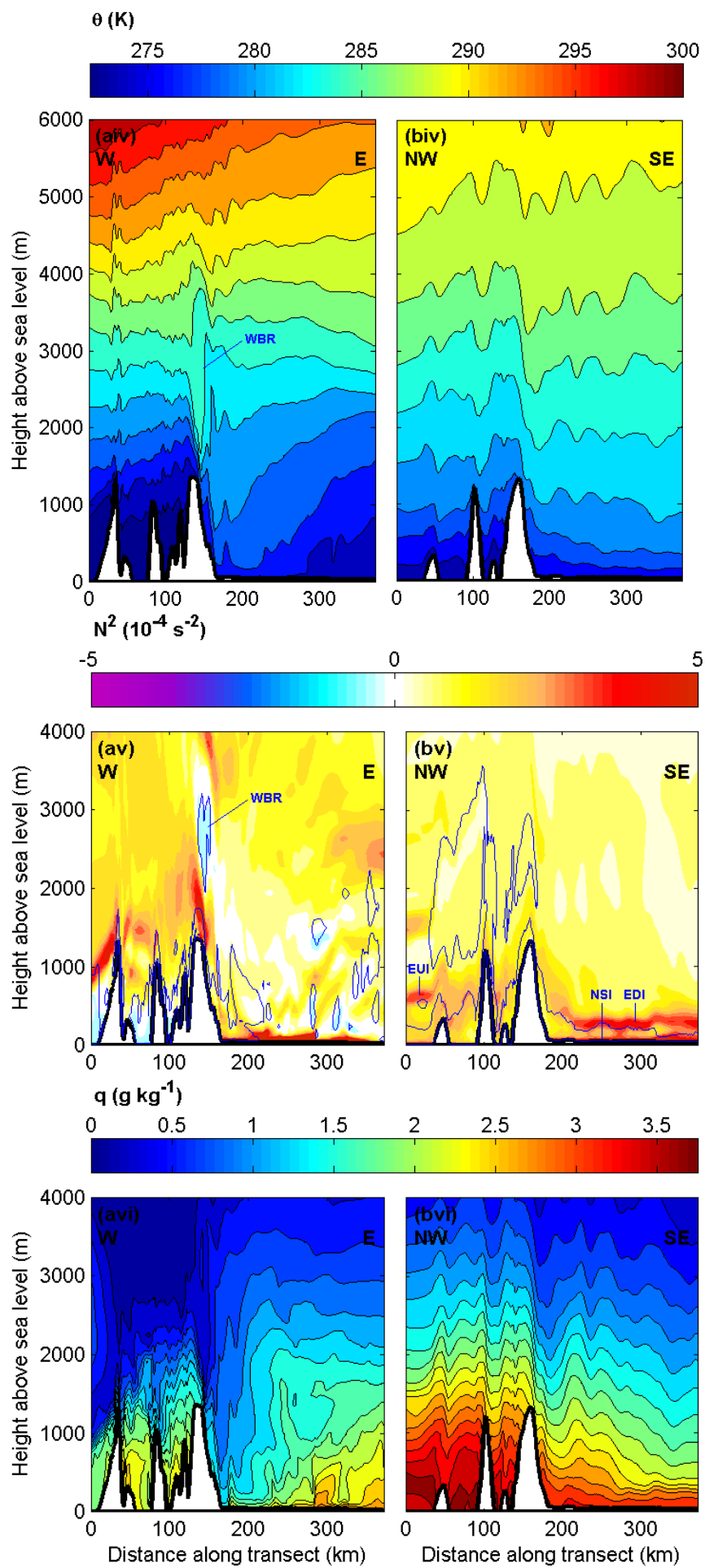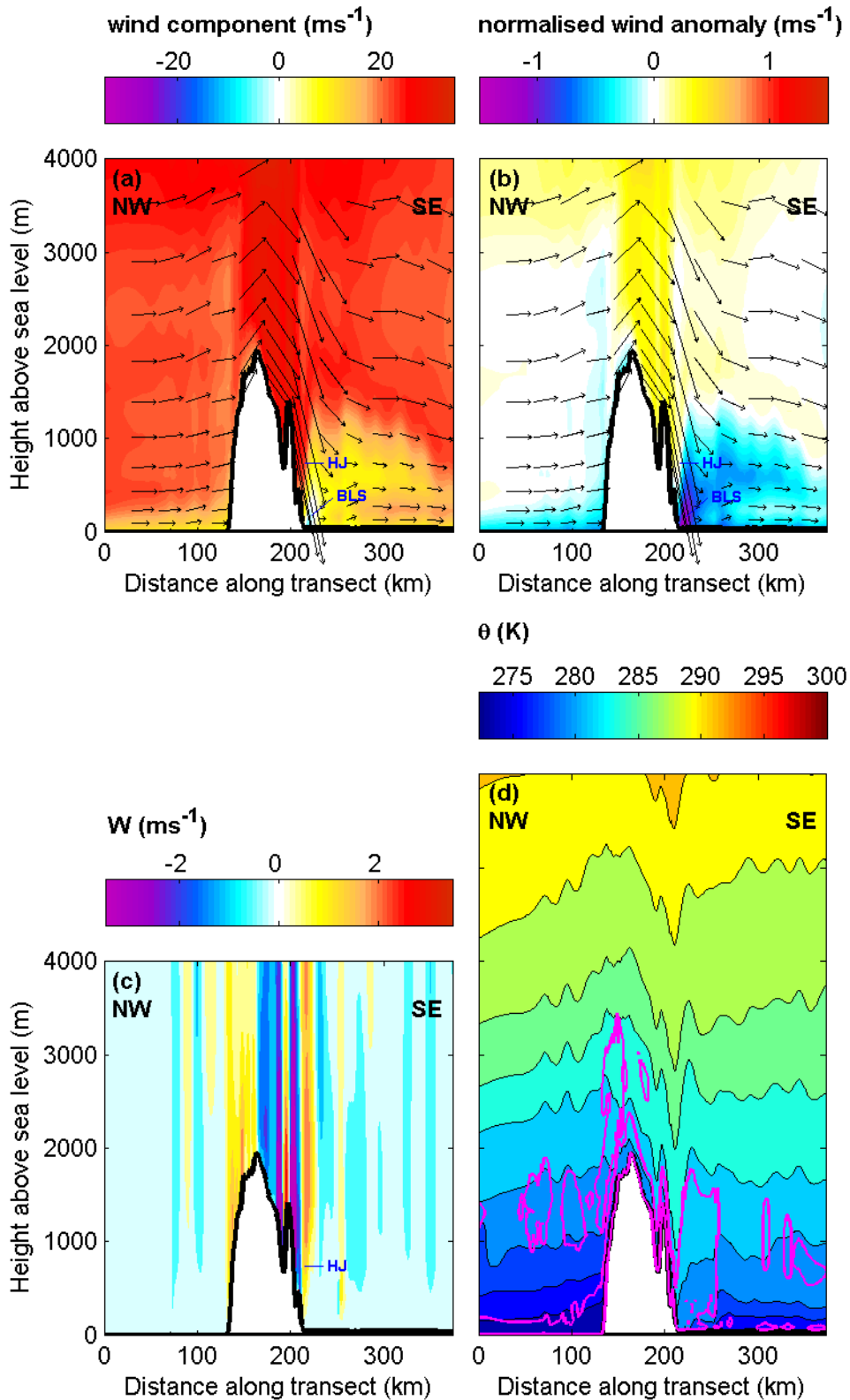
Figure 4.24: Cross sections of (a) wind component (colour) and vectors (arrows), (b) normalised wind component anomaly (see notes in text), (c) vertical velocity, and (d) θ (contours, spaced at 2K) and TKE (magenta contours mark values over 0.1 m^2 s^{-2}) during Case C at 22 UTC on 15 November 2011, derived from MetUM 1.5 km data across *transect peak* (see Figure 4.18 for transect start and end locations). HJ = hydraulic jump, BLS = boundary layer separation. Note that the y-axis in (c) extends to 6000m AMSL, whilst all other plots extend to 4000m. See caption for Figure 4.23 for further details regarding this figure. Note that the colour scales are the same as for the equivalent plots in Figure 4.23.

4.3.3 Evaluation of the dynamical differences distinguishing *Case C* from the other cases

Case C, being a highly linear case of cross-mountain flow, is associated with little low-level blocking and so the ascent of warm and moist air from low altitudes upwind of the AP is responsible for the föhn warming. As such, in contrast to *Case A*, the contribution of isentropic drawdown towards the föhn warming effect is small and the contribution of latent heating dominates.

In *Case C*, greater warming is apparent at 150 m above the Larsen C than at ~2.5 m (Figure 4.14), in line with the other cases. Note that at model level 1 temperature is significantly influenced by air-ice interactions and the fact that surface temperature cannot surpass 0°C. In Chapter 5 this is discussed in more detail.

Along the jets above the Larsen C during *Case C* at 20 UTC on 15 November (representative of daytime conditions throughout the föhn event) a leeside temperature gradient is not apparent at 150 m AMSL, and barely apparent at model level 1 (Figure 4.14c). However, relatively warm regions are, as established above, found in the immediate lee of relatively high terrain, in the 'wake' regions.

There is a marked difference in temperature gradients above the Larsen C between the most linear of the three case – *Case C* – and the most non-linear of the three cases – *Case A*. *Case A* exhibits the larger amplitude leeside föhn warming effect (evident in Figure 4.14 as well as in comparison of Figures 3.22, Figure 4.11 and Figure 4.22; in consideration of Figure 4.14 note that upwind flow direction in *Case A* is southwesterly, and the majority of the air passing over the Peninsula originates from south of Adelaide Island, hence the position of the region chosen to represent upwind conditions from which temperature anomalies in this figure are calculated). This may be due to the relative non-linearity of *Case A*. It could be speculated that the more strongly accelerated downslope föhn winds associated with upwind flow blocking and isentropic drawdown may induce a greater positive leeside temperature anomaly than the latent heating föhn mechanism in *Case C*.

Towards the eastern extremities of the Larsen C, whilst there is little difference in the amplitude of föhn warming (temperature anomaly plotted in Figure 4.14a and c) between cases *A* and *C* during daytime, nighttime cooling is far more apparent here

for *Case A* than Case *C* (Figure 4.25a and c). This is due to the greater downwind extent of turbulent mixing in the boundary layer above the Larsen C in *Case C* as a result of the higher wind speeds and greater eastward extent at near-surface level of the polar föhn jets (permitted by the lack of a prominent leeside hydraulic jump).

More generally, nighttime leeside cooling above the Larsen C is clear in all three cases (Figure 4.25). This is driven by the surface energy balance (nocturnal cooling), and is discussed further in Chapter 5.

Case B can be considered somewhere in between the two cases with regard to linearity. The lower upwind source altitude of the föhn and weaker descent above the lee slope suppresses the amplitude of the föhn warming effect in the immediate lee of the AP. The relatively weak föhn advection and expansive stagnation above the Larsen C appears to be largely responsible for the event exhibiting the weakest warming above the Larsen C of all three cases. At night above the Larsen C away from the lee slope the stable layer deepens considerably (more so than in cases *A* and *C*; Figure 4.25b).
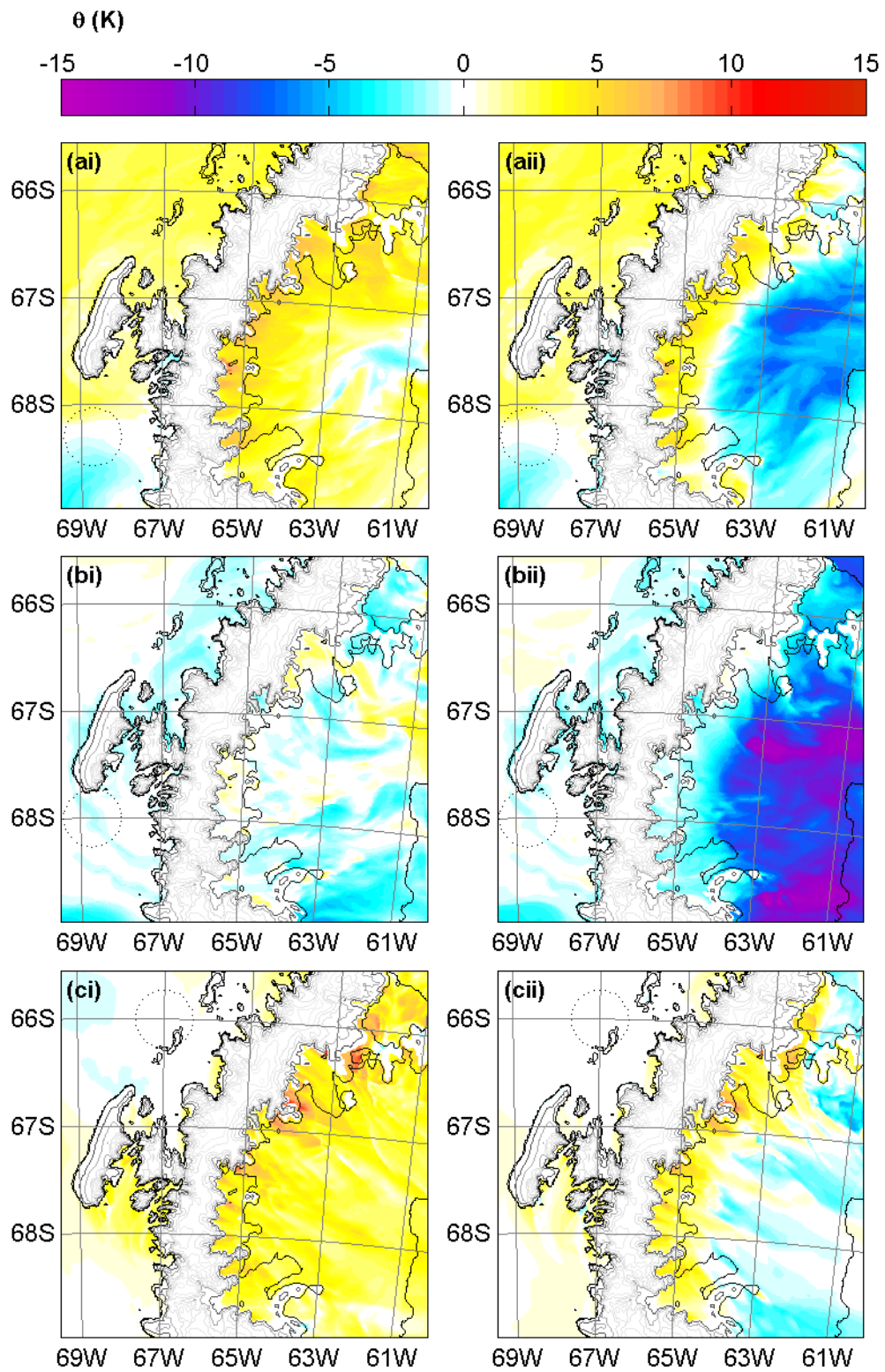
Figure 4.25 As in Figure 4.14 (θ anomaly at (i) 150 m AMSL and (ii) ~2.5 m AMSL; model level 1), but 12 hours later (at 8 UTC on (a) 5 February 2011 during *Case A*, (b) 28 January 2011 during *Case B* and (c) 16 November 2010 during *Case C*).

4.4 Summary and implications

- Two more föhn events are analysed; *Case B* with the aid of both observational and model data, and *Case C* solely with model data.

- Many of the characteristics of these new cases closely resemble those of *Case A*. Jets are again found downwind of passes along the Peninsula ridge, the constituent air being for the most part cool and moist relative to adjacent wake regions.

- As was the case for *Case A*, the MetUM performs well in the reproduction of conditions both upwind and downwind for *Case B*. There are no major inconsistencies with the observations apparent in the model results.

- Despite being characterised by slightly greater $\hat{h}$, due to differences in upwind vertical stability structure (a crest level inversion below weakly stratified air in *Case A*, versus generally increasing stratification with height in *Case B*) *Case B* depicts a more linear case of cross-mountain flow than *Case A*. Less upwind flow blocking (lower upwind dividing streamline), little evidence of low level mountain wave breaking, weaker descent above the lee slopes and the absence of a hydraulic jump result in smaller amplitude leeside föhn warming at the foot of the Peninsula. Characterised by weaker upwind flow than *Case A*, the advection of warm föhn air across the Larsen is weaker and there are expansive regions of stagnation within which air is not (even towards the end of the föhn event) sourced from west of the Peninsula within the preceding 24 hours (i.e. is not föhn-derived). For this reason föhn warming across the AP is comparatively weak.

- *Case C* describes the final couple of days of a particularly prolonged (over one month), relatively uninterrupted period of north westerly flow in the vicinity of the AP. It is characterised by significantly stronger upwind flow and weaker static stability than either cases *A* or *B*. The resultant $\hat{h}$ is considerably smaller (<1), which is reflected in the linear nature of the cross-Peninsula flow, with minimal upwind blocking, no low level wave breaking or significant hydraulic jump, comparatively weaker acceleration of flow across the Peninsula. The event constitutes a smaller amplitude cross-Peninsula warming effect close to the base of the lee slope, but, in the absence of a hydraulic jump, relatively

warm föhn air is advected right across the Larsen C, generating Boundary Layer turbulence and preventing the persistent of a deep SBL.

- In both cases *B* and *C* diabatic contributions to the cross-Peninsula temperature gradient are significant. The linearity of *Case C* (specifically the fact that air is sourced from low altitudes upwind where conditions are relatively warm and moist) is reflected in particularly small isentropic drawdown contributions and large latent heating contributions.

- It is believed that such a thorough investigation as to the relative importance of the various mechanisms to warming during a föhn event has not been achieved previously, and its results show that different mechanisms dominate dependant on upwind conditions. Sensible heating – previously rarely discussed or dismissed as unimportant as a föhn mechanism – has again (as in Chapter 3 for *Case A*) been found to provide significant, sometimes dominant, contributions to leeside warming.

Chapter 5

Air-ice interaction, boundary layer processes and Larsen C ice melt during westerly föhn

Contents

List of figures

5.1 Introduction

A key motivation behind this study and the OFCAP project as a whole was to investigate the influence of föhn flow on Larsen C Ice Shelf melt rates. As discussed in Section 2.2.2, previous studies have revealed that the highest melt rates observed at the AWS at Larsen Camp (named AWS Larsen; location marked on Figure 5.1) are associated with northwesterly flow (Van den Broeke, 2005), and that föhn conditions in this region may lead to high melt rates due to the combination of high solar radiation due to cloudless skies ("föhn clearance") and a large surface sensible heat flux due to a warm turbulent boundary layer (King et al., 2008 and Kuipers Munneke et al., 2012).
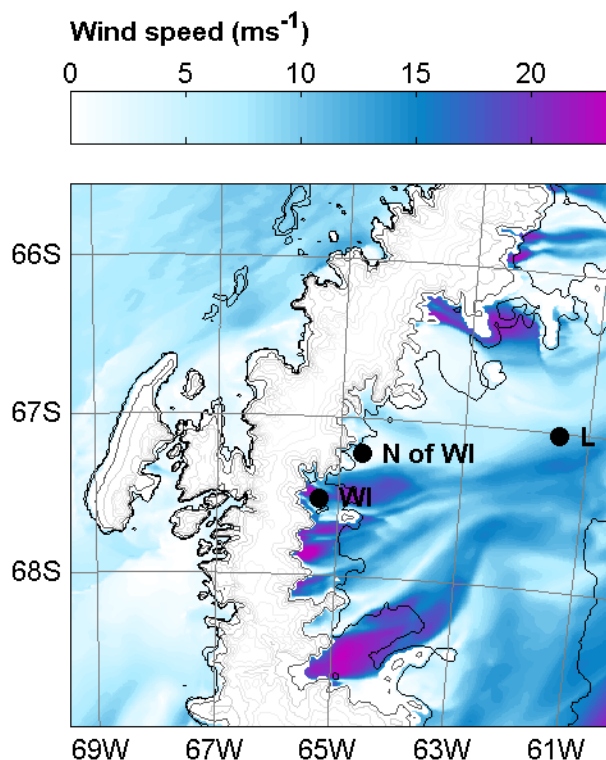
Figure 5.1: Map of important locations overlaying a MetUM 1.5 km plot of wind speed. WI = Whirlwind Inlet, N of WI = North of Whirlwind Inlet, L = Larsen Camp.

In Chapter 3 the föhn event of 4 to 5 February 2011 (*Case A*, during the OFCAP field campaign) was examined through the analysis of aircraft and MetUM data. The event was transient (lasting approximately 1 day) and characterised by non-linear phenomena due to moderate to low cross-Peninsula wind speeds and an elevated inversion. Föhn warming was found to be considerably more apparent at the base of the lee slope than further east.

In Section 3.4, previously unknown jets above the Larsen C were identified, flowing from the mouths of inlets downwind of 'gaps' in the Peninsula ridge. The strong winds of the jets were found to extend to near-surface level. As such, differences in air-surface heat and moisture fluxes should be expected between the jet and calm regions.

In Chapter 4 two more föhn cases were studied. *Case C* differed the most from *Case A*, being characterised by persistent strong northwesterly cross-Peninsula flow and consequently a relatively linear downwind flow response. The absence of a significant leeside hydraulic jump facilitated the low-level advection of strong föhn flow across the Larsen C to its eastern extent.

This chapter gives a brief insight into the effect of westerly föhn on air-ice exchanges on the Larsen C. Differences in simulated turbulent surface heat fluxes at three distinct locations on the Larsen C during *Case A* are investigated. With the aid of AWS measurements the surface energy budget at Larsen Camp (towards the eastern reaches of the Larsen C) is studied for cases *A* and *C*. Contrasts between these budgets and the ensuing melt rates are assessed with reference to the upwind forcing and boundary layer processes.

Finally, ECMWF ERA-Interim reanalysis data are used in concert with AWS data at climatological time scales to investigate whether there is a link between upwind flow characteristics and melt rates, and whether this supports the case study analysis.

5.2 Surface energy budget at Larsen Camp

5.2.1 The föhn effect at near-surface level during *Case A*

An AWS positioned at Larsen Camp (Figure 5.1), owned by the Institute for Marine and Atmospheric Research Utrecht (IMAU), is named AWS 14. It incorporates radiation sensors for the measurement of shortwave (SWF) and longwave (LWF) radiative fluxes. Furthermore, a surface energy budget (SEB) model has been employed (for details, see Kuipers Munneke et al., 2012) to ascertain turbulent heat fluxes as well as sub-surface heat fluxes.

At midday on 4 February 2011, winds detected at AWS 14 are relatively strong and largely southerly, until about 18 UTC (Figure 5.2a and b). A wind rose taken from Kuipers Munneke et al. (2012) of daily mean wind speed and direction measured by

this AWS for the period 1 February 2009 – 31 January 2011 indicates that such conditions are typical (Figure 5.3). It would appear from MetUM output that the southerlies were likely associated with a synoptic scale low pressure system residing to the east of the AP (evident in Figure 3.3a).

After 18 UTC on 4 February, the wind vector gradually rotates in a clockwise manner as wind speeds subside, becoming a weak westerly by the early morning of 5 February. The dashed vertical line in Figure 5.2 marks the approximate beginning of this transition (18 UTC on 4 February). This change in wind velocity is accompanied by increasing temperatures (Figure 5.2c) despite decreasing net downward SWF (not shown). This trend is consistent with the advection of warm föhn air into the region as night falls. Counterintuitively, however, the transition is characterised by an increase in specific humidity (Figure 5.2d) yet no increase in the upward latent heat flux (see later: Figure 5.4), indicating the low-level advection of air which is moist relative to that which it replaces. Whilst this near-surface leeside moistening appears to contradict föhn theory, it may reflect either the replacement of relatively dry continentally-derived air by maritime-sourced westerly föhn or enhanced near-surface humidities due to sublimation of the ice surface.

Both temperature and humidity time series exhibit a large amplitude diurnal cycle. After 21 UTC and until sunrise at ~7:40 UTC on 5 February, temperature assumes a broadly decreasing trend and specific humidity continues to decrease. By sunrise, winds are broadly south-southwesterly. Daytime surface temperatures are greater (reaching a peak of ~-1°C) and specific humidities are lower on 5 February than the previous day.
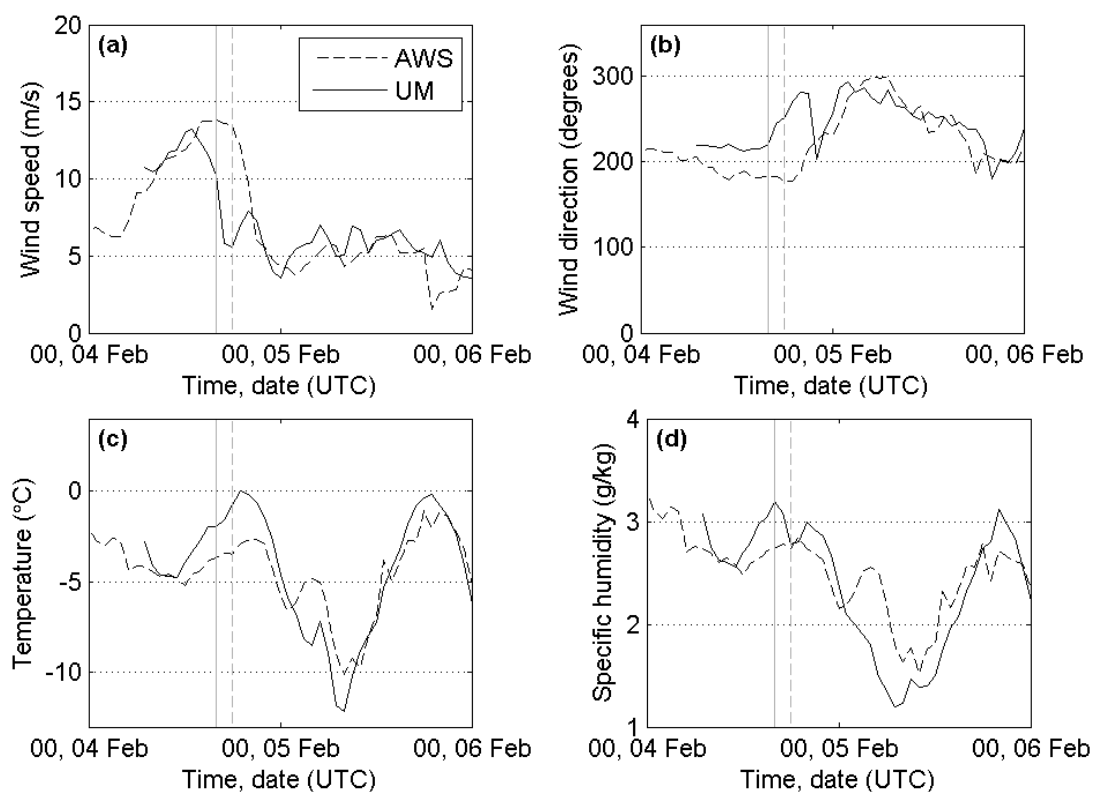
Figure 5.2: Observational fields (dashed lines) from AWS 14 (at Larsen camp; location marked in Figure 5.1) and equivalent model data (solid lines) for 4 and 5 February (during which *Case A* occurs).
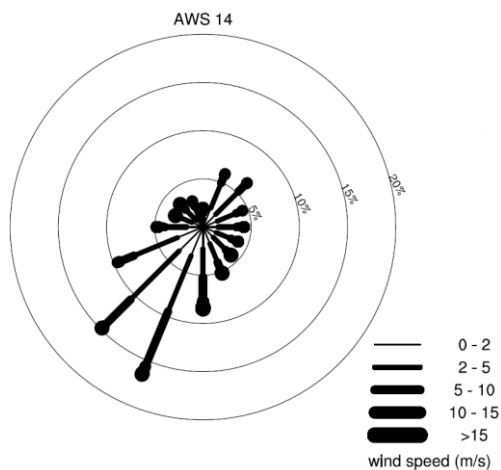
Figure 5.3: Wind rose of daily mean wind speed and direction measured at AWS 14 for the period 1 February 2009 – 31 January 2011, taken from Kuipers Munneke et al. (2012).

The model reproduces the major changes in flow velocity at AWS 14 about two hours too early (Figure 5.2). The shift towards westerly flow is associated with an abrupt warming and, in contrast to the observations, drying effect. This transition to föhn conditions is more distinct than in the observations, perhaps partly due to it occurring during day time, before the effects of nighttime cooling obscure the föhn warming signal. The premature incursion of the föhn in the model (which is noted in

Chapter 3 and investigated further in the Appendix) explains the exaggerated temperatures on the first day of the föhn event (4 February; Figure 5.2c). The following day simulated temperatures rise to values similar to those observed. The model exaggerates the amplitude of the diurnal cycle for both temperature and specific humidity.

In short, for *Case A* the model does a reasonable job of capturing the near-surface meteorology observed near Larsen Camp, although the timing of the relatively weak föhn effect is 2 hours out.

5.2.2 Comparison of surface energy budget and melt rates during a nonlinear (*Case A*) and linear (*Case C*) föhn event

5.2.2.1 Case A

In Figure 5.4, air temperature at ~2.5 m height, surface temperature, the near-surface temperature gradient with height (between the surface and ~2.5 m height), and the major components of the surface energy budget (SEB) at AWS 14 are plotted as time series of both observational and model data for *Case A*. Note that, as mentioned in Section 5.2.1, the 'observed' turbulent heat fluxes are in fact calculated as part of Kuipers Munneke et al. (2012)'s SEB model using a bulk method applied to the air layer between the level of the sensor and surface. The downward net residual flux (R_{SL}) refers to the net energy exchange between the atmosphere and the surface, which goes towards cooling, warming or melting the ice. Note that the derivation of R_{SL} treats the surface as a single layer (hence the '$_{SL}$' in R_{SL}), i.e. subsurface fluxes are not included. If the surface temperature is at freezing point and R_{SL} is positive (downward) then it is assumed that melt is occurring (such periods are marked in Figure 5.4b). That ice shelf temperatures sometimes decrease (and periods of melt end) even when R_{SL} is still positive is due to the treatment of the surface as a single layer.
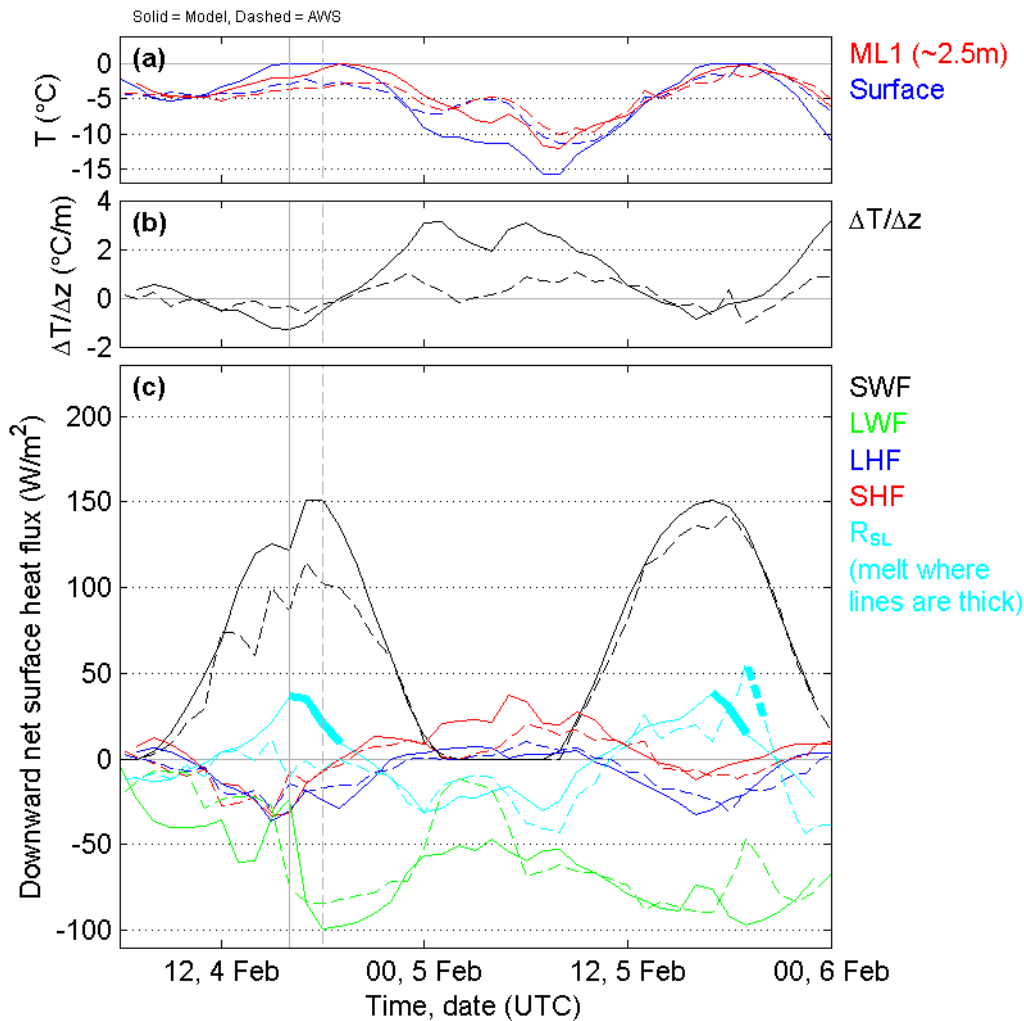
Figure 5.4: Time series of a) temperature at ~2.5 m (model level 1) and surface temperature, b) air-ice temperature gradient with height, and c) SEB components from observations (dashed lines) at AWS 14 (at Larsen camp; location marked in Figure 5.1) and equivalent model data (solid lines) during *Case A*. R_{SL} = Residual energy flux from air to ice. Where R_{SL} lines are thicker melt is assumed to be occurring (due to ice temperatures being at the melting point).

At the approximate time of the initiation of the shift in flow from strong southwesterlies to weak westerlies in the model (16 UTC; solid vertical line in Figure 5.4), a number of changes in the simulated flux components illustrated in Figure 5.4c are apparent. The downward net shortwave radiative flux (SWF) increases markedly, consistent with the clearing of clouds as the dry föhn air is advected into the region between this and the next model time step (confirmed by model data not shown). The downward sensible heat flux (SHF) increases (becomes a smaller negative value) abruptly, indicative of warmer near-surface air temperatures consistent with the influx of föhn air. Coincidentally, at this same model time step (16 UTC), ice melt is simulated to commence at the AWS 14 site. The increase in surface absorptivity/emissivity of radiation as ice turns to standing water induces a sudden

decrease in downward net longwave radiation flux (LWF). The resultant effect on R_{SL} is the initiation of a decreasing trend (after steady increase throughout the day up until that point).

The transition to föhn conditions is not clear in the observed fluxes. A decreasing trend in SWF does, however, level off despite the solar zenith having past, suggestive of the transition towards a clearer drier atmosphere. Due largely to smaller SWF, the observed residual flux is considerably smaller than that simulated on 4 February (close to 0 Wm^{-2} for the entire day in the observations), and there is no melt observed as ice sheet temperatures do not reach 0°C (Figure 5.4a). So, in the model the arrival of föhn conditions is premature and, contrary to that observed by the AWS, a period of melt (lasting at least 3 hours) is simulated. However, even before the transition to föhn conditions, simulated R_{SL} was considerably greater than that observed owing to larger downward net radiative flux (Figure 5.4c) as a result of clearer skies. For this reason, the erroneous melt simulated by the model cannot be simply attributed to the timing of föhn arrival. It is clear that surface melt is a highly sensitive quantity.

On 5 February 2011 SWF is larger than the day before in both the AWS observations and the simulation (Figure 5.4c) due to the föhn clearance (see Figure 3.16). Brief periods of melt are apparent in both observations (at least 1 hour in duration) and the simulation (at least 2 hours in duration).

Regarding relative contributions towards R_{SL}, the individual radiative fluxes clearly dominate over the individual turbulent heat fluxes. However, due to the opposing signs of the two radiative fluxes (where during the daytime |SWF|>|LWF| and during nighttime |LWF|>|SWF|), the relative significance of the turbulent fluxes is heightened when one considers the net radiative flux (SWF + LWF) and the net turbulent flux (SHF + LHF). The former reaches a föhn-period-maximum of ~83 Wm^{-2} during daytime on 5 February, whilst the latter reaches a minimum of ~-40 Wm^{-2} at a similar time.

A key observation regarding the SEB during the two-day period is that during the daytime, even during föhn conditions, the SHF is negative, indicating convective (or statically unstable) conditions i.e. the ice surface is in fact warmer than the near-surface air (evident in Figure 5.4a and b, which shows the change in temperature with height, $\Delta T/\Delta z$). This is the case for both the AWS and model data. Kuipers Munneke et

al. (2012) identified that such a convective boundary layer is common during the summer season, due to the large incoming solar radiation. Despite this, sublimation during the daytime is still apparent in negative values of LHF. During nighttime the lack of incoming radiation results in lower ice surface temperatures. The air temperature becomes higher than the ice surface temperature, leading to positive SHF. This flux acts to insulate the ice shelf at night, keeping the ice surface temperature from falling further. Note the nighttime cooling in the model is more pronounced than in the observations (Figure 5.4a). Given the dominance of the radiative fluxes in the SEB, there is no ice melt during nighttime.

So, during *Case A* maximum surface temperatures and consequently surface melt are achieved as a result of radiative rather than turbulent heat exchange.

The MetUM 1.5 km reproduces the SEB components during *Case A* with reasonable accuracy with the exception of the overestimation in SWF on 4 February and some discrepancies in LWF (Figure 5.4c).

5.2.2.2 Case C

Figure 5.5 shows, a) R_{SL} – as described above, the residual energy available for warming, cooling or melting the ice shelf where no subsurface layers are considered – and b) M_{ML} – defined as the residual energy available for ice melt in consideration of a multi-layer surface/subsurface, calculated according to Kuipers Munneke et al. (2012)'s SEB model. Note that whilst M_{ML} may seem to be a more relevant diagnostic in the context of this work, R_{SL} is useful for model-comparison (hence its use in Figure 5.4c and Figure 5.7c) since M_{ML} is not available as a MetUM diagnostic. The diurnal cycle is clearly apparent in both plots. The yellow shaded region marks the period for which upwind and synoptic conditions were discussed in Section 4.3.1 and illustrated in Figures 4.15 (with the equivalent yellow shaded region), 4.16 and 4.17; the latter two of which use data derived from a succession of MetUM 4 km simulations. Throughout this period – except for the final MetUM 4 km simulation – consistently small westerly to northwesterly $\hat{h}$ is simulated (Figure 4.17b). Simulated daytime melt rates are generally very high during this period.
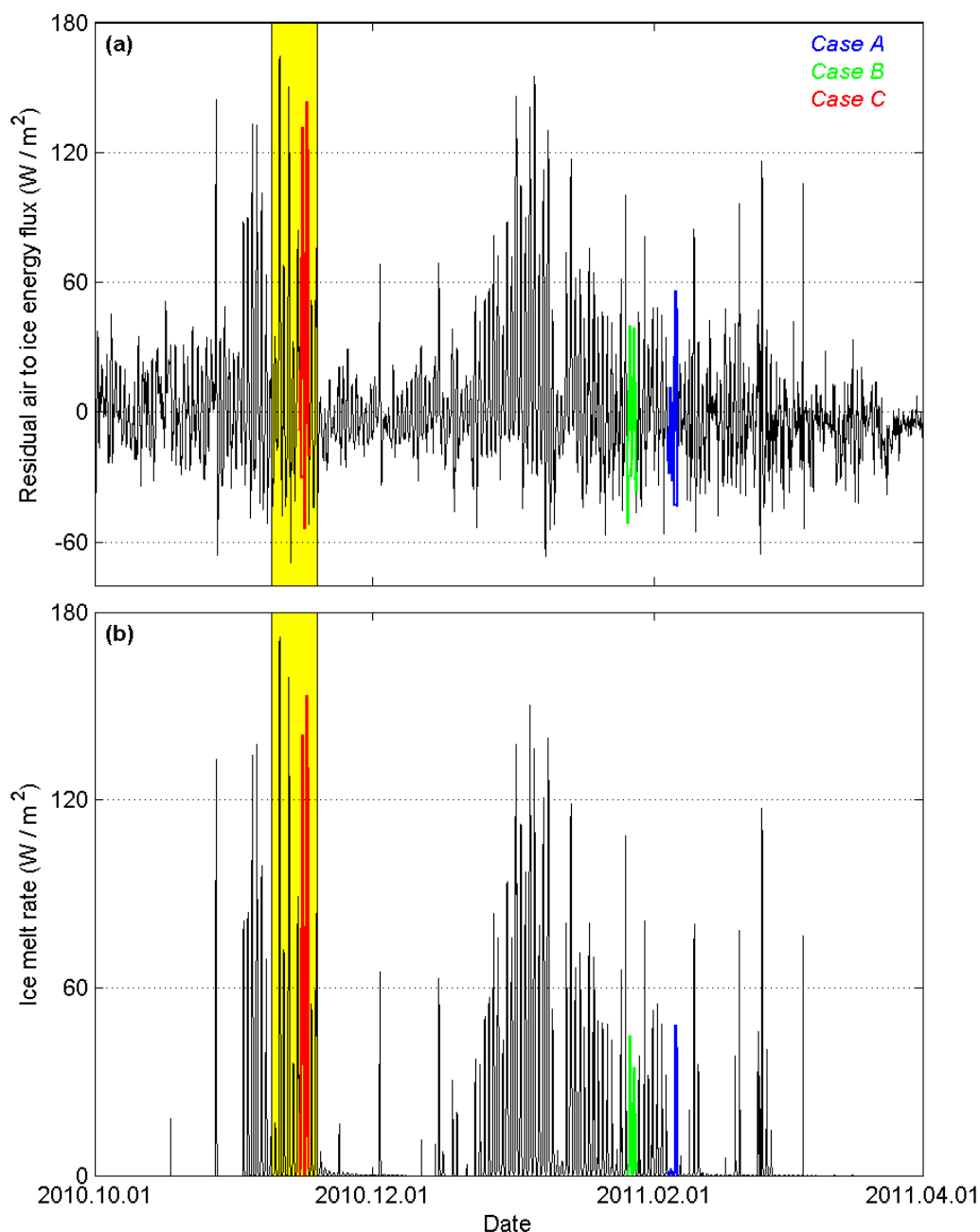
Figure 5.5: Time series of a) R_{SL} (residual air to ice energy transfer) and b) M_{ML} (ice melt rate) during the 2010/11 melt season from AWS 14 data. The section coloured cyan marks *Case A*, green marks *Case B* and red marks *Case C*. The period shaded yellow marks that for which synoptic conditions were discussed in 4.3.1 and is equivalent to the period shaded yellow in Figure 4.15.

This figure shows that Cases *A* and *B* are characterised by moderate rates of melt, with *Case A* rates peaking at 48 Wm^{-2} (equating to ice melt of ~13.5 mm of water per day). *Case C* exhibits much larger melt rates, peaking at over 150 Wm^{-2} (over 42 mm of water per day). The mean value of M_{ML} during 15 November 2010 is 38 Wm^{-2} (10.7 mm of water per day). This rate, if taken to be the mean value across the entire

Larsen C on this day, and ignoring re-freezing of melt water, translates to 135 million tonnes of melt water generated across the entire ice shelf.

Figure 5.6 shows surface meteorology at AWS 14 for *Case C* (equivalent to Figure 5.2). Observed near-surface winds are largely northwesterly throughout 15 November and persisting until ~8 UTC on 16 November 2010, after which flow direction becomes changeable and wind speeds weaken (Figure 5.6a and b). Wind speeds average ~9 ms^{-1} during the period of predominantly northwesterly flow; stronger than the ~5 ms^{-1} mean speed characterising the period of southwesterly to northwesterly near surface flow during *Case A* (21 UTC 4 February 2011 until 18 UTC 5 February 2011; Figure 5.2a and b).
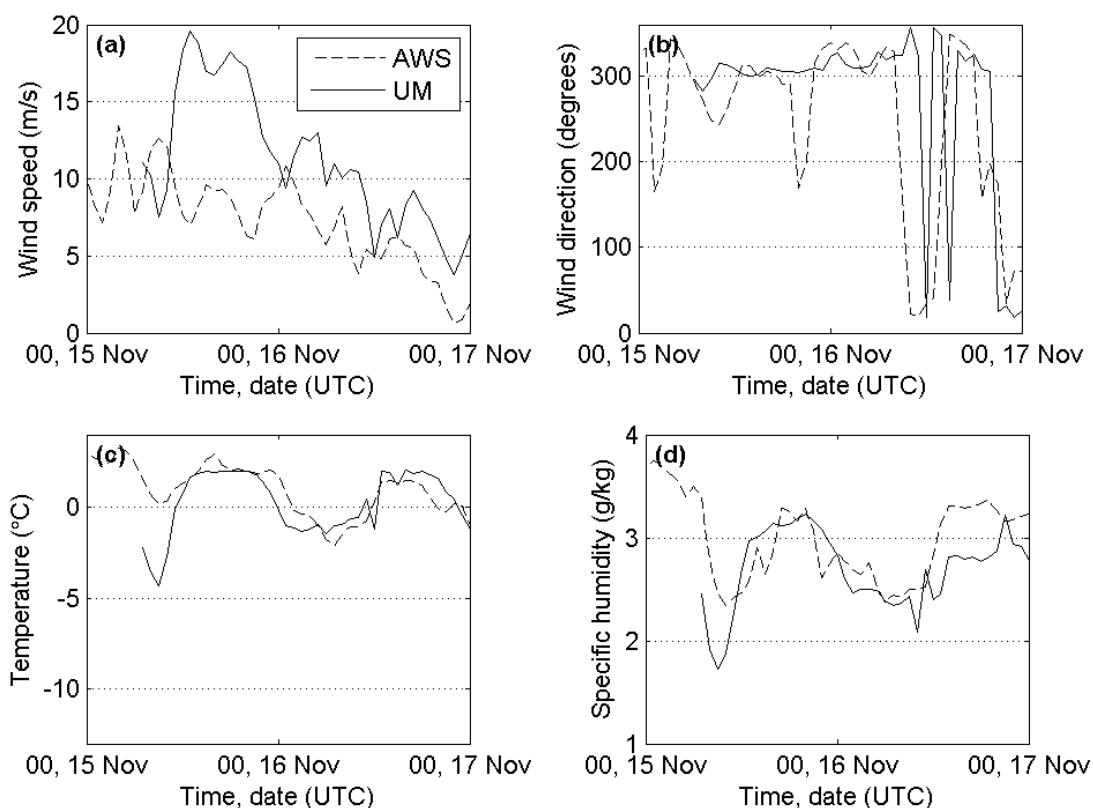
Figure 5.6: As in Figure 5.2 but for *Case C*.

Whereas during *Case A* near-surface air temperatures remained below 0 °C, during *Case C* they rise to a maximum of almost 3 °C at 16 UTC on 15 November, and ~1.5 °C during the afternoon of 16 November (Figure 5.6c). Furthermore, nighttime temperatures do not plummet as in *Case A*, with minimums of just above 0 °C and ~-2 °C during the early mornings of 15 and 16 November respectively, in contrast to ~-10 °C during *Case A* (Figure 5.2c). *Case C* specific humidities at AWS 14 are larger than during *Case A* (Figure 5.2d and Figure 5.6d). This is probably at least partly due to the

lower altitude upwind sourcing of föhn air in *Case C* (as discussed in Section 4.3), but also perhaps due to greater surface sublimation rates.

The MetUM 1.5km simulation relatively accurately reproduces the near-surface flow direction during *Case C* (Figure 5.6b), but overestimates wind speeds (Figure 5.6a), particularly on 15 November between 11 UTC until 23 UTC. Spatial plots reveal that the model simulates the particularly strong winds in the vicinity of AWS 14 due to the Cabinet Inlet polar föhn jet passing through the region. It could be that the path of the jet is inaccurately reproduced in the model (near-surface wind speeds away from jet maxima's at a similar distance from the AP are of similar values to those observed at AWS 14), or perhaps that the model overestimates wind shear immediately above the surface (i.e. that the strong winds of the jet pass a little higher above the ice than simulated).

The model significantly underestimates both temperature and humidity from its initiation until ~5 hours into the simulation (late morning of 15 November). Interestingly, the accuracy subsequently improves significantly, particularly in the case of temperature, for which the model otherwise performs very well. In the following I focus on the period that is accurately modelled.

Figure 5.7 is the *Case C* equivalent of Figure 5.4. Figure 5.7b shows that daytime R_{SL} is considerably larger during *Case C* than *Case A*, with a longer melt period consisting of higher melt rates (as already shown in Figure 5.5b). The maximum observed R_{SL} during *Case C* on 15 (16) November 2010 was 132 (143) Wm^{-2}. During the melt periods net radiation contributed ~99 % of R_{SL}, with net turbulent heat making up the small remainder. Splitting the turbulent heat fluxes into separate components, the SHF contributed ~21 %, whilst LHF removed energy equivalent to ~20 % of R_{SL} from the ice, i.e. in this case the turbulent heat fluxes are approximately equal in magnitude but opposite in sign. During *Case A* the maximum R_{SL} was 56 Wm^{-2} on 5 February 2011, and contributions towards R_{SL} during the relatively short period of melt on this day are as follows: net radiative warming of the ice shelf ~164 % and net turbulent cooling ~64 % (comprising SHF cooling of ~20% and LHF cooling of ~44%) of mean R_{SL}.
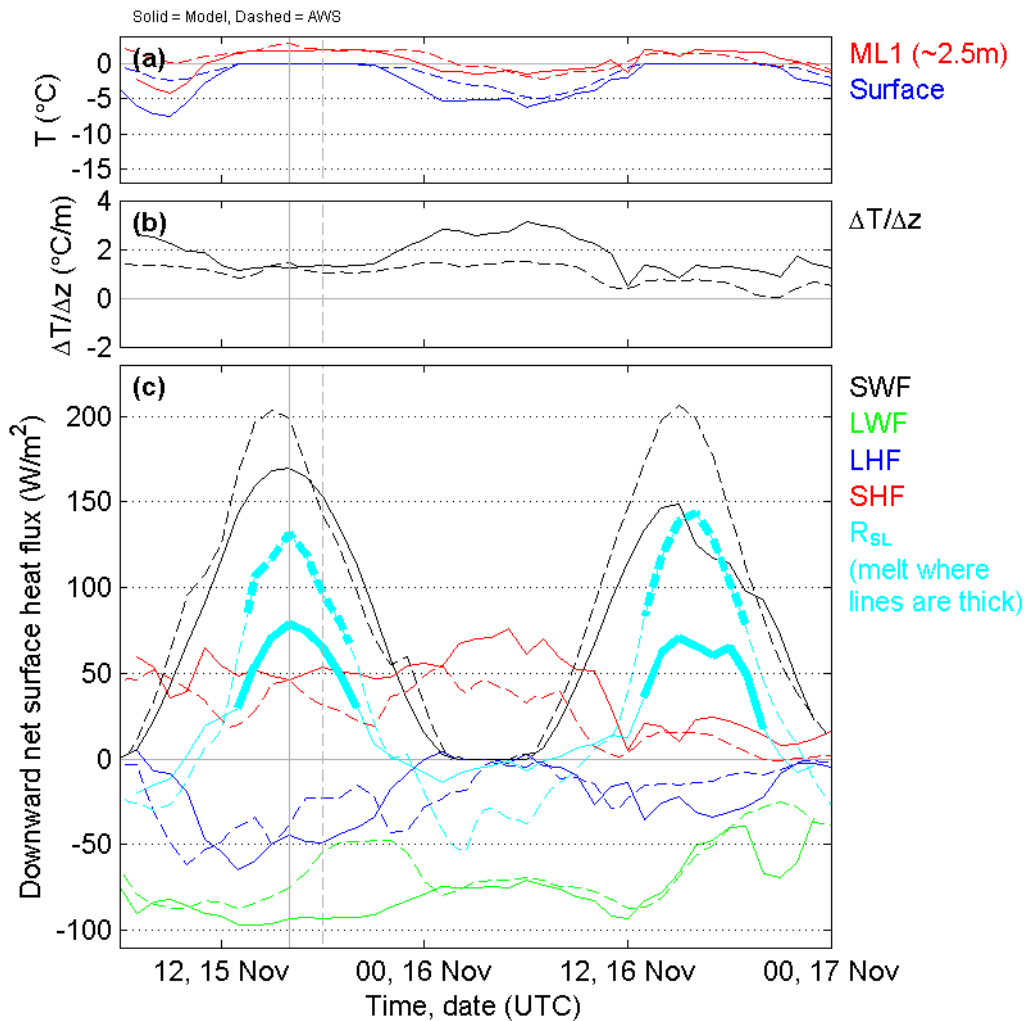
Figure 5.7: As in Figure 5.4 but for *Case C*.

The major reasons for greater daytime R_{SL} during *Case C* than *Case A* are larger SWF (compare Figure 5.4b and Figure 5.7b) and larger SHF. SWF is significantly larger during *Case C* due to the time of this event being closer to that of the summer solstice, and the skies, as in *Case A*, being cloud-free. SHF in *Case A* was negative during the middle of the day (i.e. contributed a cooling effect on the ice) due to near-surface air temperatures being lower than surface temperatures (which were at or near the melting point). During *Case C* the near-surface air is warmer than the ice (i.e. positive $\Delta T/\Delta z$) throughout (Figure 5.7a) and near-surface wind shear acts to maintain relatively large SHF towards the surface.

King et al. (2008) used afternoon aircraft measurements in the vicinity of AWS 14 to, in the same manner as above, gauge contributions towards R_{SL} during a föhn event in January 2006. Net radiative flux was found to contribute ~92 %, and SHF ~25 % towards mean observed R_{SL} of 52 Wm^{-2}. This 2006 event, exhibiting similar values of SWF as *Case C* (at the same time of day), appears to be characterised by lower melt

rates due to greater negative values of LWF and smaller (though still positive) SHF (suggestive of a weaker föhn event).

In some respects the MetUM performs well in its reproduction of the heat fluxes illustrated in Figure 5.7. SHF and LHF are relatively well captured (Figure 5.7b), though SHF is generally overestimated, in correspondence with overestimated values of air-ice $\Delta T/\Delta z$ (Figure 5.7a).

LWF is very well reproduced on 16 November 2010, though during the latter half of 15 November values are considerably underestimated (Figure 5.7b). Apart from this discrepancy, the other major disagreement between model and observations is in peak SWF, which is significantly underestimated by the model, especially during 16 November, where the error peaks at almost 75 Wm^{-2}. During 15 November and the first half of 16 November, there are no clouds simulated in the model above the Larsen C, and so the error is attributable to either surface albedo or atmospheric humidity. The only available observations for leeside humidity are at surface level at AWS 14, and there are no major problems with the model's reproduction of these (Figure 5.6d). Incorrect representation of albedo over ice shelves is known to be a common problem in NWP models (Birch et al., 2009). Further analysis of the individual components of the radiation budget (not shown), however, suggests that both surface albedo and atmospheric absorption of incoming radiation were responsible for the discrepancy. The errors in the radiative fluxes provide the principle cause for the underestimated MetUM values of daytime R_{SL} and hence underestimated melt rates (Figure 5.7b).

5.2.2.3 Differences in boundary layer processes between cases A and C

Figure 5.8 shows early morning profiles directly above AWS 14 of various model diagnostics at 6 UTC on 5 February during *Case A* and 6 UTC on 16 November during *Case C*. Note that 6 UTC is 1-2 hours (4-5 hours) before sunrise (after sunset) in *Case A*, and less than an hour (4-5 hours) before sunrise (after sunset) in *Case C*. This time was chosen since, being just before sunrise, it coincides roughly with the lowest temperatures in the diurnal cycle. Similar plots are presented in Figure 5.9 for daytime conditions, at 15 UTC.

The predominantly stronger boundary layer winds and greater near-surface temperatures during *Case C* are evident (Figure 5.8a and b). Although temperatures at

250 m above surface are similar, below this level static stability is considerably weaker in *Case C* (Figure 5.8c); hence the warmer near surface air.
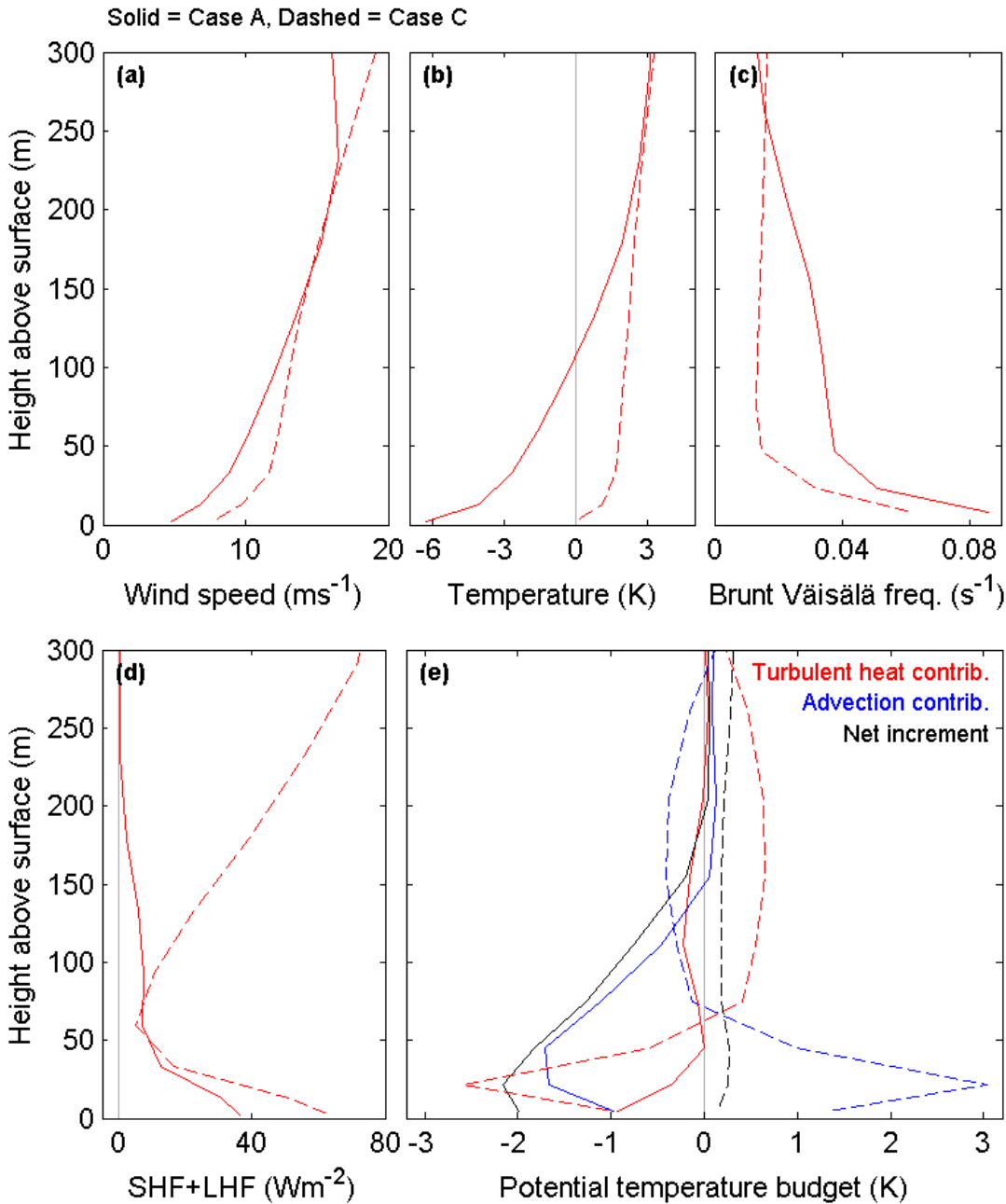
Figure 5.8: Vertical profiles of model diagnostics taken from the MetUM 1.5 km simulation above AWS 14 at 6 UTC on 5 February during *Case A* (solid lines) and 6 UTC on 16 November during *Case C* (dashed lines). Note that at these times SWF = 0 (0) Wm^{-2} and LWF = ~-60 (~-70) Wm^{-2}, giving a net surface heat flux of ~-25 (~-5) Wm^{-2} for *Case A* (*Case C*).

Figure 5.8d shows the downward net turbulent heat flux (THF; the sum of SHF and LHF), and Figure 5.8e shows the contributions to the θ budget at this location for the half hour period between 6 and 6:30 UTC by turbulent heat exchange ($\Delta\theta^{TH}$, where Δ indicates a change over the half hour period) and advection ($\Delta\theta^{A}$). Also plotted in Figure 5.8e is the net change in θ ($\Delta\theta^{net}$) during this period. Note that this is

not quite the sum of the $\Delta\theta^{TH}$ and $\Delta\theta^A$ terms, since there are other contributions (not plotted) of which only that of radiative heat exchange is significant, providing a small (relative to the $\Delta\theta^{TH}$ and $\Delta\theta^A$ contributions) negative contribution at all levels. Note that Figure 5.8e corresponds closely but not directly with the other profiles in Figure 5.8, since data making up the former are time-averaged (between 6 and 6:30 UTC) and are on different vertical levels.

Figure 5.8d reveals very large downward THF – of over 90 Wm^{-2} – at 300 m in *Case C*, decreasing downwards to ~60 m above the surface, below which THF increases once more. The positive gradient in SHF with height between ~60 m and 300 m implies a positive contribution to the temperature budget between these levels (as confirmed in the plot of $\Delta\theta^{TH}$ for *Case C* in Figure 5.8e) due to turbulent heat cascading down from above. Conversely, the negative gradient below ~60 m implies a negative contribution (Figure 5.8e) as the heat lost to the surface is greater than that gained from above. In the *Case A* profile, THF is greatest at the lowest level (~2.5 m above surface), decreasing sharply upwards until 30-60 m height. This indicates turbulent 'drainage' of heat from the low-level air to the surface (note the negative values of $\Delta\theta^{TH}$ for *Case A* below ~40 m in Figure 5.8e). This 'drainage' decreases in magnitude dramatically upwards from the surface up to ~60 m, then slowly above that.

Note from Figure 5.8e that the negative values of $\Delta\theta^{TH}$ at near-surface level (below ~60 m) are of greater magnitude (inducing a greater cooling effect) in *Case C* than *Case A*. Despite this, $\Delta\theta^{net}$ is positive in *Case C*. This is because the negative $\Delta\theta^{TH}$ is offset by $\Delta\theta^A$ of slightly larger magnitudes. So, despite the large turbulent heat loss to the ice shelf in *Case C* (larger than in Case A; Figure 5.8d) and the associated sapping of heat from the near-surface levels, in situ warming nevertheless occurs due to the advection of relatively warm föhn air from the northwest.

In *Case* C, above ~60 m both $\Delta\theta^{TH}$ and $\Delta\theta^A$ switch signs, with the positive $\Delta\theta^{TH}$ of larger magnitude than the negative $\Delta\theta^A$. So, in this section of the profile it is the turbulent cascading of heat down from above – inducing a warming of the incoming air – that maintains the weak (relative to *Case A*) static stability of the air column.

In *Case A*, both $\Delta\theta^{TH}$ and $\Delta\theta^A$ are negative below ~150 m, resulting in negative values of $\Delta\theta^{net}$, becoming large in magnitude at near-surface level (minimum value of under -2 K at a height of ~20 m).

It should be noted that Figure 5.8 is for one time step only. Though representative of the key boundary layer processes typical of each case at this location, there are changes in the various fluxes and potential temperature budget contributions throughout the night. For example, boundary layer warming did not occur all night during *Case C*. Earlier in the night net boundary layer cooling occurred as conditions adjusted to the decreasing solar radiation. Despite this there is, almost consistently throughout the night, a balance between $\Delta\theta^{TH}$ and $\Delta\theta^{A}$ – one compensating for the other, resulting in small negative values of $\Delta\theta^{net}$ during the early stages of the night, and small positive values of $\Delta\theta^{net}$ towards sunrise. Rarely are both $\Delta\theta^{TH}$ and $\Delta\theta^{A}$ negative, as they are regularly overnight during *Case A*. Nevertheless, during *Case A* after 6 UTC $\Delta\theta^{net}$ becomes positive as the atmosphere warms with sunrise.

Figure 5.9 constitutes similar profiles though for daytime at 15 UTC on 5 February 2011 during *Case A* and 15 UTC on 15 November 2010 during *Case C*. Note that in contrast to Figure 5.8 the N and θ budget plots are not shown, whilst the two turbulent heat fluxes are plotted individually in Figure 5.9c. This time of day was chosen since it is late enough in the day to be representative of daytime conditions on the ice shelf whilst not being too late as to miss föhn conditions in *Case A* (during which cross-Peninsula flow subsided gradually throughout the day of 5 February 2011).

Case C winds are considerably stronger and temperatures considerably higher than those characterising *Case A* throughout the depth of the profile (Figure 5.9a and b). *Case A* (*C*) near-surface temperature is below (above) freezing; consistent with the negative (positive) air-ice $\Delta T/\Delta z$ in Figure 5.4a (Figure 5.7a). This difference appears to be partly due simply to *Case C* being characterised by a warmer local air mass (derived as it is from the northwest as opposed to the southwest), but also to the stronger föhn flow, with warm winds continually flooding into the region (see discussion of $\Delta\theta^{A}$ in relation to Figure 5.8e above) and turbulent mixing encouraging the exchange of heat. In testament to the latter, in *Case C*, below ~230 m large turbulent heat exchange is evident, with consistently large positive SHF carrying heat to the surface, offset by large negative LHF returning heat upwards (Figure 5.9c). The net exchange of turbulent heat between the atmosphere and ice shelf is negligible. In *Case A* the near surface levels are warming at this time due to turbulent exchange of heat (i.e. positive

$\Delta\theta^{TH}$; note the positive gradient in THF (SHF + LHF) with height below ~90 m in Figure 5.9c) from the ice shelf to the air above (i.e. convective conditions).
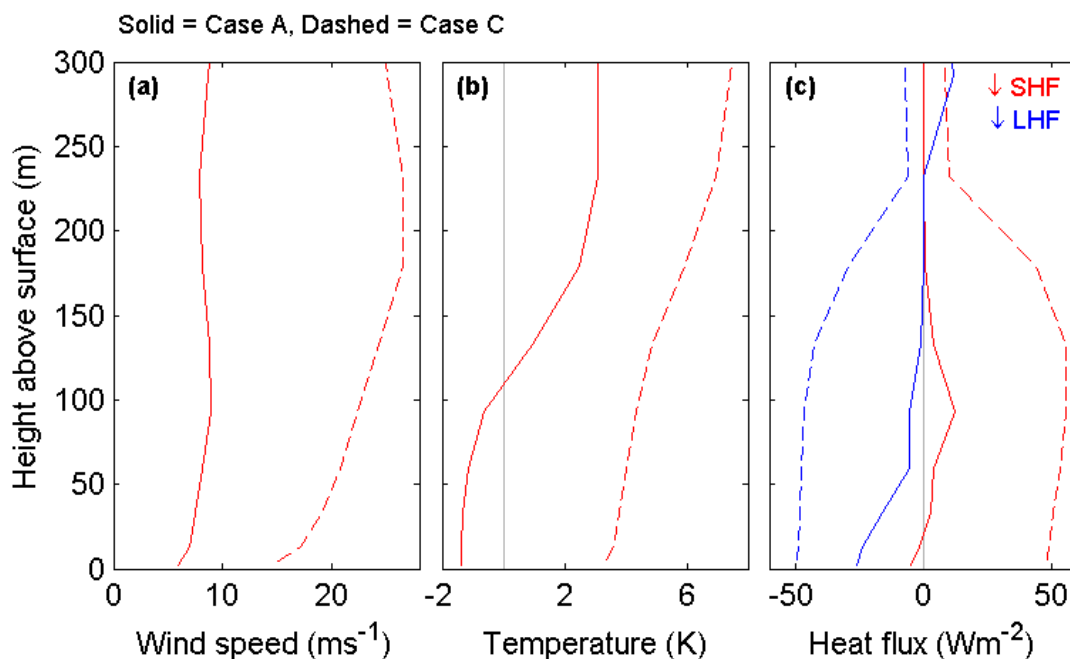
Figure 5.9: As in Figure 5.8 but at 15 UTC on 5 February during *Case A* (solid) and 15 UTC on 15 November during *Case C* (dashed). Note that at these times SWF = 140 (170) Wm^{-2} and LWF = ~-90 (~-95) Wm^{-2}, giving a net surface heat flux of ~20 (~70) Wm^{-2} for *Case A* (*Case C*).

In short, in *Case C* nighttime boundary layer temperatures are maintained via a balance of downward turbulent heat flux and the advective influx of warm air. During *Case A* these mechanisms are relatively weak and so near-surface temperatures plummet overnight (compare Figure 5.2c and Figure 5.6c). The differences in $\Delta\theta^{TH}$ and $\Delta\theta^{A}$ are in line with discussion in Sections 4.3.2.3 and 4.3.3 regarding the perpetuation eastwards above the Larsen C of warm turbulent föhn flow at low level in *Case C* versus the hydraulic ascent of the föhn close to the AP's eastern slopes in *Case A*.

Due to the interdependency of boundary layer and surface temperatures, the maintenance of high near-surface air temperatures during the night helps maintain relatively warm ice temperatures (it can be seen that surface THF in Figure 5.7b for *Case C* is consistently larger than that in Figure 5.4b for *Case A*) i.e. the relatively warm air insulates the ice shelf from excessive cooling at night. This means that a smaller negative temperature 'deficit' is developed in *Case C*, the recovery from which is far quicker, with simulated daytime ice melt periods initiating 3 – 4 hours earlier than in *Case A* (Figure 5.4b and Figure 5.7b). It should be noted however that the larger SWF in *Case C* – due to its occurrence being closer to the summer solstice – also significantly aides the recovery of surface temperatures towards the melting point.

During the daytime negligible surface THF (SHF and LHF offset each other; Figure 5.7b) in *Case C* contributes towards a prolonged melt period relative to that during *Case A*. During *Case A* daytime air-surface ΔT/Δz is negative (Figure 5.4a) and THF contributes a cooling effect (THF reaches a minimum of -40 Wm^{-2}) on the ice shelf (both SHF and LHF are negative; Figure 5.4b).

5.2.2.4 Summary

In this section two contrasting föhn cases have been examined in the context of air-ice interaction at a location towards the eastern reaches of the Larsen C. During the more linear föhn event of *Case C*, strong föhn winds helped to maintain near surface temperatures above 0°C via warm air advection and turbulent mixing manifested by downward sensible heat exchange. During the non-linear *Case A*, weaker föhn winds are unable to prevent the development of a strongly statically stable boundary layer during the night, whereupon the ice shelf cools dramatically. Furthermore, background air temperatures during *Case C* are greater than those during *Case A*. In *Case C*, due to turbulent heat flux from the air to the ice being largely balanced (the sensible and latent heat fluxes cancelling each other out, as opposed to both fluxes drawing heat away from the surface, as is in *Case A*), together with greater downward shortwave radiation, melt period durations are longer and melt rates are substantially higher in the more linear *Case C*, than in the weaker non-linear *Case A*.

5.3 Spatial variation in surface energy balance across the Larsen C during cases *A* and *C*

5.3.1 Differences between cases *A* and *C*

In Section 5.2 time series and profiles of observed and simulated diagnostics at a single location (AWS 14 at Larsen Camp) were presented and discussed. In this section variability across the Larsen C is investigated using model data, so that the results presented in Section 5.2 may be contextualised spatially and key differences between regions may be investigated.

Figure 5.10 and Figure 5.11 show net surface heat flux across the Larsen C at nighttime and daytime respectively during cases *A* and *C*. The times chosen for these plots are the same as those chosen for Figure 5.8 and Figure 5.9 (6 UTC for Figure 5.10

and 15 UTC for Figure 5.11). Figure 5.10a shows that the net nighttime cooling at AWS 14 (where the net surface heat flux $\approx$ -25 Wm^{-2}; Figure 5.8) for *Case A* extends across the majority of the ice shelf at 6 UTC 5 February 2011, despite small isolated regions of warming. Figure 5.10b shows that for *Case C* at the same time of day there are large regions of both surface cooling and surface warming on the ice shelf. The regions of cooling constitute smaller amplitude heat fluxes, and the regions of warming cover a larger area than for *Case A* at the equivalent time (Figure 5.10a). Consistent with greater heat loss from the surface, nighttime temperatures on the ice shelf are considerable warmer during *Case C* than *Case A* (Figure 5.12). In both cases the warmest ice temperatures are found in bands extending downwind from the mouths of the major inlets, beneath polar föhn jets (the jets are labelled in Figure 5.12). This spatial heterogeneity is investigated in Section 5.3.2. Note that there is no nighttime ice melt in either cases.

During the day surface warming is apparent across almost the entire ice shelf during *Case A* at 15 UTC on 5 February 2011 (Figure 5.11a), and the entire ice shelf during *Case C* at 15 UTC on 15 November 2010 (Figure 5.11b). The exception in the case of the latter is in the south-east corner, which coincides with a region of cloud cover (and hence smaller SWF). Consistent with the single grid point comparison at Larsen Camp, the magnitude of simulated daytime surface heat flux is considerably greater right across the Larsen C during *Case C* than during C*ase A* (Figure 5.11).

Figure 5.13 shows daytime surface temperature for both cases, at the same times during each case as used for Figure 5.11). In *Case C* the entire ice sheet is at the melting point (Figure 5.13b), whereas in *Case A* temperatures beneath the major polar föhn jets (particularly apparent beneath the WI, Seligman Inlet and MOI jets) and in a large region to the northeast of the Larsen C are up to 3.5 K lower than the melting point (Figure 5.13a). Note that AWS 14 is located within this region to the northeast of the Larsen C. By 18 UTC (three hours later) the vast majority of the ice shelf is at the melting point. Note that melt at AWS 14 on 5 February is simulated to begin at 17 UTC (Figure 5.4c).
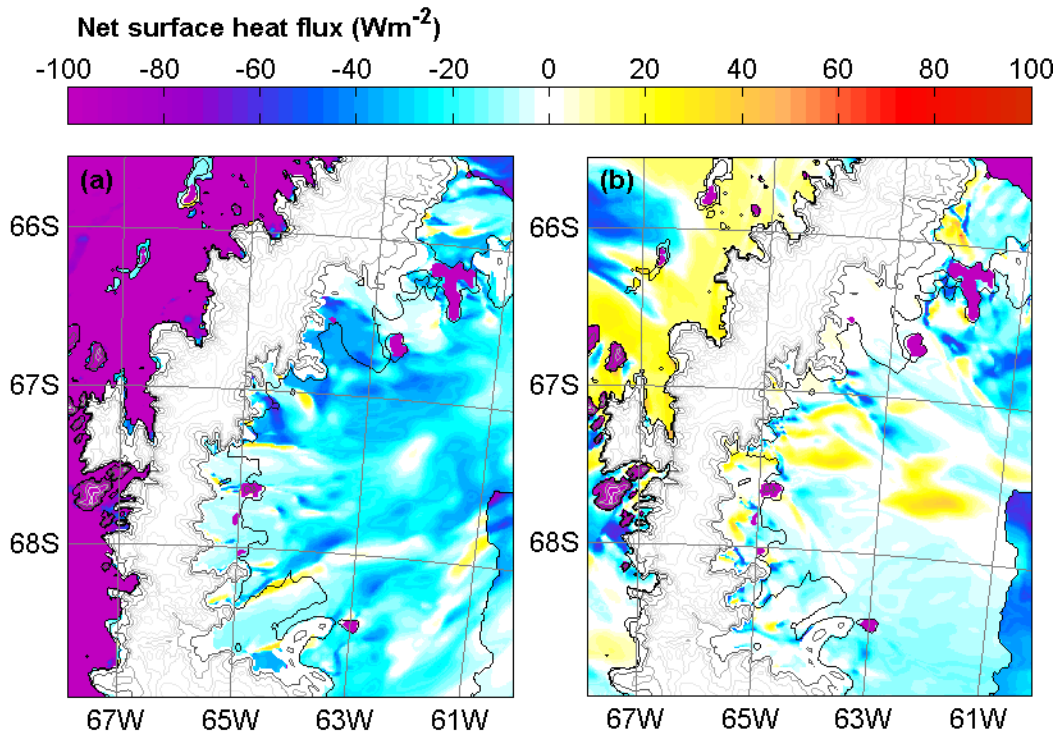
Figure 5.10: Net surface heat flux (positive downwards) at 6 UTC on a) 5 February 2011 during *Case A* and b) 16 November 2010 during *Case C*.
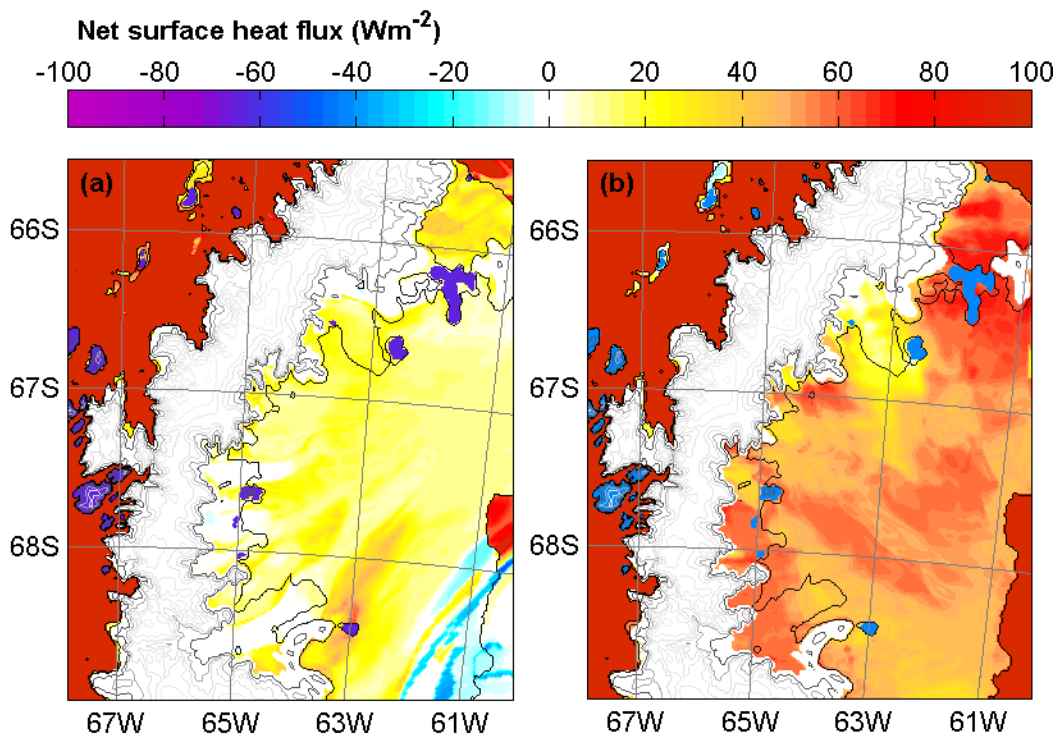
Figure 5.11: As in Figure 5.10 but for 15 UTC on a) 5 February 2011 during *Case A* and b) 15 November 2010 during *Case C*.
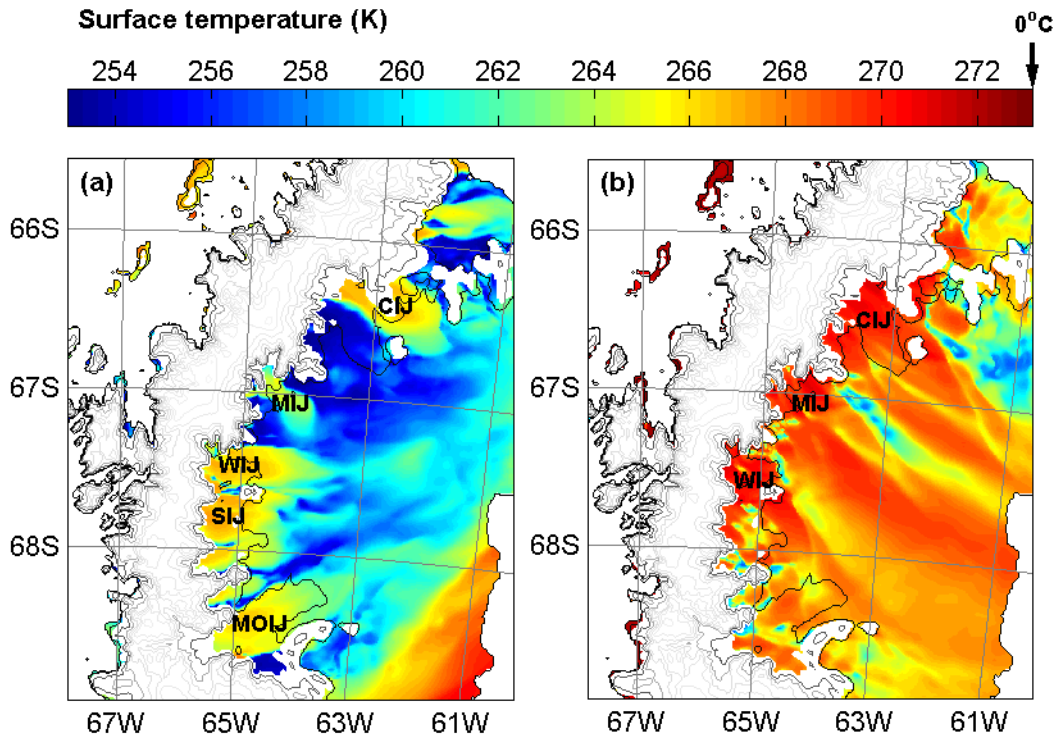
Figure 5.12: Ice temperature at 6 UTC on a) 5 February 2011 during *Case A* and b) 16 November 2010 during *Case C*. Note that 0°C is the highest temperature on the colour scale (dark red). The positions immediately downwind of the AP's lee slopes of the following polar föhn jets are given: CIJ = Cabinet Inlet jet, MIJ = Mill Inlet jet, WIJ = Whirlwind Inlet jet, SIJ = Seligman Inlet jet, MOIJ = Mobil Oil Inlet jet.
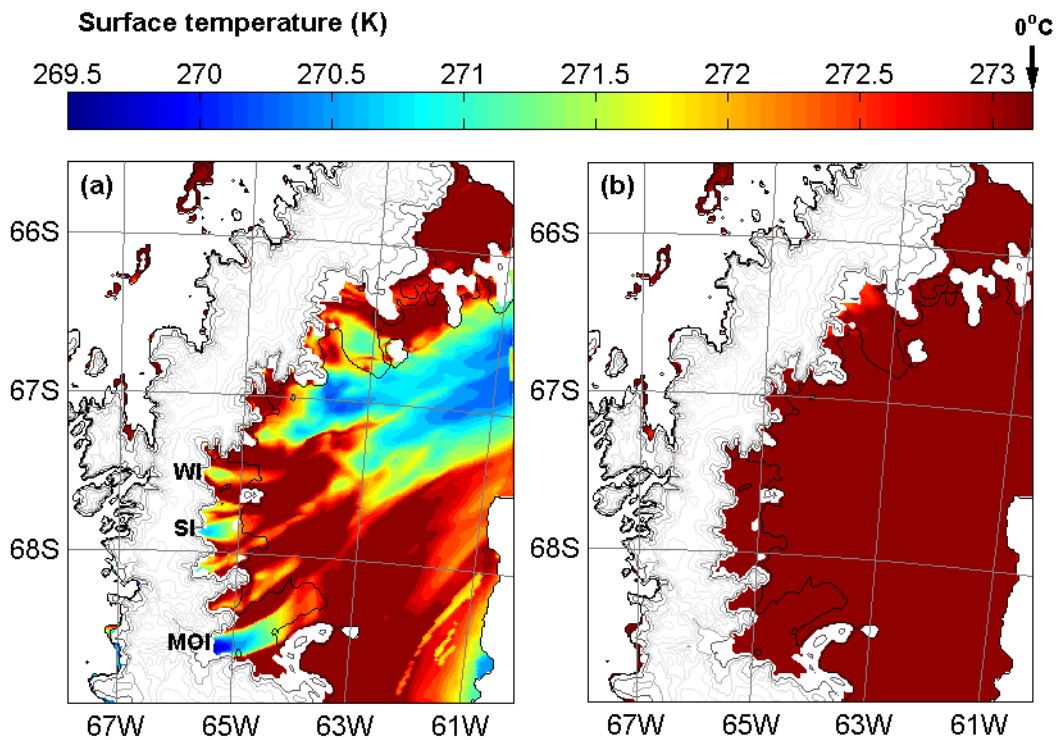
Figure 5.13: As in Figure 5.12 but for 15 UTC on a) 5 February 2011 during *Case A* and b) 15 November 2010 during *Case C*. WI = Whirlwind Inlet, SI = Seligman Inlet, MOI = Mobil Oil Inlet.

It is apparent from Figure 5.13a and from similar plots for earlier and later times (not shown) that surface temperatures reach melting point quickest during the afternoon of 5 February 2011 (during *Case A*) close to the foot of the AP's lee slopes, where the föhn effect is greatest. However, as described above, surface temperatures beneath the strongest polar föhn jets (within the mouths of many of the inlets) are distinctly cooler than those in the adjacent wake regions. This is investigated further in Section 5.3.2.

5.3.2 Spatial variation in the immediate lee of the AP

At the base of flight profiles within the WI jet (for flight track see Figure 3.2) during flight 176 (early morning of 5 February) a stable near-surface layer is observed and humidities up to ~150 metres above the surface are anomalously high (Figures 3.9 and 3.12). With distance downwind within the jet the stable layer appears to deepen and strengthen (due to cooler near-surface temperatures; Figure 3.12b) whilst near-surface humidities increase (Figure 3.12c). Although a stable near-surface layer is also apparent above the Larsen C in a region of calm flow north of WI (at the site named *Larsen West* in Chapter 3 – see Figure 3.2b for location, which is roughly equivalent to the N of WI wake region used in Chapter 3 trajectory analysis – see Figure 3.12 for location), near-surface humidities are not distinctively moist (Figure 3.9). As in Section 5.2, the evolution of the near-surface meteorological conditions is examined to investigate these observations.

Figure 5.14 and Figure 5.15 show MetUM 1.5 km simulated temperature at ~2.5 m (model level 1) and surface temperature, wind speed components at ~2.5 m, and turbulent heat fluxes at ~2.5 m for single grid point locations within the WI jet and N of WI wake regions respectively (see Figure 5.1 for locations). The strong westerly component of flow (U) within the jet and largely stagnant conditions within the wake are apparent (Figure 5.14b and Figure 5.15b).

Whilst the westerly jet persists, relatively large amplitude sensible and latent surface heat fluxes are simulated (Figure 5.14b and c). This is to be expected given the positive downwards air-ice temperature gradient (Figure 5.14a) and the turbulence generated by large wind shear in the boundary layer. The sensible heat flux is very large, peaking at ~150 Wm^{-2}, transferring heat from the föhn air to the cool ice surface. This peak corresponds approximately with sunrise, when the air-ice

temperature gradient is greatest. The latent heat flux, associated with sublimation of the ice at the surface, acts in the opposite direction. This provides a likely explanation for the moist near-surface conditions observed within the jet, as described above. The dominance of the downward sensible heat flux over the upward latent heat flux during nighttime is also consistent with the strong surface inversion. The fact that the inversion deepens, whilst humidities increase with distance downwind within the jet, is consistent with surface turbulent heat flux as the cause, with air-ice heat and moisture fluxes inducing Lagrangian cooling and moistening of the near-surface flow, and turbulent mixing within the boundary layer subsiding as the jet progresses downwind above the smooth ice surface. Within the wake region, on the other hand, stagnant conditions lead to a decoupling of atmosphere and surface, with small amplitude turbulent heat and moisture fluxes (Figure 5.15c). Surface temperatures plummet to nearly -20°C beneath the N of WI wake during night (Figure 5.14a), whilst beneath the WI jet they remain above -7°C (Figure 5.15a). This is a result of the insulating effect of the large nighttime turbulent flux of heat from the air within the jet to the ice below.

Figure 5.12a shows that this warm jet signature is apparent in ice temperatures beneath not just the WI jet, but all major polar föhn jets at nighttime (6 UTC) during *Case A*. Figure 5.12a shows that the same is true for *Case C*, during which leeside near-surface winds were stronger and the polar föhn jets were considerably broader and extended further downwind above the Larsen C (Figure 4.18ai).

In Figure 5.13a – equivalent to Figure 5.12a but for daytime (15 UTC) during *Case A* – the ice beneath the jets exhibits a cool signature; the opposite of what is seen in Figure 5.12a. This can be explained by a difference in the balance between sensible and latent surface heat fluxes. During nighttime the air-ice temperature gradient is large (a net surface turbulent heat flux of ~90 Wm^{-2} is apparent within the WI jet at 6 UTC on 5 February during *Case A*; Figure 5.14a), incurring a large downward sensible heat flux which dominates over the upward latent heat flux (Figure 5.14c). The net turbulent effect is a warming of the ice beneath the jets. During daytime, the air-ice temperature gradient is much smaller (Figure 5.14a), such that the upward latent heat flux is larger in magnitude than the downward sensible heat flux (a net surface turbulent heat flux of ~-23 Wm^{-2} within the WI jet at 15 UTC

on 5 February; Figure 5.14c). This results in a net turbulent cooling of the ice beneath the jets.

Beneath the wake regions, air-surface decoupling means there is no such turbulent warming at nighttime and turbulent cooling during the day. Consequently a larger amplitude diurnal cycle in surface temperature is apparent beneath the wake regions, and the ice reaches melting point earlier in the day than that beneath the jets (compare Figure 5.14a and Figure 5.15a – as shown in Figure 5.12 and Figure 5.13, differences in surface temperature beneath the WI jet and N of WI wake regions are generally representative of the differences in surface temperature beneath other distinct jet and wake regions).

So, the model suggests there is more melt beneath wakes than beneath jets during a föhn event. However, this result is highly sensitive to the relative quantities of the individual turbulent heat fluxes, and there are no relevant observations in the region with which to verify the accuracy of these simulated fluxes.
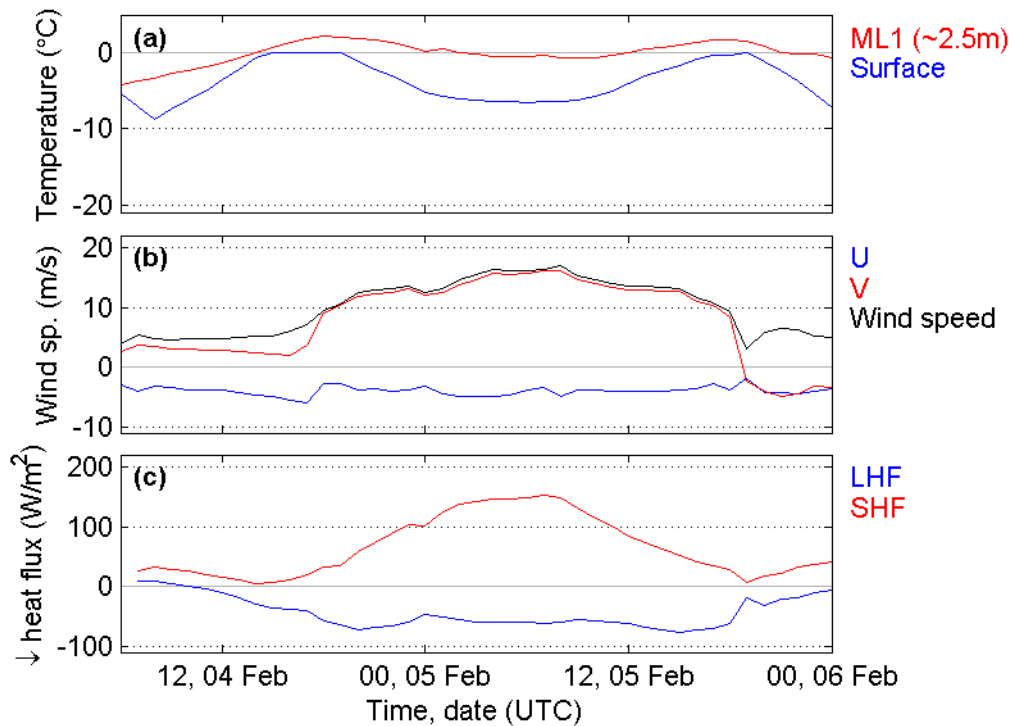
Figure 5.14: Timeseries of a) temperature at ~2.5 m (model level 1) and surface temperature, b) horizontal wind components (U and V) and wind speed at ~2.5 m, and c) downward sensible and latent heat fluxes (SHF and LHF) between ~2.5 m and the surface within the WI jet (location marked in Figure 5.1) during *Case A*. Data is from the MetUM 1.5 km simulation and covers the entire simulation period.
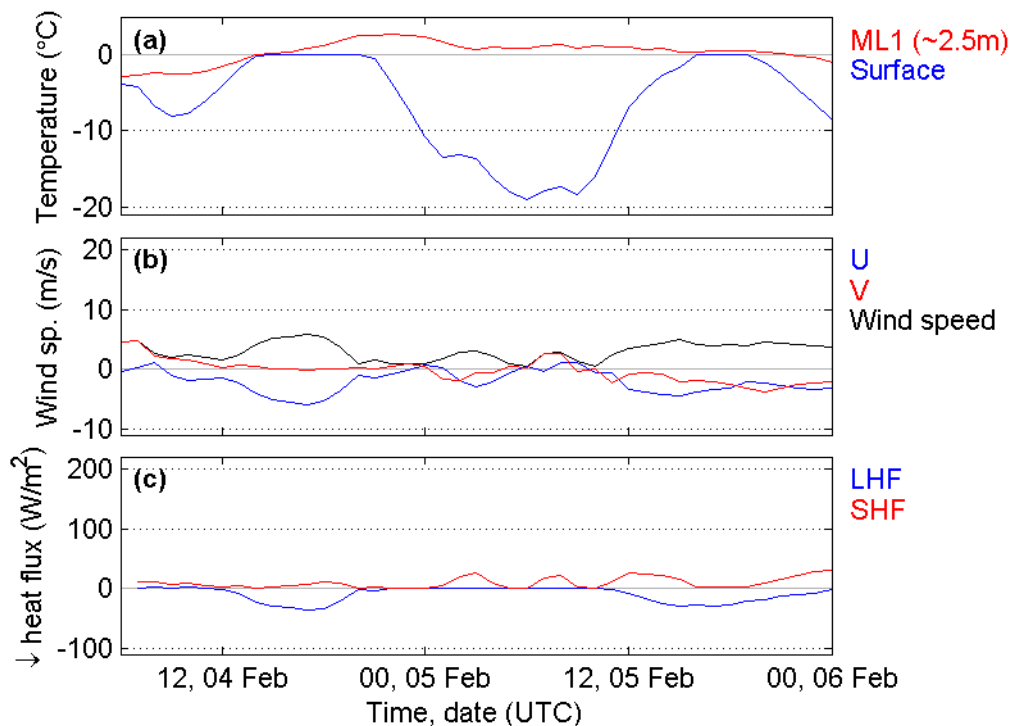
Figure 5.15: As in Figure 5.14 but for the N of WI wake region (location marked in Figure 5.1).

5.4 The relationship between melt rate at Larsen Camp and flow velocity in the vicinity of the AP

In this section we look for a relationship between melt rates on the Larsen C and flow velocity in the vicinity of the AP. From these results we hope to ascertain whether föhn conditions (presumed to be present when there is westerly cross-Peninsula flow) are, as hypothesised, associated with greater melt rates. We will go on to identify whether melt rates are sensitive to different types of föhn event (determined here according to flow speed and direction alone). Are the highest melt rates commonly associated with fast flowing linear föhn events such as *Case C* – characterised by strong northwesterly cross-Peninsula flow?

To address these questions ~14 summer month's worth of M_{ML} data from AWS 14 and ~12 summer months of M_{ML} data from another IMAU-owned AWS to the southwest (AWS 15; for location see Figure 5.16) are used to filter ECMWF ERA-Interim reanalysis (ERA-Interim) wind data at the 750 hPa level (~2.5 km). The 750 hPa level height was chosen as it is deemed to be high enough not to be significantly influenced by local orographic effects, yet not too high as to be unrepresentative of the lower-levels. The three summer periods considered – limited by the duration for which AWS data is available – are 1) 22 January 2009 until 31 March 2009, 2) 1 October 2009 and 31 March 2010, and 3) 1 October 2010 until 31 March 2011 for AWS 14 and 1 October 2010 until 28 January 2011 for AWS 15. Figure 5.16 shows the six locations for which the ERA-Interim wind data is derived. Locations 1, 2 and 3 form a roughly southeast-northwest transect across the AP with location 1 being the closest grid point in the ERA-Interim domain to AWS 14, location 2 being above the AP's crest, and location 3 to the west of the AP. Locations 4 to 6 form a similar transect but oriented east-west and with 4 being the closest grid point to AWS 15. The reason for the addition of AWS 15 to the analysis here is that high melt rate at AWS 14 – located towards the north of the Larsen C – may favour northwesterly föhn events simply due to the closer proximity of the SW-NE-orientated section of the AP ridge (north of ~67° W) than the S-N-orientated section. AWS 15 is located a similar distance from both sections, so this potential bias is avoided. Note that AWS 15 measurements are not used in Section 5.2 since the period for which they are available ends shortly before *Case A*.
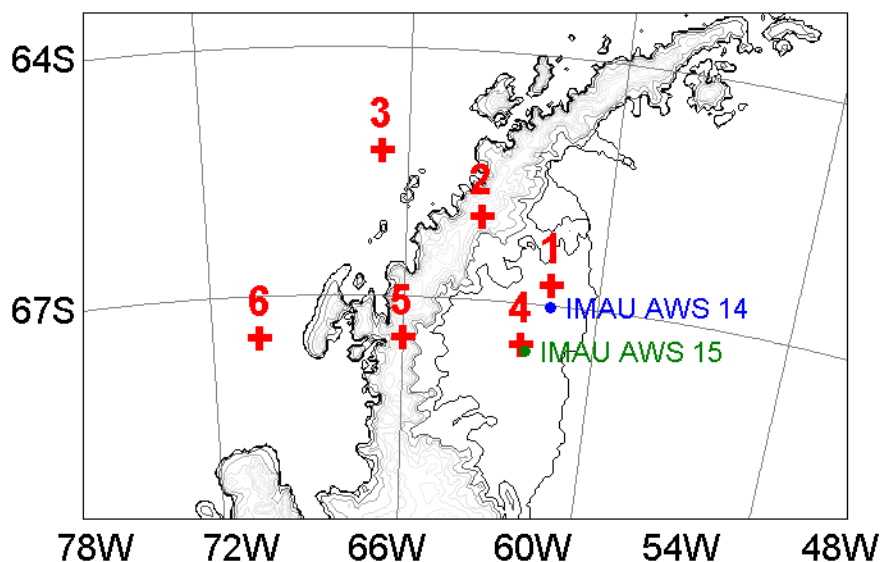
Figure 5.16: Locations (1 to 6) used for the ERA-Interim wind velocity climatology. Also marked are the positions of the two AWSs.

Figure 5.17 and Figure 5.18 consist of wind rose plots of the ERA-Interim wind data at specified locations filtered according to melt rates (given by the quantity M_{ML} output from Kuipers Munneke et al. (2012)'s SEB model) at AWS 14 and AWS 15 respectively. The melt rate thresholds used to confine the wind data are 0 Wm^{-2} (described in the figures as periods of 'melt') and 20 ('significant melt') Wm^{-2}. Also presented for means of comparison is a climatology plot (i.e. no filter; 'summer climatology').

Location 1 (using AWS 14 melt data):
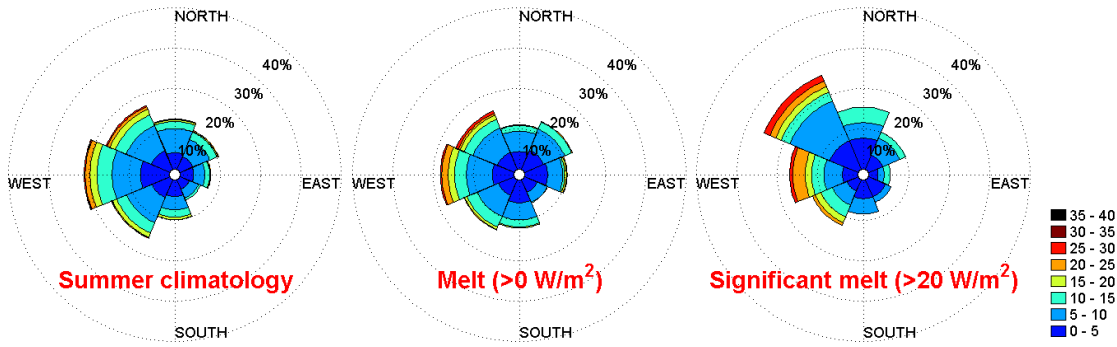
Location 2 (using AWS 14 melt data):
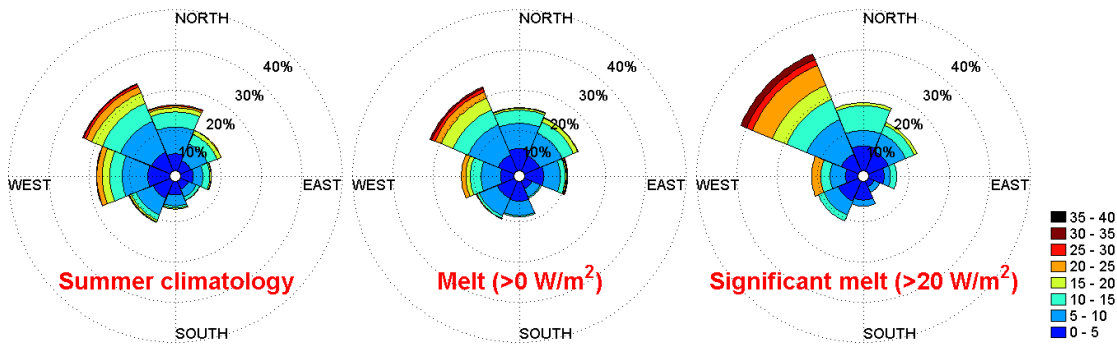
Location 3 (using AWS 14 melt data):
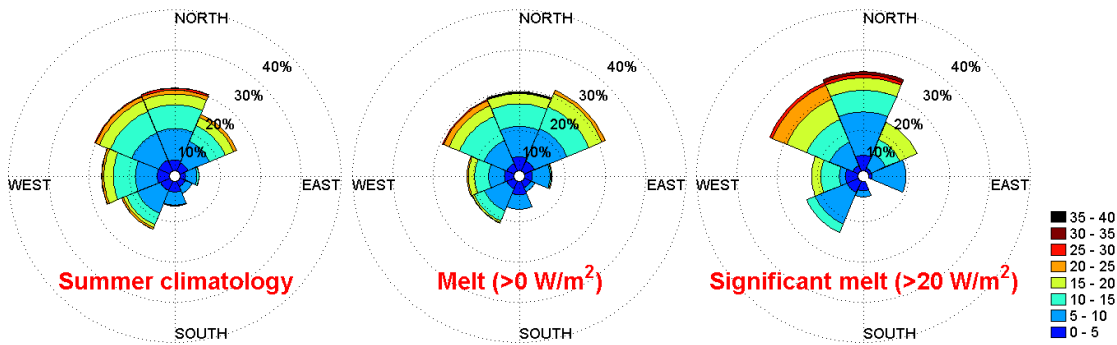
Location 5 (using AWS 14 melt data):
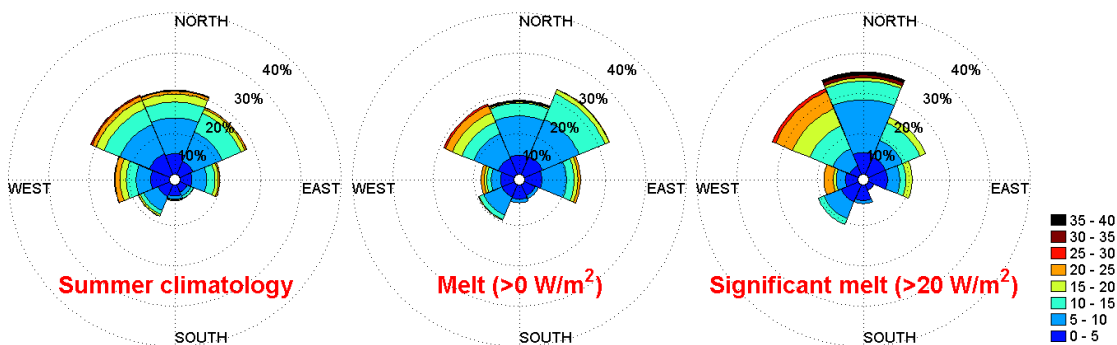
Figure 5.17: Wind rose plots of three summer period's worth of ECMWF ERA-Interim wind field data at the 750 hPa height at locations 1, 2, 3 and 5 (see Figure 5.16). The wind data is constrained by AWS 14 melt rate data. For each location, illustrated are plots for the entire period ('summer climatology'), where there is melt detected at AWS 14 ('melt') and where melt rates exceed 20 Wm^{-2} at AWS 14 ('significant melt').

Location 4 (using AWS 15 melt data):
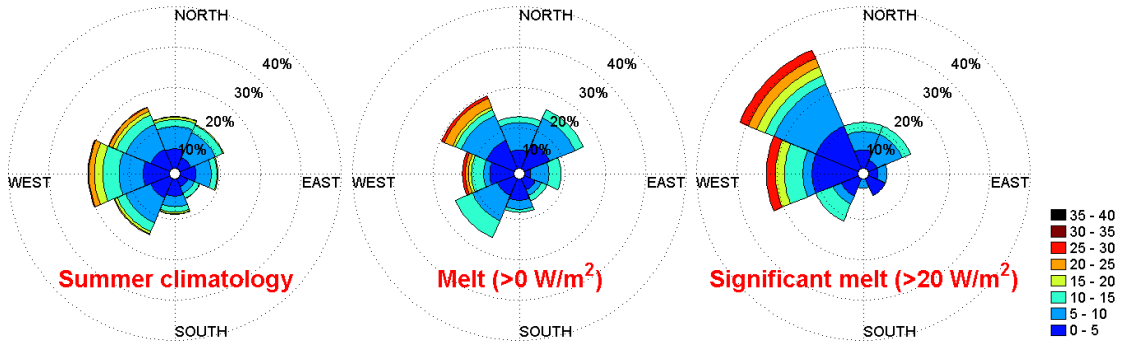
Location 5 (using AWS 15 melt data):
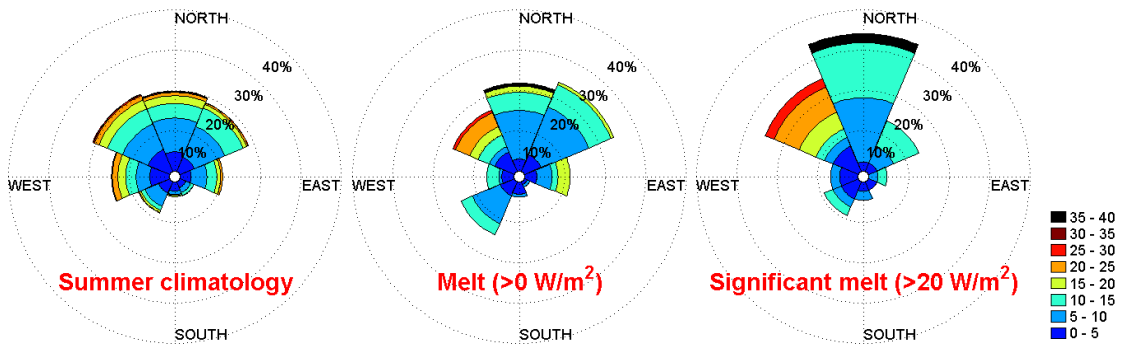
Location 6 (using AWS 15 melt data):
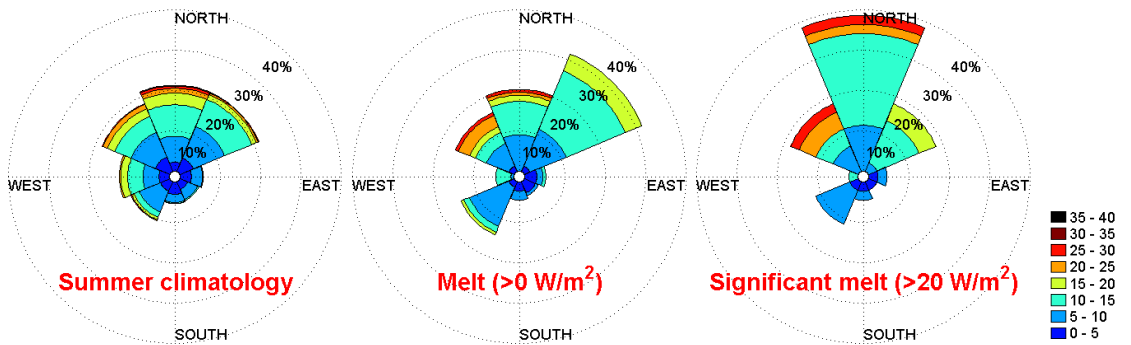
Location 2 (using AWS 15 melt data):
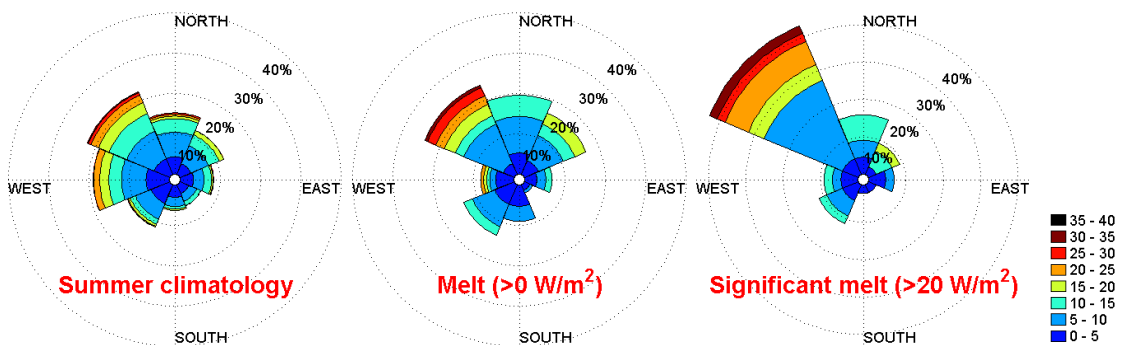
Figure 5.18: As in Figure 5.17 but for locations 4, 5, 6 and 3 (see Figure 5.16). This time the wind data is constrained by AWS 15 melt rate data.

In Figure 5.17 and Figure 5.18, the only discernible consistent difference between the 'melt' and 'summer climatology' plots for all locations shown is greater

northeasterly components of flow; not indicative of föhn conditions on the Larsen C. However, at AWS 14, during periods of 'significant melt' the flow direction is considerably more often than the summer climatological mean from the northwest above the Larsen C at location 1 (consistent with Van den Broeke (2005)'s finding that the highest melt rates are most often associated with northwesterly flow at the BAS AWS at Larsen camp) and above the Peninsula's crest at location 2, and from the northwest and north to the west of the AP at location 3 (Figure 5.17). Moreover, mean wind speeds for these enhanced flow directions are generally stronger during 'significant melt' than usual. Such conditions are indicative of strong northerly and northwesterly mean flow incurring a northwesterly föhn event similar to that of *Case C*, with northwesterly flow across the AP north of ~67°S. Wind data for location 5 is also plotted here, showing increases in the frequency of northerly and northwesterly winds during periods of 'significant melt'. Given the north-south orientation of the AP here (south of ~67°S), this suggests either oblique cross-Peninsula flow or along-Peninsula flow.

Periods of significant melt at AWS 15 are also characterised by an increase (relative to the summer climatological mean) in the occurrence and speed of northwesterly flow across the AP at location 2 (Figure 5.18). Further south above the Peninsula's crest at location 5 the major enhancement is once again in northwesterly and northerly flow, whilst flow from the west is less frequent than usual. West of the Peninsula (at location 6), flow from the north sees the most significant increase in frequency, whilst above AWS 15 itself (location 4), northwesterly and – to a lesser extent – westerly flow is most enhanced in frequency and speed.

Above the crest and to the west of the AP (locations 5 and 6) there is also a notable increase in the frequency of southwesterly flow during periods of 'melt' (> 0 Wm^{-2}) at AWS 15 (Figure 5.18). This enhancement is also apparent, though to a lesser extent, in Figure 5.17 for location 5 during periods of 'melt' at AWS 14. *Case A* is an example of a southwesterly föhn event which incurred moderately high melt rates at AWS 14 (Figure 5.5). Such events are indeed more likely to result in relatively high melt rates at AWS 15 than AWS 14 due to (as previously mentioned) the closer proximity of the former to the south-north orientated section of the AP south of ~67°S, and the subsiding influence of the föhn with distance downwind of the AP.

In summary, wind velocities during periods of high melt rates at the IMAU AWSs are stronger and considerably more often northwesterly than climatologically usual, suggesting that föhn events similar to that seen during *Case C* are the most significant causal mechanism (after the solar cycle) of elevated melting. Southwesterly föhn events such as *Case A* have a lesser though still detectable impact on melt rates. These conclusions support the case study comparisons presented in Section 5.3, which showed *Case C* to be associated with more prolonged melt periods defined by greater melt rates (see Figure 5.5,Figure 5.11 and Figure 5.13).

5.5 Summary and implications

- During polar föhn events on the Larsen C, two mechanisms commonly induce warming of the ice surface; large downward solar radiation due to clear, dry leeside air (the föhn clearance), and large sensible heat fluxes from the air to the ice due to a positive-upwards air-ice temperature gradient. Due to the importance of the former, ice melt only occurs during the day.

- During both cases *A* and *C* solar radiation at the surface was large (though larger in *Case C* due to it occurring closer to the summer solstice), but only in *Case C* did the sensible heat flux contribute to surface warming at Larsen Camp. This positive sensible heat flux was offset by upward latent heat flux such that the total turbulent heat flux was negligible. In *Case A* near-surface conditions on the Larsen C were convective during the daytime (i.e. the ice was warmer than the near-surface air; a common occurrence during the summer on the Larsen C) and both sensible and latent heat fluxes had a cooling effect on the ice surface at Larsen Camp. For this reason periods of ice melt at Larsen Camp were more prolonged and defined by greater melt rates during *Case C* than *Case A*.

- The strong near-surface föhn winds extending across the Larsen C during *Case C*, a linear föhn event, prevented the development or persistence of a surface inversion via turbulent mixing and warm air advection, ensuring near-surface air temperatures remained above ice temperatures. During the weaker föhn flow of *Case A*, a more non-linear föhn event, the winds did not extend to the eastern reaches of the Larsen C at near-surface level. Consequently the combination of turbulent warming and warm air advection in the boundary

layer were considerably less effective in maintaining near-surface air temperatures above the melting point. Moreover, the northwesterly air advected in to the region during *Case C* was warmer than the southwesterly flow during *Case A*.

- The UM generally performs well in its reproduction of near-surface conditions during cases *A* and *C* in a comparison with the AWS observations at Larsen Camp. However, as previously identified in Chapter 3, the influx of föhn air during *Case A* is premature in the model. Also, peak shortwave radiative flux is considerably misrepresented during *Case C* due, it would appear, to a combination of errors in the reproduction of surface albedo and atmospheric absorption of shortwave radiation.

- Due largely to variability in near-surface wind velocities, there is a degree of non-random spatial heterogeneity in simulated surface heat fluxes and ensuing ice temperatures and melt rates above the Larsen C. Within the polar föhn jets, large air to ice sensible heat fluxes and opposing latent heat fluxes (due to sublimation) were found. This is consistent with aircraft observations of cool, moist near-surface conditions within the jets. At nighttime the downward sensible heat flux dominates over the upward latent heat flux, resulting in net turbulent warming of the ice. During the day the opposite is true due to reduced sensible heat flux in association with smaller air-ice temperature gradients (a result of radiative surface warming). Within the wake regions stagnant near-surface conditions lead to a decoupling of air and ice, resulting in much smaller surface fluxes than those beneath the jets. Consequently, relative to adjacent regions, ice beneath jets is simulated to be warm during the night and cool during the day. For this reason there is less melt beneath jets than wakes in the model. Due to a lack of suitable observations it is unknown as to whether these surface energy balance features occur in reality as they do in the model. This remains an open question.

- When melt rates observed during 12 to 14 summer months at two AWSs on the Larsen C are significant (>20 Wm^{-2}), winds above the Larsen C, above the AP ridge and to the west of the AP are stronger and considerably more frequently from the northwest than climatologically usual. This suggests that relatively linear (associated with strong upwind flow) northwesterly föhn

events such as *Case C* are often responsible for high melt rates above the

Larsen C.

Chapter 6

Conclusions

In this study föhn flow above the Larsen C Ice Shelf as a result of westerly flow across the Antarctic Peninsula has been investigated. The predominant approach has been the analysis of individual case studies; making use of observations gathered during the OFCAP (Orographic Flow and Climate of the Antarctic Peninsula) field campaign in conjunction with UK Met Office Unified Model (MetUM) simulations at a minimum horizontal resolution of 1.5 km. Accompanying and giving context to the case study work, a brief climatology section is included. The OFCAP project was motivated by the "föhn hypothesis" for contributing to recent rapid regional warming and ice shelf collapse on the east coast of the Antarctic Peninsula. In addition to addressing this hypothesis, the study also offers new insight into the characteristics of the previously little-studied polar föhn, the sensitivity of leeside warming to upwind conditions and associated flow regimes, and the causes of leeside warming during a föhn event.

Prior to the OFCAP field campaign, observations of föhn flow across the AP had been very limited. The new aircraft, radiosonde and AWS observations presented here thoroughly document the evolution of two westerly polar föhn events. In addition to affording new insight into the spatial and temporal aspects of such events, these measurements have provided model validation, and thus confidence in further case study analysis using the high resolution NWP simulations.

Although there has been much research, both observation and model based, into föhn flow, there has been little in the way of quantitative examination of the amount of leeside warming and the sensitivity of such warming to conditions upwind of the mountains in the undisturbed flow. In the present study, the high resolution model analysis together with Lagrangian analysis (using the trajectory model) has, for the first time, allowed a quantitative evaluation of the relative importance of the

various mechanisms responsible for inducing the föhn warming effect. This is achieved using a novel temperature budget model.

Three case studies of westerly polar föhn (cases *A*, *B* and *C*) have been examined, two of which (cases *A* and *B*) were documented by OFCAP aircraft and radiosonde observations. In all cases the föhn effect was apparent, with leeside temperatures greater, and humidities lower, than those upwind of the AP. Föhn air was able to penetrate to near-surface level, mixing and flushing away any residual cool air which typically pools above the Larsen Ice Shelf.

The MetUM 1.5 km simulations were found, via comparisons with aircraft, radiosonde and AWS observations, to provide reasonably accurate reproductions of the föhn events, such as to justify the contribution of their results towards the understanding of the dynamics of the events. There were a couple of noticeable deficiencies in the model results: the advection of föhn air in *Case A* above the Larsen C was found to be premature in the model, and shortwave radiative flux is considerably misrepresented during *Case C* due, it would appear, to a combination of errors in the reproduction of surface albedo and atmospheric absorption of shortwave radiation.

In *Case A* upwind flow was characterised by non-dimensional mountain height, $\hat{h}$ appreciably greater than 1 and an upwind inversion was present roughly at the height of the AP's crest. Consequently a highly non-linear cross-Peninsula flow regime evolved. Mountain wave breaking and upwind flow blocking was apparent, with föhn air being derived from relatively high elevations upwind. Consequently, the dominant mechanism found to be responsible for föhn warming at the base of the lee slope was isentropic drawdown, i.e. the differential advection of potentially warm dry air from aloft. The presence of strong downslope flow above the lee slopes and a hydraulic jump immediately downwind (both characteristics of a non-linear flow regime) were found to have a significant effect on the leeside spatial distribution of föhn warming. The amplitude of föhn warming was considerably greater close to the base of the lee slopes than further east above the Larsen C, due to hydraulic re-ascent of föhn air.

In *Case C* strong northwesterly, comparatively weakly stratified flow was characterised by $\hat{h}$ of below 1 for a period of about one full day, defining a relatively linear flow regime. Little upwind flow blocking was observed, with föhn trajectories derived from low level to the west of the AP. For this reason, in contrast to *Case A*, the

contribution of isentropic drawdown towards the föhn warming effect was insignificant. This time the dominant föhn warming mechanism was latent heat release due to the ascent from low level of warm (though *potentially* cool relative to the air above), moist maritime air above the windward slope.

The relatively linear flow regime in *Case C* dictates that the relative disturbance of the mountain on the flow was smaller, with less flow acceleration above the lee slope and no hydraulic jump. As such, although characterised by smaller amplitude cross-Peninsula warming close to the base of the lee slope (than in *Case A*), a strong föhn flow was able to extend at low levels across the entire Larsen C with no hydraulic re-ascent. The presence of this low level föhn advection prevented – via turbulent mixing and warm air advection – the development and persistence of a strong nighttime surface inversion beneath the föhn jets and ensured near-surface air temperatures remained above ice temperatures even during the day as the ice surface warmed to melting point. Moreover, the northwesterly air advected in to the region during *Case C* was warmer than the southwesterly flow during *Case A*.

During the weaker föhn flow of *Case A*, such strong föhn winds did not extend to the eastern reaches of the Larsen C at near-surface level. Consequently the combination of turbulent warming and warm air advection in the boundary layer was considerably less effective in maintaining near-surface air temperatures above the melting point. At nighttime near-surface temperatures plummeted and, as expanded upon below, during daytime the near-surface air was cooler than the ice surface below. It is important to note then that in *Case A* the ice has a warming effect on the föhn air away from the APs lee slopes, whereas in *Case C* it has a cooling effect.

Air-ice interaction has been investigated using measurements at an AWS towards the eastern reaches of the Larsen C and output from MetUM 1.5 km simulations. During both cases *A* and *C*, daytime downward SW radiation on the Larsen C was large (though larger in *Case C* due to it occurring closer to the summer solstice) as a result of the clear dry leeside föhn air. However, due to the warmer near-surface air temperatures in *Case C* (as discussed above), only in *Case C* did air-ice sensible heat flux contribute to surface warming across the entirety of the ice shelf. This positive sensible heat flux was offset by upward latent heat flux such that the total turbulent heat flux was negligible. In *Case A* near-surface conditions on the Larsen C were convective during the daytime (i.e. the ice was warmer than the near-

surface air; a common occurrence during the summer on the Larsen C) and both sensible and latent heat fluxes had a cooling effect on the ice surface at Larsen Camp. For these reasons periods of ice melt away from the Peninsula's lee slopes were more prolonged and defined by greater melt rates during *Case C* than *Case A*.

Case B is another non-linear föhn event, though characterised by weaker upwind flow than in *Case A* and no crest-level upwind inversion. The advection of warm föhn air across the Larsen is weaker and there are expansive regions of stagnation at near-surface level, within which air is not (even towards the end of the föhn event) sourced from west of the Peninsula within the preceding 24 hours (i.e. is not föhn-derived). For this reason föhn warming across the AP is comparatively weak in this case.

In *Case B* no one föhn mechanism dominates; which of the three mechanisms provide the greatest contribution towards the cross-Peninsula temperature gradient is dependent upon the section of the AP over which the calculations are made. Indeed, in *Case A*, despite isentropic drawdown constituting the dominant föhn mechanism for all other regions, for one of the trajectory initiation regions – due to greater upwind ascent above the AP's western slopes – the sensible heat mechanism makes marginally the largest warming contribution.

The implication of the temperature budget analysis is that there is no one consistently dominant föhn mechanism; the effects of isentropic drawdown, latent heating and sensible heating are all significant and different mechanisms are dominant for each case. This is contrary to the conclusions of previous studies. Which mechanism dominates depends upon the linearity of the flow regime and the humidity of the approaching air mass (i.e. how much precipitation is available to generate latent heating during ascent). Notably the contribution of warming due to sensible heating along föhn trajectories has been revealed to be significant; a contribution that has generally been overlooked or neglected up until now. These results imply a new paradigm for leeside foehn warming in which the isentropic drawdown, latent heating and sensible heating mechanisms all contribute significantly and are each vital in explaining the leeside response to cross-mountain flow.

During cases of föhn flow across the AP, the near surface flow field immediately to the lee of the AP consists of jets emanating from the mouths of inlets,

separated by regions of calmer flow (referred to as 'wakes' here). These jets above the Larsen C are a new discovery: such features of föhn flow in polar regions had not previously been discussed in the literature. The jets have been named 'polar föhn jets' and revealed to be the downwind continuation of gap flows across lower sections of the AP's ridge. On account of the constituent air being sourced from lower altitudes upwind of the AP, they generally exhibit cooler and moister conditions than the adjacent wake regions. Beneath the polar föhn jets rates of ice sublimation are large in the model simulations, associated with large downward (upward) surface sensible (latent) heat flux. During the night the dominance of the sensible over the latent heat flux acts to insulate the ice shelf. Conversely, during the day, due to a smaller air-ice temperature gradient the latent heat flux is larger than the sensible heat flux. This results in lower melt rates beneath the jets than beneath the wakes at least in the model simulations. Note that these differences in turbulent heat fluxes are small and sensitive, and that there are no relevant surface observations beneath the jets or wakes with which to validate the surface energy budget contrasts that are simulated.

A limited wind climatology has been performed using roughly three summer season's worth (12-14 months) of data from ECMWF ERA-Interim at 6 locations (consisting of 2 cross-Peninsula transects of 3 locations each) at the 750 hPa height. When melt rates detected at AWSs on the Larsen C are significant (>20 Wm^{-2}), winds above the Larsen C, above the AP ridge and to the west of the AP are stronger and considerably more frequently from the northwest than climatologically usual. This suggests that relatively linear (associated with strong cross-Peninsula flow) northwesterly föhn events such as *Case C* are often responsible for particularly high melt rates above the Larsen C; a result which supports the findings of Van den Broeke (2005).

This thesis supports the hypothesis which motivated the OFCAP project: showing that westerly föhn events are associated with leeside warming extending down to near-surface levels, and that high melt rates on the Larsen C can be a consequence. The 'ingredients' required for a föhn event that incurs particularly high leeside melt rates are listed below:

1) Large downward SW radiative flux at the surface, due to:
   - dry cloudless leeside conditions (the 'föhn clearance');

- small solar zenith angle (the closer the timing of the event to the summer solstice the smaller the solar zenith angle).

2) Near-surface temperatures above 0 °C, due to the advection of warm, well mixed föhn air to near-surface level (permitted by the absence of a leeside hydraulic jump, so encouraged by a relatively non-linear flow regime);

3) Non-stagnant near-surface conditions to encourage turbulent air-ice heat exchange.

During the strong northwesterly *Case C* these three 'ingredients' were present and Larsen C melt was indeed significant. The climatology section of this study suggests that such föhn events (associated with strong northwesterly cross-Peninsula flow) may incur the highest melt rates.

It has been established that an increase in the frequency or strength of westerly foehn flows across the AP in association with the recent enhancement of circumpolar westerly winds is likely to be largely responsible for the particularly severe climatic warming observed during the summer to the east of the AP. Stronger mean westerly winds may be causing enhanced melt rates on the Larsen C by not only increasing the frequency of foehn events, but in particular increasing the occurrence of linear foehn events such as Case C, which are encouraged by strong westerly flow and appear to be bring about particularly strong and widespread leeside melting. Indeed the ice shelf collapses in this region – associated with the gradual southern migration of annual-mean isotherms and particularly warm summer seasons – may to a substantial degree be attributed to this phenomenon. The long duration (over a month) of the period of westerly flow during which *Case C* occurred, and the particularly high melt rates and extensive region affected, demonstrates the impact the foehn could have on vulnerable ice shelves. From the conclusions of this study it seems entirely plausible that the particularly warm summer of 2002 – which culminated in extensive melt water ponding and the eventual collapse of the Larsen B – may have been characterised by such a period of sustained westerly foehn. Investigation into the large scale circulation in the vicinity of the AP during this period is required in future work to test this hypothesis.

Although supporting evidence presented in previous work and that presented in the case study sections of this study, confidence in the conclusions drawn from the

climatological work is limited by the short length of time considered. A similar more comprehensive climatological study considering a longer time period would be useful in furthering the understanding of the sensitivity of Larsen C ice melt rates to upwind and synoptic conditions (i.e. the type of föhn event). The ultimate aim here would be towards the ability to forecast the amplitude of leeside warming and ice shelf melt given upwind flow conditions. Indeed, via knowledge of the expected amount and spatial extent of leeside near-surface warming and melting dependent upon the flow regime (which may be diagnosed from upwind characteristics), foehn-induced warming and associated surface heat fluxes and available melt energy could be parameterised in climate models. Such models are otherwise unable to resolve the mesoscale complexities of orographic flows and hence leeside near-surface foehn warming. Furthermore, results from this study have demonstrated the importance of the cloudless 'foehn clearance' in allowing large SW radiative surface fluxes to contribute significantly to leeside ice melt. Evidently the accurate calculation of surface energy budgets during foehn conditions in climate models would require this feature to be correctly accounted for.

Another recommended avenue for future study would be to further investigate the spatial heterogeneity of conditions above and ice melt rates on the Larsen C during westerly föhn flow. Additional near-surface and surface observations within polar föhn jets and wakes would be very useful in verifying or otherwise the simulated differences in surface energy balance components between these regions.

Whether there is comparatively more or less ice melt beneath the inlets through which polar föhn jets flow is an interesting question. As discussed, during strong föhn flow, where the föhn air is able to penetrate to near-surface level downwind of both the high and low sections of the AP (although this result is rather sensitive to environmental conditions) melt rates and durations are simulated to be greater beneath the wakes than the jets. However, it could be that föhn air more commonly reaches surface level within the inlets due to smaller $\hat{h}$ characterising flow across the AP upwind of these inlets (where mountain passes tend to be located, defining comparatively lower mountain height, h).

Although there are several elements to this study which are unique to the specific region and/or more generally to polar regions, many of the findings are applicable elsewhere. How applicable they are could be addressed by using similar

approaches and methods to cases of föhn flow in different regions. Relevant questions include whether polar föhn jets occur elsewhere in polar regions and whether the findings regarding differences in the amount and spatial distribution of föhn warming dependent on upwind conditions are consistent with cases of föhn in other parts of the world.

The use of the temperature budget model used here to quantify the relative importance of the various föhn mechanisms could be of great benefit to föhn theory more generally. For example, are different föhn mechanisms important in different regions? Antarctic air is generally very cool and dry. However, the maritime nature of westerly flow approaching the AP (a narrow continental ridge extending into the ocean) means it is, considering its location, relatively moist. The typically statically stable nature of polar air masses defines relatively large $\hat{h}$ (associated with flow over the AP), leading to a greater height of upwind flow separation, z_d, and enhancing the relative importance of isentropic drawdown towards föhn warming. It could also enhance the relative importance of the sensible heat mechanism via a larger downward exchange of turbulent heat to the ascending flow. In the Alps or the Rockies, the greater height of mountains compared to those of the AP encourages larger $\hat{h}$; however, gap flows defined by smaller $\hat{h}$ may be more common due to the greater large-scale complexity of terrain found in these regions. Such questions demonstrate the numerous regionally variable factors that are important in the assessment of the causes of leeside warming during föhn events.

This study advanced our understanding of the föhn effect in polar regions and its potential to, in the case of the AP, induce climatically important warming and ice melt. It re-examines the föhn warming theory, providing new insight into the causes of leeside warming and overturning the existing paradigm. It is hoped that the many unanswered questions provoked by this study and the potential for the development of ideas and methods contained within it will help to motivate and guide future developments in this field.

Appendix

Investigation into the premature arrival of leeside föhn in the MetUM 1.5 km simulation of *Case A*

Model-based evidence suggests that the unrealistic westerlies found at near-surface level may be associated with the premature onset of downslope flow. A plot of wind speed at 10 metres above surface at 07 UTC on 04.02.11 (1 hour after UM 1.5 km model initiation, 7 hours after UM 4 km initiation; see Section 2.5.1) derived from the UM 1.5 km shows that predominantly weak westerly flow is already simulated above the surface of the Larsen C between the eastern slopes of the AP and the region of strong southerly to southwesterly flow further east (Figure A.1a). Wind vectors above the Peninsula show no indication of broad-scale westerly cross-Peninsula flow at this time, which, together with evidence that the leeside flow is confined to near-surface level (not shown for this time, but evident 9 hours later in Figure 3.7bi) suggests that these jets are likely katabatic in nature. The adiabatic compression heating associated with such flows is evident in Figure A.1b.

By 16 UTC on 4 February 2011 (roughly coincident with the time of the flight 174 *Larsen West* profile) relatively strong westerly winds are simulated above the crest and eastern slope of the AP, diagnostic of cross Peninsula flow (Figure A.1c). The most consistently strong downslope winds are found south of the Avery Plateau (i.e. south of ~67.2°S), as a result of the orientation of the AP relative to the upwind flow and the deflection of southerly to southwesterly flow to the right by Adelaide Island. The shallow (Figure 3.7bi) and relatively cool (compared to the two major jets to the south within Whirlwind Inlet and Mobil Oil Inlet; Figure A.1d) characteristics of the Mill Inlet outflow suggest a still predominantly katabatically-forced flow. Conditions above the Larsen C at an elevation of 150 m are warmer (Figure A.1d) and drier close to the AP (especially in the region downwind of the strongest lee slope winds south of the Avery Plateau) than in the region dominated by strong southerlies further east. This suggests that the weak downslope westerlies present in the model, whether of katabatic or cross-barrier flow origin, may have prematurely eroded the near surface

cold pool, inducing a near-surface warming and drying not evident (at least at *Larsen West*) in the observations.
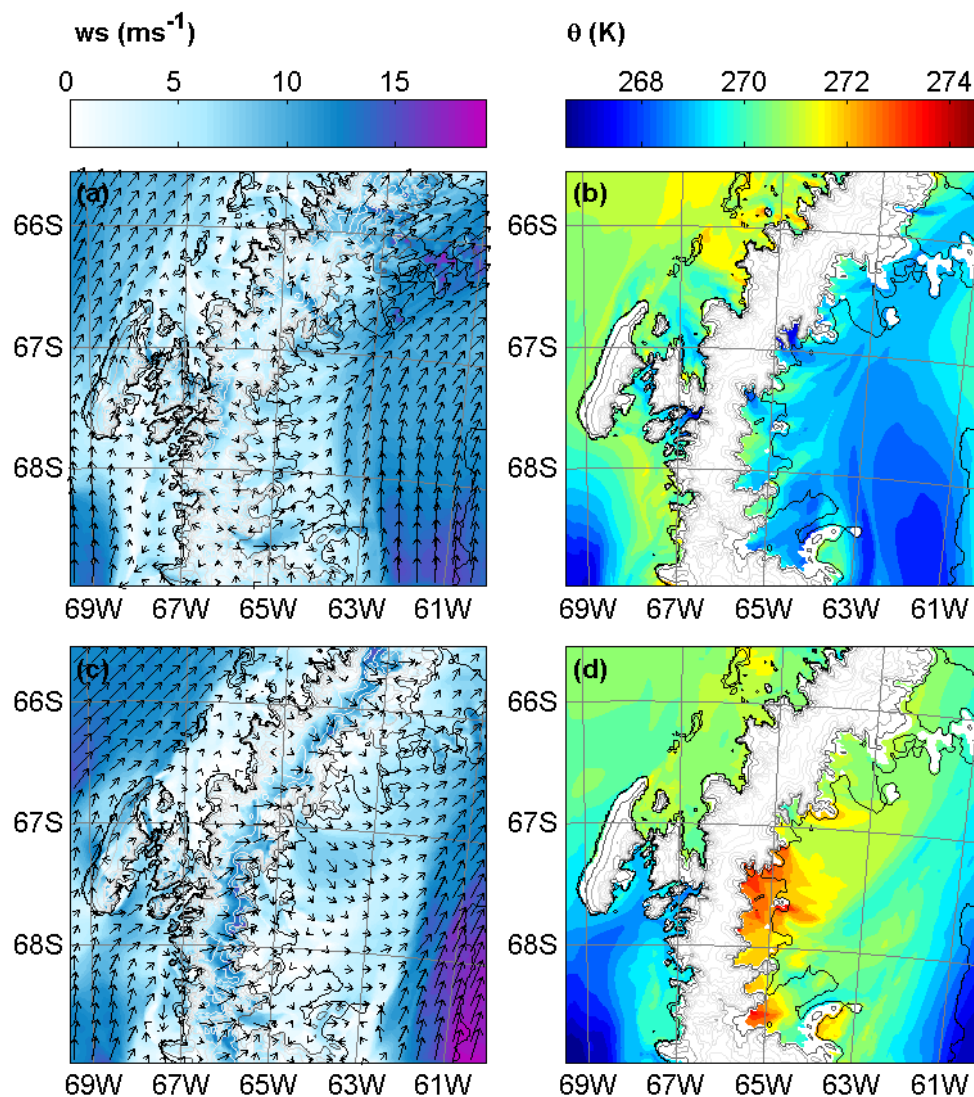
Figure A.1: MetUM 1.5 km simulation of (a and c) wind speed (contours, in ms^{-1}) and vectors (arrows) at 10 m above the surface, and (b and d) temperature (K) at 150 m AMSL at (a and b) 07UTC 4 February and (c and d) 16UTC 4 February.

Additionally, it could be that temperatures above the Larsen C were exaggerated from the outset, i.e. that the cool pool was inadequately represented before any föhn warming took place. However, due to the absence of relevant observational data prior to flight 174, this hypothesis cannot be tested.

References

Andreassen, Ø., Wasberg, C. E., Fritts, D. C., & Isler, J. R. (1994). Gravity wave breaking in two and three dimensions: 1. Model description and comparison of two-dimensional evolutions. *Journal of Geophysical Research: Atmospheres (1984–2012)*, *99*(D4), 8095-8108.

Arakawa, S. (1969). Climatological and dynamical studies on the local strong winds, mainly in Hokkaido, Japan. *Geophys. Mag*, *34*, 359-425.

Bacmeister, J. T., & Pierrehumbert, R. T. (1988). On high-drag states of nonlinear stratified flow over an obstacle. *Journal of the atmospheric sciences*, *45*(1), 63-80.

Baines, P. G. (1987). Upstream blocking and airflow over mountains. *Annual review of fluid mechanics*, *19*(1), 75-95.

Baines, P. G. (1997). *Topographic effects in stratified flows*. Cambridge University Press.

Barstad, I., Grabowski, W. W., & Smolarkiewicz, P. K. (2007). Characteristics of large-scale orographic precipitation: Evaluation of linear model in idealized problems. *Journal of Hydrology*, *340*(1), 78-90.

Bauer, M. H., Mayr, G. J., Vergeiner, I., & Pichler, H. (2000). Strongly nonlinear flow over and around a three-dimensional mountain as a function of the horizontal aspect ratio. *Journal of the atmospheric sciences*, *57*(24), 3971-3991.

Beran, D. W. (1967). Large amplitude lee waves and chinook winds. *Journal of Applied Meteorology*, *6*(5), 865-877.

Berrisford, P., Dee, D. P. K. F., Fielding, K., Fuentes, M., Kallberg, P., Kobayashi, S., & Uppala, S. (2009). The ERA-Interim Archive. *ERA report series*, (1), 1-16.

Birch, C. E., Brooks, I. M., Tjernström, M., Milton, S. F., Earnshaw, P., Söderberg, S., & Persson, P. O. G. (2009). The performance of a global and mesoscale model over the central Arctic Ocean during late summer. *Journal of Geophysical Research: Atmospheres (1984–2012)*, *114*(D13).

Bougeault, P., Binder, P., Buzzi, A., Dirks, R., Houze, R., Kuettner, J., ... & Volkert, H. (2001). The MAP special observing period. *Bull. Amer. Meteor. Soc*, *82*(3), 433-462.

Bower, J. B., & Durran, D. R. (1986). A study of wind profiler data collected upstream during windstorms in Boulder, Colorado. *Monthly weather review*, *114*(8), 1491-1500.

Brinkmann, W. A. (1974). Strong downslope winds at Boulder, Colorado. *Monthly Weather Review*, *102*(8), 592-602.

Broeke, van den, M. R. (2000). On the interpretation of Antarctic temperature trends. *Journal of Climate*, *13*(21), 3885-3889.

Broeke, van den, M. R. (2005). Strong surface melting preceded collapse of Antarctic Peninsula ice shelf. *Geophysical Research Letters*, *32*(12).

Broeke, van den, M. R., & Van Lipzig, N. P. (2004). Changes in Antarctic temperature, wind and precipitation in response to the Antarctic Oscillation. *Annals of Glaciology*, *39*(1), 119-126.

Campana, M., Li, Y., Staehelin, J., Prevot, A. S., Bonasoni, P., Loetscher, H., & Peter, T. (2005). The influence of south foehn on the ozone mixing ratios at the high alpine site Arosa. *Atmospheric Environment*, *39*(16), 2945-2955.

Clark, T. L., & Peltier, W. R. (1977). On the evolution and stability of finite-amplitude mountain waves. *Journal of the Atmospheric Sciences*, *34*(11), 1715-1730.

Clark, T. L., & Peltier, W. R. (1984). Critical level reflection and the resonant growth of nonlinear mountain waves. *Journal of the Atmospheric Sciences*, *41*(21), 3122-3124.

Clark, T. L., Hall, W. D., Kerr, R. M., Middleton, D., Radke, L., Ralph, F. M., ... & Levinson, D. (2000). Origins of aircraft-damaging clear-air turbulence during the 9 December 1992 Colorado downslope windstorm: Numerical simulations and comparison with observations. *Journal of the atmospheric sciences*, *57*(8), 1105-1131.

Colle, B. A., & Mass, C. F. (1998). Windstorms along the western side of the Washington Cascade Mountains. Part I: A high-resolution observational and modeling study of the 12 February 1995 event. *Monthly weather review*, *126*(1), 28-52.

Cook, A. J., Fox, A. J., Vaughan, D. G., & Ferrigno, J. G. (2005). Retreating glacier fronts on the Antarctic Peninsula over the past half-century. *Science*, *308*(5721), 541-544.

Cook, A. J., & Vaughan, D. G. (2010). Overview of areal changes of the ice shelves on the Antarctic Peninsula over the past 50 years. *The Cryosphere, Volume 4, Issue 1, 2010, pp. 77-98*, *4*, 77-98.

Cullen, M. J. P. (1993). A unified forecast climate model. *Meteorological Magazine*, *122*, 81–94.

Cullen, M. J. P., Davies, T., Mawson, M. H., James, J. A., Coulter, S. C., & Malcolm, A. (1997). An overview of numerical methods for the next generation UK NWP and climate model. *Atmosphere-Ocean*, *35*(sup1), 425-444.

Davies, T., Cullen, M. J. P., Malcolm, A. J., Mawson, M. H., Staniforth, A., White, A. A., & Wood, N. (2005). A new dynamical core for the Met Office's global and regional modelling of the atmosphere. *Quarterly Journal of the Royal Meteorological Society*, *131*(608), 1759-1782.

Dee, D. P., & Uppala, S. (2009). Variational bias correction of satellite radiance data in the ERA-Interim reanalysis. *Quarterly Journal of the Royal Meteorological Society*, *135*(644), 1830-1841.

Ding, L., Calhoun, R. J., & Street, R. L. (2003). Numerical simulation of strongly stratified flow over a three-dimensional hill. *Boundary-layer meteorology*, *107*(1), 81-114.

Doyle, J. D., Shapiro, M. A., Jiang, Q., & Bartels, D. L. (2005). Large-amplitude mountain wave breaking over Greenland. *Journal of the atmospheric sciences*, *62*(9), 3106-3126.

Doyle, J. D., & Durran, D. R. (2002). The dynamics of mountain-wave-induced rotors. *Journal of the atmospheric sciences*, *59*(2), 186-201.

Doyle, J. D., & Shapiro, M. A. (1999). Flow response to large-scale topography: The Greenland tip jet. *Tellus A*, *51*(5), 728-748.

Drobinski, P., Haeberli, C., Richard, E., Lothon, M., Dabas, A. M., Flamant, P. H., ... & Steinacker, R. (2003). Scale interaction processes during the MAP IOP 12 south föhn event in the Rhine Valley. *Quarterly Journal of the Royal Meteorological Society*, *129*(588), 729-753.

Dunkerton, T. (1980). A Lagrangian mean theory of wave, mean-flow interaction with applications to nonacceleration and its breakdown. *Reviews of Geophysics*, *18*(2), 387-400.

Durran, D. R. (1986). Another Look at Downslope Windstorms. Part I: The Development of Analogs to Supercritical Flow in an Infinitely Deep, Continuously Stratified Fluid. *Journal of the Atmospheric Sciences*, *43*, 2527–2543.

Durran, D. R. (1990). Mountain waves and downslope winds. In: Blumen, B., ed. Atmospheric processes over complex terrain. *American Meteorological Society*, 59-81.

Durran, D. R. (1992). Two-Layer Solutions to Long's Equation For Vertically Propagating Mountain Waves: How Good Is Linear Theory?. *Quarterly Journal of the Royal Meteorological Society*, *118*(505), 415-433.

Durran, D. R. (2003). Lee waves and mountain waves. *The Encyclopedia of the Atmospheric Sciences*, 1161-1169.

Durran, D. R., & Klemp, J. B. (1982). On the effects of moisture on the Brunt-Väisälä frequency. *Journal of the Atmospheric Sciences*, *39*(10), 2152-2158.

Durran, D. R., & Klemp, J. B. (1987). Another look at downslope winds. Part II: Non-linear amplication beneath wave-overturning layers. *Journal of the Atmospheric Sciences*, *44*, 3402-3412.

Eliassen, A., & Palm, E. (1961). On the transfer of energy in stationary mountain waves. *Geofysiske Publikasjoner*, *22*, 1-23.

Epifanio, C. C., & Durran, D. R. (2001). Three-dimensional effects in high-drag-state flows over long ridges. *Journal of the atmospheric sciences*, *58*(9), 1051-1065.

Ficker, H. (1920). *Der Einfluß der Alpen auf Fallgebiete des Luftdruckes und die Entstehung von Depressionen über dem Mittelmeer*. Vieweg.

Flamant, C., Drobinski, P., Nance, L., Banta, R., Darby, L., Dusek, J., ... & Richard, E. (2002). Gap flow in an Alpine valley during a shallow south föhn event: Observations,

numerical simulations and hydraulic analogue. *Quarterly Journal of the Royal Meteorological Society*, *128*(582), 1173-1210.

Fritts, D. C., Wang, L., & Tolson, R. H. (2006). Mean and gravity wave structures and variability in the Mars upper atmosphere inferred from Mars Global Surveyor and Mars Odyssey aerobraking densities. *Journal of geophysical research*, *111*(A12), A12304.

Fueglistaler, S., Buss, S., Luo, B. P., Wernli, H., Flentje, H., Hostetler, C. A., ... & Peter, T. (2003). Detailed modeling of mountain wave PSCs. *Atmos. Chem. Phys*, *3*, 697-712.

Gohm, A., Mayr, G. J., Fix, A., & Giez, A. (2008). On the onset of bora and the formation of rotors and jumps near a mountain gap. *Quarterly Journal of the Royal Meteorological Society*, *134*(630), 21-46.

Gray, S. L. (2006). Mechanisms of midlatitude cross-tropopause transport using a potential vorticity budget approach. *Journal of geophysical research*, *111*(D17), D17113.

Greed, G. (2010). Unified Model Basic User Guide: Introduction (1-24). Retrieved March 1, 2013, from http://cms.ncas.ac.uk/documents/vn7.x/p000_73.pdf

Grubišíc, V. (2004). Bora-driven potential vorticity banners over the Adriatic. *Quarterly Journal of the Royal Meteorological Society*, *130*(602), 2571-2603.

Hamann, R. R. (1943). The Remarkable Temperature Fluctuations in the Black Hills Region, January 1943*. *Monthly Weather Review*, *71*, 29.

Hann, J. (1866). Zur Frage über den Ursprung des Föhn. *Zeitschrift der österreichischen Gesellschaft für Meteorologie*, *1*(1), 257-263.

Hann, J. (1901). *Lehrbuch der meteorologie* (1st edition). CH Tauchnitz.

Hegglin, M. I., Brunner, D., Wernli, H., Schwierz, C., Martius, O., Hoor, P., ... & Peter, T. (2004). Tracing troposphere-to-stratosphere transport above a mid-latitude deep convective system. *Atmos. Chem. Phys*, *4*(3), 741-756.

Hertenstein, R. F., & Kuettner, J. P. (2005). Rotor types associated with steep lee topography: Influence of the wind profile. *Tellus A*, *57*(2), 117-135.

Hoinka, K. P. (1980). Synoptic-scale atmospheric features and foehn. *Beitraege zur Physik der Atmosphaere*, *53*(4), 486-508.

Hoinka, K. P. (1985). Observation of the airflow over the Alps during a foehn event. *Quarterly Journal of the Royal Meteorological Society*, *111*(467), 199-224.

Holland, M. M., & Raphael, M. N. (2006). Twentieth century simulation of the southern hemisphere climate in coupled models. Part II: sea ice conditions and variability. *Climate Dynamics*, *26*(2-3), 229-245.

Holton, J. (2004). Dynamic meteorology.

Hunt, J. C. R., & Snyder, W. H. (1980). Experiments on stably and neutrally stratified flow over a model three-dimensional hill. *Journal of Fluid Mechanics*, *96*(04), 671-704.

Huppert, H. E., & Miles, J. W. (1969). Lee waves in a stratified flow. Part 3. Semi-elliptical obstacle. *J. Fluid Mech*, *35*, 481-496.

Jaubert, G., & Stein, J. (2003). Multiscale and unsteady aspects of a deep foehn event during MAP. *Quarterly Journal of the Royal Meteorological Society*, *129*(588), 755-776.

Jiang, Q., & Doyle, J. D. (2005). Wave breaking induced surface wakes and jets observed during a bora event. *Geophysical research letters*, *32*(17).

Jones, C. N., Colton, J. D., McAnelly, R. L., & Meyers, M. P. (2002). An examination of a severe downslope windstorm west of the Colorado Park Range. *NATIONAL WEATHER DIGEST*, *26*(3/4), 73-81.

King, J. C. (1994). Recent climate variability in the vicinity of the Antarctic Peninsula. *International journal of climatology*, *14*(4), 357-369.

King, J. C., & Comiso, J. C. (2003). The spatial coherence of interannual temperature variations in the Antarctic Peninsula. *Geophysical Research Letters*, *30*(2).

King, J. C., & Harangozo, S. A. (1998). Climate change in the western Antarctic Peninsula since 1945: observations and possible causes. *Annals of Glaciology*, *27*, 571-575.

Klemp, J. B., & Lilly, D. R. (1975). The dynamics of wave-induced downslope winds. *Journal of Atmospheric Sciences*, *32*, 320-339.

King, J. C., Lachlan-Cope, T. A., Ladkin, R. S., & Weiss, A. (2008). Airborne measurements in the stable boundary layer over the Larsen Ice Shelf, Antarctica. *Boundary-layer meteorology*, *127*(3), 413-428.

Kuipers Munneke, P., Van den Broeke, M. R., King, J. C., Gray, T., & Reijmer, C. H. (2012). Near-surface climate and surface energy budget of Larsen C ice shelf, Antarctic Peninsula. *The Cryosphere*, *6*(2), 353-363.

Ladkin, R. S. MASIN Instruments. Retrieved March 1 2013, from http://www.camracers.org.uk/masin/instruments.php

Lilly, D. K. (1978). A severe downslope windstorm and aircraft turbulence event induced by a mountain wave. *Journal of the Atmospheric Sciences*, *35*(1), 59-77.

Lilly, D. K., & Klemp, J. B. (1979). The effects of terrain shape on nonlinear hydrostatic mountain waves. *Journal of Fluid Mechanics*, *95*, 241-261.

Lipzig, van, N. P. M., Turner, J., Colwell, S. R., & van Den Broeke, M. R. (2004). The near-surface wind field over the Antarctic continent. *International Journal of Climatology*, *24*(15), 1973-1982.

Lipzig, van, N. P. M., Marshall, G. J., Orr, A., & King, J. C. (2008). The relationship between the Southern Hemisphere Annular Mode and Antarctic Peninsula summer

temperatures: Analysis of a high-resolution model climatology. *Journal of climate*, *21*(8), 1649-1668.

Long, R. R. (1953). Some aspects of the flow of stratified fluids: I. A theoretical investigation. *Tellus*, *5*(1), 42-58.

Long, R. R. (1954). Some Aspects of the Flow of Stratified Fluids: II. Experiments with a Two-Fluid System. *Tellus*, *6*(2), 97-115.

Long, R. R. (1955). Some aspects of the flow of stratified fluids. III. Continuous density gradients. *Tellus*, *7*, 341.

Marshall, G. J. (2002). Trends in Antarctic geopotential height and temperature: A comparison between radiosonde and NCEP-NCAR reanalysis data. *Journal of Climate*, *15*(6), 659-674.

Marshall, G. J. (2003). Trends in the Southern Annular Mode from observations and reanalyses. *Journal of Climate*, *16*(24), 4134-4143.

Marshall, G. J., Lagun, V., & Lachlan-Cope, T. A. (2002). Changes in Antarctic Peninsula tropospheric temperatures from 1956 to 1999: a synthesis of observations and reanalysis data. *International Journal of Climatology*, *22*(3), 291-310.

Marshall, G. J., Orr, A., Van Lipzig, N. P., & King, J. C. (2006). The impact of a changing Southern Hemisphere Annular Mode on Antarctic Peninsula summer temperatures. *Journal of Climate*, *19*(20), 5388-5404.

Mass, C. F., & Albright, M. D. (1985). A severe windstorm in the lee of the Cascade Mountains of Washington State. *Monthly weather review*, *113*(8), 1261-1281.

Math, F. A. (1934). Battle of the Chinook Wind at Havre, Mont. *Monthly Weather Review*, *62*, 54.

Meredith, M. P., & King, J. C. (2005). Rapid climate change in the ocean west of the Antarctic Peninsula during the second half of the 20th century. *Geophysical Research Letters*, *32*(19).

Moore, G. W. K., & Renfrew, I. A. (2005). Tip jets and barrier winds: A QuikSCAT climatology of high wind speed events around Greenland. *Journal of Climate*, *18*(18), 3713-3725.

Morris, E. M., & Vaughan, D. G. (2003). *Spatial and temporal variation of surface temperature on the Antarctic Peninsula and the limit of viability of ice shelves* (Vol. 79, pp. 61-68). American Geophysical Union.

Nicholls, K. W., Abrahamsen, E. P., Buck, J. J. H., Dodd, P. A., Goldblatt, C., Griffiths, G., ... & Wilkinson, J. P. (2006). Measurements beneath an Antarctic ice shelf using an autonomous underwater vehicle. *Geophysical Research Letters*, *33*(8).

Nylen, T. H., Fountain, A. G., & Doran, P. T. (2004). Climatology of katabatic winds in the McMurdo dry valleys, southern Victoria Land, Antarctica. *Journal of Geophysical Research: Atmospheres (1984–2012)*, *109*(D3).

Ólafsson, H., & Bougeault, P. (1996). Nonlinear flow past an elliptic mountain ridge. *Journal of the atmospheric sciences*, *53*(17), 2465-2489.

Ólafsson, H., & Bougeault, P. (1997). The effect of rotation and surface friction on orographic drag. *Journal of the atmospheric sciences*, *54*(1), 193-210.

Orr, A., Cresswell, D., Marshall, G. J., Hunt, J. C. R., Sommeria, J., Wang, C. G., & Light, M. (2004). A 'low-level' explanation for the recent large warming trend over the western Antarctic Peninsula involving blocked winds and changes in zonal circulation. *Geophysical research letters*, *31*(6).

Orr, A., Marshall, G. J., Hunt, J. C., Sommeria, J., Wang, C. G., Van Lipzig, N. P., ... & King, J. C. (2008). Characteristics of summer airflow over the Antarctic Peninsula in response to recent strengthening of westerly circumpolar winds. *Journal of the atmospheric sciences*, *65*(4), 1396-1413.

Overland, J. E., & Walter Jr, B. A. (1981). Gap winds in the Strait of Juan de Fuca. *Monthly Weather Review*, *109*(10), 2221-2233.

Pan, F., & Smith, R. B. (1999). Gap winds and wakes: SAR observations and numerical simulations. *Journal of the Atmospheric Sciences*, *56*(7), 905-923.

Parish, T. R. (1983). The influence of the Antarctic Peninsula on the wind field over the western Weddell Sea. *Journal of Geophysical Research: Oceans (1978–2012)*, *88*(C4), 2684-2692.

Peltier, W. R., & Clark, T. L. (1979). The evolution and stability of finite-amplitude mountain waves. Part II: Surface wave drag and severe downslope windstorms. *J. Atmos. Sci*, *36*(8), 1498-1529.

Peltier, W. R., & Clark, T. L. (1983). Nonlinear mountain waves in two and three spatial dimensions. *Quarterly Journal of the Royal Meteorological Society*, *109*(461), 527-548.

Phillips, D. S. (1984). Analytical surface pressure and drag for linear hydrostatic flow over three-dimensional elliptical mountains. *Journal of the atmospheric sciences*, *41*(6), 1073-1084.

Preusse, P., Ern, M., Eckermann, S. D., Warner, C. D., Picard, R. H., Knieling, P., ... & Riese, M. (2006). Tropopause to mesopause gravity waves in August: Measurement and modeling. *Journal of atmospheric and solar-terrestrial physics*, *68*(15), 1730-1751.

Queney, P. (1947). *Theory of perturbations in stratified currents with applications to air flow over mountain barriers*. University of Chicago Press.

Rabier, F., McNally, A., Andersson, E., Courtier, P., Undén, P., Eyre, J., ... & Bouttier, F. (1998). The ECMWF implementation of three-dimensional variational assimilation (3D-Var). II: Structure functions. *Quarterly Journal of the Royal Meteorological Society*, *124*(550), 1809-1829.

Reed, T. R. (1931). Gap winds of the Strait of Juan de Fuca. *Monthly Weather Review*, *59*(10), 373-376.

Renfrew, I. A., & Anderson, P. S. (2006). Profiles of katabatic flow in summer and winter over Coats Land, Antarctica. *Quarterly Journal of the Royal Meteorological Society*, *132*(616), 779-802.

Saito, K. (1993). A numerical study of the local downslope wind Yamaji-kaze'in Japan. II: Non-linear aspect of the 3-D flow over a mountain range with a col. *Journal of the Meteorological Society of Japan*, *71*(2), 247-271.

Schär, C., & Smith, R. B. (1993). Shallow-water flow past isolated topography. Part I: Vorticity production and wake formation. *Journal of the atmospheric sciences*, *50*(10), 1373-1400.

Schwerdtfeger, W. (1974). Mountain barrier effect on the flow of stable air north of the Brooks Range. In *Proceedings of the 24th Alaskan Science Conference* (pp. 204-208).

Schwerdtfeger, W. (1975). The effect of the Antarctic Peninsula on the temperature regime of the Weddell Sea. *Monthly Weather Review*, *103*(1), 45-51.

Scorer, R. S. (1949). Theory of waves in the lee of mountains. *Quarterly Journal of the Royal Meteorological Society*, *75*(323), 41-56.

Seibert, P. (1990). South foehn studies since the ALPEX experiment. *Meteorology and Atmospheric Physics*, *43*(1-4), 91-103.

Sheppard, P. A. (1956). Airflow over mountains. *Quarterly Journal of the Royal Meteorological Society*, *82*, 528–529.

Shutts, G. (1992). Observations and numerical model simulation of a partially trapped lee wave over the Welsh mountains. *Monthly weather review*, *120*(9), 2056-2066.

Shutts, G., & Broad, A. (1993). A case study of lee waves over the Lake District in northern England. *Quarterly Journal of the Royal Meteorological Society*, *119*(511), 377-408.

Smith, C. M., & Skyllingstad, E. D. (2011). Effects of inversion height and surface heat flux on downslope windstorms. *Monthly Weather Review*, *139*(12), 3750-3764.

Smith, R. B. (1979). The influence of mountains on the atmosphere. *Advances in geophysics.*, *21*, 87-230.

Smith, R. B. (1980). Linear theory of stratified hydrostatic flow past an isolated mountain. *Tellus*, *32*(4), 348-364.

Smith, R. B. (1982). Synoptic observations and theory of orographically disturbed wind and pressure. *Journal of the Atmospheric Sciences*, *39*(1), 60-70.

Smith, R. B. (1985). On severe downslope winds. *Journal of the atmospheric sciences*, *42*(23), 2597-2603.

Smith, R. B. (1987). Aerial observations of the Yugoslavian bora. *Journal of the atmospheric sciences*, *44*(2), 269-297.

Smith, R. B. (1989a). Mountain-induced stagnation points in hydrostatic flow. *Tellus A*, *41*(3), 270-274.

Smith, R. B. (1989b). Hydrostatic airflow over mountains. *Advances in Geophysics*, *31*, 1-41.

Smith, R. B., & Grønås, S. (1993). Stagnation points and bifurcation in 3-D mountain airflow. *Tellus A*, *45*(1), 28-43.

Smith, S. A. (2004). Observations and simulations of the 8 November 1999 MAP mountain wave case. *Quarterly Journal of the Royal Meteorological Society*, *130*(599), 1305-1325.

Smolarkiewicz, P. K., & Rotunno, R. (1990). Low Froude number flow past three-dimensional obstacles. Part II: Upwind flow reversal zone. *Journal of the Atmospheric Sciences*, *47*(12), 1498-1511.

Snyder, W. H. (1985). Fluid modeling of pollutant transport and diffusion in stably stratified flows over complex terrain. *Annual review of fluid mechanics*, *17*(1), 239-266.

Sprenger, M., & Schär, C. (2001). Rotational aspects of stratified gap flows and shallow föhn. *Quarterly Journal of the Royal Meteorological Society*, *127*(571), 161-187.

Sprenger, M., Maspoli, M. C., & Wernli, H. (2003). Tropopause folds and cross-tropopause exchange: A global investigation based upon ECMWF analyses for the time period March 2000 to February 2001. *Journal of geophysical research*, *108*(D12), 8518.

Steig, E. J., Schneider, D. P., Rutherford, S. D., Mann, M. E., Comiso, J. C., & Shindell, D. T. (2009). Warming of the Antarctic ice-sheet surface since the 1957 International Geophysical Year. *Nature*, *457*(7228), 459-462.

Svejkovsky, J. (1985). Santa Ana airflow observed from wildfire smoke patterns in satellite imagery. *Monthly Weather Review*.

Thompson, D. W., & Solomon, S. (2002). Interpretation of recent Southern Hemisphere climate change. *Science*, *296*(5569), 895-899.

Trombetti, F., & Tampieri, F. (1987). An application of the dividing-streamline concept to the stable airflow over mesoscale mountains. *Monthly weather review*, *115*(8), 1802-1806.

Vaughan, D. G., Marshall, G. J., Connolley, W. M., King, J. C., & Mulvaney, R. (2001). Devil in the detail. *Science*, *293*(5536), 1777-1779.

Vaughan, D. G., Marshall, G. J., Connolley, W. M., Parkinson, C., Mulvaney, R., Hodgson, D. A., ... & Turner, J. (2003). Recent rapid regional climate warming on the Antarctic Peninsula. *Climatic change*, *60*(3), 243-274.

Vosper, S. B. (2004). Inversion effects on mountain lee waves. *Quarterly Journal of the Royal Meteorological Society*, *130*(600), 1723-1748.

Webster, S., Uddstrom, M., Oliver, H., & Vosper, S. (2008). A high-resolution modelling case study of a severe weather event over New Zealand. *Atmospheric Science Letters*, *9*(3), 119-128.

Wells, H., Webster, S., & Brown, A. (2005). The effect of rotation on the pressure drag force produced by flow around long mountain ridges. *Quarterly Journal of the Royal Meteorological Society*, *131*(608), 1321-1338.

Wernli, B. H., & Davies, H. C. (1997). A Lagrangian-based analysis of extratropical cyclones. I: The method and some applications. *Quarterly Journal of the Royal Meteorological Society*, *123*(538), 467-489.

Woods, B. K., & Smith, R. B. (2010). Energy flux and wavelet diagnostics of secondary mountain waves. *Journal of the Atmospheric Sciences*, *67*(11), 3721-3738.

Wu, D. L., & Eckermann, S. D. (2008). Global gravity wave variances from Aura MLS: Characteristics and interpretation. *Journal of the Atmospheric Sciences*, *65*(12), 3695-3718.

Yoshino, M. (1975). Climate in a small area: an introduction to local meteorology (p. 549). *Tokyo: University of Tokyo Press*.

Zängl, G. (2002). Idealized numerical simulations of shallow föhn. *Quarterly Journal of the Royal Meteorological Society*, *128*(580), 431-450.

Zängl, G. (2003). Deep and shallow south foehn in the region of Innsbruck: Typical features and semi-idelized numerical simulations. *Meteorology and Atmospheric Physics*, *83*(3-4), 237-261.

Zängl, G., Chimani, B., & Häberli, C. (2004). Numerical simulations of the foehn in the Rhine Valley on 24 October 1999 (MAP IOP 10). *Monthly weather review*, *132*(1), 368-389.